Taylor-Couette turbulence

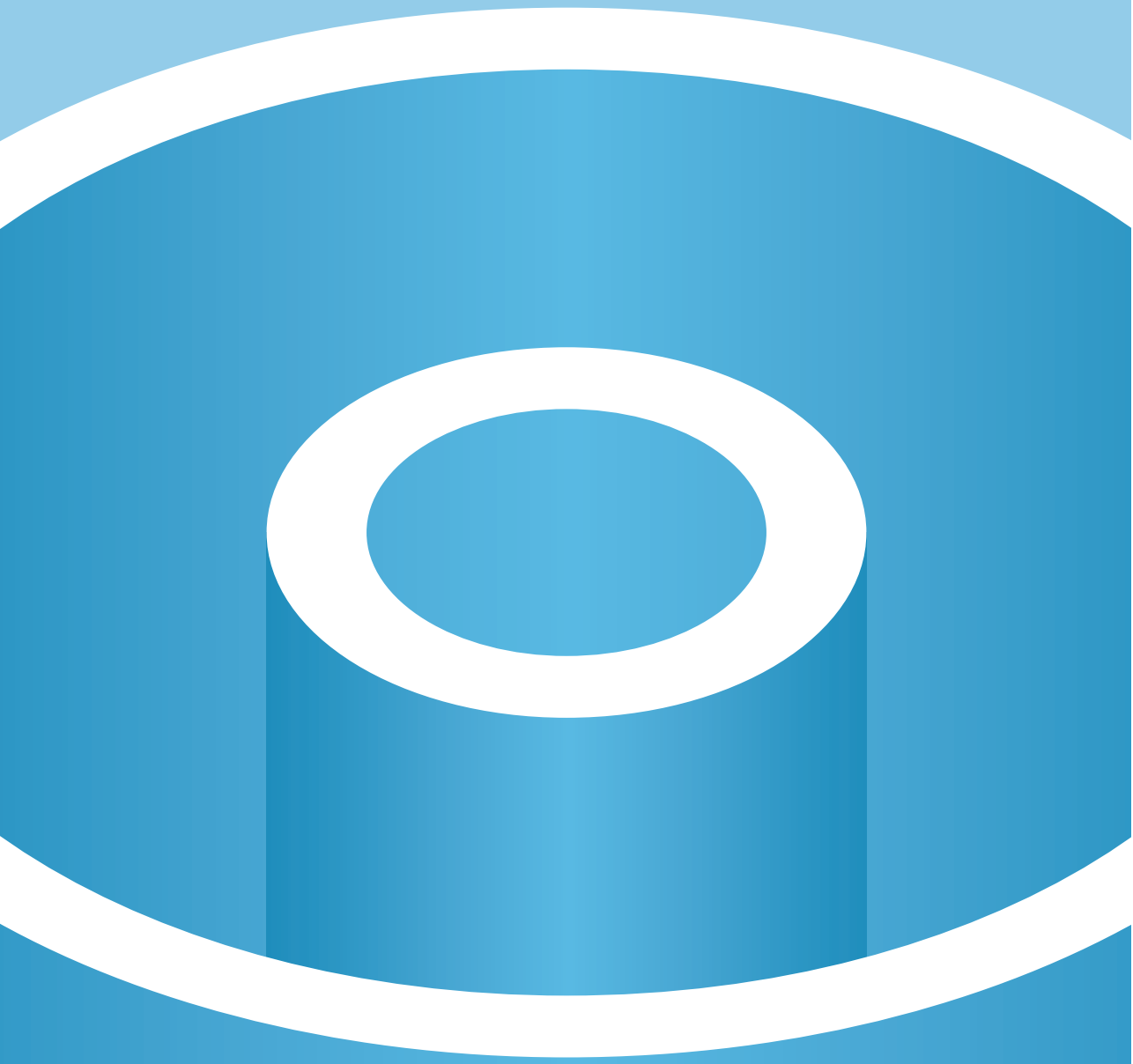

Sander G. Huisman

Taylor-Couette turbulence

Sander Gerard Huisman

Thesis committee members:

Prof. Dr. Ir. Leen van Wijngaarden (chairman)	UT, Enschede
Prof. Dr. Detlef Lohse (promotor)	UT, Enschede
Assoc. Prof. Dr. Chao Sun (copromotor)	UT, Enschede
Dr. Ir. C.H. Venner	UT, Enschede
Prof. Dr. Theo van der Meer	UT, Enschede
Prof. Dr. François Daviaud	CEA, Paris
Prof. Dr. Ir. Willem van de Water	TUE, Eindhoven
Prof. Dr. Eberhard Bodenschatz	MPI, Göttingen

Enabling new technology

The work in this thesis was carried out at the Physics of Fluids group of the Faculty of Science and Technology of the University of Twente. This thesis was financially supported by the Simon Stevin Prize of the Technology Foundation STW of The Netherlands.

Dutch title:
Taylor-Couette turbulentie

Publisher:
Sander G. Huisman, Physics of Fluids, University of Twente,
P.O. Box 217, 7500 AE Enschede, The Netherlands
`http://www.shuisman.com`

ISBN: `978-90-365-3704-9`

Taylor-Couette turbulence

DISSERTATION

to obtain
the degree of doctor at the University of Twente,
on the authority of the rector magnificus,
Prof. Dr. H. Brinksma,
on account of the decision of the graduation committee,
to be publicly defended
on Friday the 19th of September 2014 at 16:45

by

Sander Gerard Huisman
Born on the 2nd of July 1987
in Sneek, The Netherlands

This dissertation has been approved by the promotor:

Prof. Dr. rer. nat. Detlef Lohse

and the copromotor:

Assoc. Prof. Dr. Chao Sun

Contents

Introduction

Turbulence is omnipresent. It's in our blood, in our respiratory system, in our tea and coffee, in the hot air that rises above us, in the wake behind us when we walk, in the air in a room, around our cars and planes, in the wind above our farmlands, in the water of all the seas and oceans, in our sun, and in all the other stars.

For macroscopic flows of water and air the Reynolds number, the ratio of inertial to viscous forces and describing the amount of turbulence, is generally much larger than unity. This means practically that all the common flows around us are turbulent. The difficulty in describing turbulence resides in the fact that turbulent flows are generally irregular, chaotic, and therefore very hard to predict. Think of the weather; we can only predict a few days ahead—at best. In addition, turbulent flows have characteristics across many length- and time scales, so describing them is non-trivial. Although the equations describing them are well known, it has puzzled scientists for centuries and we have not yet 'solved' turbulence.
In order to accurately extrapolate laboratory results to higher Reynolds numbers we need to know the characteristics of the turbulence we are dealing with. This means knowing how the flow behaves fundamentally; which transitions the flows undergo, what the statistical properties of the flows are, the patterns that are formed inside the flows, as well as knowing the energy and momentum transport in the flows.

Taylor Couette

The Taylor-Couette apparatus is one of the fundamental configurations to test theories in fluid dynamics. Fluid is confined between two independently rotating concentric cylinders. This simple closed geometry has many symmetries,

can be constructed relatively easily, and allows for a well-controlled environment to perform shear experiments. In addition, this geometry allows the derivation of global balances easily. The apparatus has been used to measure the viscosity of a fluid, to study hydrodynamic instabilities, pattern formation, and turbulence. The geometry of the device can be described by the outer-radius of the inner cylinder r_i, the inner-radius of the outer cylinder r_o, and the height of the cylinders L. This gives rise to two geometrical ratios: the radius ratio $\eta = r_i/r_o$ and the aspect ratio $\Gamma = L/(r_o - r_i)$. The driving is characterised by two Reynolds numbers: $\mathrm{Re}_{i,o} = \omega_{i,o} r_{i,o}(r_o - r_i)/\nu$, where ν is the kinematic viscosity, and ω the angular velocity of the cylinder, and i and o subscripts denote quantities pertaining to the inner and outer cylinder, respectively.
The response of the system after setting the control parameters η, Γ, Re_i, and Re_o, is a torque $\mathcal{T}$ (G in nondimensionalised form) in order to maintain the cylinders at constant speed, and a 'wind' velocity inside the flow. This is a typical flow velocity that is in the direction of the transport, in this case this is radially; the angular velocity (torque, momentum) is transported from one cylinder to the other. Given the closed nature of the apparatus, it is now straightforward to calculate the (average) energy dissipation rate. The energy input is given by $P = \omega\mathcal{T}$. This energy is transferred though the flow, and is finally dissipated by viscous dissipation. The average energy dissipation rate can thus be found by $\epsilon = P/M$ where M is the mass of the working fluid.

Analogy with Rayleigh-Bénard

In Rayleigh-Bénard convection heat is transported from a hot bottom plate to a cool top plate. The driving of the system is given by the Rayleigh number $\mathrm{Ra} = \beta g \Delta L^3/(\kappa\nu)$, where β is the thermal expansion coefficient, g the acceleration due to gravity, Δ the temperature difference between top and bottom, L the height of the system, κ the thermal diffusivity, and ν the kinematic viscosity. The response of the system, once setting the geometry of the setup and the amount of driving (Ra), is a heat-transport and a 'wind' velocity inside the flow. The former is given by a Nusselt number $\mathrm{Nu} = J/J_{\mathrm{conductive}}$, where J is the heat flux from bottom to top, and $J_{\mathrm{conductive}}$ the heat flux in the case of pure conduction (no convection).
Both system have in common that some quantity is conserved: heat in the case of Rayleigh-Bénard, and angular velocity (torque) in the case of Taylor-

Couette. Based on the underlying equations one can derive analogies between Taylor-Couette (TC) flow and Rayleigh-Bénard (RB) convection. It is found that the driving in TC is better given by a Taylor number $\mathrm{Ta} = \frac{1}{4}(\frac{1+\eta}{2\sqrt{\eta}})^4(r_o - r_i)^2(r_i + r_o)^2(\omega_i - \omega_o)^2/\nu^2$ (which in complete analogy with the Rayleigh number), and that the transport is better given by Nu_ω. Here $\mathrm{Nu}_\omega = J_\omega/J_{\omega,\mathrm{laminar}}$ (in complete analogy with the Nusselt number in RB), where J_ω is now the angular velocity flux from one cylinder to the other and can be directly related to the torque $\mathcal{T}$, and $J_{\omega,\mathrm{laminar}}$ is the flux in case of pure laminar flow. We summarize this analogy in table 1.

	Taylor-Couette	Rayleigh-Bénard
Driving:	$\mathrm{Ta} = \frac{(1+\eta)^4(r_o-r_i)^2(r_i+r_o)^2(\omega_i-\omega_o)^2}{64\nu^2\eta^2}$	$\mathrm{Ra} = \frac{\beta g \Delta L^3}{\kappa\nu}$
Conserved:	angular velocity flux	heat flux
	$J_\omega = r^3\left(\langle u_r\omega\rangle_{A,t} - \nu\partial_r\langle\omega\rangle_{A,t}\right)$	$J = \langle u_z\theta\rangle_{A,t} - \kappa\partial_z\langle\theta\rangle_{A,t}$
Transport:	$\mathrm{Nu}_\omega = J_\omega/J_{\omega,\mathrm{laminar}}$	$\mathrm{Nu} = J/J_{\mathrm{conductive}}$
Dissipation:	$\epsilon = (\mathrm{Nu}_\omega - 1)\mathrm{Ta}/\sigma^2$	$\epsilon = (\mathrm{Nu} - 1)\mathrm{Ra}/\mathrm{Pr}^2$
'Prandtl':	$\sigma = \left(\frac{1+\eta}{2\sqrt{\eta}}\right)^4$	$\mathrm{Pr} = \frac{\nu}{\kappa}$
Scaling:	$\mathrm{Nu}_\omega \propto \mathrm{Ta}^\gamma$	$\mathrm{Nu} \propto \mathrm{Ra}^\gamma$

Table 1: List of analogous relations between Taylor-Couette flow and Rayleigh-Bénard convection. Taken from [1].

In addition to the aforementioned analogies for the conserved quantities and driving parameters, we can also derive that dissipation has an analogous form for both systems. Furthermore one can derive that the transport should scale as a function of the driving parameter with a certain exponent γ, for both the RB and TC flow. The full analogy, with all its details, can be read in Ref. [1]. Details will be explained in the individual chapters where necessary.

Open Questions

- How does the torque (or equivalently, angular velocity transport) scale with increasing Reynolds (Taylor number) for very high Reynolds numbers?
- How is this transport altered when rotation of the outer cylinder is introduced?

- How is this transport affected when the ratio of the cylinder radii is changed?
- How does the 'wind' Reynolds number scale with increasing Reynolds number (Taylor number)?
- Are there large-scale structures inside the flow, and if so, are multiples states possible?
- What are the statistical properties of the flow?
- What do the velocity profiles look like, and how do they depend on the rotation of the outer cylinder?
- What can be said about the boundary layer?

A guide through the thesis

Up to now, for the high Reynolds numbers ($> 10^4$), the focus has been on describing the *global* (*i.e.* torque) flow properties, and mostly for the case where the outer cylinder is stationary. In this thesis we will focus on local quantities and their connection to global quantities, not only for the case of pure inner cylinder rotation, but also for the case where both cylinders are rotating. In chapter 1 (page 5) the global transport is characterized by finding the scaling exponent of the transport $\mathrm{Nu}_\omega \propto \mathrm{Ta}^\gamma$. In chapter 2 (page 15) the focus is on the local flux J_ω inside the flow and we will define and measure the 'wind' velocity of the flow. Following the analogy described in Ref. [1], the boundary layer properties are measured and compared to RB flow [2], see chapter 3 (page 25). In chapter 4 (page 37) the possibility of multiple flow states, even for very high Ta (Re), is exemplified by simultaneous global and local measurements. In chapter 5 (page 49) the local flow is analyzed with statistical tools: probability density functions (PDFs), PDFs of velocity increments, structure functions, and spectral analysis. In chapter 6 (page 67) we perform velocity profile measurements, and we will have a look at the bi-modality of the flow. In chapter 7 (page 109) we will have a look at the η dependence of the flow for the global and local quantities. The experimental values are accompanied by numerical results by Rodolfo Ostilla Mónico. Chapter 8 (page 147) explains how laser Doppler anemometry measurements can be performed inside the Taylor-Couette device, despite its curved outer surface. All the conclusions can be found on page 161.

1

Torque scaling in turbulent Taylor-Couette flow with co- and counter-rotating cylinders°

We analyze the global transport properties of turbulent Taylor-Couette flow in the strongly turbulent regime for independently rotating outer and inner cylinder, reaching Reynolds numbers of the inner and outer cylinder of $\mathrm{Re}_i = 2 \cdot 10^6$ and $\mathrm{Re}_o = \pm 1.4 \cdot 10^6$, respectively. For all Re_i, Re_o, the dimensionless torque G scales as a function of the Taylor number Ta (which is proportional to the square of the difference between the angular velocities of the inner and outer cylinder) with a universal effective scaling law $G \propto \mathrm{Ta}^{0.88}$, corresponding to $\mathrm{Nu}_\omega \propto \mathrm{Ta}^{0.38}$ for the Nusselt number characterizing the vorticity transport between the inner and outer cylinder. The transport is most efficient for the counter-rotating case along the diagonal in phase space with $\omega_o \approx -0.4\omega_i$.

°Published as: Dennis P.M. van Gils, **Sander G. Huisman**, Gert-Wim Bruggert, Chao Sun, and Detlef Lohse, *Torque scaling in turbulent Taylor-Couette flow with co- and counter-rotating cylinders*, Phys. Rev. Let. **106**, 024502 (2011). This publication was selected as Editors' Suggestion, selected for a synopsis in Physics *"Heat and twist of turbulent flows"*, and was covered by Physics Today [3]. The experiments are performed by Huisman, Sun, and van Gils, analysis is done by Huisman, Sun, and van Gils, and the manuscript is written by Lohse. Discussion of the results and proofreading of the manuscript by everyone.

1.1 Introduction

Global transport properties of turbulent flows are of prime importance for many applications of fluid dynamics, but also for a fundamental understanding, as they reflect the interplay between boundary layer and bulk. The two canonical systems used to analyze the transport properties in closed turbulent systems are Rayleigh-Bénard (RB) convection and Taylor-Couette (TC) flow, and they are conceptionally closely related [4, 5, 1]. In RB flow, heat (in dimensionless form the Nusselt number) is transported from the hot bottom plate to the cold top plate [6, 7], whereas in TC flow angular velocity is transported from the inner to the outer cylinder (for $\omega_i > \omega_o$). In analogy to RB flow, Eckhardt *et al.* [1] identified, from the underlying Navier-Stokes equations,

$$J^\omega = r^3(\langle u_r\omega\rangle_{A,t} - \nu\partial_r \langle\omega\rangle_{A,t}) \tag{1.1}$$

as relevant conserved transport quantity, representing the flux of angular velocity from the inner to the outer cylinder. Here $u_r(u_\phi)$ is the radial (azimuthal) velocity, $\omega = u_\phi/r$ the angular velocity, and $\langle\dots\rangle_{A,t}$ denotes averaging over time and an area with constant r from the axis. J^ω is made dimensionless with its value $J^\omega_{\text{lam}} = 2\nu r_i^2 r_o^2(\omega_i - \omega_o)/(r_o^2 - r_i^2)$ for the laminar case, giving a "Nusselt number" as dimensionless transport quantity,

$$\text{Nu}_\omega = J^\omega/J^\omega_{\text{lam}}, \tag{1.2}$$

where $r_{i,o}$ and $\omega_{i,o}$ denote the radius and the angular velocity of the inner and outer cylinder, respectively, ν is the kinematic viscosity of the fluid. Nu_ω is closely connected to the torque τ that is necessary to keep the inner cylinder rotating at constant angular velocity, or in dimensionless form to

$$G = \frac{\tau}{2\pi\ell\rho_{\text{fluid}}\nu^2} = \text{Nu}_\omega\frac{J^\omega_{\text{lam}}}{\nu^2} = \text{Nu}_\omega G_{\text{lam}}, \tag{1.3}$$

where ℓ is the height of the cylinder and ρ_{fluid} the density of the fluid. Yet another often used possibility to represent the data is the friction coefficient $c_f = ((1-\eta)^2/\pi)G/\text{Re}_i^2$ [8].
For RB flow, the scaling properties of the Nusselt number in the fully turbulent regime (*i.e.* for very large Rayleigh numbers, say $\text{Ra} \geq 10^{10}$) have received tremendous attention in the last decade and various heat flux measurements

have been performed; again, see the review article [6]. In contrast, TC flow in the fully turbulent regime got much less attention, with the only exception being the Texas experiment by Swinney, Lathrop, and coworkers [9, 8, 10, 11]. In that experiment a Reynolds number $\mathrm{Re}_i = 10^6$ of the inner cylinder was reached (with the outer cylinder at rest) and an effective power law of $G \propto \mathrm{Re}_i^{\gamma}$ with $\gamma \approx 1.6$–1.85 was detected [9, 8] in the turbulent regime, though the scaling properties are not particularly good and strictly speaking γ depends on Re_i, *i.e.* there is no pure scaling. Indeed, in refs. [12, 13, 1] we have argued that there should be a smooth transition from $\gamma = 3/2$ for the small Reynolds number of a boundary layer dominated flow to $\gamma = 2$ for the larger Reynolds number of a flow dominated by the turbulent bulk. Turbulent TC experiments get even more scarce for TC flow with inner and outer cylinder rotating independently. We are only aware of the Wendt experiments in the 1930s [14], reaching $\mathrm{Re}_i \approx 10^5$ and $\mathrm{Re}_o \approx \pm 10^5$, and the recent ones by Ravelet *et al.* [15], reaching $\mathrm{Re}_i \approx 5 \cdot 10^4$ and $\mathrm{Re}_o = 2 \cdot 10^4$. The hitherto explored phase diagram of TC flow with independently rotating cylinders is shown in fig. 1.1a. An alternative representation of the phase diagram is given by Dubrulle *et al.* [16], who introduces a shear Reynolds number and a rotation number as alternative representation of the phase space, see below.

In the phase diagram fig. 1.1a we have also added the Re_i, Re_o numbers which we explored with our newly constructed Twente turbulent TC facility ($\mathrm{T}^3\mathrm{C}$), which we have described in great detail in ref. [21]. In short, at this facility the cylinders are $\ell = 0.97$ m high; the inner cylinder has a radius of $r_i = 20$ cm, and the outer cylinder of $r_o = 27.9$ cm, and the maximal inner and outer angular velocity are $\omega_i/(2\pi) = 20$ Hz and $\omega_o/(2\pi) = \pm 10$ Hz, respectively, corresponding to $\mathrm{Re}_i = r_i\omega_i d/\nu = 2 \cdot 10^6$ and $\mathrm{Re}_o = r_o\omega_o d/\nu = \pm 1.4 \cdot 10^6$, with $d = r_o - r_i$. The system is fully temperature controlled through cooling of the upper and lower plate. The torque is measured at the middle part of the inner cylinder (similarly as done in [9]) by load cells imbedded inside the inner cylinder and not by measuring the torque through the sealing. One of the goals we want to achieve with this new facility is to explore the (Re_i, Re_o, $\eta = r_i/r_o$) parameter space, thus entering *terra incognita*, and measure the torque (*i.e.*, transport of angular velocity—Nu_ω in dimensionless form—or, again expressed differently, the overall drag) and the internal Reynolds number of the flow.

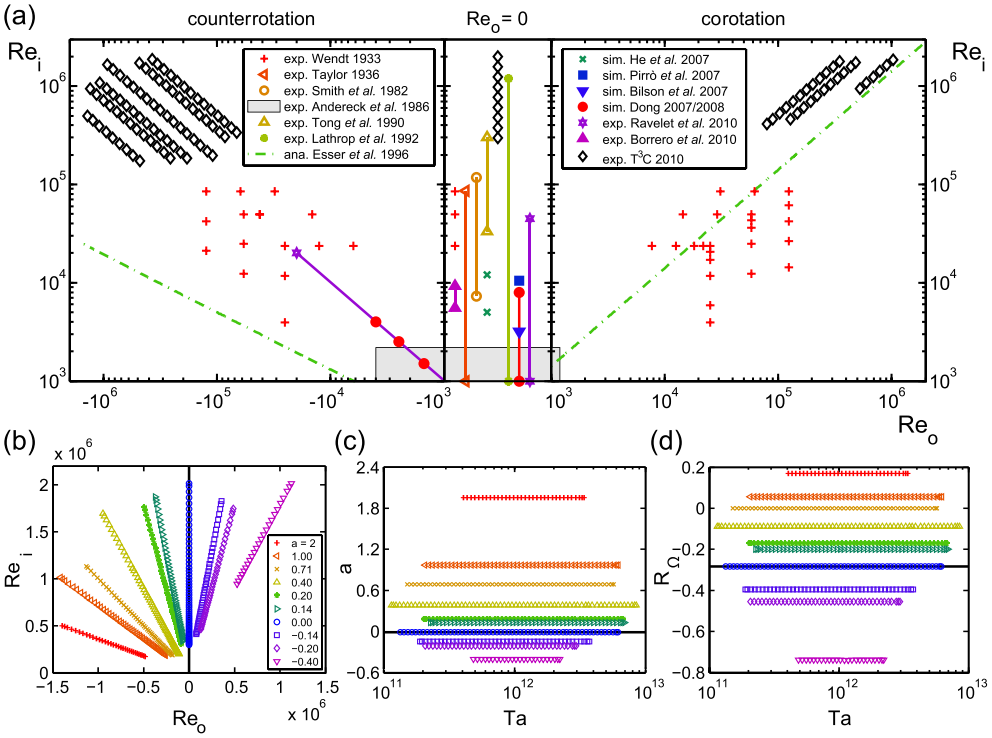

Figure 1.1: (a) Explored phase space (Re_o, Re_i) of TC flow with independently rotating inner and outer cylinder. Right of the horizontal axis the cylinders are co-rotating, to the left of it they are counterrotating, and a log-log representation has been chosen. The dashed lines are Esser and Grossmann's [17] estimate for the onset of turbulence with $\eta = 0.71$. The many data points in the small Reynolds number regime of pattern formation and spatial temporal chaos (see *e.g.* [18, 19, 20]) have not been included in this phase diagram. Our data points of this publication are the black diamonds. (b) Our data points in the phase diagram on a linear scale. (c) Our data points in the phase space (Ta, a); note that Ta also depends on a. (d) Our data points in the phase space (Ta, R_Ω) (see eq. (1.7)).

1.2 Results and Analysis

In this chapter we will focus on the required torque for fully developed turbulent flow (Re_i, $\mathrm{Re}_o > 10^5$), where $\eta = 0.716$ with independently rotating inner and outer cylinder, which hitherto has not been explored. The examined parameter space in this chapter is shown in the space of (Re_i, Re_o) in fig. 1b, and (Ta, a) in fig. 1c, and (Ta, R_Ω) in fig. 1d to be explained below. We will not address the question whether pure scaling laws exist: First, the explored Reynolds number range is too short to answer this question, and second, the earlier work [9, 8, 10, 12, 13, 1] gives overwhelming experimental and theoretical evidence that there are no pure scaling laws even up to Reynolds numbers of 10^6. So all scaling exponents in this chapter have to be read as effective scaling laws.

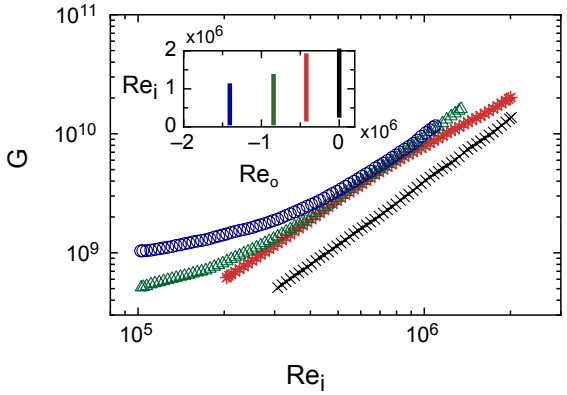

Figure 1.2: The dimensionless torque $G(\mathrm{Re}_i)$ for counterrotating TC flow for four different fixed values of $\mathrm{Re}_o/10^5 = -15, -8, -5$, and 0 (top to bottom data sets), see inset for the probed area of the parameter space.

Our results for the counterrotating case for the dimensionless torque G as function of Re_i for fixed Re_o are shown in fig. 1.2. One immediately sees that counterrotation enhances the torque (and thus the overall drag), but that for general $\mathrm{Re}_o \neq 0$ the effective power law $G \propto \mathrm{Re}_i^{1.76}$, that holds in the case of inner cylinder rotating only, gets lost; in fact, there is even no effective power law at all.

How to represent the data to better reveal the transport properties of the

system? The analysis of Eckhardt *et al.* [1] and the analogy of the TC system to the RB system suggest to better plot Nu_ω as function of the Taylor number

$$\mathrm{Ta} = \frac{1}{4}\sigma d^2 (r_i + r_o)^2 (\omega_i - \omega_o)^2 \nu^{-2}, \tag{1.4}$$

where $\sigma = (((1+\eta)/2)/\sqrt{\eta})^4$, *i.e.* along the diagonals

$$\omega_o = -a\omega_i \tag{1.5}$$

in the parameter space fig. 1.1b. Indeed, Eckhardt *et al.* [1] derived from the underlying Navier-Stokes equation the exact relation

$$\epsilon_w = \epsilon - \epsilon_{\mathrm{lam}} = \nu^3 d^{-4} \sigma^{-2} \mathrm{Ta}(\mathrm{Nu}_\omega - 1) \tag{1.6}$$

for the excess kinetic energy dissipation rate ϵ_w (*i.e.*, total kinetic energy dissipation rate ϵ minus the kinetic energy dissipation rate in the laminar case $\epsilon_{\mathrm{lam}} = 4\nu r_i^2 r_o^2 (r_i + r_o)^{-2} d^{-2} (\omega_i - \omega_o)^2$. In eq. (1.6) σ can be interpreted as a (geometric) Prandtl number, and Ta and Nu_ω are the exact TC analogs to the Rayleigh and Nusselt number in RB flow. Along the diagonal, eq. (1.5) in parameter space, one has $\mathrm{Ta} = \frac{1}{4}\sigma d^2 (r_i + r_o)^2 (1+a)^2 \omega_i^2 \nu^{-2}$, and the well-studied [6] effective scaling law $\mathrm{Nu} \propto \mathrm{Ra}^{\tilde{\gamma}}$ for RB flow (with $\tilde{\gamma} \approx 0.31$ [22, 6]) now would correspond to an effective scaling law $\mathrm{Nu}_\omega \propto \mathrm{Ta}^\gamma$ for TC flow.
Nu_ω vs. Ta is shown in fig. 1.3a for various a, *i.e.* along various straight lines through the origin of the parameter space fig. 1.1b. An *universal*, *i.e.* a-independent, effective scaling $\mathrm{Nu}_\omega \propto \mathrm{Ta}^\gamma$ with $\gamma \approx 0.38$ is clearly revealed. This corresponds to a scaling of $G \propto \mathrm{Re}_i^{1.78}$ for the dimensionless torque along the straight lines eq. (1.5) in the parameter space fig. 1.1, to $c_f \propto \mathrm{Re}_i^{-0.24}$ for the drag coefficient, and to $G \propto \mathrm{Ta}^{0.88}$. The compensated plots $\mathrm{Nu}_\omega/\mathrm{Ta}^{0.38}$ in fig. 1.3b demonstrate the quality of the effective scaling and in addition show the a-dependence of the prefactor of the scaling law.
That a-dependence of the prefactor $\mathrm{Nu}_\omega/\mathrm{Ta}^{0.38}$ is plotted in figure 1.4. It shows a pronounced maximum around $a = 0.4$, *i.e.* for the moderately counterrotating case, signaling the most efficient angular velocity transport from the inner to the outer cylinder at that value. We mention that it is obvious that this curve has a maximum, as in both limiting cases $a \to \pm\infty$ (only rotating of the outer cylinder) the flow is laminar and $\mathrm{Nu}_\omega = 1$, but it is interesting to note that the maximum does not occur for the most pronounced counter-rotating case $\omega_o = -\omega_i$ (or $a = 1$). Compared to the case of pure inner cylinder rotation ($a = 0$), at $a = 0.4$ the angular velocity transport from inner to outer cylinder is enhanced by more than 20%.

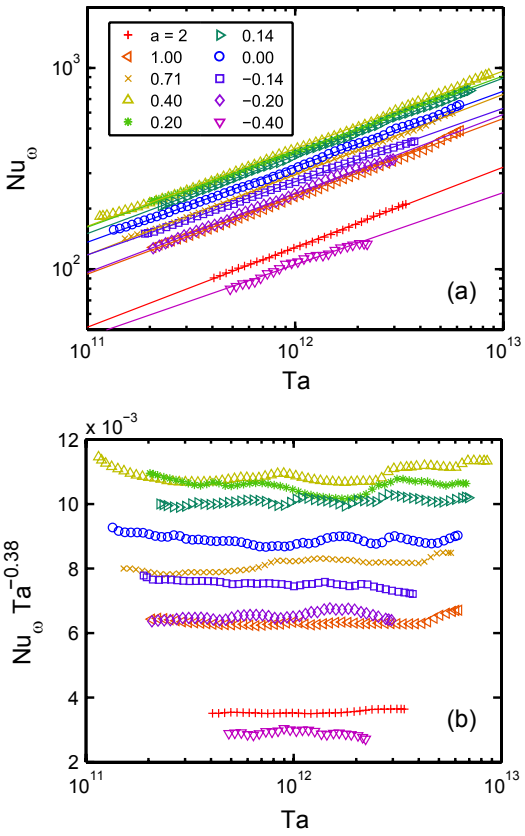

Figure 1.3: (a) Nu_ω vs. Ta for various a; see fig. 1.1b for the location of the data in parameter space. A universal effective scaling $\mathrm{Nu}_\omega \propto \mathrm{Ta}^{0.38}$ is revealed. The compensated plots $\mathrm{Nu}_\omega/\mathrm{Ta}^{0.38}$ in (b) show the quality of the effective scaling and the a-dependent prefactor of the scaling law.

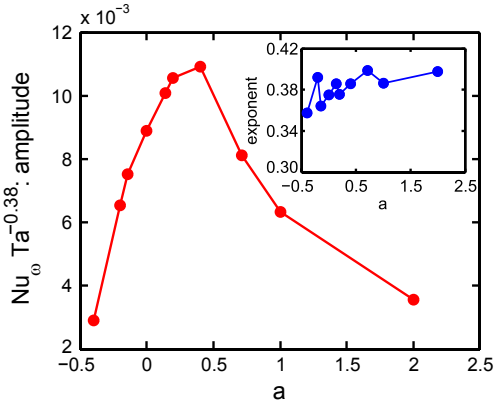

Figure 1.4: Prefactor of the effective scaling law $\mathrm{Nu}_\omega \propto \mathrm{Ta}^{0.38}$ (shown in fig. 1.3) as function of $a = -\omega_o/\omega_i$. The inset shows the effective exponents γ which results from an individual fit of the scaling law $\mathrm{Nu}_\omega \propto \mathrm{Ta}^{\gamma}$.

The parameter $a = -\omega_o/\omega_i$ is connected to the so-called rotation number

$$R_\Omega = (1-\eta)(\mathrm{Re}_i + \mathrm{Re}_o)/(\eta \mathrm{Re}_o - \mathrm{Re}_i) \tag{1.7}$$

introduced by Dubrulle *et al.* [16] and used by Ravelet *et al.* [15], namely $R_\Omega = (1-\eta)\eta^{-1}(a-\eta)(a+1)^{-1}$. We also plot our data points in the phase space of (Ta, R_Ω) as shown in fig. 1d. The optimal value $a \approx 0.4$ we found for the transport properties of the system corresponds to $R_\Omega \approx -0.09$. In this chapter we prefer a as compared to R_Ω as the sign of a immediately signals whether the system is corotating or counterrotating.

1.3 Conclusion

In conclusion, we have explored the *terra incognita* of fully developed turbulent TC flow with independently rotating inner and outer cylinder, beyond Reynolds numbers of 10^6, finding an universal effective scaling law $G \propto \mathrm{Ta}^{0.88}$, corresponding to $\mathrm{Nu}_\omega \propto \mathrm{Ta}^{0.38}$, for all (fixed) $a = -\omega_o/\omega_i$, with optimal transport quantities at $a \approx 0.4$. It is remarkable that the effective scaling exponent 0.38 exactly resembles the analogous effective scaling exponent in $\mathrm{Nu} \propto \mathrm{Ra}^{0.38}$ in RB convection in the ultimate regime of thermal convection [23, 24], reflecting the analogy between TC and RB flow also in the strongly turbulent regime.

The next steps will be to further extend the parameter space fig. 1.1 towards higher radius ratios η to see whether the observed universality carries on towards an even larger parameter range, and to also measure the Taylor-Reynolds number and the wind Reynolds numbers of the internal flow, which are closely connected to Nu_ω and for which theoretical predictions exist [1]. With such measurements and characterizations of the flow structures we will also be able to check whether these are reflected in the overall transport properties.

2

Ultimate turbulent Taylor-Couette flow°

The flow structure of strongly turbulent Taylor-Couette flow with Reynolds numbers up to $\mathrm{Re}_i = 2 \cdot 10^6$ of the inner cylinder is experimentally examined with high-speed particle image velocimetry (PIV). The wind Reynolds numbers Re_w of the turbulent Taylor-vortex flow is found to scale as $\mathrm{Re}_w \propto \mathrm{Ta}^{1/2}$, exactly as predicted [2] for the ultimate turbulence regime, in which the boundary layers are turbulent. The dimensionless angular velocity flux has an effective scaling of $\mathrm{Nu}_\omega \propto \mathrm{Ta}^{0.38}$, also in correspondence with turbulence in the ultimate regime. The scaling of Nu_ω is confirmed by *local* angular velocity flux measurements extracted from high-speed PIV measurements: though the flux shows huge fluctuations, its spatial and temporal average nicely agrees with the result from the global torque measurements.

°Published as: **Sander G. Huisman**, Dennis P.M. van Gils, Siegfried Grossman, Chao Sun, and Detlef Lohse, *Ultimate Turbulent Taylor-Couette Flow*, Phys. Rev. Let. **108**, 024501 (2012). This publication was selected as Editors' Suggestion, and was featured in a Physics Viewpoint *"The Twins of Turbulence Research"* [25]. Experiments, analysis and writing are done by Huisman, supervision by Sun, and Lohse. Proofread by everyone.

2.1 Introduction

The Taylor-Couette (TC) system is one of the fundamental geometries conceived in order to test theories in fluid dynamics. Fluid is confined between two coaxial, differentially rotating cylinders. The system has been used to measure viscosity, study hydrodynamic instabilities, pattern formation, and the flow was found to have a very rich phase diagram [18]. In the fully turbulent regime, the focus up to now has been on *global* transport quantities [9, 8, 10, 26, 27], which can be connected to the torque τ, which is necessary to keep the inner cylinder rotating at constant angular velocity. In ref. [1] the analogy between the angular velocity flux in TC turbulence and the heat flux in Rayleigh-Bénard (RB, see ref. [6]) flow was worked out, suggesting to express the former in terms of the Nusselt number, Nu_ω, which in ref. [26] was found to have an effective scaling $\mathrm{Nu}_\omega \propto \mathrm{Ta}^{0.38}$ with the Taylor number (the analog to the Rayleigh number Ra in RB flow). Such effective scaling $\mathrm{Nu} \propto \mathrm{Ra}^{0.38}$ characterizes the so-called ultimate scaling regime in RB flow [23, 24, 28]. Following these papers, Grossmann and Lohse [2] have interpreted this scaling as signature of turbulent boundary layers. They derived $\mathrm{Nu} \propto \mathrm{Ra}^{1/2} \times$ log-corrections (RB) and $\mathrm{Nu}_\omega \propto \mathrm{Ta}^{1/2} \times$ log-corrections (TC). The log-corrections imply the effective scaling law exponent of 0.38. They also made a prediction for the accompanying scaling of the wind Reynolds number Re_w, namely

$$\begin{aligned} \mathrm{Re}_w &\propto \mathrm{Ra}^{1/2} \\ &\text{and} \\ \mathrm{Re}_w &\propto \mathrm{Ta}^{1/2} \end{aligned} \tag{2.1}$$

for RB and TC turbulence, respectively. Here the logarithmic corrections remarkably cancel out, in contrast to what Kraichnan had predicted [29] earlier, namely

$$\begin{aligned} \mathrm{Re}_w &\propto \mathrm{Ra}^{1/2}(\log \mathrm{Ra})^{-1/2} \\ &\text{and} \\ \mathrm{Re}_w &\propto \mathrm{Ta}^{1/2}(\log \mathrm{Ta})^{-1/2}, \end{aligned} \tag{2.2}$$

which leads to an effective scaling exponent of about 0.47 in the relevant turbulent regime. In order to verify the interpretation of ref. [2] and to check

the prediction (2.1), *local* flow measurements are required to extract the wind Reynolds number Re_w. However, what happens locally, inside the TC flow, has up to now only been studied for relatively low Reynolds numbers $\mathrm{Re} < 10^5$, and has been restricted to flow profiles and single-point statistics [14, 30, 19, 31, 32, 33, 9, 10, 34, 35, 36, 15].
In this chapter we supply local flow measurements from high-speed particle image velocimetry (PIV) at strongly turbulent TC flow. From these we will verify that indeed $\mathrm{Re}_w \propto \mathrm{Ta}^{1/2}$. In addition, from the PIV measurements we are able to also extract *local* angular velocity fluxes. These are found to strongly fluctuate in time, but when averaged azimuthally, radially, and in time, for the lower Ta show a slight axial dependence, which we interpret as reminiscence of the turbulent Taylor vortices, and which nearly vanishes for the largest Ta we achieve.

2.2 Experiment

The apparatus used for the experiments has an inner cylinder with a radius of $r_i = 0.200$ m, a transparent outer cylinder with an inner-radius of $r_o = 0.279$ m, resulting in a gap-width of $d = r_o - r_i = 0.079$ m and a radius ratio $\eta = r_i/r_o = 0.716$. The height is $L = 0.927$ m implying an aspect ratio of $\Gamma = L/(r_o - r_i) = 11.7$. More details regarding the experimental facility can be found in ref. [21]. Here we focus on the case of inner cylinder rotation and fixed outer cylinder. The local velocity is measured using PIV. We utilize the viewing ports in the top plate of the apparatus to look at the flow from the top. The flow is illuminated from the side using a pulsed Nd-YLF laser [37], creating a horizontal laser sheet. The working fluid (water) is seeded with 20 μm polyamide seeding particles, and is recorded using a high speed camera [38]. The PIV system is operated in double-frame mode which allows us to have a Δt far smaller than $1/f$, where f is the frame rate. The PIV measurements give us direct access to both the angular velocity $\omega(\theta, r, z, t) = u_\theta(\theta, r, z, t)/r$ and the radial velocity $u_r(\theta, r, z, t)$, simultaneously.
From the latter we extract the wind Reynolds number as $\mathrm{Re}_w := u_{r,\sigma} d/\nu$, where $u_{r,\sigma}$ is the standard deviation of the radial velocity. In fig. 2.1 Re_w is shown as a function of the Taylor number

$$\mathrm{Ta} = \frac{1}{4}\sigma(r_o - r_i)^2(r_i + r_o)^2(\omega_i - \omega_o)^2/\nu^2. \tag{2.3}$$

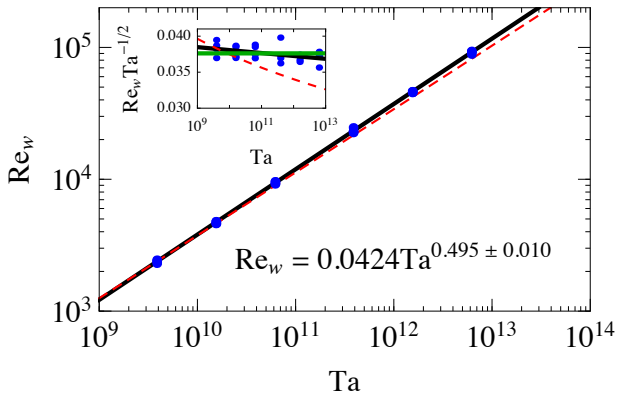

Figure 2.1: Re_w vs. Ta. The data from repeated experiments at mid-height are plotted as separate (blue) dots, showing the quality of the reproducibility and the statistical stationarity of the measurements. We have averaged azimuthally, over time, and in the bulk flow ($0.23\,\mathrm{m} \leq r \leq 0.25\,\mathrm{m}$). The straight line is the best fit $\mathrm{Re}_w = 0.0424\mathrm{Ta}^{0.495\pm0.010}$ and the (red) dashed line is the Kraichnan prediction [29] eq. (2.2). The inset shows the compensated plot $\mathrm{Re}_w/\mathrm{Ta}^{1/2}$ vs Ta. The horizontal (green) line is the prediction (2.1) of ref. [2].

In refs. [1, 26] Ta had been suggested as most appropriate independent variable of the TC system in order to work out the analogy with RB. Here $\sigma = \left((1+\eta)/(2\sqrt{\eta})\right)^4$ can be interpreted as a geometric "Prandtl number" [1], $\omega_{i,o}$ is the angular velocity of the inner and outer cylinder, respectively, and ν is the kinematic viscosity. Note that $\mathrm{Ta} \propto (\omega_i - \omega_o)^2$: while Ra in RB convection is proportional to the temperature difference times the given gravity force, Ta in TC flow is proportional to the angular velocity difference $\omega_i - \omega_o$ times the centrifugal force, which itself is also proportional to $\omega_i - \omega_o$, implying the square-dependence. Therefore, by definition, the two control parameters Re_i (refering to the imposed azimuthal velocity) and Ta are connected by $\mathrm{Re}_i \sim \mathrm{Ta}^{1/2}$, but such a trivial relation of course does not exist between the wind Reynolds number Re_w and Ta (which is a response of the systems and refers to the radial velocity).

2.3 Analysis and Results

Fig. 2.1 reveals a clear scaling of the wind Reynolds number with the Taylor number, namely $\mathrm{Re}_w \propto \mathrm{Ta}^{0.495\pm0.010}$, which is consistent with the prediction [2] $\mathrm{Re}_w \propto \mathrm{Ta}^{1/2}$ for the ultimate TC regime, but inconsistent with Kraichnan's earlier prediction (2.2) of a scaling exponent 1/2 *with* logarithmic corrections [29]. For comparision, we included this relation into fig. 2.1, which clearly is inconsistent with the experimental data. We stress that the cancellation of the log-correction for Re_w as suggested in [2] is highly non-trivial and that in RB flow in the non-ultimate regimes the wind Reynolds number scales as $\mathrm{Re}_w \sim \mathrm{Ra}^{0.44}$ [39], pronouncedly different than the 1/2 exponent we find here in the ultimate regime. Only very recently the wind Reynolds number scaling in ultimate RB flow could be measured, also finding $\mathrm{Re}_w \sim \mathrm{Ra}^{1/2}$ [40] as predicted in ref. [2].

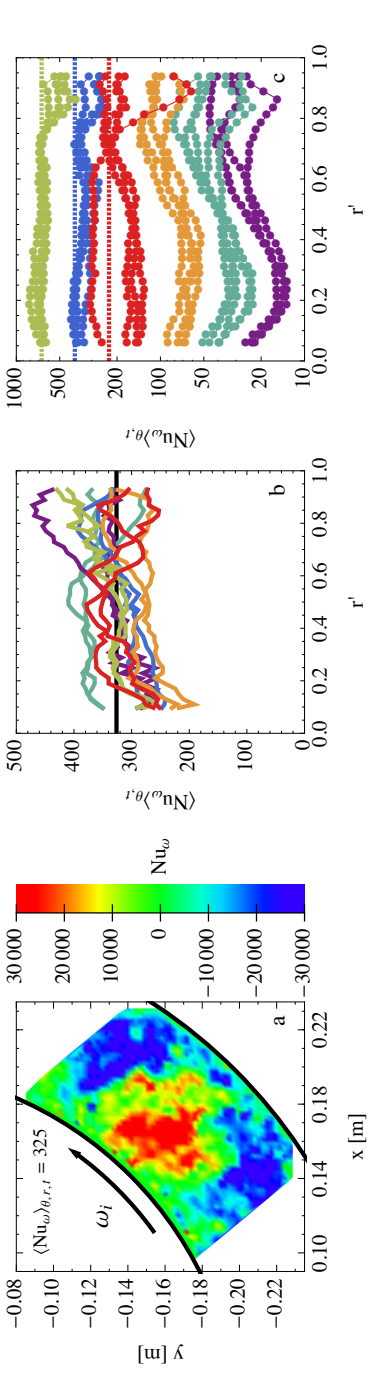

Figure 2.2: (a) Snapshot of the instantaneous convective angular velocity flux, measured at $z = L/2$, for $\mathrm{Ta} = 1.5 \cdot 10^{12}$. The (r, θ)-plane and time averaged flux is found to be equal to $\langle \mathrm{Nu}_\omega \rangle_{\theta,r,t} = 325$. (b) Local normalized convective ω-flux as functions of $r' = (r - r_i)/(r_o - r_i)$ for 6 heights varying between $0.5 \leq z/L \leq 0.73$, for $\mathrm{Ta} = 1.5 \cdot 10^{12}$. The black solid line is the average of the 12 experiments ($\langle \mathrm{Nu}_\omega \rangle_{\theta,r,z,t}$), which is very close to the expected value 326 ± 6 from global torque measurements [26]. (c) Local normalized convective angular velocity flux vs. radial position r' for various rotation rates, measured at $z = L/2$. From bottom to top we have repeated experiments for $\mathrm{Ta} = 3.8 \cdot 10^9$, $1.5 \cdot 10^{10}$, $6.2 \cdot 10^{10}$, $3.8 \cdot 10^{11}$, $1.5 \cdot 10^{12}$, and $6.2 \cdot 10^{12}$. The dashed lines for the three highest Ta represent the Nu_ω value derived from global torque measurements [26].

Next, as the PIV measurements give us both the angular velocity and the radial velocity ($\omega(\theta, r, z, t)$ and $u_r(\theta, r, z, t)$ respectively), we can directly calculate the (total) angular velocity flux (convective + molecular)

$$J^\omega(\theta, r, z, t) := r^3 \left(u_r \omega - \nu \partial_r \omega\right), \tag{2.4}$$

which is made dimensionless with its value for the laminar infinite aspect ratio case, $J^\omega_{\text{lam}} = 2\nu r_i^2 r_o^2(\omega_i - \omega_o)/(r_o^2 - r_i^2)$, giving [1] the local "Nusselt number"

$$\text{Nu}_\omega(\theta, r, z, t) = J^\omega(\theta, r, z, t)/J^\omega_{\text{lam}}.$$

Indeed, as shown in ref. [1], the angular velocity is the relevant quantity transported from the inner to the outer cylinder, as its flux (2.4) is radially conserved, once it is averaged azimuthally, axially, and over time,

$$\frac{d}{dr} \langle J^\omega(\theta, r, z, t) \rangle_{\theta,z,t} = 0.$$

In the turbulent regime the convective term is the major contributor to the flux in the bulk [41].

In fig. 2.2a we show a snapshot of $\text{Nu}(\theta, r)$ at mid-height $z = L/2$ for $\text{Ta} = 1.5 \cdot 10^{12}$. The quantity shows *huge* fluctuations, ranging from $+10^5$ to -10^5 and beyond, whereas the average $\langle \text{Nu}_\omega(\theta, r, t) \rangle_{\theta,r,t} = 325$ is very close to the value $\text{Nu}^{\text{glob}}_\omega = 326 \pm 6$ obtained from global torque measurements [26]. The local flux can thus be more than ± 300 times as large as the mean flux. Large fluctuations have also been reported for the local heat-flux in RB flow [42], but in that case the largest fluctuations were only 25 times larger than the mean flux.

After azimuthal and time averages, $\langle \text{Nu}_\omega(\theta, r, t) \rangle_{\theta,t}$, the fluctuations nearly vanish, see fig. 2.2b (revealing some radial and height dependence for fixed $\text{Ta} = 1.5 \cdot 10^{12}$, presumably reminisent of the Taylor vortices) and fig. 2.2c, where we show the local angular velocity flux r'-profiles for rotation rates from $\omega_i/(2\pi) = 0.5$ Hz to 20 Hz, corresponding to $\text{Ta} = 3.8 \cdot 10^9$ to $6.2 \cdot 10^{12}$. Each profile is based on azimuthal averaging, radial binning, and averaging over 3200 frames (corresponding to 25.6 rotations for the three lowest rotation rates, and 32, 64, and 128 rotations for the fastest rotations rates). For each rotation rate repeated experiments have been performed and the profiles are reproducible. Only in one case the turbulent Taylor vortex flow seems to be in a different state(s). From fig. 2.2c we conclude that the spread in the repeated experiments decreases with increasing Ta, for which the Taylor vortex structure will be more and more washed out. In addition, for increasing Ta, not

only do we measure during more revolutions, but also the transverse velocity increases, both improving the statistics. The dashed lines in fig. 2.2c correspond to the measured global transport for the three highest rotation rates; these values were obtained from the torque measurements [26] and show already good agreement with our local measurements.
An additional *axial* average is necessary to obtain the exact relation between Nu_ω and the global torque τ required to drive the inner cylinder at constant velocity [1],

$$\tau = 2\pi L \rho J^{\omega}_{\mathrm{lam}} \langle \mathrm{Nu}_\omega \rangle_{\theta,z,t} \,. \tag{2.5}$$

It is the lack of sufficient axial averaging, which accounts for the small deviations between $\langle \mathrm{Nu}_\omega(\theta,z,t)\rangle_{\theta,r,t}$ and $\mathrm{Nu}^{\mathrm{glob}}_\omega$. Indeed, due to the Taylor-vortex structure of the TC flow one would expect some axial dependence of $\langle \mathrm{Nu}_\omega(\theta,r,z,t)\rangle_{\theta,r,t}$, which should become weaker with increasing degree of turbulence and thus increasing Ta, just as fig. 2.2c suggests. This picture is confirmed in figure 2.3. Here we present local measurements of the convective angular velocity flux for varying rotation rates, resulting in a Taylor number range of $3.8 \cdot 10^9$–$6.2 \cdot 10^{12}$. For each Taylor number we performed multiple experiments and measured the Nu_ω transport at mid-height. The blue points are results obtained from PIV measurements at mid-height, where the length of the bars indicate the error obtained from the repeated experiments. The green and orange points are repeated measurements at $z = L/2 + d/2$ and $z = L/2 + d$, respectively. An effective scaling $\mathrm{Nu}_\omega \propto \mathrm{Ta}^{0.45\pm0.04}$ is revealed for the blue data points, while a scaling of $\mathrm{Nu}_\omega \propto \mathrm{Ta}^{0.39\pm0.08}$ is revealed for the orange data points.
It is remarkable how the flow provides angular velocity transport from the inner to the outer cylinder, in spite of the fluctuative nature, which are seen in figure 2.2a. In fig. 2.4 we provide a statistical analysis of these fluctuations: While the probability distribution functions (PDFs) of the angular velocity (fig. 2.4a) and the radial velocity (fig. 2.4b) are nearly symmetric, the PDF of their product $r^3 u_r \omega \propto \mathrm{Nu}_\omega$ (fig. 2.4c) is clearly positively skewed. Indeed, the cross-correlation coefficient of u_r and ω (fig. 2.4d) is relatively large.
We note that thanks to the PIV measurements of the full velocity field, the extraction of the local angular velocity flux $\mathrm{Nu}_\omega(\theta,r,z,t) \propto \omega u_r$ is easier in TC as compared to the analog temperature flux $\mathrm{Nu}(\vec{x},t) \propto T u_z$ in RB flow: in order to obtain this latter quantity locally, one has to measure the temperature T and the velocity simultaneously. Because a high-precision field measurement of the temperature is presently not possible and thus not available, the best one can do for RB flow is to measure $\mathrm{Nu}(\vec{x},t)$ point by point [42, 43] or use

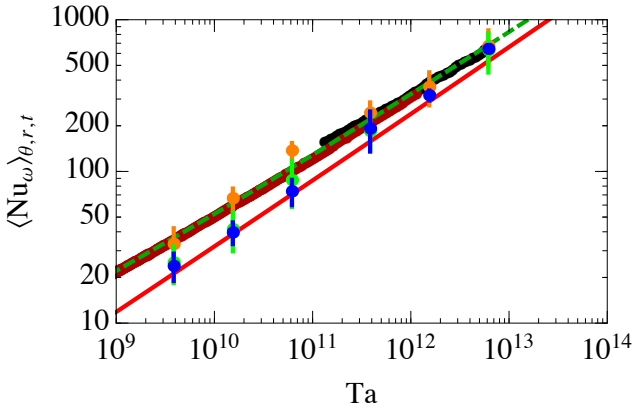

Figure 2.3: Local convective angular velocity flux as a function of Taylor number. The blue dots are results obtained from PIV measurements and show a scaling of $\mathrm{Nu}_\omega \propto \mathrm{Ta}^{0.45\pm0.04}$. The green and orange dots are repeated measurements at a height of $z = L/2+d/2$ and $z = L/2+d$, respectively. The black data points are obtained from global torque measurements and show a scaling that is less steep: $\mathrm{Nu}_\omega \propto \mathrm{Ta}^{0.38}$. The dashed green line is obtained by matching two log-layers [8], and has a scaling exponent of 0.37 at $\mathrm{Ta} = 10^9$, and 0.41 at $\mathrm{Ta} = 10^{13}$. The red line is from the turbulent boundary layer theory of ref. [2]. It has a scaling exponent of 0.43 around $\mathrm{Ta} = 10^9$ and 0.44 around $\mathrm{Ta} = 10^{13}$. Dark red data points are obtained by means of global torque measurements [10].

an instrumented tracer [44].

2.4 Conclusion

In conclusion, from high-speed PIV measurements we have found the wind Reynolds number in strongly turbulent TC flow to scale as $\mathrm{Re}_w \propto \mathrm{Ta}^{0.495\pm0.010}$, in accordance with the theory of ref. [2] and in conflict with Kraichnan's [29] prediction (2.2). In addition, we extracted the local angular velocity flux and found that $\mathrm{Nu}_\omega \propto \mathrm{Ta}^\gamma$ with $\gamma \sim 0.39 - 0.45$ depending on the axial position and consistent with earlier global torque measurements [26, 27]. For increasing Ta, a small axial dependence of Nu_ω is fading away, reflecting the decreasing

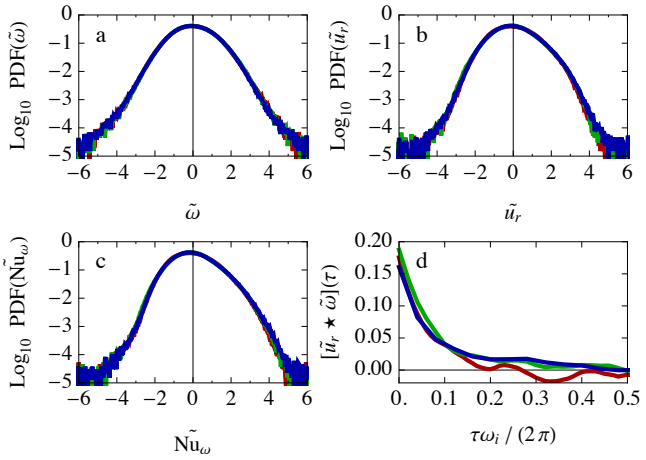

Figure 2.4: Results of three experiment with varying rotation rate resulting in Ta $= 3.8 \cdot 10^{11}$, $1.5 \cdot 10^{12}$, and $6.2 \cdot 10^{12}$, colored in red, green, and blue, respectively. All the data shown is averaged over the region $0.23\ \mathrm{m} \leq r \leq 0.25\ \mathrm{m}$, and measured at mid-height. All quantities with tildes are standardized (shifted and scaled such as to have zero mean and unit variance). (a) PDF of the standardized angular velocity. (b) PDF of the standardized radial velocity. (c) Standardized normalized local convective angular velocity flux PDF. (d) Cross-correlation coefficient of the angular velocity and the radial velocity, the dimensionless decaying time (in number of rotations) is found to be 0.07. The corresponding length scale can be found by multiplying this number with the circumference of the inner cylinder giving $\delta = 88$ mm, which is of the same order of magnitude as the gap width $d = 80$ mm.

importance of the Taylor vortices. The next step will be to provide full velocity and angular velocity profile measurements, including those in the boundary layers, and to extend the present measurements to the counter-rotating case and other radii ratios η, in order to further theoretically understand the local flow organization and the interplay between bulk and boundary layers in turbulent TC flow. A further highly interesting support for the presented idea of the close correspondence between the TC angular velocity transport in the studied Ta-range with the ultimate range of RB thermal convection is to identify the onset of this ultimate range when increasing Ta; here we expect a change of the Nu_ω scaling exponent and also a transitional change in the widths and profiles of the BLs.

3

Logarithmic boundary layers in strong Taylor-Couette turbulence°

We provide direct measurements of the boundary layer properties in highly turbulent Taylor-Couette flow up to Re $= 2 \cdot 10^6$(Ta $= 6.2 \cdot 10^{12}$) using high-resolution particle image velocimetry and particle tracking velocimetry; PIV and PTV, respectively. We find that the mean azimuthal velocity profile at the inner and outer cylinder can be fitted by the von Kármán log law $u^+ = \frac{1}{\kappa} \ln y^+ + B$. The von Kármán constant κ is found to depend on the driving strength Ta and for large Ta asymptotically approaches $\kappa \approx 0.40$. The variance profiles of the local azimuthal velocity have a universal peak around $y^+ \approx 12$ and collapse when rescaled with the driving velocity (and not with the friction velocity), displaying a log-dependence of y^+ as also found for channel and pipe flows.

°Published as: **Sander G. Huisman**, Sven Scharnowski, Christian Cierpka, Christian J. Kähler, Detlef Lohse, and Chao Sun *Logarithmic boundary layers in strong Taylor-Couette turbulence*, Phys. Rev. Let. **110**, 264501 (2013). Experiments performed by Huisman, Scharnowski, and Cierpka. Vector calculation and preliminary analysis done by Scharnowski and Cierpka. Further analysis, plotting, and writing of the manuscript done by Huisman. Supervision by Kähler, Lohse, and Sun. Proofread by everyone.

3.1 Introduction

Taylor-Couette (TC) flow is one of the paradigmatical flows in physics of fluids next to Rayleigh-Bénard convection, channel, flat plate, and pipe flow. It consists of two rotating coaxial cylinders shearing a fluid in between the cylinders, see fig. 3.1. For only inner cylinder rotation the Reynolds number $\mathrm{Re} = \omega_i r_i (r_o - r_i)/\nu$ quantifies the driving of this system. It is closely connected to the Taylor number $\mathrm{Ta} = \frac{1}{4}(\frac{1+\eta}{2\sqrt{\eta}})^4 (r_o - r_i)^2 (r_i + r_o)^2 \omega_i^2/\nu^2$, the ratio of centrifugal forces to viscous forces. Here, $\omega = u_\theta/r$ is the angular velocity component, r the radius, ν the kinematic viscosity, $\eta = r_i/r_o$ the radius ratio, and i and o subscripts denote quantities related to the inner and outer cylinder, respectively. For increasing Re the system is first dominated by coherent structures [18] whose length scale is of similar size as the gap width. For further increasing Re turbulence develops in the bulk at length scales between the integral and the Kolmogorov scale while the boundary layers are still of laminar type. This regime, in which the flow has a turbulent bulk and the boundary layers are of Prandtl-Blasius type, is called the classical regime [45]. By further increasing Re the system enters the so-called ultimate turbulent state in which also the boundary layers have turned turbulent [29, 2, 46, 47]. Note that vortical structures appear at the first transition above a critical Ta [48] and continue to persist within the ultimate regime [10, 49]. Based on global transport measurements, the ultimate regime of turbulence sets in at $\mathrm{Re(Ta)} \approx 10^4 (10^8)$ [9, 10, 41].

The coexistence of a laminar-type boundary layer and turbulent bulk in classical turbulent Rayleigh Bénard (RB) convection has been well established from numerous experimental and numerical investigations [50, 6, 7, 51]. This is also the case for the classical regime in TC flow [14, 31, 52, 10, 53] and the transition regime to ultimate TC flow [54, 55, 56]. Recently, a direct measurement [57] of the mean temperature profile close to the wall in the ultimate RB state revealed logarithmic behavior in the ultimate regime. For pipe, flat plate, and channel flows numerous experiments have revealed the existence of a log layer for the velocity and its variance see *e.g.* [58, 59, 60, 61, 62].

Neither for TC nor for RB there had been any direct and systematical measurement of the velocity boundary layer in the highly turbulent ultimate state due to the experimental difficulties. Assuming a logarithmic velocity profile in the boundary layers for highly turbulent TC flow, and matching the mean velocities at midgap, Lathrop *et al.* [9, 63] obtained a dependence of the

global torque and the Re, which agrees well with the torque measurements in the ultimate turbulence regime [9, 63, 64]. Only recently direct measurements on boundary layers were conducted by van Hout and Katz [54] for Ta up to $2 \cdot 10^9$, where they focused on the effect of counterrotation and found that the von Kármán constant depends on the angular velocity ratio ω_o/ω_i.

In this chapter we report the direct systematical experimental investigation of the boundary layer properties for very high Ta from Ta $= 9.9 \cdot 10^8$ to Ta $= 6.2 \cdot 10^{12}$ using high resolution PTV and PIV [65, 66, 67] with an unprecedented spatial resolution down to $\approx 10\,\mu$m. We focus on the case of inner cylinder rotation, and examine the boundary layer properties as a function of Re (Ta) in the ultimate turbulent TC regime.

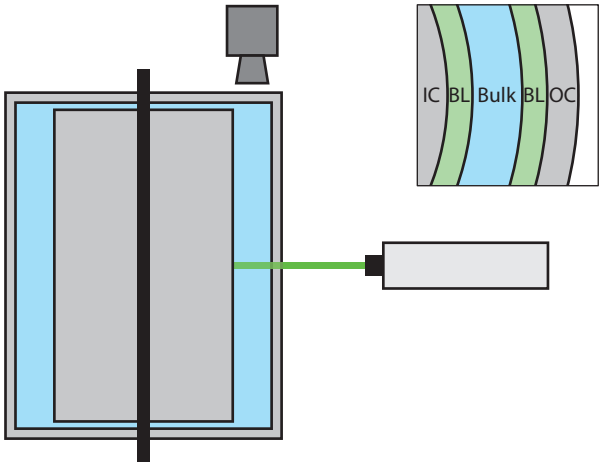

Figure 3.1: Sketch of the vertical cross section of the T^{3}C [21]. The flow is illuminated from the side in the horizontal plane using a laser, and the flow is imaged from the top using a high-resolution camera. Top-right inset: Schematic top view of different regions inside the gap: IC (inner cylinder), OC (outer cylinder), and BL (boundary layer). Measurements were done at midheight.

It was mathematically found [1] from the Navier-Stokes and continuity equations that $J_\omega = r^3(\langle u_r\omega\rangle_{z,\theta,t} - \nu\partial_r \langle\omega\rangle_{z,\theta,t})$ is strictly conserved in TC flow. Here $\langle X\rangle_{z,\theta,t}$ represents axial, azimuthal, and time averaging of X and u_r is the radial velocity. This transport quantity is independent of r; any flux going through an imaginary cylinder with radius r also goes through any other

imaginary cylinder, or mathematically $\partial_r J_\omega = 0$. This flux can be measured locally [68, 64] but also globally [9, 27, 26, 69] by measuring the torque needed to sustain constant velocity of the cylinders. The torque $\mathcal{T}$ is related to the dimensionless torque G and to J_ω as follows:

$$G = \frac{\mathcal{T}}{2\pi\ell\rho\nu^2} = \frac{J_\omega}{\nu^2} \tag{3.1}$$

where ρ is the density of the fluid, and ℓ the height of the cylinders. We can further relate these quantities to the wall shear stress τ_w, the friction velocity u_τ, and the viscous length scale δ_ν at the inner cylinder wall:

$$\tau_{w,i} = \frac{\mathcal{T}}{2\pi r_i^2 \ell} \tag{3.2}$$

$$u_{\tau,i} = \sqrt{\tau_{w,i}/\rho} \tag{3.3}$$

$$\delta_{\nu,i} = \nu/u_{\tau,i}\ . \tag{3.4}$$

Note that as J_ω is conserved radially, it is the same at both cylinders, and using eq. (3.1), also the torque $\mathcal{T}$ at both cylinders is the same. Consequently, τ_w, u_τ, and δ_ν are different at the inner and outer cylinder, and the following relations hold:

$$\tau_{w,i}/\tau_{w,o} = 1/\eta^2 \tag{3.5}$$

$$u_{\tau,i}/u_{\tau,o} = 1/\eta \tag{3.6}$$

$$\delta_{\nu,i}/\delta_{\nu,o} = \eta \tag{3.7}$$

3.2 Experiments and Results

The apparatus used for the experiments, the Twente turbulent Taylor-Couette (T^3C), has an inner cylinder with an outer radius of $r_i = 0.200$ m, a transparent outer cylinder with inner radius $r_o = 0.279$ m, giving a radius ratio of $\eta = 0.716$. The cylinders have a height of $\ell = 0.927$ m, resulting in an aspect ratio of $\Gamma = \ell/(r_o - r_i) = 11.7$. More details can be found in ref. [21]. For the PIV and PTV measurements, the working fluid (water) is seeded with fluorescent polymer particles [70]. Using a laser [71] we create a horizontal light sheet of roughly 500 μm thickness for illumination. The flow is then imaged from the top (see fig. 3.1) using a high-resolution camera [72] with large dynamical range.

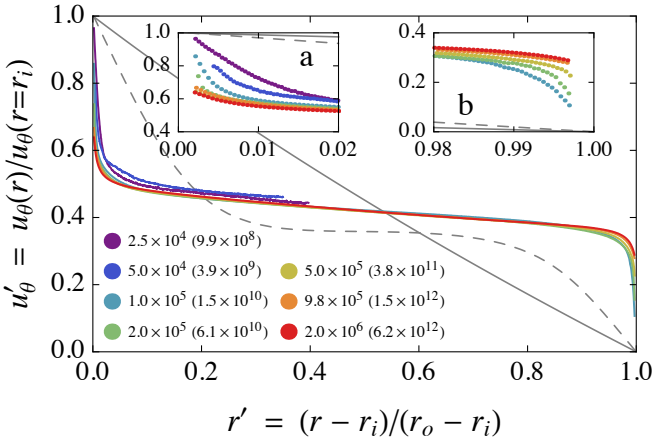

Figure 3.2: Azimuthal velocity profiles for varying Re(Ta) across the gap of the TC apparatus. The legend indicates Re(Ta) of the experiments. Insets a and b show a zoom of the data of the inner and outer boundary layer, respectively. Individual data points are plotted in the insets showing the high resolution of the measurements. The gray solid line represents the exact laminar circular-Couette (nonvortical) solution of the Navier-Stokes equations. The dashed line is the profile for Re(Ta) = $260(10^5)$, obtained from DNS [55].

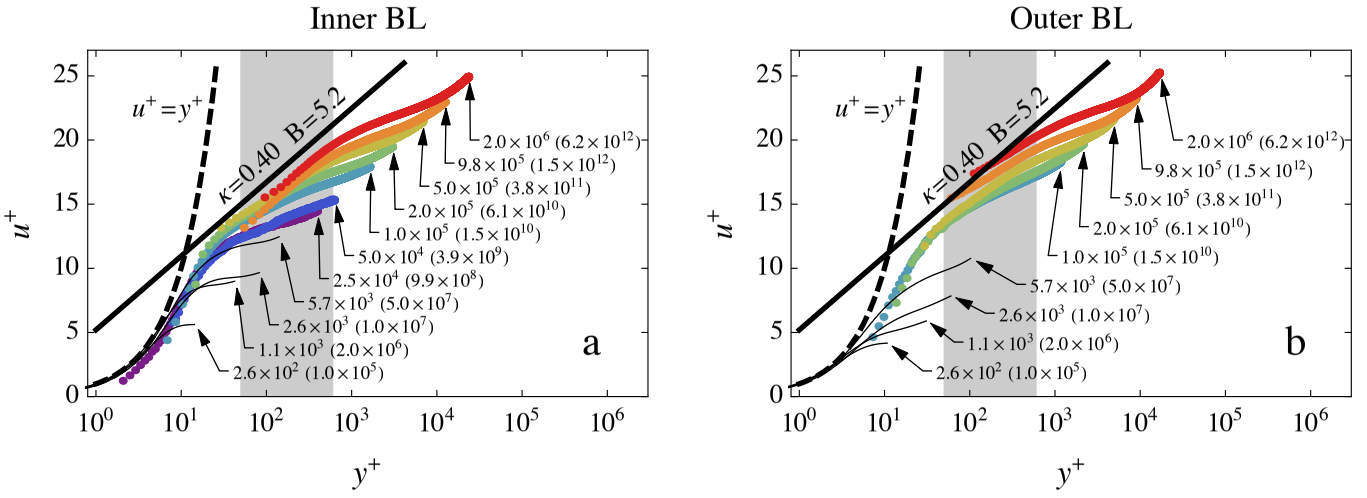

Figure 3.3: (a) Azimuthal velocity profile near the inner cylinder ($r' \in [0, 1/2]$) for varying Re(Ta). y^+ is the distance from the inner cylinder in units of the viscous length scale δ_ν. u^+ is defined as $\big(u(r_i) - u(r)\big)/u_\tau$, where $u(r)$ is the azimuthal component of the velocity, and $u(r_i)$ is the azimuthal velocity of the inner cylinder. (b) Azimuthal velocity profile near the outer cylinder $r' \in [1/2, 1]$. $y^+ = \big(r_o - r\big)/\delta_\nu$ is the distance from the outer cylinder in wall units. For the case of the outer boundary layer, the velocity is scaled as $u^+ = u(r)/u_\tau$. Both figures include the logarithmic law of the wall $u^+ = \frac{1}{\kappa} \ln y^+ + B$ by von Kármán, with the typical values of $\kappa = 0.40$ and $B = 5.2$, the viscous sublayer $u^+ = y^+$, and in gray the fitting domain $y^+ \in [50, 600]$. Each data-set is accompanied by an arrow with caption indicating Re(Ta). Thin solid lines are DNS results [55].

For each rotational velocity, 10^4 image pairs were acquired at a recording frequency of 10 Hz. The mean velocity distribution was computed using single-pixel ensemble correlation. This technique [73, 65] leads to a final resolution of ≈ 150 µm and in over 500 independent datapoints in the 80 mm gap. The standard deviation was directly computed from the velocity probability density function, which was extracted from the shape of the correlation function, as discussed in ref. [67]. This procedure ensures that all turbulent scales are included in the standard deviation. In contrast to standard PIV analysis, where only spatially low-pass filtered results are achieved, here also the contribution of the small scale fluctuations are properly considered. In order to resolve the near wall-region at the inner cylinder, a microscope [74] was mounted in front of the camera. With this setup, a scaling factor of ≈ 10 µm/px was achieved. To maximize the spatial resolution the near-wall region was evaluated with PTV methods, which is best suited for this purpose [66].

Fig. 3.2 shows all the measured mid-height profiles; five covering the full gap, and two covering just the region near the inner cylinder. As expected, the profiles do not conform to the laminar nonvortical profile, and the bulk has a much shallower slope due to turbulent mixing as the bulk flow in our parameter regime is fully turbulent [10, 64]. As a comparison, we included the profile for one of the first vortical flows, Re = 260 [55]. For the laminar axially independent solution, the convective part of J_ω is zero; any convection in the bulk of the system therefore decreases the $\partial_r \omega$ term in the bulk, resulting in a shallower angular velocity gradient. From the insets we can clearly see that for increasing Re(Ta) the boundary layers become steeper, and indeed the angular velocity profile has then to become steeper as u_r in J_ω is zero at the wall, and we are only left with the term $\partial_r \omega$. We now split our data in two parts: $r' \in [0, 1/2]$ (inner boundary layer) and $r' \in [1/2, 1]$ (outer boundary layer) and normalize velocities with the appropriate u_τ (eqs. (3.3) and (3.6)) and distances with the respective δ_ν (eqs. (3.4) and (3.7)), see fig. 3.3. We used *global* torque measurements [10, 26] to find u_τ and δ_ν. We spatially resolved the viscous sublayer ($y^+ < 5$) for the lowest Re. It is known that in this viscous sublayer the velocity profile follows $u^+ = y^+$. This concept also applies to TC flow, as supported by numerical simulations at low Re(Ta) (see e.g. ref. [55]). It should be noted that global torque measurements provide an average torque $\mathcal{T}$, while the local torque depends on height (following the large-scale Taylor vortex structure). So while eq. (3.2) holds for the average $\tau_{w,i}$, it might have an axial dependence. However, it has been found [41] that the azimuthal velocity at mid gap only has a weak axial dependence of the

order of $\sim 1\%$ for $a = 0$. To normalize the velocity profiles, we used the globally measured torque (as only this quantity is available for all Re(Ta) with sufficient precision) and thus the *average* $\tau_{w,i}$; this causes the imperfect matching of $u^+ = y^+$.
In flat turbulent boundary layer flows, at $y^+ > 50$ the effects of viscosity diminish. Furthermore, as suggested by Prandtl and von Kármán [75], in this limit the velocity profile converges to:

$$u^+ = \frac{1}{\kappa} \ln y^+ + B, \tag{3.8}$$

with κ the von Kármán constant and B the logarithmic intercept. We will now apply this concept to TC flow.

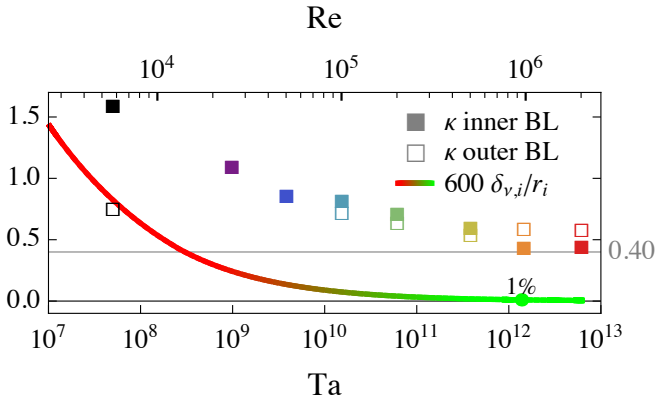

Figure 3.4: The parameter κ obtained by fitting $u^+ = \frac{1}{\kappa} \ln y^+ + B$ for $y^+ \in [50, 600]$ near the inner and outer cylinder. The color scheme is identical to figures 3.2 and 3.3, the black symbols are DNS results [55]. The solid colored line shows the ratio of the upper edge $600\delta_\nu$ of the fitting regime to the radius of curvature of the cylinder, quantifying the relative influence of the curvature. Note that $\delta_{\nu,i}/r_i = \delta_{\nu,o}/r_o$.

Outside the viscous wall region $y^+ > 50$ (inside the outer layer) fig. 3.3 shows the existence of a log-layer in the ultimate TC regime ($\mathrm{Ta} \gtrsim 10^9$), which is in sharp contrast to the laminar boundary layers found in the DNS simulations [55] (indicated by thin lines) in the classical turbulent regime. Our profiles are fitted to eq. (3.8) over the interval $y^+ \in [50, 600]$ (see the shaded area in fig. 3.3). We have chosen $y^+ = 50$ as lower edge of the interval as it is the start of the outer region, and the upper edge $y^+ = 600$ corresponds to about mid

gap ($(r_i + r_o)/2$) for our lowest Re(Ta) and the edge of the log-regime for our highest Re(Ta), see figure 3.3, but we stress that the values for κ and B only weakly depend on the exact extension of the fitting interval, as already found for pipe flow [61]. The values for κ are shown in fig. 3.4. They are different for the inner and outer boundary layer and depend on Re(Ta). For increasing Re(Ta), we see that the values for the inner boundary layer approach a value of $\kappa \approx 0.40$, close to the known classical value of $\kappa = 0.40$ [60, 62], recently systematically examined by Marusic *et al.* [61].
For the smaller Re(Ta) the value for κ is larger as the log-layer is not yet fully developed, as clearly seen from fig. 3.3. However, also geometric effects, namely the curvature of the cylinder, may contribute to this deviation. To quantify this effect, we plot the ratio of the outer edge ($600\delta_\nu$) of the fitting regime to the radius of curvature of the cylinder, see fig. 3.4, from which we conclude that for high Re $> 10^6$ the effect of the curvature becomes less than 1%, *i.e.* negligible. Finally we note that due to a possible slight height dependence of $\tau_{w,i}$ caused by the Taylor vortices even for this very turbulent flow, and the resulting imperfect matching of $u^+ = y^+$, the values of κ and B could still vary slightly with height.
In addition to PIV, also high resolution PTV measurements and analysis have been performed. For these measurement we zoomed into the area near the inner cylinder using a long-distance microscope to obtain a scaling factor of ≈ 10 µm/px. The spatial resolution of PTV depends on the number of images, and can thus be better than the pixel grid spacing projected in to physical space [65]. We extract the variance $\sigma^2(u_\theta)$ from the shape of the probability density function of the correlation function [67], see fig. 3.5. We normalize $\sigma(u_\theta)^2$ with the friction velocity u_τ (see fig. 3.5a) and with the driving velocity $u(r_i)$ (see fig. 3.5b). For both curves the maximum of $\sigma(u_\theta)^2$ is around $y^+ = 12$, which is remarkably similar to the values obtained in pipe and channel flows (see *e.g.* [59, 60]). In addition, it can be observed that the collapse of the data is better when we normalize $\sigma(u_\theta)$ with the driving velocity rather than the shear velocity u_τ. Opposed to the profiles shown in fig. 3.3 in the outer layer ($y^+ > 50$) the variance profiles universally collapse inside the buffer layer ($5 < y^+ < 30$) and seem not to depend on Re(Ta), vortical structure, and streamwise curvature. As shown in fig. 3.5a, we fit the data for $y^+ > 50$ (outer layer) with $(\sigma(u_\theta)/u_\tau)^2 = B_1 - A_1 \ln y^+$—the log law for the velocity variance [62]. The corresponding fitting parameters are indicated in fig. 3.5a. Remarkably, the slope A_1 (varying from 1.26 to 1.45) is comparable with values found ($A_1 \approx 1.25$) in high Re boundary layer flows [62].

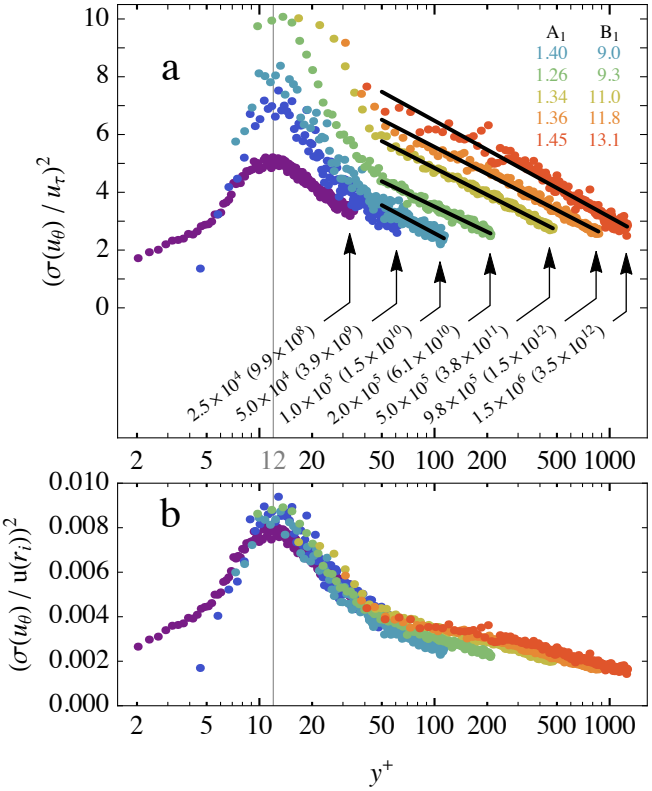

Figure 3.5: (a) The variance of the local azimuthal velocity is presented as a function of radial distance from the inner cylinder. The velocity is made dimensionless using the friction velocity u_τ, and the distance is in wall-units $y^+ = \big(r - r_i\big)/\delta_\nu$. (b) Same as in fig. a but the velocity has been rescaled using the driving velocity $u(r_i)$. Corresponding colors in figs. a and b correspond to the same data-set, and are consistent with previous figures. The Re(Ta) are indicated with arrows in figure a. For $y^+ > 50$ the five highest Ta cases are fitted with $(\sigma(u_\theta)/u_\tau)^2 = B_1 - A_1 \ln y^+$. The fitting parameters are listed inside fig. a for increasing Ta and colored accordingly.

3.3 Summary

To summarize, we performed direct measurements of the velocity boundary layer profiles in highly turbulent TC flow up to Ta $= 6.2 \cdot 10^{12}$ and found the emergence of a log layer, as theoretically proposed in refs. [29, 2]. The fitted von Kármán constant κ was found to approach the classical value of 0.40 for large enough Ta. Furthermore, we found that the peak in $\sigma(u_\theta)$ universally collapses around $y^+ = 12$, and that the height of the peak is found to collapse better when scaled with the driving velocity as compared to the friction velocity. Lastly, the variance profiles depicted a log dependence for $y^+ > 50$.

4

Multiple states in highly turbulent Taylor-Couette flow°

The ubiquity of turbulent flows in nature and technology makes it of utmost importance to fundamentally understand turbulence. Kolmogorov's 1941 paradigm suggests that for strongly turbulent flows with many degrees of freedom and its large fluctuations, there would only be *one* turbulent state as the large fluctuations would explore the entire higher dimensional phase space. Here we report the first conclusive evidence of multiple turbulent states for large Reynolds number $\mathrm{Re} = \mathcal{O}(10^6)$ (Taylor number $\mathrm{Ta} = \mathcal{O}(10^{12})$) Taylor-Couette flow in the regime of ultimate turbulence, by probing the phase space spanned by the rotation rates of the inner and outer cylinder. The manifestation of multiple turbulent states is exemplified by providing combined global torque- and local-velocity measurements. This result verifies the notion that bifurcations can occur in high-dimensional flows (that is, very large Re) and questions Kolmogorov's paradigm.

°Published as: **Sander G. Huisman**, Roeland C.A. van der Veen, Chao Sun, and Detlef Lohse, *Multiple states in highly turbulent Taylor-Couette flow*, Nat. Commun. **5**, (2014). Experiments, and analysis performed by Huisman and van der Veen. Plotting and writing of the manuscript done by Huisman. Supervision by Sun and Lohse, and proofread by everyone.

4.1 Introduction

For macroscopic flows of water or air the Reynolds number is much larger than unity; the standard type of flow is therefore turbulent. A typical Reynolds number for a person walking is already $\mathcal{O}(10^5)$. For large airplanes the Reynolds number is $\mathcal{O}(10^9)$, for atmospheric currents it is $\mathcal{O}(10^{10})$, and for ocean currents it is $\mathcal{O}(10^{11})$. Reynolds numbers are even larger for astrophysical problems [76]. It is not possible to achieve these large Reynolds numbers in a lab-environment nor is it accessible by direct-numerical simulations (DNS). To extrapolate data from $\mathrm{Re} = \mathcal{O}(10^6)$ to the scales of our atmosphere or the ocean we must bridge 4–5 decades in Reynolds number, and even more for astrophysical applications [77]. While scaling laws exist that can predict the rough magnitude of these flows, they are rendered impractical if there is a flow-transition from a turbulent state at lower Re to another turbulent state at higher Re, or if multiple turbulent states can coexist at the same Re. To extrapolate to large scales we need to know whether there are transitions and whether multiple states can coexist in high Reynolds number flows. As an answer to this question, Kolmogorov's more than 70-year-old paradigm states that for large Reynolds numbers, flows would become 'featureless' due to the fact that the highly-dimensional phase space is explored in its entirety due to the large fluctuations of said flows [78, 79].

For Rayleigh-Bénard convection at low Rayleigh number (laminar-type boundary layers, $\mathrm{Ra} < 10^{14}$), continuous switching between two different roll states, with different heat transfer properties, was found [80, 81, 82]. In this case, the turbulent fluctuations were large enough to overcome trapping in one turbulent state. In the case of high Rayleigh number (turbulent boundary layers), no multiple states have been observed in a single setup; only when the boundary conditions were changed one could trigger a transition to a different state [83, 2]. For von Kármán flow multiple turbulent states were found when driving it with impellors with curved blades [84, 85, 86]. These studies revealed the spontaneous symmetry-breaking and turbulent bifurcations in highly turbulent von Kármán flow up to $\mathrm{Re} = 10^6$. In spherical-Couette flow Zimmerman *et al.* [87] observed *spontaneous* switching between two turbulent states at fixed rotation rates. The presence of coherent structures at high Reynolds numbers in closed systems suggests that Kolmogorov's hypothesis [78, 79] is incomplete [84, 85, 86, 87] and might need revisiting in order to apply to these flow systems. For Taylor-Couette multiple states are only

observed for low Re (see *e.g.* ref. [18])—the so-called classical regime, where the bulk is laminar or turbulent but the boundary layers are still of laminar type. Around Re $\sim 10^4$ [55, 88] the system transitions into the ultimate state [29, 8, 2], in which the boundary layers are also turbulent [89], and where new scaling laws of the response parameters set in [15, 26, 27, 41, 64, 55, 56, 69]. Historically, this ultimate regime was defined based on the scaling properties of the flow [29]. Consequently, it does not necessarily exclude the existence of multiple turbulent states. To correctly extrapolate to much higher Re it is crucial to know the characteristics of the turbulent state and the existence of other such states. In ref. [90] it was shown that for increasing Re the waves on top of the Taylor vortices become increasingly complex until only turbulent Taylor vortices are left. Lewis *et al.* [10] came to the same conclusion by plotting the velocity power spectra for increasing Re up to $5 \cdot 10^5$, and observed that the peaks gradually decrease in amplitude. They noted that turbulent Taylor vortices remained. On the other hand, the findings of Lathrop *et al.* [8] suggest that the Taylor-vortices are *not* present for Reynolds numbers beyond $1.2 \cdot 10^5$.

Here we demonstrate that roll structures remain for Taylor-Couette flow even in the ultimate regime up to at least Re $= \mathcal{O}(10^6)$ and show that multiple states are even possible far beyond the transition into this ultimate regime.

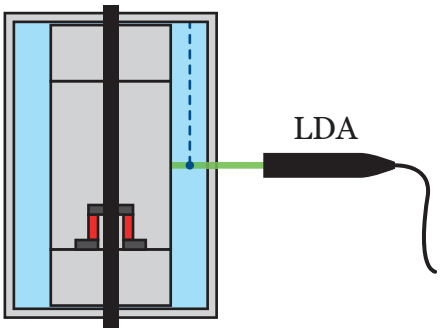

Figure 4.1: Experimental apparatus. Schematic of the cross section of the T^3C [21]: the apparatus has been outfitted with a new coaxial torque transducer (shown in red), see the Methods section. The azimuthal velocity is probed at the middle of the gap and in the top half of the apparatus using laser Doppler anemometry (LDA).

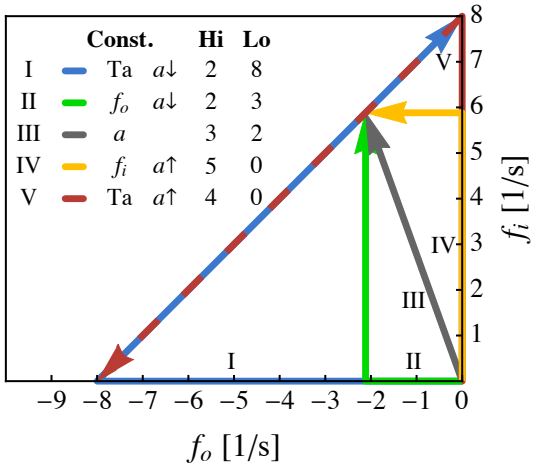

Figure 4.2: Phase space of the trajectories I to V. The arrows indicate the direction in which the phase space is probed. The legend shows which parameter is kept constant, whether the parameter $a = -f_o/f_i$ is going down ($a \downarrow$) or up ($a \uparrow$), and the number of times it went to a high (Hi) or a low (Lo) state. All trajectories go through (or end at) $f_i = 5.882$ Hz, $f_o = -2.118$ Hz ($a = 0.36$, and Ta $\approx 10^{12}$ or Re $\approx 10^6$).

4.2 Results

For TC flow [26, 27, 41, 64, 55, 56, 69] and using the analogy of TC flow with Rayleigh-Bénard (RB) convection [45] it was found that the Taylor number $\mathrm{Ta} = \frac{1}{4}(\frac{1+\eta}{2\sqrt{\eta}})^4(r_o - r_i)^2(r_i + r_o)^2(\omega_i - \omega_o)^2/\nu^2$ is a very well suited parameter to describe the driving of the system [1]. Here $\omega_{i,o} = 2\pi f_{i,o}$ are the angular rotation rates and ν the kinematic viscosity. The response of the system is the torque required to sustain constant angular velocity or a 'Nusselt' number [1], $\mathrm{Nu}_\omega = \tau/\tau_{\mathrm{lam}}$, which is the angular velocity flux nondimensionalised with the flux of the laminar, nonvortical, flow. This Nusselt number scales approximately as $\mathrm{Nu}_\omega \propto \mathrm{Ta}^{0.38}$ [26, 27] around $\mathrm{Ta} = 10^{12}$, which is interpreted as $\mathrm{Nu}_\omega \propto \mathrm{Ta}^{1/2} \cdot$ Log-corrections [29, 2]. We now find with our new sensor with improved accuracy that the exponent is closer to 0.40 (results not shown), which is still consistent with the aforementioned interpretation. The Twente Turbulent Taylor-Couette facility ($\mathrm{T}^3\mathrm{C}$) [21] was used for the experiments, see fig. 4.1. The $\mathrm{T}^3\mathrm{C}$ [21] has an inner cylinder with an outer radius

of $r_i = 200$ mm, a transparent outer cylinder with inner radius $r_o = 279$ mm, and a height of $L = 927$ mm, giving a radius ratio of $\eta = r_i/r_o = 0.716$ and an aspect ratio of $\Gamma = L/(r_o - r_i) = 11.7$. The top and bottom caps rotate along with the outer cylinder. The apparatus was filled with water and actively cooled to keep the temperature constant. The torque is measured on the middle section of the inner cylinder using a new co-axial torque transducer (Honeywell `2404-2K`, maximum capacity of 225 Nm), with improved accuracy compared to our former load cell [26]. The azimuthal velocity is obtained by laser Doppler anemometry (LDA), see fig. 4.1. The laser beams go through the outer cylinder and are focused in the middle of the gap, see fig. 4.1 The water is seeded with 5 µm diameter polyamide tracer particles (Dantec) with a maximum Stokes number of $\mathrm{St} = \tau_p/\eta_K = 0.004 \ll 1$. Curvature effects of the outer cylinder to our LDA system are accounted for by numerically ray-tracing the LDA-beams [91].

First we follow trajectory I and V shown in the parameter space of fig. 4.2, which have as a characteristic that $f_i - f_o = 8$ Hz is kept constant (except for the initial and the final part) and is equivalent to approximately $\mathrm{Ta} = 10^{12}$ or $\mathrm{Re} = (\omega_i r_i - \omega_o r_o)(r_o - r_i)/\nu = \mathcal{O}(10^6)$. While traversing the trajectory we continuously measure the torque, scanning over a in one experiment. This is in contrast to experiments that were performed before, where the torque was measured by performing separate ramps of constant $a = -f_o/f_i$ [8, 26, 27, 41, 69]. We slowly follow a trajectory in phase space, such as to be in a statistically quasi-steady state the entire time [26]. The temperature variation within the system is 0.04 K, the variation during each measurement is 0.3 K, and the mean temperature for each run is between 19 °C and 24 °C. The Taylor number depends on viscosity and thus temperature; we therefore remove the main temperature dependence by compensating the Nusselt number with $\mathrm{Ta}^{0.4}$, because $\mathrm{Nu}_\omega \propto \mathrm{Ta}^{0.4}$ in the present parameter regime. This approach has been followed before, see *e.g.* [26, 27].

As can be seen in figure 4.3, for increasing a (red shades, trajectory V), the torque is continuous and shows a peak around $a = 0.36$, as found before [26, 27, 41, 69]. For trajectory I the torque is found to be the same as trajectory V for $a < 0.17$ and $a > 0.51$, however for $0.17 < a < 0.51$ the torque is found to be different. For decreasing a the system is able to enter another state around $a = 0.51$ which is characterised by a lower torque (from here on called 'low state'), around $a = 0.17$ the system sharply jumps back to a higher torque state ('high state'), see also the close up view in figure 4.4. We have repeated these experiments in order to see how sharp this transition is, and to see in

which state the system is, see fig. 4.2. For trajectory V we observe that it always goes into the high state, while for the reverse trajectory I the system goes to the low state (for $0.17 < a < 0.51$) with a high probability (8 out of 10).

To verify that the high and low torque states originate from two different physical states, we measure the azimuthal velocity at half-height $z = L/2$ and center of the gap $r = (r_i + r_o)/2$, while the system is let to move along trajectories I and V in phase space, see fig. 4.3b. As in fig. 4.3a, it is found that the local velocity inside the system bifurcates and that two states are possible. The presence of multiple states in a local measurement (azimuthal velocity) and at the same time a global measurement (torque) provides convincing evidence that the system can indeed be in different turbulent states, despite the very high Taylor number of $\mathcal{O}(10^{12})$ (ultimate regime).

To further characterize the turbulent state of the system, we perform axial scans of the azimuthal velocity in the top half of our apparatus for several a for both the high and the low state, see figures 4.3c and 4.3d. For each a the azimuthal velocity is standardized (zero mean, unit standard deviation) and color-coded. Fig. 4.3c shows the local velocity for the high state (trajectory V), and shows the presence of 5 large minima/maxima for $a \leq 0.45$; a clear characteristic of 4 turbulent Taylor vortices. For $a \geq 0.5$ the state of the system is less clear, and the system appears to jump between states (without a well-defined a-dependence), as seen in the local velocity in fig. 4.3b. This behavior looks similar to what was found in RB convection in the classical turbulent regime [82]. However, the mechanism is different owing to the shorter turnover time scale of the TC system, and the presence of the additional control parameter a in TC, with which we can control the transition. Furthermore, the observed transition is different from Ref. [87] where *spontaneous* switching back and forth between two states was found, based on global and local measurements. Fig. 4.3d shows the same switching behavior as the high state of fig. 4.3c for a outside $[0.17, 0.51]$. For $0.17 < a < 0.51$ it is found that the azimuthal velocity has 4 large minima/maxima, which is the signature of 3 turbulent Taylor vortices (in the top half of the system).

In addition, we provide, for selected a, the angular velocity profiles as lines in fig. 4.5. The angular profiles for trajectories I and V are identical (within experimental and statistical error) for a outside $[0.17, 0.51]$. For $a \in [0.17, 0.51]$ the profiles are different and show distinguishing features of 3 or 4 rolls (6 and 8 rolls in the entire setup), see also the schematics on the right of fig. 4.5. At the boundary of the last (top) roll and the penultimate roll high velocity fluid

from the inner cylinder is advected towards the middle, increasing the velocity at the center of the gap. Similarly, at the boundary of the penultimate and the antepenultimate roll the low velocity fluid from the outer cylinder is advected inwards, decreasing the velocity at the center of the gap. The corresponding average aspect ratio of the vortices is 1.96 (3 rolls) and 1.46 (4 rolls), which is consistent with previous studies (see *e.g.* fig. 2.5 in ref. [92]). Close inspection of fig. 4.3c and fig. 4.5a shows that the roll around $z/L = 0.5$ slightly drifts upwards for $0.3 < a < 0.45$ (compared to $a < 0.3$), which could be a signature of symmetry breaking; the top half of the system behaves slightly differently from the bottom half. This is an explanation of the anomaly in the local angular velocity for trajectory V around $a \approx 0.28$. Such symmetry-breaking behavior has also been found in von Kármán flow [93]. Note that the middle section of the inner cylinder with height $z/L = 0.578$ does not cover all the rolls, therefore the exact mean torque value over the entire inner cylinder could be different. It is, however, unlikely that this difference takes away the 'jumping' behavior.

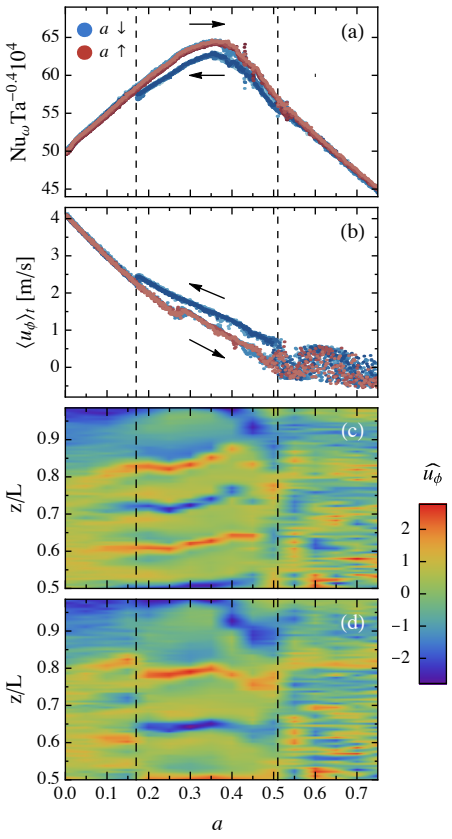

Figure 4.3: (a) Compensated Nu_ω as a function of a. Experiments following trajectories I and V are colored in blue and red, respectively. Experiments following trajectory I either go into a high or a low state for $0.17 < a < 0.51$, while experiments of trajectory V are always in the high state. (b) Azimuthal velocity measured at $r = (r_i + r_o)/2$ and $z/L = 0.5$ as a function of a for trajectories I and V. Same colors as in fig. (a). For the local velocity we also see that the system bifurcates when following trajectory I around $a = 0.51$, choosing the high or low state for $0.17 < a < 0.51$. (c) and (d) show axial scans of the standardized u_ϕ for varying a following trajectories V and I, respectively. 4 rolls are present in the top half of the system in fig. (c), while in fig. (d) only 3 rolls are present for $0.17 < a < 0.51$. For $a < 0.17$ and $a > 0.51$ the system is in the same state, regardless of the trajectory. $\widehat{u_\phi} = (u_\phi - \langle u_\phi \rangle_z)/\sigma_a(u_\phi)$, where σ_a is the standard deviation of u_ϕ for each a, and $\langle\rangle_x$ stands for averaging over x. The torque of trajectory V is 2.5% larger than for trajectory I at $a = 0.36$.

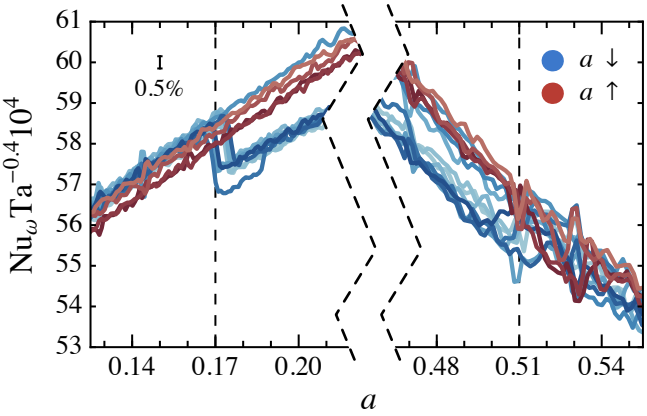

Figure 4.4: Close up view of figure 4.3a. The trajectories I ($a \downarrow$) that are in the low state sharply transition to the high state around $a = 0.17$. Trajectories I start to transition around $a = 0.51$, though the process seems more gradual, and sometimes stay in the high state. Trajectories V ($a \uparrow$) never transition and are always in the high state. The error bar, shown in the top-left of the figure, is based on the accuracy of the torque sensor in the system.

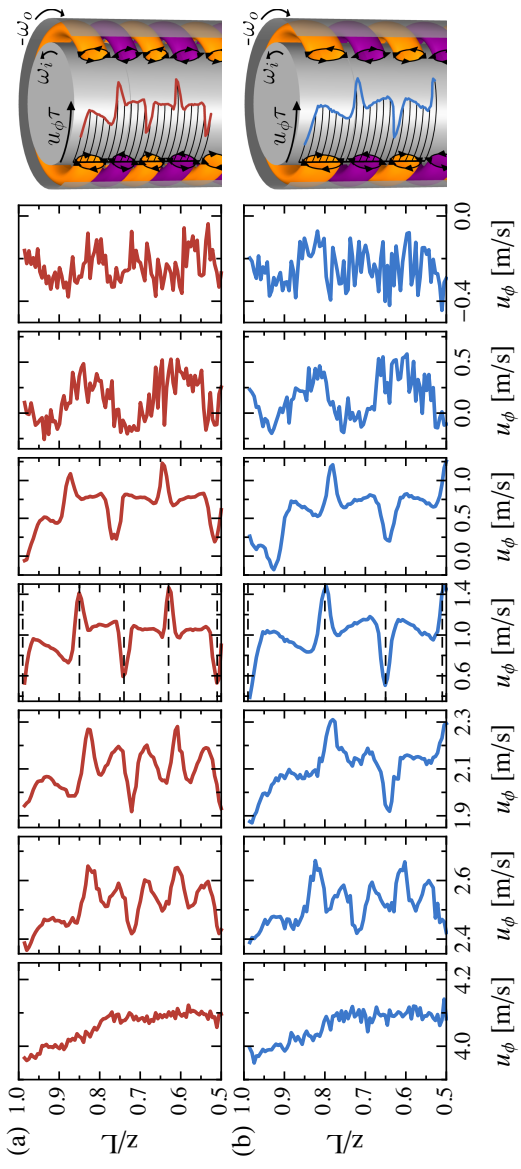

Figure 4.5: Flow structures at different rotation ratios. Azimuthal velocity as a function of height z/L for various a. Subset of the data shown in figures 4.3c and 4.3d. (a) Profiles following trajectory V. (b) Profiles following trajectory I. For $a \in \{0.00, 0.15, 0.55, 0.75\}$ the velocity profiles are the same for both trajectories. For intermediate values ($a \in \{0.20, 0.35, 0.40\}$) the profiles are different; trajectory V (red) shows the emergence of 4 rolls in the top half of the system, while trajectory I (blue) shows only 3 rolls in the top half of the system. For the case of maximum torque ($a = 0.35$), dashed lines are drawn to indicate the boundaries between the rolls. For $a = 0.15$ the system shows the high state (with 4 rolls in the top half). This structure seems to fade once the system is pushed towards $a = 0$, see also figures 4.3(c) and 4.3(d). On the right we show a schematical overview of the rolls and the angular velocity profile for $a = 0.35$ in 3D, $\tau = 0.2$ s.

From our findings of trajectory I and V (constant Ta) we find that the maximum torque is at $a = 0.36$ ($f_i = 5.882$ Hz, $f_o = -2.118$ Hz). We now look at other trajectories reaching this maximum but keeping either f_o, a, or f_i constant, see trajectories II–IV in fig. 4.2. For constant f_o and constant a (trajectories II and III) the system was found to have the ability to go in either the high or the low state as well, see the legend of fig. 4.2. Like trajectory V, trajectory IV (constant f_i) was found to be characterised by a high state of the system. It seems that if $a = 0.36$ is approached from below (trajectories IV and V) the flow does not bifurcate. However, the system does bifurcate when $a = 0.36$ is approached from the top, or if a is kept constant but the driving strength is increased.

4.3 Discussion

We have shown that Taylor-Couette flow displays flow structure even for a very high Taylor number of roughly 10^{12} (Re $= \mathcal{O}(10^6)$), which is beyond Reynolds numbers for which large-scale structures were believed to vanish in Kolmogorov's picture. In addition, we found that the system is hysteretic and can be in multiple stable turbulent states for the same driving parameters. The multiple states are simultaneously measured globally and locally by performing torque and LDA measurements. It was found that multiple states can occur for rotation ratios $0.17 < a < 0.51$. For $0 \leq a < 0.17$ there is only a single stable state, though we cannot exclude that other trajectories in phase space might trigger multiple states in this region. For $a > 0.51$ the system does not possess a state with a clear roll structure. Presently, a theoretical understanding of the values $a = 0.17$, $a = 0.51$ and the sharp and smooth behaviour of the jumps around those a is lacking. Finally we note that the presented experiments, performed in the $\mathrm{T^3C}$ facility, will be challenging to simulate in DNS in the foreseen future: simulations of such high Ta are difficult, especially for $\Gamma = \mathcal{O}(10)$. The present work highlights the importance of the coherent structures and their selectability in highly turbulent flows, which demand continued effort and investigation. The question of whether or not these structures survive for even larger Reynolds numbers, remains open but is important for understanding the myriad of large-scale flows in nature.

5

Statistics of turbulent fluctuations in counter-rotating Taylor-Couette flows°

The statistics of velocity fluctuations of turbulent Taylor-Couette flow are examined. The rotation rate of the inner and outer cylinder are varied while keeping the Taylor number fixed to $1.49 \cdot 10^{12}$ [$\mathcal{O}(\mathrm{Re}) = 10^6$]. The azimuthal velocity component of the flow is measured using laser Doppler anemometry. For each experiment $5 \cdot 10^6$ datapoints are acquired and carefully analyzed. Using extended self-similarity [Benzi *et al.*, Phys. Rev. E **48**, R29 (1993)] the longitudinal structure function exponents are extracted, and are found to weakly depend on the ratio of the rotation rates. For the case where only the inner cylinder rotates the results are in good agreement with results measured by Lewis and Swinney [Phys. Rev. E **59**, 5457, 1999] using hot-film anemometry. The power spectra show clear $-5/3$ scaling for the intermediate angular velocity ratios $-\omega_o/\omega_i \in \{0.6, 0.8, 1.0\}$, roughly $-5/3$ scaling for $-\omega_o/\omega_i \in \{0.2, 0.3, 0.4, 2.0\}$, and no clear scaling law can be found for $-\omega_0/\omega_i = 0$ (inner cylinder rotation only); the local scaling exponent of the spectra has a strong frequency dependence. We relate these observations to the shape of the probability density function of the azimuthal velocity and the presence of a neutral line.

°Published as: **Sander G. Huisman**, Chao Sun, and Detlef Lohse, *Statistics of turbulent fluctuations in counter-rotating Taylor-Couette flows*, Phys. Rev. E **88**, 063001 (2013). Experiments, analysis, plotting, and writing of the manuscript done by Huisman. Supervision by Sun and Lohse, proofread by everyone.

5.1 Introduction

Taylor-Couette (TC) flow, among others like Rayleigh-Bénard convection, and von Kármán, pipe, channel and plate flow, played a pivotal role in exploring fundamental concepts in fluid mechanics [94]. In a TC apparatus, fluid is confined between two independently rotating coaxial cylinders; see Fig. 3.1. The TC geometry is best described with cylindrical coordinates: radial distance ρ, azimuth θ, and height z. The driving of the TC apparatus is given by two Reynolds numbers:

$$\mathrm{Re}_{i,o} = \frac{\omega_{i,o}\rho_{i,o}(\rho_o - \rho_i)}{\nu},$$

where ω is the angular velocity defined as u_θ/ρ, ρ the radius, ν the kinematic viscosity, and the i and o subscripts denote quantities related to the inner and outer cylinder, respectively. Another way of describing the flow is by a Taylor number $\mathrm{Ta} = \frac{1}{4}\sigma(\rho_o - \rho_i)^2(\rho_o + \rho_i)^2(\omega_i - \omega_o)^2/\nu^2$, which is the ratio of centrifugal forces to viscous forces, along with a parameter describing the ratio of the driving velocities, for which we have chosen:

$$a = -\frac{\omega_o}{\omega_i}. \tag{5.1}$$

σ is defined as $[(1+\eta)/\sqrt{4\eta}]^4$ with the radius ratio $\eta = \rho_i/\rho_o$. By measuring the torque $\mathcal{T}$ [10, 16, 95, 26, 27, 64, 69, 56], required to maintain constant angular velocity of both cylinders, we can find the power input (P) of our system using $P = \mathcal{T}\,|\omega_i - \omega_o|$. Note that we can measure the torque on either cylinder as it has the same magnitude on the inner and the outer cylinders [1]. As all the energy that enters the system globally will be dissipated by viscous dissipation, the torque can be related to the average energy dissipation rate:

$$\epsilon = \frac{(\text{power input})}{(\text{mass})} = \frac{\mathcal{T}\,|\omega_i - \omega_o|}{\rho_{\text{fluid}}\pi(\rho_o^2 - \rho_i^2)L}, \tag{5.2}$$

where ρ_{fluid} is the density of the working fluid and L the length of the cylinders. Using the energy dissipation rate and the viscosity we can now find the average Kolmogorov length scale [78, 79] in our flow: $\eta_K = \left(\nu^3/\epsilon\right)^{1/4}$.
Using hot-film anemometry, Lewis and Swinney [10, 34] measured the statistics of velocity fluctuations for the case of inner cylinder rotation for Re up to $5.4 \cdot 10^5$. They found that the energy spectrum does not show power

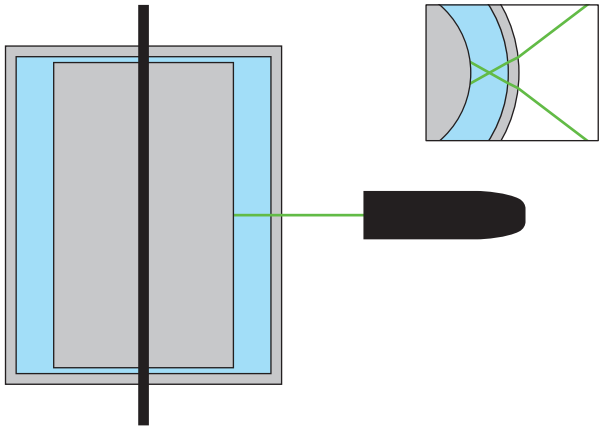

Figure 5.1: Sketch of the vertical cross section of the Twente Turbulent Taylor-Couette facility (T^3C) [21]. The beams of the laser Doppler anemometer (LDA) are in the horizontal plane at middle height, $z = L/2$. Top right inset: Horizontal cross section showing the beams of the LDA. The beams refract twice on the outer cylinder and intersect at the middle of the gap. The angle between the beams is exaggerated to highlight the refraction on the inner and outer surface of the outer cylinder.

law scaling, and that the structure function exponents—calculated using extended self-similarity [96]—are close to those found in other flows [10]. In this chapter we quantify the turbulent statistics of Taylor-Couette flow with various rotation ratios [Eq. (5.1)] for fixed Taylor number of $\mathrm{Ta} = 1.49 \cdot 10^{12}$ [$\mathcal{O}(\mathrm{Re}) = 10^6$]. We used the Twente Turbulent Taylor-Couette facility (T^3C) [21], which was filled with water and actively cooled to keep the temperature constant. The T^3C has an inner cylinder with an outer radius of $\rho_i = 200$ mm and a transparent outer cylinder with inner radius $\rho_o = 279$ mm, giving a radius ratio of $\eta = 0.716$. The cylinders have a height of $L = 927$ mm, resulting in an aspect ratio of $\Gamma = L/(\rho_o - \rho_i) = 11.7$. We measured the azimuthal velocity using laser Doppler anemometry (LDA). The advantage of this technique is that it allows for a nonintrusive measurement of a velocity component. For the case of counterrotation the mean flow direction is not always in a single direction, and using, *e.g.* a hot-film probe or a pitot tube to measure the local velocity would result in measuring the *speed* in the wake of the probe. The laser beams go through the outer cylinder and are focused in the middle of the

gap ($2\rho = \rho_i + \rho_o$) at midheight ($z = L/2$), and lie in the θ–r plane; see also Fig. 5.1. The water is seeded with tracer particles [70] with a mean radius of 2.5 µm and density of 1.03 g/cm^3. This radius is roughly six times smaller than our Kolmogorov length scale. We equate the drag force $F_{\text{drag}} = 6\pi\mu r_{\text{seed}}\Delta u_\theta$ and the centrifugal force $F_{\text{cent}} = (\rho_{\text{seed}} - \rho_{\text{fluid}})(4\pi r^3/3)u_\theta^2/\rho$ of the seeding particles, and compute $\Delta u_\theta = |u_{\theta,\text{seed}} - u_{\theta,\text{fluid}}|$ to make sure the particles faithfully follow the flow. For our measurements we find that $\Delta u_\theta \approx 40$ µm/s, which is much smaller than the driving velocities $\mathcal{O}(\omega_i\rho_i - \omega_o\rho_o) = 10$ m/s, so we are sure that the particles follow the flow. In addition one could calculate the Stokes number; we find that $\text{St} = \tau_p/\tau_\eta = 0.006 \ll 1$ in the worst case ($a = 0.3$). Due to the curvature of the outer cylinder we have to correct the measured velocity by multiplying it with a constant factor. We find this constant numerically by ray-tracing [91] the LDA beams in our optical geometry.

a	$\frac{\omega_i}{2\pi}$	$\frac{\omega_o}{2\pi}$	Re	$\langle u_\theta \rangle_t$	σ	ϵ	Re_λ	$\frac{\mu_4}{\sigma^4}$
	1/s	1/s	10^6	m/s	m/s	m^2/s^3		
0.0	9.99	0.00	1.38	5.08	0.31	12.9	106	3.37
0.2	8.32	-1.66	1.32	2.42	0.38	15.3	144	3.00
0.3	7.67	-2.30	1.29	1.62	0.32	16.3	97	3.96
0.4	7.13	-2.85	1.27	1.48	0.35	15.8	120	2.77
0.6	6.24	-3.74	1.24	0.36	0.47	13.2	240	3.02
0.8	5.54	-4.44	1.21	-0.43	0.49	11.0	278	2.89
1.0	4.99	-5.00	1.19	-0.83	0.43	9.2	235	3.27
2.0	3.32	-6.66	1.12	-3.10	0.32	5.1	173	3.23

Table 5.1: Experimental parameters for the various rotation ratios. For each experiment the Taylor number is fixed to $1.49 \cdot 10^{12}$ and the number of data points is fixed to $5 \cdot 10^6$. ω_i and ω_o are measured using high precision magnetic encoders. All the measurements are done at midheight and in the middle of the gap. $\langle \cdot \rangle_t$ denotes averaging over time. The Taylor-Reynolds number is found by combining local velocity and global torque measurements: $\text{Re}_\lambda = \sqrt{\frac{15\sigma^4}{\epsilon\nu}}$, where ϵ comes from the global torque, see Eq. (5.2). The standard deviation of u_θ is given by σ and the kurtosis by $\frac{\mu_4}{\sigma^4}$.

5.2 Experiments and Results

In our experiments we fixed $\Delta\omega \equiv \omega_i - \omega_o$ (see Table 5.1); the consequence of this is that our Taylor number is fixed, while our Reynolds number varies slightly. For each experiments we acquire $5 \cdot 10^6$ data points. Because the arrival times of LDA measurements are of stochastic nature the time series are then linearly interpolated using twice the average acquisition frequency ($2f_\mathrm{a}$), such as to create a time series with equal temporal spacing. We chose double the frequency to also capture fast fluctuations which are otherwise lost. It can happen that for a relatively long time there is no measurement, while for other moments a burst of measurements is taken. We take care to disable parts of the interpolated time series for which the temporal gap in the original data is too big ($3/f$ is chosen; although the effect is hardly noticeable we wanted to account for the time that the LDA beams are blocked by vertical supporting rods), and for which interpolation is not justified. These disabled data points are not used in any of the calculations, except for the spectra.
We will first look at the probability density function (PDF) of the velocimetry data; see Fig. 5.2. For the cases $a = 0.6$, $a = 0.8$, and $a = 1$, we see that the PDF $\mathcal{F}$ seems to be comprised of two parts, as it has two bumps; one bump for $u_\theta > 0$ and one for $u_\theta < 0$. It seems that the presence of a neutral line ($u_\theta = 0$) alters the flow dynamics, as was also found in Ref. [41]. The outer region is stabilized by the outer cylinder, while the inner region is destabilized by the inner cylinder. Somewhere in between there must therefore be an interface where $u_\theta = 0$. For $a \in \{0.6, 0.8, 1.0\}$ our measurement position is on the border of this interface [41]. Also indicated in Fig. 5.2 and in Table 5.1 is the mean velocity. As expected, the mean velocity decreases monotonically with increasing a, while the standard deviation is quite similar throughout, but slightly higher for the cases where the PDF is comprised of two contributions [41].
In order to compare the shapes of the PDFs we standardize the velocities (transforming the data set such that it has zero mean and unit variance):

$$\begin{aligned} \mu_n &= \left\langle \left(u_\theta - \langle u_\theta \rangle_t\right)^n \right\rangle_t \\ \sigma &= \sqrt{\mu_2} \\ \tilde{u_\theta} &= \left\langle u_\theta - \langle u_\theta \rangle_t \right\rangle_t / \sigma \end{aligned} \tag{5.3}$$

where $\langle . \rangle_t$ denotes averaging over time. In Fig. 5.3 we plot the PDFs of the standardized velocities. We now see that the tails of most of the distributions

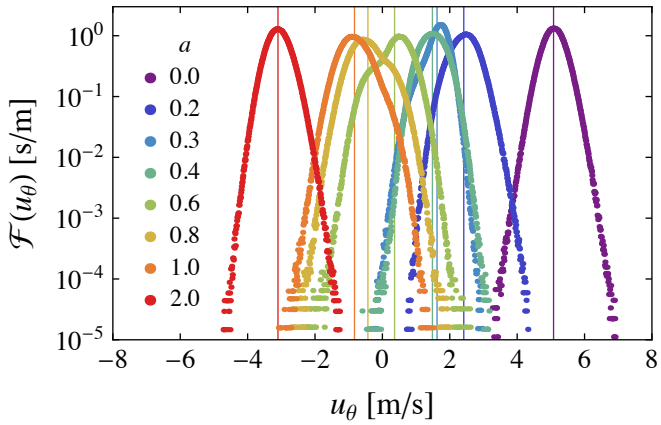

Figure 5.2: Probability density functions of the azimuthal velocity $[\mathcal{F}(u_\theta)]$ measured at midheight for varying $a = -\omega_o/\omega_i$. The means of the velocities are indicated by grid lines with their respective color. a increases from right to left.

behave much like Gaussians. This is also reflected in the value for the kurtosis (μ_4/σ^4), see Table 5.1. The values that we find are close to 3 (except for the case $a = 0.3$) and the distributions are only slightly leptokurtic (> 3) or platykurtic (< 3.

Table 5.1 also includes the Taylor-Reynolds number Re_λ. We find that the Taylor-Reynolds number is not necessarily the largest for the case when the torque is the highest ($a \approx 0.33$), as a higher torque means a higher σ [Eq. (5.3)], but also a higher ϵ [Eq. (5.2)]. Furthermore, we note that σ depends on the radial and axial position and that therefore the Taylor-Reynolds number is a function of position.

Although the PDF of the velocity is of importance in describing a turbulent flow, it obviously does not describe the dynamics of the flow. We therefore look at velocity increments $\Delta_r u_\theta$:

$$\Delta_r u_\theta \equiv u_\theta(x + r) - u_\theta(x). \tag{5.4}$$

Here r is the distance between the two measurement positions x and $x + r$. As we probe the velocity at only one position, we have to invoke Taylor's frozen flow hypothesis [97] to obtain the velocity increments: $u_\theta(x + r, t) = u_\theta(x, t - r/U)$ where U is a typical velocity scale. Here we chose the rms velocity of u_θ, as it best describes the displacement of a fluid parcel for the

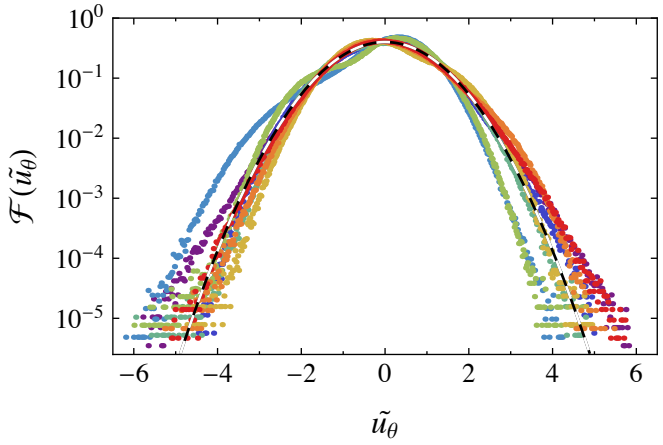

Figure 5.3: Probability density function of the standardized azimuthal velocity $[\mathcal{F}(\tilde{u_\theta})]$ for various a. Colors are the same as in Fig. 5.2. The dashed line is a Gaussian with zero mean and unit variance.

cases where the velocity is in both directions ($a = 0.6$, $a = 0.8$, and $a = 1.0$). For the cases where the velocity is mainly in one direction the rms velocity is very close to the absolute of the mean velocity. We plot the PDF of $\Delta_r u_\theta$ [Eq. (5.4)] for several different r for the cases of $a = 0$ and $a = 1$, see Fig. 5.4. For both a we can clearly see that for small r/η_K the distributions are very leptokurtic (the kurtosis $\mu_4/\sigma^4 = 3.3 \cdot 10^3$ for $r/\eta_K = 36$, $a = 0$, and $\mu_4/\sigma^4 = 2.4 \cdot 10^3$ for $r/\eta_K = 37$, $a = 1$). Here η_K is calculated based on globally measured torque values at the corresponding a. At $a = 0$ the PDF does not recover to a Gaussian [Fig. 5.4(a)] for very large r, whereas it does become normally distributed for other a; see, *e.g.* Fig. 5.4(b) for $a = 1$. We speculate that, for large r and due to the periodic nature of our geometry and the coherent structures in our flow (Taylor vortices), the flow can stay correlated for an unusually long time for certain a and for certain positions in the flow. We will systematically characterize the r dependence of different moments using longitudinal structure functions: $D_p(r) = \langle(\Delta_r u_\theta)^p\rangle$. For odd moments p, $D_p(r)$ is converging very slowly; we therefore use the absolute [98, 99] values of the velocity increments:

$$D_p^* = \langle|\Delta_r u_\theta|^p\rangle \tag{5.5}$$

for all p. Note that there is no theoretical justification that $D_p^*(r)$ and $D_p(r)$

scale in the same way, although the scaling of D_p^* (for odd p) has been found to be similar to that of D_p but not essentially the same; see, *e.g.* [100, 101]. Figure 5.5(f) shows the structure functions for $p \in [1, 6]$ for the case of $a = 0$. We carefully examine the convergence when computing the structure functions. While D_p^* can be calculated using Eq. (5.5), we can alternatively express it as an integral:

$$D_p^* = \int_{-\infty}^{\infty} \mathrm{PDF}(\Delta_r u_\theta) |\Delta_r u_\theta|^p \mathrm{d}(\Delta_r u_\theta). \tag{5.6}$$

We now take a careful look at the integrand of Eq. (5.6) and plot this integrand for points ⓐ–ⓔ in Fig. 5.5(f), corresponding to figures 5.5(a)–5.5(e), respectively. For increasing p the structure functions measure the influence of increasingly rare events. We see in Figs. 5.5(a) and 5.5(b) that the tails of the integrands at points ⓐ and ⓑ are not fully converged, and we therefore have to omit these points from the structure functions. We do this analysis for all p and for all r for each case of a and omit data from the analysis; these omitted data are plotted gray in fig. 5.5f. For high p and low r we find that we do not have sufficient statistics to capture all the rare events necessary to faithfully calculate D_p^*.

For fully developed turbulent flows the structure functions are suggested to scale as power laws in the inertial subrange [97]:

$$D_p(r) \propto r^{\zeta_p}$$

Kolmogorov predicted [78, 79, 97] these exponents to scale as $\zeta_p = p/3$; any deviation from this model is the result of the intermittency of the flow. For our case we will denote the scaling exponents as ζ_p^*, as we are using $D_p^*(r)$ in the analysis rather than $D_p(r)$. We expect an inertial subrange for roughly $10\eta < r < L_{11}$—where L_{11} is the integral length scale—because these length scales are separated by roughly two decades for our flow. But, as seen in Fig. 5.5(f), we do not see an inertial subrange where the structure functions show power-law scaling, a finding also observed in Ref. [10]. We therefore are unable to extract structure function exponents directly from our structure functions; this results holds for all our a. As suggested by Benzi *et al.* [96], we can extend the range over which scaling holds by employing extended self-similarity (ESS). The pth-order structure function is plotted as a function of the third-order structure function; the scaling exponent is now given by ζ_p^*/ζ_3^*. From the Navier–Stokes equations one can derive the Kolmogorov–Howard–von Kármán (KHvK) relation, from which we can determine that

for $r \gg \nu^{3/4}\epsilon^{-1/4}$, $D_3 \propto -\frac{4}{5}\epsilon r$, or $\zeta_3 = 1$. In this work we will assume that $\zeta_3 = \zeta_3^* = 1$, and we would like to note that the KHvK relation is derived under the assumption of isotropic homogeneous turbulence, which is questionable in our flow arrangement. Nevertheless, we employ ESS analysis for our longitudinal structure functions; see Figs. 5.6(a) ($a = 0$) and 5.7(a) ($a = 1$).

We now clearly see that in the ESS representation the scaling is much better, and that we are able to extract structure function exponents from our data. In addition, we also compensate our data with Kolmogorov's prediction ($p/3$); see Figs. 5.6(b) and 5.7(b). Note that in these compensated plots [98, 99] (plotted in double-logarithmic scales) any deviation from a perfect power scaling is amplified and clearly visible. Furthermore, we expect a straight line in the case of perfect scaling. We perform power-law fits to our ESS data for all a, and extract ζ_p^*; see Table 5.2 and Fig. 5.8.

a	0	0_{LS}	0.2	0.3	0.4	0.6	0.8	1	2
p									
1	0.37	0.37	0.37	0.37	0.39	0.37	0.37	0.37	0.37
2	0.70	0.70	0.71	0.71	0.72	0.70	0.71	0.70	0.70
3^*	1	1	1	1	1	1	1	1	1
4	1.27	1.27	1.27	1.26	1.25	1.26	1.26	1.27	1.28
5	1.51	1.50	1.51	1.50	1.49	1.53	1.51	1.53	1.53
6	1.71	1.72	1.73	1.71	1.70	1.69	1.71	1.78	1.77

Table 5.2: Structure function exponents ζ_p^*, for different a. 0_{LS} are the data from Lewis and Swinney [10], for which $a = 0$ and $\mathrm{Re} = 5.4 \cdot 10^5$. Because of the usage of ESS by definition $\zeta_3^* \equiv 1$.

Lewis and Swinney [10] have performed a similar analysis on Taylor-Couette flow for pure inner cylinder rotation, and we have included their structure function exponents (obtained using ESS, $\mathrm{Re} = 5.4 \cdot 10^5$) also in the aforementioned table. We see that for $1 \leq p \leq 5$ the structure function exponents are similar, independent of the Reynolds number, and almost independent of the amount of counter rotation applied to the system. It is only for $p = 6$ that the differences between the exponents become noticeable; 1.69 for $a = 0.6$ and 1.78 for $a = 0$. This difference might be caused by not including the high-p and low-r data in our fits due to lack of statistics. We notice that for increased counter-rotation (*i.e.* increased a) we do not see a systematic trend for the structure function exponents. From global torque measurements

[26, 27, 41, 102] we know that there is a maximum in the torque needed to sustain a constant angular velocity for both cylinders. This peak in the torque has been found around $a \approx 0.33$. This peak in the torque has as a consequence that the Kolmogorov length scale is smallest for the rotation ratio $a = 0.3$ ($\eta_K = 15.7$ μm) and largest for $a = 2.0$ ($\eta_K = 21.0$ μm)—assuming homogeneous turbulence for both cases. We, however, do not see any similar trend in the structure function exponents. It seems that all the exponents are nearly *universal*; independent of the Reynolds number (Lewis and Swinney [10] also performed their experiments for $\mathrm{Re} = 6.9 \cdot 10^4$ and found similar structure function exponents as for our $\mathrm{Re} = 1.38 \cdot 10^6$) and independent of the amount of counter-rotation applied to the system. Our structure functions are tabulated in Table 5.2 and plotted in Fig. 5.8, for comparison we have included the data from Lewis and Swinney [10] and the She-Lévêque model with its standard parameters [103]. We find that, for nearly all the exponents and for nearly all the a cases, Taylor-Couette flow seems more intermittent than the She-Lévêque model predicts, as already reported in Ref. [10].

In Fig. 5.9(a) we plot the spectra for all cases. We see that most of the energy is kept in the low frequencies [93], even lower than the driving frequency: $\omega_i - \omega_o = 2\pi \times 10\ \mathrm{s}^{-1}$ for the cases $a \in \{0.6, 0.8, 1.0\}$. Furthermore, we see for $a = 0$ that we do not have any power-law scaling behavior, as was already found in the TC experiments of Ref. [10]. However, for $a \in \{0.6, 0.8, 1.0\}$—the same as for which the PDF of the azimuthal velocity showed that it was made up of two distributions—we see a power law scaling with exponent $-5/3$. To reveal the quality of the scaling we compensate the data by $\omega^{5/3}$, see Fig. 5.9(b). We indeed see in Fig. 5.9(b) that the power spectra for $a \in \{0.6, 0.8, 1.0\}$ level out over roughly two decades. Furthermore, for the case $a = 0$ we see that there is no scaling whatsoever. In addition, we also plot the local exponent of the spectrum. Here we also see that the power-law scaling for $a \in \{0.6, 0.8, 1.0\}$ is around $-5/3$ close to $\omega = 10^3\ \mathrm{s}^{-1}$, and that for $a = 0$ the exponent is constantly changing. The curving up of our spectra at the high-frequency end is due to our limited measuring frequency. We therefore do not recover the steep slopes ($\gg 2$) found by Lewis and Swinney [10]. However, they also found that for $a = 0$ the local slope is never constant and is a monotonic function of ω.

In this work we relied on Taylor's hypothesis, which certainly has to be experimentally justified in the future using a field measurement technique, *e.g.* particle imaging velocimetry. In addition we assumed concepts of homogeneous isotropic turbulence to obtain ϵ and therefore η. Future work will be

necessary to study the anisotropic properties of the flow [104, 105].

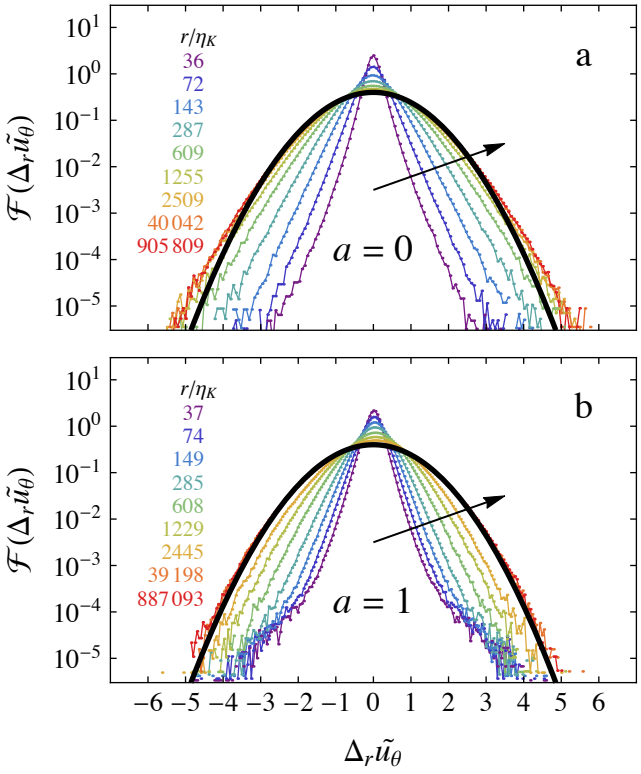

Figure 5.4: (a) Probability density functions of velocity increments $[\mathcal{F}(\Delta_r u_\theta)]$ for varying r for the case of $a = 0$. Values of r are shown as multiples of the Kolmogorov length scale, and are colored accordingly. (b) As in (a) but for $a = 1$. (a),(b) The black line is a Gaussian with zero mean and unit variance. Arrows indicate increasing r/η_K.

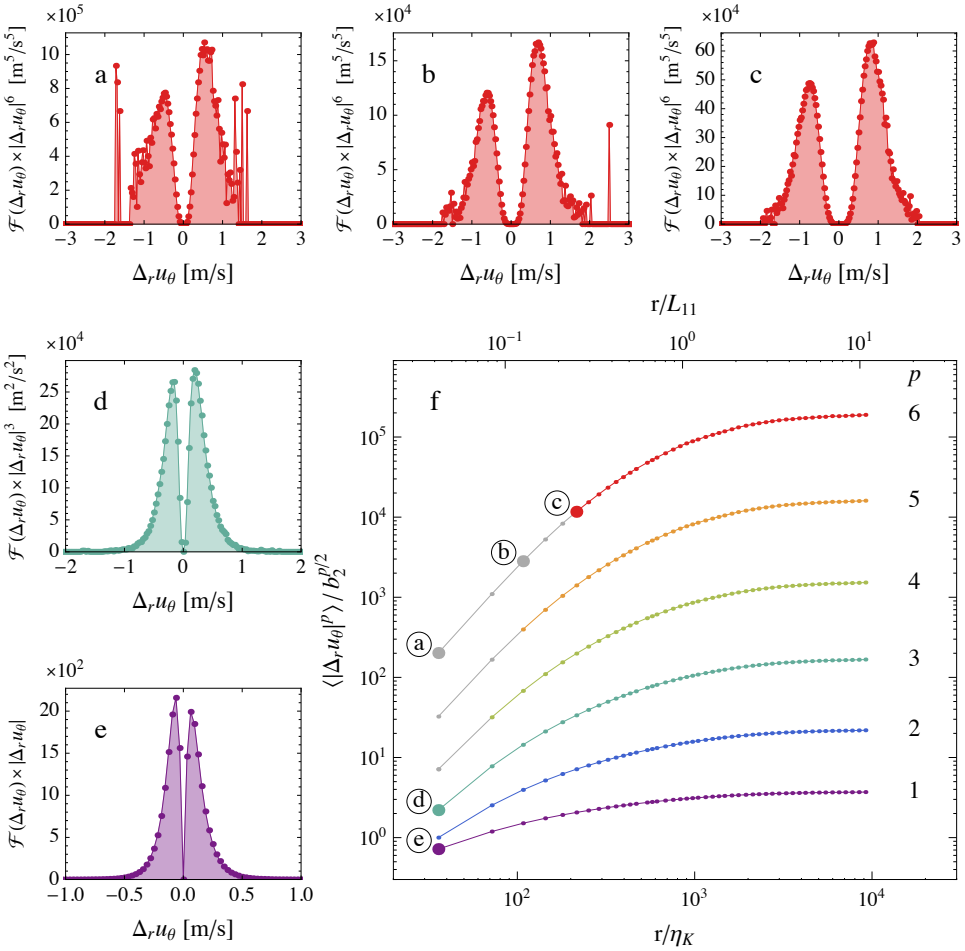

Figure 5.5: (a)–(e) Integrand of Eq. (5.6) for various positions in (f). The area under the graphs are the values of $D_p^*(r)$. (a),(b) Nonconverged structure function integrands. (c)–(e) Converged structure function integrands. (f) Longitudinal structure functions $[D_p^*(r)]$ for varying powers p (indicated on the right) for the case of $a = 0$. Structure functions are scaled using a constant $b_2 = D_2^*(r_{\min})$. The separation distance r is normalized using the Kolmogorov length scale η_K and the integral length scale L_{11}. For various p and r (thick points labeled ⓐ–ⓔ) the integrand of Eq. (5.6) is plotted. Data in gray color are not fully converged, and are omitted in the ESS calculation.

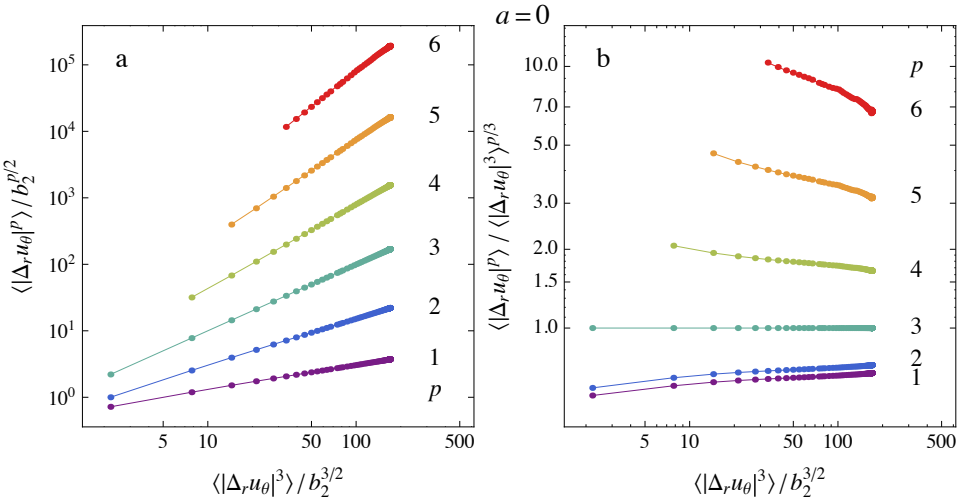

Figure 5.6: (a) Extended self-similarity for the case of $a = 0$. Powers p are indicated on the right. Power-law scaling can be seen for each power p. (b) Extended self-similarity compensated by Kolmogorov scaling $p/3$. The quality of the scaling can now be seen better. Gray data in Fig. 5.5(f) are omitted in this analysis as they are not fully statistically converged.

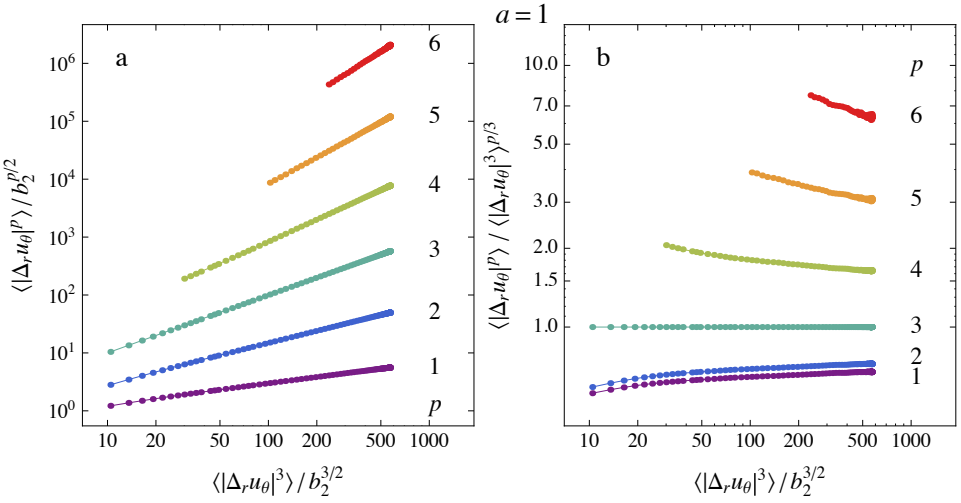

Figure 5.7: (a) Extended self-similarity for the case of $a = 1$. Powers p are indicated on the right. Power-law scaling can be seen for each power p. (b) Extended self-similarity compensated by Kolmogorov scaling $p/3$. The quality of the scaling can now be seen better. As in the analysis of Fig. 5.5 ($a = 0$), non-converged data are omitted from the structure functions.

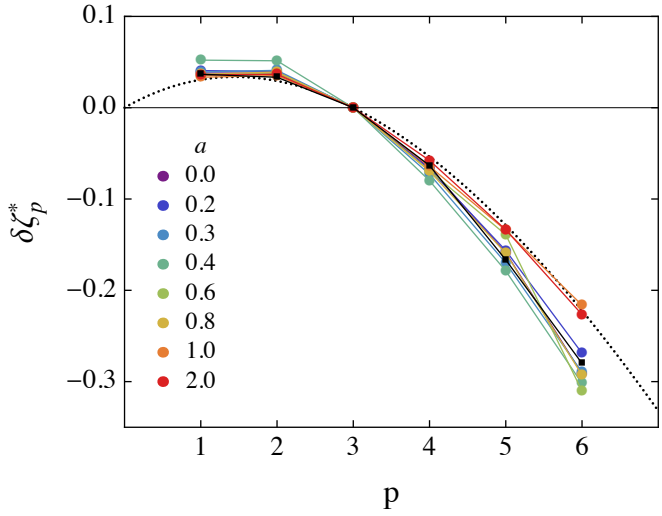

Figure 5.8: Longitudinal structure function exponents deviations: $\delta\zeta_p^* = \zeta_p^* - p/3$. Black dotted line shows the She-Lévêque model $[\zeta_p = p/9+2+2(2/3)^{p/3}]$. Black squares are the data from Lewis and Swinney [10] for $a = 0$.

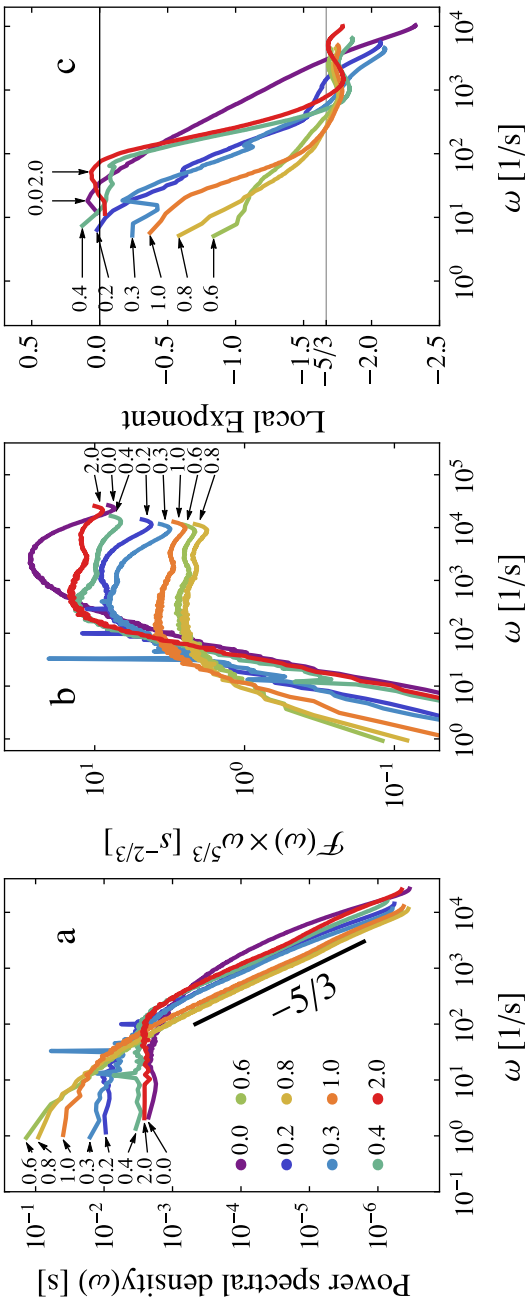

Figure 5.9: (a) Spectral density of the azimuthal velocity for various a; $-5/3$ scaling is indicated with a black line. (b) Spectral density compensated by $\omega^{5/3}$. (c) Local scaling exponent over an interval of one decade as a function of frequency ω. Kolmogorov's inertial subrange scaling ($-5/3$) is included as a horizontal line. The legend displayed in (a) corresponds also to the colors used in (b) and (c). Arrows indicate the corresponding a.

5.3 Summary

To summarize, we have measured the local azimuthal velocity in a turbulent Taylor-Couette flow with various amounts of counterrotation using laser Doppler anemometry. We found that the structure functions show no inertial subrange for all p and for all cases a. Using extended self-similarity analysis [96], we extracted the structure function exponents, which are in good agreement with earlier results by Lewis and Swinney [10]. We find that for $a = 0$ the structure function exponents are nearly independent of the Reynolds number: previous results [10] are for $\mathrm{Re} = 6.9 \cdot 10^4$ and $\mathrm{Re} = 5.4 \cdot 10^5$, while our current results are for $\mathrm{Re} = 1.38 \cdot 10^6$. Any discrepancy between these exponents could easily be caused by different fitting intervals and are certainly within experimental error. Furthermore, we find that adding rotation of the outer cylinder of the system to create counterrotation does not strongly influence the structure function exponents, but does strongly change the scaling of the spectra. While for $a \in \{0.6, 0.8, 1.0\}$ we see a clear power-law scaling in the spectra, we do not observe such clear scaling in the second-order structure function.

6

Optimal Taylor-Couette turbulence°

Strongly turbulent Taylor-Couette flow with independently rotating inner and outer cylinder with a radius ratio of $\eta = 0.716$ is experimentally studied. From global torque measurements, we analyze the dimensionless angular velocity flux Nu_ω as a function of the Taylor number Ta and the angular velocity ratio $a = -\omega_o/\omega_i$ in the large Taylor number regime $\mathcal{O}(\mathrm{Ta}) = 10^{11}$–$10^{13}$. We analyse the data with the common power law ansatz for the dimensionless angular velocity transport flux $\mathrm{Nu}_\omega(\mathrm{Ta}, a) = f(a) \cdot \mathrm{Ta}^\gamma$. The data is consistent with one effective exponent $\gamma = 0.39 \pm 0.03$ for all a, but we discuss a possible a-dependence in the co- and weakly counter-rotating regimes. The amplitude of the angular velocity flux $f(a) \equiv \mathrm{Nu}_\omega(\mathrm{Ta}, a)/\mathrm{Ta}^{0.39}$ is measured to be maximal at slight counter-rotation, namely at an angular velocity ratio of $a_{\mathrm{opt}} = 0.33 \pm 0.04$. This value is theoretically interpreted as the result of a competition between the destabilizing inner cylinder rotation and the stabilizing but shear-enhancing outer cylinder counter-rotation. With the help of laser Doppler anemometry, we provide angular velocity profiles and, in particular, identify the radial position r_n of the neutral line, defined by $\langle \omega(r_n) \rangle_t = 0$ for fixed height z. Furthermore, we characterise the flow by the position of zero velocity for the various flow regimes (co- and counter-rotation) and observe that the probability density functions of the flow velocity is either

°Published as: Dennis P.M. van Gils, **Sander G. Huisman**, Siegfried Grossman, Chao Sun, and Detlef Lohse, *Optimal Taylor-Couette turbulence*, J. Fluid Mech. **706**, 118 (2012). Experiments, analysis, and writing are done by van Gils, and Huisman contributed to setting up the LDA and signal analysis. Supervision by Sun and Lohse. Discussions of the results and proofreading of the manuscript by everyone.

6.1 Introduction

Taylor-Couette (TC) flow (the flow between two coaxial, independently rotating cylinders) is next to Rayleigh-Bénard (RB) flow (the flow in a box heated from below and cooled from above) the most prominent *'Drosophila'* on which to test hydrodynamic concepts for flows in closed containers. For outer cylinder rotation and fixed inner cylinder, the flow is linearly stable. In contrast, for inner cylinder rotation and fixed outer cylinder the flow is linearly unstable thanks to the driving centrifugal forces, see *e.g.* Refs. [94, 106, 19, 107, 31, 32, 108, 109, 110, 17]. The case of two independently rotating cylinders has been well analyzed for low Reynolds numbers, see *e.g.* Ref. [18]. For large Reynolds numbers, where the bulk flow is turbulent, studies have been scarce—see for example the historical work by Wendt [14] or the experiments by Refs. [18, 111, 16, 112, 15, 54]. Refs. [95, 113] examined the local angular velocity flux with LDA in independently rotating cylinders at high Reynolds numbers up to $2 \cdot 10^6$. Recently, in two independent experiments, Refs. [26, 27] supplied precise data for the global torque scaling in the turbulent regime of the flow between independently rotating cylinders.
We use cylindrical coordinates r, ϕ, and z. Next to the geometric ratio $\eta = r_i/r_o$ between the inner cylinder radius r_i and the outer cylinder radius r_o, and the aspect ratio $\Gamma = L/d$ of the cell height L and the gap width $d = r_o - r_i$, the dimensionless control parameters of the system can either be expressed in terms of the inner and outer cylinder Reynolds numbers $\mathrm{Re}_i = r_i\omega_i d/\nu$ and $\mathrm{Re}_o = r_o\omega_o d/\nu$, respectively, or in terms of the ratio of the angular velocities

$$a = -\omega_o/\omega_i \tag{6.1}$$

and the Taylor number

$$\mathrm{Ta} = \frac{1}{4}\sigma(r_o - r_i)^2(r_i + r_o)^2(\omega_i - \omega_o)^2\nu^{-2}. \tag{6.2}$$

Here, according to the theory by Ref. [1] (from now on called EGL), $\sigma = ((1+\eta)/(2\sqrt{\eta}))^4$ (thus $\sigma = 1.057$ for the current $\eta = 0.716$ of the used TC facility) can be formally interpreted as a 'geometrical' Prandtl number and ν is the kinematic viscosity of the fluid. With $r_a = (r_i + r_o)/2$ and $r_g = \sqrt{r_i r_o}$, the

arithmetic and the geometric mean radii, the Taylor number can be written as

$$\mathrm{Ta} = r_a^6 r_g^{-4} d^2 (\omega_i - \omega_o)^2 \nu^{-2}. \tag{6.3}$$

The angular velocity of the inner cylinder ω_i is always defined as positive, whereas the angular velocity of the outer cylinder ω_o can be either positive (co-rotation) or negative (counter-rotation). Positive a thus refers to the counter-rotating case on which our main focus will lie.
The response of the system is the degree of turbulence of the flow between the cylinders (*e.g.* expressed in a wind Reynolds number of the flow, measuring the amplitude of the r and z components of the velocity field) and the torque τ, which is necessary to keep the inner cylinder rotating at constant angular velocity. Following the suggestion of EGL, the torque can be non-dimensionalized in terms of the laminar torque to define the (dimensionless) 'Nusselt number'

$$\mathrm{Nu}_\omega = \frac{\tau}{2\pi L \rho_{\mathrm{fluid}} J^\omega_{\mathrm{lam}}}, \tag{6.4}$$

where ρ_{fluid} is the density of the fluid between the cylinders and

$$J^\omega_{\mathrm{lam}} = 2\nu r_i^2 r_o^2 \frac{\omega_i - \omega_o}{r_o^2 - r_i^2} \tag{6.5}$$

is the conserved angular velocity flux in the laminar case. The reason for the choice (6.4) is that

$$J^\omega = J^\omega_{\mathrm{lam}} \mathrm{Nu}_\omega = r^3 \left(\langle u_r \omega \rangle_{A,t} - \nu \partial_r \langle \omega \rangle_{A,t} \right) \tag{6.6}$$

is the relevant conserved transport quantity, representing the flux of angular velocity from the inner to the outer cylinder. This definition of J^ω is an immediate consequence of the Navier-Stokes equations[⊙]. Here u_r (u_ϕ) is the radial (azimuthal) velocity, $\omega = u_\phi / r$ the angular velocity, and $\langle \dots \rangle_{A,t}$ characterizes averaging over time and a cylindrical surface with constant radius r. With this choice of control and response parameters, EGL could work out a close analogy between turbulent TC and turbulent RB flow, building on Ref. [45] and extending the earlier work of Refs. [4, 5]. This was further elaborated by Ref. [26].

[⊙]The authors would like to point out that Eq. 6.6 appeared first, in a different notation, in Ref. [114], where J^ω was called the 'torque'. Eq. 3.4 and Eq. 4.13 of Ref. [1] are analogous to Eq. 3.2 and Eq. 3.4 of Ref. [114].

The main findings of Ref. [26], who operated the TC set-up, known as the Twente turbulent Taylor-Couette system or T^3C, at fixed $\eta = 0.716$ and for $\mathrm{Ta} > 10^{11}$ as well as the variable a well off the stability borders $-\eta^2$ and ∞, are as follows: (i) in the (Ta, a) representation, $\mathrm{Nu}_\omega(\mathrm{Ta}, a)$ within the experimental precision factorizes into $\mathrm{Nu}_\omega(\mathrm{Ta}, a) = f(a) \cdot F(\mathrm{Ta})$. (ii) $F(\mathrm{Ta}) = \mathrm{Ta}^{0.38}$ for all analyzed $-0.4 \le a \le 2.0$ in the turbulent regime. (iii) $f(a) = \mathrm{Nu}_\omega(\mathrm{Ta}, a)/\mathrm{Ta}^{0.38}$ has a pronounced maximum around $a_{\mathrm{opt}} \approx 0.4$. Also Ref. [27], at slightly different $\eta = 0.725$ found such a maximum in $f(a)$, namely at $a_{\mathrm{opt}} \approx 0.35$. For this a_{opt} the angular velocity transfer amplitude $f(a_{\mathrm{opt}}(\eta))$ for the transport from the inner to the outer cylinder is maximal. From these findings one has to conclude that for not too strong counter-rotation $0 < a < 0.4$ the angular velocity transport flux is still further enhanced as compared to the case of fixed outer cylinder $a = 0$. This stronger turbulence is attributed to the enhanced shear between the counter-rotating cylinders. Only for strong enough counter-rotation ($a > a_{\mathrm{opt}}$) the stabilization through the counterrotating outer cylinder takes over and the transport amplitude decreases with further increasing a.

The aims of this chapter are to provide further and more precise data on the maximum in the conserved turbulent angular velocity flux $\mathrm{Nu}_\omega(\mathrm{Ta}, a)/\mathrm{Ta}^\gamma = f(a)$ as a function of a and a theoretical interpretation of this maximum, including a speculation on how it depends on η. We also put our findings in the perspective of the earlier results on highly turbulent TC flow by Refs. [9, 8, 10] and on recent results on highly turbulent Rayleigh-Bénard flow [47]. We think that all these experiments achieve the so-called 'ultimate regime' in which the boundary layers are already turbulent. Next we provide laser Doppler anemometry (LDA) measurements of the angular velocity profiles $\langle \omega(r) \rangle_t$ as functions of height, and show that the flow close to the maximum in $f(a)$, for these asymptotic Ta and deep in the instability range at $a = a_{\mathrm{opt}}$, has a vanishing angular velocity gradient $\partial\omega/\partial r$ in the bulk of the flow. We identify the location of the neutral line r_n, defined by $\langle \omega(r_n) \rangle_t = 0$ for fixed height z, finding that it remains still close to the outer cylinder r_o for weak counter-rotation, $0 < a < a_{\mathrm{opt}}$, but starts moving towards the inner cylinder r_i for $a > a_{\mathrm{opt}}$. Finally we show that the turbulent flow organization totally changes for $a > a_{\mathrm{opt}}$, where the stabilizing effect of the strong counter rotation reduces the angular velocity transport. In this strongly counter-rotating regime the probability distribution function of the angular velocity in the bulk becomes bi-modal, reflecting intermittent bursts of turbulent structures beyond the neutral line towards the outer flow region, which otherwise, *i.e.* in between

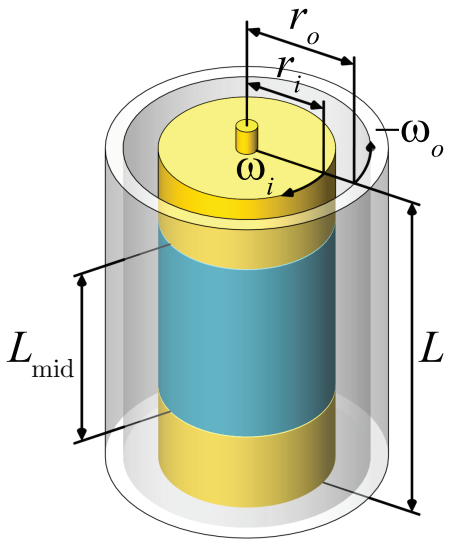

Figure 6.1: Sketch of the T^{3}C cell employed for the measurements presented here [21]. The total height of the cell is $L = 92.7$ cm. The torque measurements are made with the middle part of the cell with length $L_{\mathrm{mid}} = 53.6$ cm only, in order to minimize edge effects. The outer and inner cylinder radii are $r_o = 27.94$ cm and $r_i = 20.00$ cm, leading to a radius ratio of $\eta = 0.716$, a gap width of $d = r_o - r_i = 7.94$ cm, a total aspect ratio of $\Gamma = L/d = 11.68$, and an internal fluid volume of 111 liters. The inner and outer cylinder angular velocities are denoted by ω_i and ω_o, respectively. $\omega_i > 0$ by definition, implying that $\omega_o < 0$ or $a = -\omega_o/\omega_i > 0$ represents counter-rotation, on which we focus in this chapter. The top and bottom plates are attached to the outer cylinder.

such bursts, is stabilized by the counter-rotating outer cylinder.

The outline of this chapter is as follows. The experimental setup is introduced in section 6.2 and we discuss, additionally, the height dependence of the flow profile and finite size effects. The global torque results are reported and discussed in section 6.3. Section 6.4 and 6.5 provide laser Doppler anemometry (LDA) measurements on the angular velocity radial profiles and on the turbulent flow structures inside the TC gap. This chapter ends, in section 6.6, with a summary and further discussions of the neutral line inside the flow.

6.2 Experimental setup and discussion of end-effects

The core of our experimental setup, the Taylor-Couette cell, is shown in Fig. 6.1. In the caption of that figure we give the respective length scales and their ratios. The details of the setup are given in Ref. citegil11tttc. The working liquid is water at a continuously controlled constant temperature (precision ± 0.5 K) in the range 19 °C–26 °C. The accuracy in setting and maintaining a constant a is ± 0.001 based on the angular velocity stability of the T^3C facility. To reduce edge effects, similarly as in Refs. [9, 8] the torque is measured at the middle part (length ratio $L_{\mathrm{mid}}/L = 0.578$) of the inner cylinder only. The original motivation of Ref. [9] for this choice was that the height of the remaining upper and lower parts of the cylinder roughly equals the size of a pair of Taylor-vortices. While the respective first or last Taylor vortex indeed will be affected by the upper and lower plates (which in our T^3C cell are attached to the outer cylinder), the hope is that in the strongly turbulent regime the turbulent bulk is not affected by such edge effects. Note that for the laminar case (*e.g.* for pure outer cylinder rotation) this clearly is not the case, as has been known since 1923 [94], see *e.g.* the classical experiments by Ref. [115], the numerical work by Ref. [116], or the review by Ref. [117]. For such weakly rotating systems, profile distortions from the plates propagate into the fluid and dominate the whole laminar velocity field. The velocity profile will then be very different from the classical height-independent laminar profile (see *e.g.* Ref. [118]) with periodic boundary conditions in vertical direction,

$$u_{\phi,\mathrm{lam}} = Ar + B/r \tag{6.7}$$

$$A = \frac{\omega_o - \eta^2 \omega_i}{1 - \eta^2} \tag{6.8}$$

$$B = \frac{(\omega_i - \omega_o) r_i^2}{1 - \eta^2} \tag{6.9}$$

To control edge effects and ensure that they are indeed negligible in the strongly turbulent case under consideration here ($10^{11} < \mathrm{Ta} < 10^{13}$ and $-0.40 \leq a \leq 2.0$, so well off the instability borders), we have measured time series of the angular velocity $\omega(\mathbf{r}, t) = u_\phi(\mathbf{r}, t)/r$ for various heights $0.32 < z/L < 1$ and radial positions $r_i < r < r_o$ with laser Doppler anemometry (LDA). We employ a backscatter LDA configuration set-up with a measurement volume of 0.07 mm × 0.07 mm × 0.3 mm. The seeding particles

(PSP-5 Dantec Dynamics) have a mean radius of $r_{\text{seed}} = 2.5$ µm and a density of $\rho_{\text{seed}} = 1.03\ \text{g/cm}^3$. We estimate the minimum velocity difference $\Delta v = v_{\text{seed}} - v_{\text{fluid}}$ between a particle v_{seed} and its surrounding fluid v_{fluid} needed for the drag force

$$F_{\text{drag}} = 6\pi\mu r_{\text{seed}}\Delta v \tag{6.10}$$

to outweigh the centrifugal force

$$F_{\text{cent}}(r) = 4\pi {r_{\text{seed}}}^3 \left(\rho_{\text{seed}} - \rho_{\text{fluid}}\right) v^2/(3r). \tag{6.11}$$

We put in $v = 5$ m/s as a typical azimuthal velocity inside the TC-gap at mid-gap radial position $r = 0.24$ m, with $\rho_{\text{fluid}} = 1.00\ \text{g/cm}^3$ as the density and $\mu = 9.8 \times 10^{-4}\ \text{Ns/m}^2$ as the dynamic viscosity of water at 21 °C. This results in $\Delta v = 2{r_{\text{seed}}}^2 \left(\rho_{\text{seed}} - \rho_{\text{fluid}}\right) v^2/(9\mu r) \approx 4 \times 10^{-6}$ m/s, which is several orders of magnitude smaller than the typical velocity fluctuation inside the TC-gap of order 10^{-1} m/s and hence centrifugal forces on the seeding particles are negligible.

We account for the refraction due to the cylindrical interfaces, details are given by [91]. Figure 6.2a shows the height dependence of the time-averaged angular velocity at mid-gap, $\tilde{r} = (r - r_i)/(r_o - r_i) = 1/2$, for $a = 0$ and $\text{Ta} = 1.5 \times 10^{12}$, corresponding to $\text{Re}_i = 10^6$ and $\text{Re}_o = 0$. The dashed-dotted line at $z/L = 0.79$ corresponds to the transition from the middle-part of the inner cylinder, with which we measure the torque, and the upper part. Along the middle-part the time-averaged angular velocity is z-independent within 1%, as is demonstrated in the inset, showing the enlarged relevant section of the ω axis. From the upper edge of the middle-part of the inner cylinder towards the highest position that we can resolve, 0.5 mm below the top plate, the mean angular velocity decays by only 5%. This finite difference might be due to the existence of Ekman layers near the top and bottom plate [119]. Since at $z/L = 1$ we have $\omega(r, t) = 0$, as the upper plate is at rest for $a = 0$ or $\omega_o = 0$, 95% of the edge effects on ω occur in such a thin fluid layer near the top (bottom) plate that we cannot resolve it with our present LDA measurements. For the angular velocity fluctuations shown in Fig. 6.2b we observe a 25% decay in the upper 10% of the cylinder, but again in the measurement section of the inner cylinder $0.21 < z/L < 0.79$ there are no indications of any edge effects. The plots of Fig. 6.2 together confirm that edge effects are unlikely to play a visible role for our torque measurements in the middle-part of the cylinder. Even the Taylor-vortex roll-structure, which dominates TC flow at

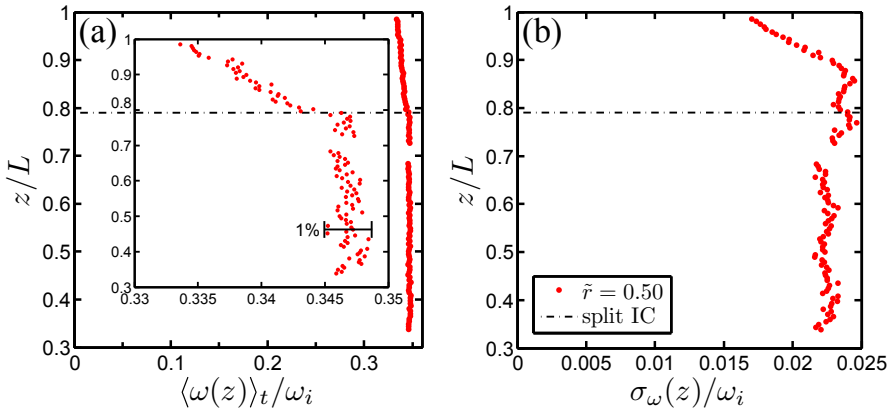

Figure 6.2: Time averaged axial profiles of the azimuthal angular velocity inside the T^3C measured with LDA at mid-gap, *i.e.* $\tilde{r} = (r - r_i)/(r_o - r_i) = 0.5$, for the case $\mathrm{Re}_i = 1.0 \times 10^6$ and $\mathrm{Re}_o = 0$ (corresponding to $a = 0$ and $\mathrm{Ta} = 1.5 \times 10^{12}$). The height z from the bottom plate is normalized against the total height L of the inner volume of the tank. (a): the time-averaged angular velocity $\langle \omega(z, \tilde{r} = 1/2) \rangle_t$ normalized by the angular velocity of the inner cylinder wall ω_i. (b): the standard deviation of the angular velocity $\sigma_\omega(z)$ normalized by the angular velocity of the inner wall. The split between the middle and the top inner cylinder sections is indicated by the dash-dotted line at $z/L = 0.79$. As can be appreciated in this figure, the end-effects are negligible over the middle section where we measure the global torques as reported in this work. The velocities near the top plate, $z/L = 1$, are not sufficiently resolved to see the boundary layer.

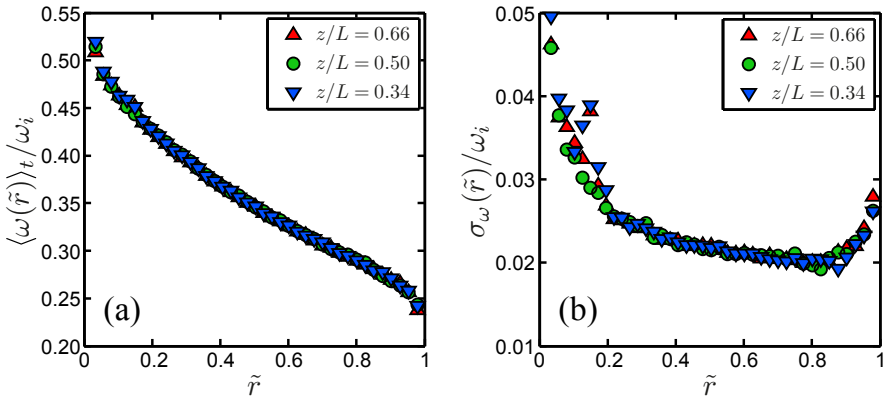

Figure 6.3: Radial profiles of the azimuthal angular velocity as presented in Fig. 6.2, scanned at three different heights $z/L = 0.66$, 0.50 and 0.34, plotted against the dimensionless gap distance $\tilde{r} = (r - r_i)/(r_o - r_i)$, again for $\mathrm{Re}_o = 0$ and $\mathrm{Re}_i = 1 \times 10^6$. (a): the time-averaged angular velocity $\langle\omega(\tilde{r})\rangle_t$ normalized by the angular velocity of the inner wall ω_i. All profiles fall on top of each other, showing no axial dependence of the flow in the investigated axial range. (b) Standard deviation of the angular velocity $\sigma_\omega(\tilde{r})$ normalized by the angular velocity of the inner wall. The velocity fluctuations show no significant axial dependence in the investigated axial range. The boundary layers at the cylinder walls are not resolved.

low Reynolds numbers [120, 121, 18, 117], is not visible at all in the time averaged angular velocity profile $\langle\omega(z, \tilde{r} = 1/2, t)\rangle_t$.
To double check that this z-independence not only holds at mid-gap $\tilde{r} = 1/2$ but also for the whole radial ω profiles, we measured time series of $\omega(z, \tilde{r}, t)$ at three different heights $z/L = 0.34$, 0.50, and 0.66. The radial dependence of the mean value and of the fluctuations are shown in Fig. 6.3. The profiles are nearly identical for the three heights, with the only exception of some small irregularity in the fluctuations at $z/L = 0.34$ in the small region $0.1 < \tilde{r} < 0.2$, whose origin is unclear to us. Note that in both plots of Fig. 6.3 the radial inner and outer boundary layers are again not resolved; in this chapter we will focus on bulk properties and global scaling relations.
Based on the results of this section, we feel confident to claim that (i) edge effects are unimportant for the global torque measurements done with the middle-part of the inner cylinder reported in section 6.3 and that (ii) the local profile and fluctuation measurements done close to mid-height $z/L = 0.44$, which will be shown and analyzed in sections 6.4 and 6.5, are representative for any height in the mid-part of the cylinder.

6.3 Global torque measurements

In this section we will present our data from the global torque measurements for independently inner and outer cylinder rotation, which complement and improve precision of our earlier measurements [26]. The data as functions of the respective pairs of control parameters (Ta, a) or $(\mathrm{Re}_i, \mathrm{Re}_o)$ for which we performed our measurements are given in tabular form in table 6.1 and in graphical form in Figs. 6.4a and 6.5, respectively.
A three-dimensional overview of the found parameter dependencies of the angular velocity transport $\mathrm{Nu}_\omega(\mathrm{Ta}, a)$ is shown in Fig. 6.6. One immediately observed a pronounced maximum in $\mathrm{Nu}_\omega(\mathrm{Ta}, a)$ with a considerable offset from the line $a = 0$. A more detailed view is obtained in cross-sections through Fig. 6.6 and in particular in *compensated plots* as shown in Fig. 6.7a, where we divided Nu_ω by the approximate effective scaling $\sim \mathrm{Ta}^{0.39}$. In this way we identify an universal effective scaling $\mathrm{Nu}_\omega(\mathrm{Ta}, a) \propto \mathrm{Ta}^{0.39}$ by averaging over the complete Ta-range, ignoring Ta-dependence and thus calling the scaling effective. If each curve for each a is fitted individually, the resulting Ta-scaling exponents $\gamma(a)$ scatter with a, but at most very slightly depend on a, see Figs. 6.7b and 6.7c. For linear fits different below and above $a_{\mathrm{opt}} = 0.33$ (actually

a	ψ	Ta min	Ta max	ω_i min	ω_i max	ω_o min	ω_o max	Re_i min	Re_i max	Re_o min	Re_o max	G min	G max	Nu_ω min	Nu_ω max	$\gamma(a)$	$f(a)$
	°	10^{11}	10^{11}	1/s	1/s	1/s	1/s	10^5	10^5	10^5	10^5	10^9	10^9				10^{-3}
2.000	43.1	4.07	34.0	10.5	30.7	-61.5	-21.1	1.72	4.99	-13.95	-4.82	0.49	3.29	91	212	0.397	2.71
1.000	27.2	2.07	62.3	11.3	61.9	-61.9	-11.3	1.84	10.12	-14.15	-2.58	0.49	10.30	129	492	0.386	4.84
0.714	17.7	1.52	57.1	11.4	69.3	-49.5	-8.1	1.84	11.31	-11.29	-1.84	0.47	12.08	143	603	0.399	6.21
0.650	15.0	1.85	52.3	12.0	62.6	-40.7	-7.8	2.12	11.25	-10.21	-1.92	0.58	11.91	162	621	0.396	6.58
0.600	12.8	1.52	52.2	11.4	65.8	-39.5	-6.9	1.97	11.59	-9.71	-1.65	0.53	12.57	162	656	0.392	6.98
0.550	10.3	1.63	53.7	11.9	67.4	-37.1	-6.5	2.11	12.13	-9.33	-1.63	0.57	13.42	168	691	0.401	7.23
0.500	7.7	1.43	57.5	11.7	73.3	-36.7	-5.9	2.04	12.97	-9.06	-1.43	0.55	15.32	172	762	0.398	7.66
0.450	4.9	1.33	66.5	12.0	83.0	-37.4	-5.4	2.04	14.43	-9.08	-1.28	0.54	18.07	177	836	0.396	7.98
0.400	2.0	1.15	85.4	12.6	93.6	-37.5	-5.0	1.97	16.93	-9.47	-1.10	0.52	22.96	184	937	0.386	8.36
0.368	0.0	2.65	63.2	18.9	89.2	-32.8	-7.0	3.05	14.90	-7.67	-1.57	1.08	18.20	250	864	0.389	8.60
0.350	-1.2	1.16	64.6	12.3	90.1	-31.5	-4.3	2.04	15.28	-7.47	-1.00	0.52	18.67	181	876	0.391	8.61
0.300	-4.5	1.15	65.0	12.4	93.0	-27.9	-3.7	2.11	15.91	-6.67	-0.89	0.52	18.36	185	859	0.383	8.60
0.250	-8.0	1.07	63.4	13.0	97.5	-24.4	-3.2	2.12	16.35	-5.71	-0.74	0.48	17.35	177	822	0.381	8.37
0.200	-11.6	2.03	67.7	19.0	105.8	-21.2	-3.8	3.05	17.59	-4.91	-0.85	0.83	17.57	219	805	0.375	8.07
0.143	-15.9	2.27	69.4	22.1	112.5	-16.1	-3.2	3.38	18.70	-3.73	-0.68	0.83	17.21	208	779	0.386	7.69
0.100	-19.3	4.78	60.0	31.5	112.6	-11.3	-3.2	5.10	18.08	-2.52	-0.71	1.56	14.72	269	717	0.395	7.37
0.000	-27.2	1.34	61.7	18.2	124.0	0.0	0.0	2.97	20.15	0.00	0.00	0.49	13.73	158	660	0.375	6.81
-0.140	-38.3	1.90	37.4	25.5	112.4	3.6	15.7	4.11	18.25	0.80	3.57	0.55	7.07	151	436	0.364	5.76
-0.200	-42.8	2.08	29.6	28.6	107.7	5.7	21.5	4.62	17.44	1.29	4.87	0.49	5.10	128	354	0.392	5.00
-0.400	-56.4	4.87	22.2	58.3	124.3	23.3	49.8	9.44	20.16	5.28	11.27	0.47	1.68	80	135	0.358	2.21

Table 6.1: The measured global torque data for the individual cases of fixed $a \equiv -\omega_o/\omega_i$ at increasing Ta, as presented in Fig. 6.5, equivalent to straight lines in the (Re_o, Re_i) parameter space, as presented in Fig. 6.4a. We list the minimum and maximum values of the driving parameters (Ta, ω_i, ω_o, Re_i, and Re_o) and we list the minimum and maximum values of the response parameters (G and Nu_ω). The variable a can be transformed to the angle ψ, *i.e.* the angle in (Re_o, Re_i) space between the straight line characterized by a and the one characterized by a_{bis}, describing the angle bisector of the instability range, see Fig. 6.4a and Eq. (6.16). The penultimate column lists the effective scaling exponent $\gamma(a)$ obtained from fitting $\mathrm{Nu}_\omega(\mathrm{Ta}, a)$ to a linear fit in log-log space for each individual case of a, as presented in Fig. 6.6b and c. The pre-factor $f(a)$ is determined by fixing $\gamma(a)$ to the average value of $\gamma \approx 0.39$ and by computing $\left\langle \mathrm{Nu}_\omega \mathrm{Ta}^{-0.39} \right\rangle_{\mathrm{Ta}}$.

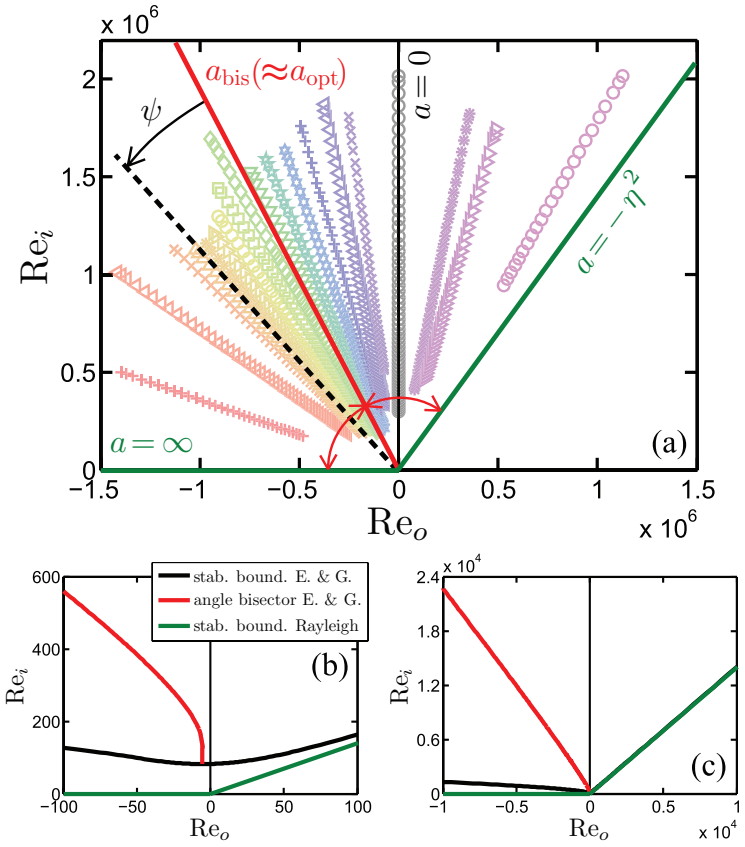

Figure 6.4: (a): Reynolds number phase space showing the explored regime of the T^3C as symbols with washed-out colors. The solid green lines are the boundaries between the unstable (upper-left) and stable (lower-right) flow region, shown here for the radius ratio $\eta = 0.716$ as experimentally examined in this work. The green line in the right quadrant is the analytical expression for the stability boundary as found by Ref. [17], which recovers to the Rayleigh stability criterion $\mathrm{Re}_o/\mathrm{Re}_i = \eta$ for $\mathrm{Re}_i, \mathrm{Re}_o \gg 1$, the viscous corrections decreasing $\propto \mathrm{Re}_o^{-2}$. The green line in the left quadrant also follows the stability boundary by Esser and Grossmann ($\mathrm{Re}_i \propto \mathrm{Re}_o^{3/5}$), but is taken here as $\mathrm{Re}_o = 0$. This inviscid approximation is sufficient, if a is not too large, *i.e.* away from the stability curve. Similar to Ref. [26], we define the parameter $a \equiv -\omega_o/\omega_i$ as the (negative) ratio between the angular rotation rates of the outer and inner cylinders. We assume maximum instability and hence optimal turbulence on the bisector of the unstable region, indicated by the solid red line. (b) and (c): enlargements of the Re-space at different scales showing the curvatures of the stability boundaries and the corresponding bisector (red). Above $\mathrm{Re}_i, \mathrm{Re}_o > 10^5$ the viscous deviation from straight lines becomes negligible.

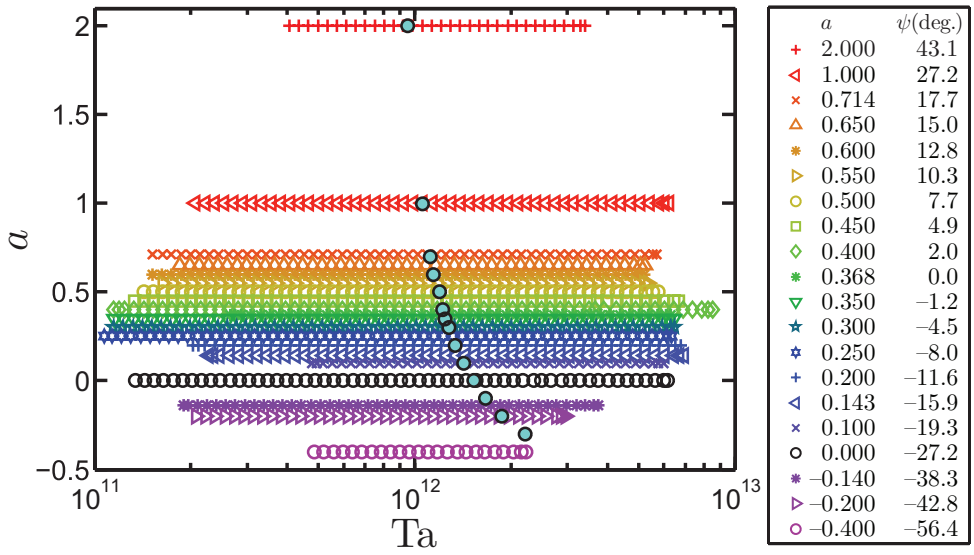

Figure 6.5: The probed (Ta, a) parameter space, equivalent to the $(\mathrm{Re}_i, \mathrm{Re}_o)$ space shown in Fig. 6.4. Each horizontal data line corresponds to a global torque measurement on the middle section of the inner cylinder at different constant a (and hence ψ). The (blue) filled circles correspond to local measurements on the angular velocity at fixed Ta and a as will be discussed in section 6.4.

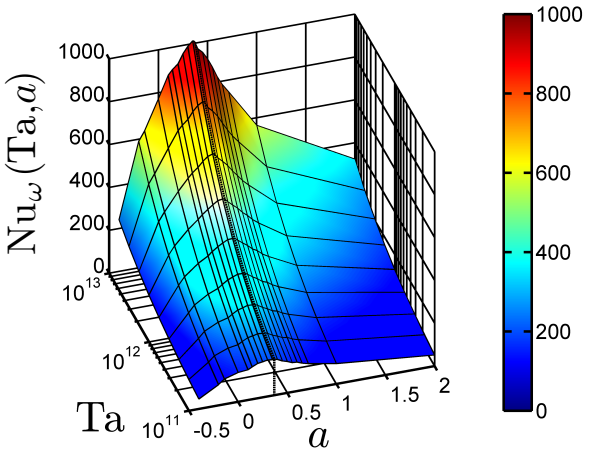

Figure 6.6: Three-dimensional (interpolated) overview $\mathrm{Nu}_\omega(\mathrm{Ta}, a)$ of our experimental results. The color and the height correspond to the Nu_ω value.

below and above $a_{\mathrm{bis}} = 0.368$ or $\psi = 0$, as will be introduced later on), we obtain $\gamma = 0.378 + 0.028a \pm 0.01$ for $a < a_{\mathrm{opt}}$, the exponent slightly decreasing towards less counter-rotation, and a constant exponent $\gamma = 0.394 \pm 0.006$ for increasing counter-rotation beyond the optimum. The trend in the exponents for $a < a_{\mathrm{opt}}$ is small and compatible with a constant $\gamma = 0.39$ and a merely statistical scatter of ± 0.03. It is in this approximation that $\mathrm{Nu}_\omega(\mathrm{Ta}, a)$ factorizes.

6.3.1 Ultimate regime

Ref. [26] interpreted the effective scaling $\mathrm{Nu}_\omega(\mathrm{Ta}, a) \propto \mathrm{Ta}^{0.38}$, similar to our currently obtained $\gamma = 0.39 \pm 0.03$, as an indication of the so-called 'ultimate regime', which is distinguished by both a turbulent bulk and turbulent boundary layers. Such scaling was predicted by Ref. [2] for very strongly driven RB flow. As detailed in Ref. [2], it emerges from a $\mathrm{Nu}_\omega(\mathrm{Ta}) \propto \mathrm{Ta}^{1/2}$ scaling with logarithmic corrections originating from the turbulent boundary layers. Remarkably, the corresponding wind Reynolds number scaling in RB flow does *not* have logarithmic corrections, *i.e.* $\mathrm{Re}_w \sim \mathrm{Ta}^{1/2}$. These RB scaling laws for the thermal Nusselt number and the corresponding wind Reynolds number have been confirmed experimentally by Ref. [28] for Nu and by Ref. [47] for

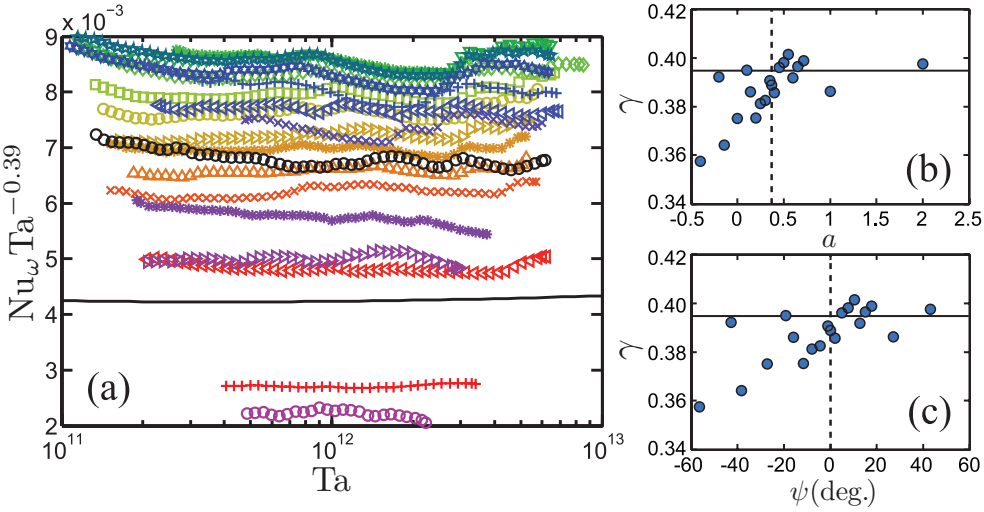

Figure 6.7: (a): $\mathrm{Nu}_\omega(\mathrm{Ta}, a)$, compensated by $\mathrm{Ta}^{0.39}$, for various a as a function of Ta, revealing effective universal scaling. The colored symbols follow the same coding as given in the legend of Fig. 6.5. The solid line has the predicted exponent from Eq. (6.12), cf. Ref. [2] and can arbitrarily be shifted in vertical direction. Here we used $\mathrm{Re}_w = 0.0424\mathrm{Ta}^{0.495}$ as found by Ref. [64] for the case $a = 0$ over the range $4 \times 10^9 < \mathrm{Ta} < 6 \times 10^{12}$, and the von Kármán constant $\bar{\kappa} = 0.4$ and $b = 0.4$, resulting in a predicted exponent of 0.395 (solid line in (b) and (c)). The $\mathrm{Nu}_\omega(\mathrm{Ta})$ exponent for each of the individual line series, fitted by a linear fit in log-log space, is plotted versus a in (b) and versus ψ in (c). Assuming a-independence the average scaling exponent is $\gamma = 0.39 \pm 0.03$, which is well consistent with the effective exponent $\gamma = 0.387$ of the first order fit on $\log_{10}(\mathrm{Nu}_\omega)$ vs. $\log_{10}(\mathrm{Ta})$ in the shown Ta-regime.

Re_w. According to the EGL theory this should have its correspondence in TC flow. That leads to the interpretation of $\gamma = 0.39$ as an indication for the ultimate state in the presently considered TC flow. Furthermore, Ref. [64] indeed found from particle image velocimetry (PIV) measurements in the present strongly driven TC system the predicted [2] scaling of the wind, $\mathrm{Re}_w \propto \mathrm{Ta}^{1/2}$. We note that in our available Ta regime the effective scaling law $\mathrm{Nu}_\omega \sim \mathrm{Ta}^{0.39}$ is practically indistinguishable from the prediction of Ref. [2], namely,

$$\mathrm{Nu}_\omega \sim \mathrm{Ta}^{1/2}\mathcal{L}(\mathrm{Re}_w(\mathrm{Ta})), \tag{6.12}$$

with the logarithmic corrections $\mathcal{L}(\mathrm{Re}_w(\mathrm{Ta}))$ detailed in Eqs. (7) and (9) of Ref. [2]. The result from Eq. (6.12) is shown as a solid line in Fig. 6.7a, showing the compensated plot $\mathrm{Nu}_\omega/\mathrm{Ta}^{0.39}$: Indeed, only detailed inspection reveals that the theoretical line is not exactly horizontal.

Thus, strictly speaking, there is a Ta-dependence of the scaling exponent $\gamma(\mathrm{Ta})$, as was clearly evidenced by Refs. [8, 10] in a much larger Ta-range. In Fig. 6.8 we present our local $\gamma(\mathrm{Ta})$ for the case of $a = 0$ and we compare it to the data from Ref. [10]. Similar to Ref. [10] we calculate $\gamma(\mathrm{Ta}) = d(\log_{10}\mathrm{Nu}_\omega)/d(\log_{10}\mathrm{Ta})$ by using a sliding linear fit over a certain $\Delta(\log_{10}\mathrm{Ta})$-range, as indicated by the top left corner of the figures (a) to (d). The narrow averaging range used in Fig. 6.8a results into a strongly fluctuating $\gamma(\mathrm{Ta})$. The origin of these fluctuations may be different turbulent flow states (*e.g.* different number of Taylor vortices); future studies should shed more light onto this. When averaging over a wider Ta-range, our data recovers a monotonously increasing $\gamma(\mathrm{Ta})$ trend, as can be seen in Fig. 6.8d, which is in line with Refs. [8, 10]. Clearly, with their large-Ta measurements these authors also already were in the ultimate TC regime.

This gives rise to the following question: Where does the ultimate turbulence regime set in turbulent TC flow? To find out we calculate the shear Reynolds number $\mathrm{Re}_s = U_s\delta/\nu$, where δ is the thickness of the kinetic boundary layer, still being of Prandtl type, and U_s the shear velocity across δ. The latter one we estimate as $U_s = U_i - U_w$. Correspondingly, we estimate the kinetic Prandtl-Blasius (PB) type BL thickness as $\delta = a_{\mathrm{PB}}d/\sqrt{\mathrm{Re}_i - \mathrm{Re}_w}$ (see *e.g.* Ref. [118]), with a_{PB} set to 2.3. This results in a shear Reynolds number of $\mathrm{Re}_s = a_{\mathrm{PB}}\sqrt{\mathrm{Re}_i - \mathrm{Re}_w}$. For the wind Reynolds number we take our experimental result based on PIV measurements [64], namely $\mathrm{Re}_w = 0.0424Ta^{0.495}$ (in the Ta-regime from 3.8×10^9 to 6.2×10^{12}, for $a = 0$). This implies that the relative contribution of the wind $\mathrm{Re}_w/\mathrm{Re}_i = U_w/U_i$ is only around 4.6% in this regime. Nonetheless, we take it into consideration in Fig. 6.9a, in which we

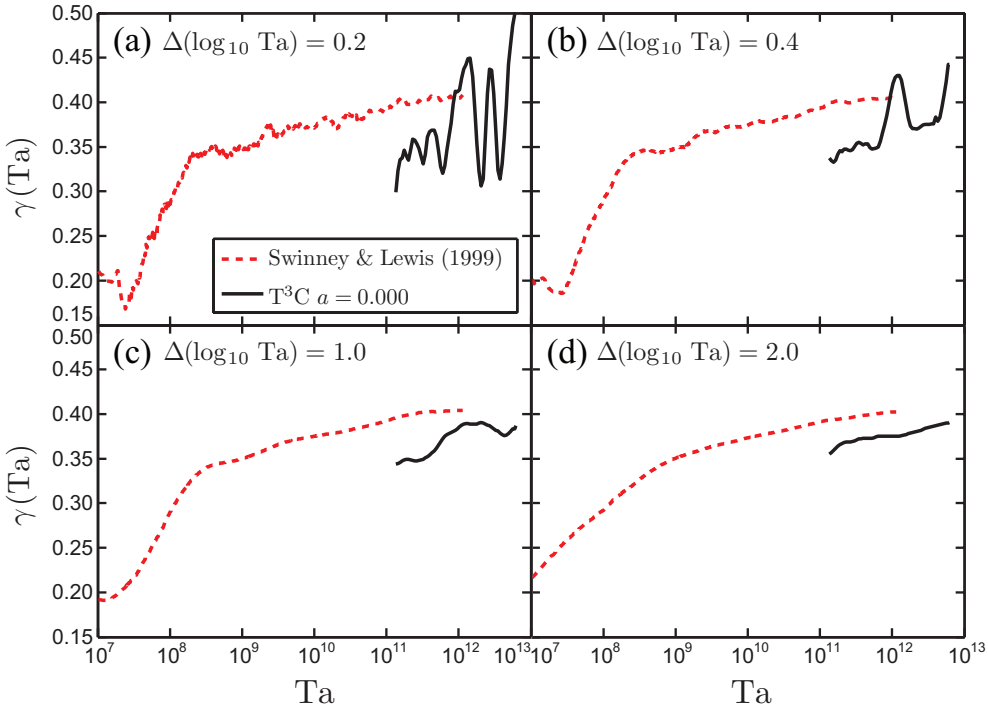

Figure 6.8: Local Ta-dependent scaling exponent γ from $\mathrm{Nu}_\omega = \mathrm{Ta}^\gamma$ for the case of inner cylinder rotation only ($a = 0$). The black solid line is our experimental data and the red dashed line is data from Ref. [10], see their Fig. 3 but now transformed into $(\mathrm{Ta}, \mathrm{Nu}_\omega)$-space. The local exponent is calculated by using a sliding linear fit over different intervals $\Delta(\log_{10} \mathrm{Ta}) =$ (a) 0.2, (b) 0.4, (c) 1.0, (d) 2.0. This method is similar to the one used in Ref. [10]. Our data reveals a detailed local sensitivity of the scaling exponent on small Ta-intervals, see (a). When fitting over wider Ta-intervals an overall increasing $\gamma(\mathrm{Ta})$ with Ta becomes apparent, see (d).

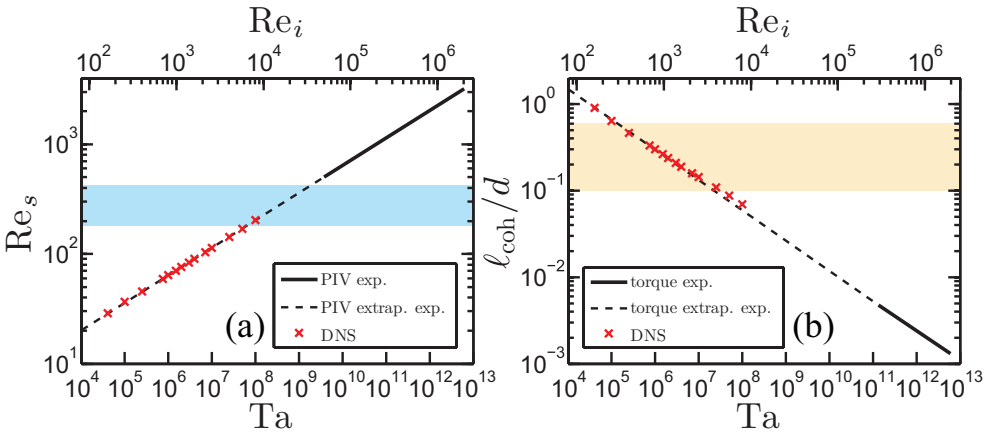

Figure 6.9: The shear Reynolds number Re_s in (a), and the coherence length ℓ_{coh}, estimated as 10 times the Kolmogorov length scale η_K, over the TC-gap width d in (b), both versus the driving strength (Ta lower abscissa, Re_i upper abscissa) for the case of pure inner cylinder rotation ($a = 0$). (a) The solid black line results from the experimental data obtained by PIV [64]. The extrapolation of this data (dashed black line) towards smaller Ta nicely agrees with the DNS data (red crosses) of [55]. The blue shaded area indicates the transitional regime from moderate turbulence at lower Ta (turbulent bulk with laminar BLs) into ultimate turbulence at higher Ta (turbulent bulk with turbulent BLs). (b) The solid black line is experimental data obtained by global torque measurements (this work). The extrapolation of this data (dashed black line) towards smaller Ta agrees with DNS data (red crosses) [55]. The yellow shaded area indicates the transitional regime where spatial coherence gets small enough to allow for a turbulent bulk beyond this regime.

plot Re_s vs Ta, retrieving the effective scaling $\mathrm{Re}_s = 2.02\mathrm{Ta}^{0.25}$. That figure also shows the result of Ref. [55] from direct numerical simulation, who found $\mathrm{Re}_w = 0.0158Ta^{0.53}$ in the Ta-regime from 4×10^4 to 1×10^7. Again, also here the relative contribution of the wind $\mathrm{Re}_w/\mathrm{Re}_i$ is very small, namely around 3%. These numerical results give an effective scaling of $\mathrm{Re}_s = 2.05\mathrm{Ta}^{0.25}$, very similar to our experimental findings, even prefactor-wise.

The Prandtl-Blasius type BL becomes turbulent for a shear Reynolds numbers larger than a critical shear Reynolds number or transition shear Reynolds number $\mathrm{Re}_{s,T}$, which is known to be in the range between 180 and 420 (see *e.g.* Ref. [118]). This range is shown as shaded in Fig. 6.9: Indeed, all of our experimental data points of this present chapter (solid line) are beyond that onset. So indeed we are in the ultimate regime. In contrast, the numerical data points by Ref. [55] are in the Prandtl-Blasius regime with laminar-type boundary layers.

The transition between these two regimes occurs in between. The range 180 to 420 for the transitional shear Reynolds number $\mathrm{Re}_{s,T}$ here (*i.e.*, for the present η and $a = 0$) corresponds to a range between 3×10^7 to 10^9 for the transitional Taylor number Ta_T and a range between 5×10^3 and 2×10^4 for the transitional (inner) Reynolds number $\mathrm{Re}_{i,T}$. Indeed, this corresponds to the transitional Reynolds number found by Ref. [10], see Fig. 3 of that paper, in which the transition to the ultimate regime is identified at a Reynolds number $\mathrm{Re}_{i,T} = 1.3 \times 10^4$. Below that value Ref. [10] found a very steep increase of the local slope $d \log \mathrm{Nu}_\omega / d \log \mathrm{Re}_i$ with Re_i, beyond the transition the increase is much less. (Here we have translated the findings of Ref. [10] in the notation of this chapter.) We stress again that the values given in this and the next subsection hold for $a = 0$. How the values of the transitional Reynolds or Taylor number depend on a remains an important question for future research.

Both in our experiment and in the experiments by Ref. [10] the logarithmic corrections in eq. (6.12) are visible and have the consequence that the "real" ultimate scaling $\mathrm{Nu}_\omega \sim \mathrm{Ta}^{1/2}$ is never achieved. As explained in Ref. [2] (and much earlier in Ref. [29], but differently and with a different result) these logarithmic corrections are a consequence of the logaritmic velocity profile in the turbulent boundary layers. Only by destroying this logarithmic profiles by extreme wall roughness as done in TC experiments [11] or in RB experiments [122] or by replacing the walls by periodic boundary conditions (and a volume forcing) as done in numerical simulations [123, 124, 67] one can recover the 1/2-scaling exponent, which is obtained in the strict upper-bound [125].

	TC	RB
loss of spatial coherence (defined via $\ell_{\rm coh}$)	$\mathrm{Ta}_{\rm on} \approx 10^6$ $\mathrm{Re}_{i,\rm on} \approx 10^3$	$\mathrm{Ra}_{\rm on} \approx 10^7$
BL shear instability (defined via Re_s)	$\mathrm{Ta}_T \approx 5 \times 10^8$ $\mathrm{Re}_{i,T} \approx 10^4$	$\mathrm{Ra}_T \approx 10^{14}$

Table 6.2: Estimates for the onset of the regime where a turbulent bulk becomes possible next to laminar-type BLs (first row) and for the transition towards the ultimate regime, in which the BLs are turbulent, for both TC and RB turbulence. For TC the estimates are derived here; for RB they are taken from the literature, namely from Ref. [126] for $\mathrm{Ra}_{\rm on}$ (for $\mathrm{Pr} \approx 1$) and for Ra_T from Ref. [127] (theoretical prediction) and from Ref. [47] (experimental confirmation). In between these values laminar-type BLs and a turbulent bulk can coexist and the transport properties can be described by the unifying RB theory [45, 127, 128, 129] which later had been extended to TC by EGL. Beyond Ta_T (Ra_T) the turbulent nature of BLs lead to different scaling properties, as elaborated in [2].

6.3.2 Comparison Taylor-Couette turbulence with Rayleigh-Bénard turbulence

To get an idea on the extension of the non-ultimate turbulence regime in TC flow we also estimate the coherence length $\ell_{\rm coh}$, below which the spatial coherence of structures in the flow gets small enough to allow for developed turbulence in the flow. Typically, one estimates the coherence length as multiple of the (mean) Kolmogorov length scale $\eta_K = \nu^{3/4}/\epsilon^{1/4}$, namely $\ell_{\rm coh} \approx 10\eta_K$. The factor of 10 between these two length scales is motivated by the transition between viscous subrange and inertial subrange which is known to happen at a scale around $10\eta_K$, see *e.g.* Ref. [130]. Here ϵ is the mean energy dissipation rate. That can be obtained from the angular velocity flux J^ω (see eq. (4.7) of EGL), namely

$$\epsilon = \frac{2(\omega_i - \omega_o)J^\omega}{r_o^2 - r_i^2} = \frac{2(\omega_i - \omega_o)J^\omega_{\rm lam}\mathrm{Nu}_\omega}{r_o^2 - r_i^2}, \tag{6.13}$$

reflecting the statistical balance between external driving and internal dissipation. As pointed out in EGL, a more elegant way to write this balance

is

$$\epsilon - \epsilon_{\rm lam} = \frac{\nu^3}{d^4}({\rm Nu}_\omega - 1){\rm Ta}\sigma^{-2}. \tag{6.14}$$

In any case, we can use our data for Nu_ω to calculate the mean Kolmogorov length scale η_K and thus the coherence length $\ell_{\rm coh} = 10\eta_K$. In Fig. 6.9b we show $\ell_{\rm coh}$ as function of Ta or Re_i (for $a = 0$ and $\eta = 0.716$). When the coherence length becomes smaller than, say, 0.1 to 0.5 times the outer length scale d, one can start to reasonably speak of a developed turbulence regime in the bulk in between the inner scale $\ell_{\rm coh} = 10\eta_K$ and the outer scale d. According to Fig. 6.9b this onset of a developed turbulence regime in the bulk, but still with Prandtl-Blasius type boundary layers (see Refs. [50, 131]), occurs at Taylor numbers $\mathrm{Ta}_{\rm on}$ between 2×10^5 and 2×10^7 or onset (inner) Reynolds numbers $\mathrm{Re}_{i,\rm on}$ between 300 and 3000, far below the regime of our present experiments, but in the regime of the numerical simulations [55]. The corresponding numbers for smaller coherence in RB flow are given in Fig. 1 of Ref. [126]: For $\mathrm{Pr} \approx 1$, a developed turbulence regime in the bulk becomes possible beyond $\mathrm{Ra} \approx 10^7$.

Figures 6.9a and 6.9b together reveal that there should be a TC flow range with Prandtl-Blasius type (laminar) BLs and a turbulent bulk roughly in between $\mathrm{Ta} \approx 10^6$ and $\mathrm{Ta} \approx 5 \times 10^8$ or Re_i in between $\mathrm{Re}_i \approx 10^3$ and 10^4. This regime has been explored in the earlier experiments by Refs. [9, 8, 10] and others—it cannot be accessed with water as operating liquid in our $\mathrm{T}^3\mathrm{C}$ setup as then the angular velocities would have to be too low for reasonable precision. We could, however, explore that regime with more viscous liquids in our $\mathrm{T}^3\mathrm{C}$ setup.

Our present estimates for TC flow and the earlier findings and estimates for RB flow are summarized in table 6.2. The table gives rise to the interesting question: Why is the "classical regime" (as it is called by Ahlers) in between $\mathrm{Ra}_{\rm on}$ and Ra_T, in which a laminar-type BL and a turbulent bulk coexist and in which the unifying theory [45, 127, 128, 129] is applicable, so extended in RB turbulence, but so small in TC turbulence? Or in other words: Why does the ultimate regime with its turbulent BLs set in for much smaller Ta in TC flow as compared to the extremely high Ra values for that onset in RB flow? We think that the answer lies in the much higher efficiency of the shear driving in TC flow as compared to the thermal driving in RB flow. In RB flow the shear instability of the kinetic BL is induced by the thermal driving only indirectly; namely, the driving first induces a large scale wind, which then in turn builds up the shear near the boundaries. In TC flow the flow is directly driven by the rotating inner cylinder, giving rise to a very large direct shear. As pointed

above, the large scale wind with its strength Re_w only means a small correction of $4-5\%$ to Re_i in the calculation of the shear Reynolds number. As roughly $\mathrm{Re}_s \sim \mathrm{Re}^{1/2} \propto \mathrm{Ta}^{1/4}$, a factor 20 in the Reynolds number leads to the huge difference $20^4 = 1.6 \times 10^5$ in the typical onset Taylor number.

6.3.3 Optimal angular velocity transport

Coming back to our experimental data on TC: The (nearly) horizontal lines in Fig. 6.7a imply that $\mathrm{Nu}_\omega(\mathrm{Ta}, a)$ within present experimental precision nearly factorizes in $\mathrm{Nu}_\omega(\mathrm{Ta}, a) = f(a) \cdot \mathrm{Ta}^{0.39\pm0.03}$. We now focus on the a-dependence of the angular velocity flux amplitude $f(a) = \mathrm{Nu}_\omega(\mathrm{Ta}, a)/\mathrm{Ta}^{0.39}$, shown in Figs. 6.10a and 6.10b, and the idea of its interpretation. One observes a very pronounced maximum at $a_{\mathrm{opt}} = 0.33\pm0.04$, reflecting the optimal angular velocity transport from the inner to the outer cylinder at that angular velocity ratio. This value is obtained by averaging over the three data points making up the small plateau visible in Fig. 6.10b. Naively, one might have expected that $f(a)$ has its maximum at $a = 0$, *i.e.* $\omega_o = 0$, no outer cylinder rotation, since outer cylinder rotation stabilizes an increasing part of the flow volume for increasing counter rotation rate. On the other hand, outer cylinder rotation also enhances the total shear of the flow, leading to enhanced turbulence, and thus more angular velocity transport is expected. The a-dependence of $f(a)$ thus reflects the mutual importance of both these effects.

Generally, one expects an increase of the turbulent transport if one goes deeper into the control parameter range (Ta, a) in which the flow is unstable. We speculate that the optimum positions for the angular velocity transport should consist of all points in parameter space, which are equally distant from both the right branch (1st quadrant, co-rotation) of the instability border and its left branch (2nd quadrant, counter-rotation). In inviscid approximation ($\nu = 0$) these two branches are given by the Rayleigh criterion, $\partial(r^2\omega)/\partial(r) > 0$, resulting in the lines given by the relations $\omega_i/\omega_o|_{\mathrm{Rayleigh}} = \eta^{-2}$ and $\omega_i = 0$, which translate into $a = -\eta^2$ and $a = \infty$, respectively. The line of equal distance from both is the angle bisector of the instability range. Its relation can easily be calculated to be

$$a_{\mathrm{bis}}(\eta) = \frac{\eta}{\tan\left[\frac{\pi}{2} - \frac{1}{2}\arctan\left(\eta^{-1}\right)\right]}. \tag{6.15}$$

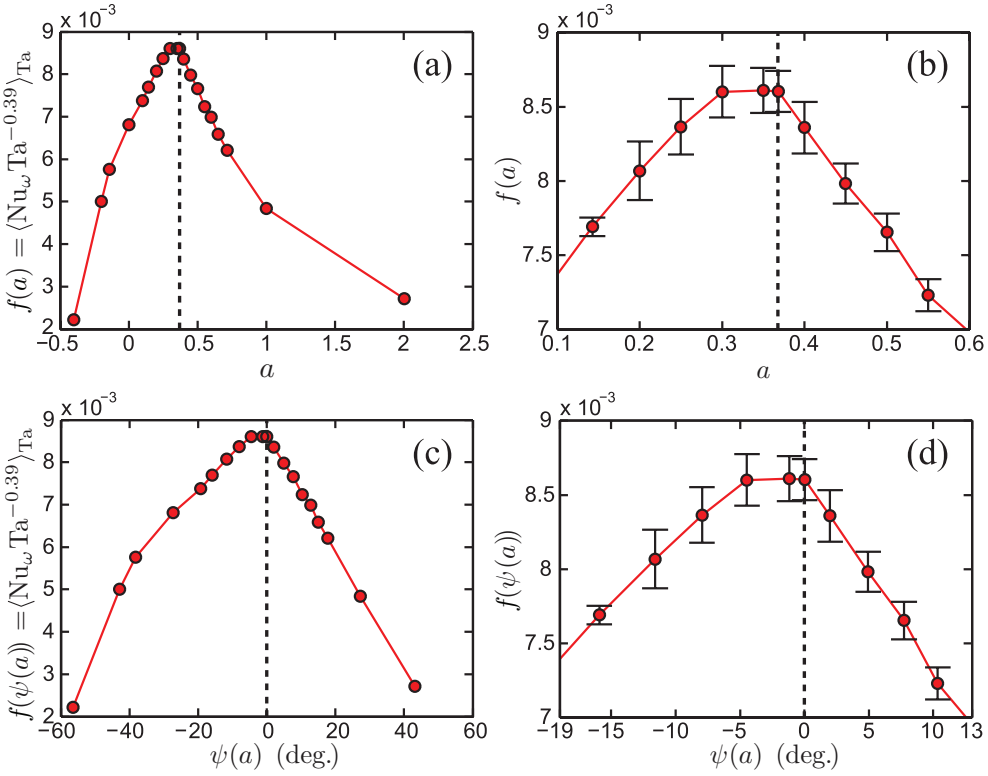

Figure 6.10: Amplitude f of the effective scaling law $\mathrm{Nu}_\omega \propto \mathrm{Ta}^{0.39}$ (shown in Fig. 6.7) as function of a (a, b) and as function of $\psi(a)$ (c, d). The dashed line in all figures corresponds to the suggested case of optimal turbulence as given by the angle bisector Eq. (6.15), *i.e.* $a_{\mathrm{bis}} = 0.368$. (The connecting lines between the data points are guides for the eyes.) The standard deviation of $\mathrm{Nu}_\omega \mathrm{Ta}^{-0.39}$ is similar to the size of the symbols in (a) and (c), and is indicated by the error bars of the zoomed-in figures (b) and (d). The angular velocity transport flux amplitude is systematically larger towards the co-rotating instability borders $a = -\eta^2$ or $\psi \approx -62.8°$ with respect to the counter-rotating instability borders $a \to \infty$ or $\psi \approx 62.8°$.

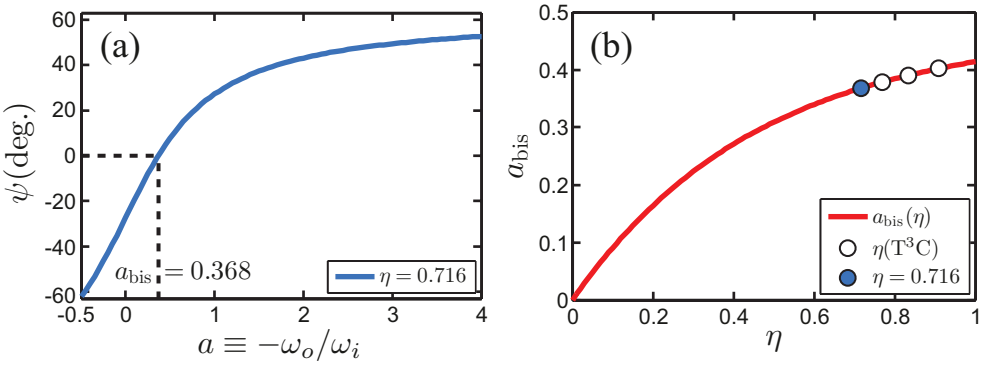

Figure 6.11: (a): The transformation from a to ψ as given by Eq. (6.16), shown here for the radius ratio $\eta = 0.716$ used in the present work. Note that the domain of $a = [-\eta^2, \infty]$ from co- to counter-rotation, spanning the complete unstable flow regime, is transformed to the range $\psi \approx [-62.80°, +62.80°]$ for this specific η. (b): The dependence of $a_{\rm bis}$ on η as given by Eq. (6.15), shown as the red line. Four circles: the radius ratios accessible in the T^3C, *i.e.* $\eta = 0.716; 0.769; 0.833; 0.909$. Blue indicated circle: radius ratio $\eta = 0.716$ of the present work, suggesting optimal turbulence at $a_{\rm bis} = 0.368$.

For $\eta = 0.716$ this gives $a_{\rm bis} = 0.368$. Note that the measured value $a_{\rm opt} = 0.33 \pm 0.04$ agrees indistinguishably within experimental precision with the bisector line, supporting our interpretation. It also explains why only the lines of constant a scan the parameter space properly. This reflects the straight character of the linear instability lines; as long as one is not too close to them to see the details of the viscous corrections, *i.e.* if Ta is large and a is well off the instability borders at $a = -\eta^2$ for co-rotation and $a \to \infty$ for counter-rotation. Instead of characterizing the lines by the slope parameter a one can introduce the angle ψ between the line of chosen a and the angle bisector of the instability range denoted by $a_{\rm bis}$; thus $a = a_{\rm bis}$ corresponds to $\psi = 0$.

$$\psi(a) = \frac{\pi - \arctan\left(\eta^{-1}\right)}{2} - \arctan\left(\frac{\eta}{a}\right). \tag{6.16}$$

The transformation (6.16) is shown in Fig. 6.11a and the resulting $f(\psi(a))$ in Fig. 6.10c. The function $f(a)$ as a function of a is strongly asymmetric both around its peak at $a_{\rm opt}$ and at its tails, presumably because of the different viscous corrections at $a = -\eta^2$ (decreasing $\propto {\rm Re}_o^{-2}$ towards the inviscid Rayleigh line) and at $a = \infty$ (nonvanishing, even increasing correction $\propto {\rm Re}_o^{3/5}$) (and

non-normal-nonlinear (shear) instability, see *e.g.* Ref. [132]).

We do not yet know whether the optimum of $f(a)$ coincides with the bisector of the Rayleigh-unstable domain for *all* η. Both could coincide incidentally for $\eta = 0.716$, analyzed here. But if this were the case for all η, we can predict the η-dependence of $a_{\rm opt}(\eta)$. This then is given by equation (6.15). This function is plotted in Fig. 6.11. In future experiments we shall test this dependence with our T^{3}C facility. The three extra points we will be able to achieve are marked as white, empty circles. The precision of our facility is good enough to test equation (6.15), but clearly further experiments at much smaller η are also needed.

We note that for smaller Ta one can no longer approximate the instability border by the inviscid Rayleigh lines. The effect of viscosity on the shape of the border lines has to be taken into account. The angle bisector of the instability range in (Re$_o$, Re$_i$)-parameter space (Fig. 6.4a) will then deviate from a straight line; we therefore also expect this for $a_{\rm opt}$. The viscous corrections of the Rayleigh instability criterion were first numerically calculated [120] for the case of $a = 0$, and then analytically estimated [17] and later fitted [133]. Figures 6.4b and 6.4c show enlargements of the (Re$_o$, Re$_i$)-parameter space, together with the Rayleigh-criterion (green) and the analytical curve [17] (black) for $\eta = 0.716$. Note that the minimum of that curve is *not* at Re$_o = 0$, but shifted to a slightly negative value Re$_o \approx -5$, where the instability sets in at Re$_i \approx 82$. If we again assume that the optimum position for turbulent transport is distinguished by equal distance to the two branches of the Esser-Grossmann curve, we obtain the red curve in Fig. 6.4b. On the Ta-scale of Figs. 6.4c and 6.4a it is indistinguishable from a straight line through the origin and can hence be described by Eq. (6.15). As another consequence of the viscous corrections, the factorization of the angular velocity transport flux Nu$_\omega = f(a) \cdot F$(Ta) will no longer be a valid approximation in the parameter regime shown in Fig. 6.4b. For this to hold Ta must be large and a well off the instability lines. This could further be tested by choosing the parameter a sufficiently large, the line approaching or even cutting the stability border for strong counter-rotation. Then the factorization property will clearly be lost.

Future low Ta experiments and/or numerical simulations for various a will show how well these ideas on understanding the existence and value of a_{opt}, being near or equal to $a_{\rm bis}$, are correct or deserve modification. Of course, there will be some deviations due to the coherent structures in the flow at lower Ta, due to the influence of the number of rolls, *etc.* Similar to how

in RB the Nu scaling shows discontinuities, the TC scaling exponent of Nu_ω shows all these structures for not sufficiently large Ta, see *e.g.* Fig. 3 of Ref. [10] in which one sees how strongly the exponent α depends on Re up to 10^4 (Ta about up to 10^8).

6.4 Local LDA angular velocity radial profiles

We now wonder on whether the distinguishing property of the flow at a_{opt}—maximal angular velocity transport—is also reflected in other flow characteristics. We therefore performed LDA measurements of the angular velocity profiles in the bulk close to mid-height, $z/L = 0.44$, at various $-0.3 \leq a \leq 2.0$, see table 6.3 for a list of all measurements, Fig. 6.12 for the mean profiles $\langle\omega(r,t)\rangle_t$ at fixed height z, and Fig. 6.13 for the rescaled profiles $(\langle\omega(r,t)\rangle_t - \omega_o)/(\omega_i - \omega_o)$, also at fixed height z. With our present LDA technique, we can only resolve the velocity in the radial range $0.04 \leq \tilde{r} \leq 0.98$; there is no proper resolution in the inner and outer boundary layers. Because the flow close to the inner boundary region requires substantially more time to be probed with LDA, due to disturbing reflections of the measurement volume on the reflecting inner cylinder wall necessitating the use of more stringent Doppler burst criteria, we limit ourselves to the range $0.2 \leq \tilde{r} \leq 0.98$.
From Fig. 6.12 it is seen that for nearly all co- and counter-rotating cases $-0.3 \leq a \leq 2.0$ the slope of $\langle\omega(\tilde{r},t)\rangle_t$ is negative. Only around $a = 0.40$ we find a zero mean angular velocity gradient in the bulk. This case is very close to $a_{\mathrm{opt}} = 0.33 \pm 0.04$ and $a_{\mathrm{bis}} = 0.368$. The normalized angular velocity gradient as function of a is shown in Fig. 6.14a. Indeed, it has a pronounced maximum and zero mean angular velocity gradient very close to $a = a_{\mathrm{bis}} \approx a_{\mathrm{opt}}$, the position of optimal angular velocity transfer. Ref. [54], who performed PIV measurements of TC flow in air around Ta $\sim 10^{10}$, report a similar trend of a diminishing angular velocity gradient in the center of the TC gap for their investigated a coming from 10.79 down towards 0.70, *i.e.* in the well counter-rotating regime. We speculate that their trend would continue and result in a diminishing slope of angular velocity when decreasing a further to their (unreported) case of a_{opt}. Interestingly, the result of a zero angular velocity gradient across the gap is quite similar to what can be found in Taylor vortex flow, for which the axially-averaged circumferential momentum or velocity is nearly uniform across the gap in the bulk, see *e.g.* Refs. [134, 135]. We note that in strongly turbulent RB flow the temperature also has a (practically)

zero mean gradient in the bulk, see *e.g.* the recent review [6].
A transition of the flow structure at $a = a_{\rm bis} \approx a_{\rm opt}$ can also be confirmed in Fig. 6.13a, in which we have rescaled the mean angular velocity at fixed height as

$$\langle\tilde{\omega}(\tilde{r})\rangle_t = \left(\langle\omega(\tilde{r})\rangle_t - \omega_o\right)/(\omega_i - \omega_o). \tag{6.17}$$

We observe that up to $a = a_{\rm bis}$ the curves for $\langle\tilde{\omega}(\tilde{r})\rangle_t$ for all a go through the mid-gap point ($\tilde{r} = 1/2, \langle\tilde{\omega}(1/2)\rangle_t \approx 0.35$), implying the mid-gap value $\langle\omega(1/2)\rangle_t \approx 0.35\omega_i + 0.65\omega_o$ for the time averaged angular velocity. However, for $a > a_{\rm bis}$, *i.e.* stronger counter-rotation, the angular velocity at mid-gap becomes larger, as seen in Fig. 6.13b.
Figure 6.14b shows the relative contributions of the molecular and the turbulent transport to the total angular velocity flux J^ω (6.6), *i.e.* for both the diffusive and the advective term. The latter always dominates by far with values beyond 99%, but at $a \approx a_{\rm bis}$ the advective term contributes 100% to the angular velocity flux and the diffusive term nothing, corresponding to the zero mean angular velocity gradient in the bulk at that a. This special situation perfectly resembles RB turbulence for which, due to the absence of a mean temperature gradient in the bulk, the whole heat transport is conveyed by the convective term. In the (here unresolved) kinetic boundary layers the contributions just reverse: The convective term strongly decreases if $\tilde{r}$ approaches the cylinder walls at 0 or 1 since $u_r \to 0$ ($u_z \to 0$ in RB), while the diffusive term (heat flux in RB) takes over at the same rate, as the total flux J^ω is an $\tilde{r}$-independent constant.
From the measurements presented in Fig. 6.12 we can extract the neutral line $\tilde{r}_n$, defined by $\langle\omega(\tilde{r}_n, t)\rangle_t = 0$ at fixed height $z/L = 0.44$ for the turbulent case. The neutral line is, of course, part of a neutral *surface* throughout the TC volume. We expect that for large $a \gg a_{\rm opt}$, the flow will be so much stabilized that an axial dependence of the location of the neutral line shows up, in spite of the large Ta numbers, in contrast to the cases $a \approx a_{\rm opt}$ where we expect the location of the neutral line to be axially independent for large enough Ta. The results on $\tilde{r}_n$ are shown in Fig. 6.15. Note that while for $a \leq 0$ (co-rotation) there obviously is no neutral line at which $\langle\omega\rangle_t = 0$, for $a > 0$ a neutral line exists at some position $\tilde{r}_n > 0$. As long as it still is within the outer kinematic BL, we cannot resolve it. This turns out to be the case for $0 < a \lesssim a_{\rm bis}$. But for $a_{\rm bis} \lesssim a$ the neutral line can be observed within the bulk and is well resolved with our measurements. So again we see two regimes: For $0 < a \lesssim a_{\rm bis}$ in the laminar case the stabilizing outer cylinder rotation shifts

a	ψ	Ta	ω_i	ω_o	Re_i	Re_o	$\mathrm{N}_{\min}$	$\mathrm{N}_{\max}$	$F_{s,\min}$	$F_{s,\max}$
	$^\circ$		1/s	1/s					Hz	Hz
		10^{12}			10^6	10^6	10^3	10^3		10^3
2.000	43.1	0.95	16.3	-32.6	0.26	-0.74	35	60	70	2.4
1.000	27.2	1.06	25.8	-25.8	0.42	-0.58	26	60	52	1.6
0.700	17.2	1.12	31.2	-21.9	0.51	-0.49	55	80	46	0.7
0.600	12.8	1.15	33.6	-20.1	0.54	-0.46	67	80	56	0.5
0.500	7.7	1.20	36.4	-18.2	0.59	-0.41	31	60	63	0.6
0.400	2.0	1.22	39.5	-15.8	0.64	-0.36	10	25	57	0.7
0.350	-1.2	1.25	41.4	-14.5	0.67	-0.33	11	25	45	0.5
0.300	-4.5	1.28	43.6	-13.1	0.70	-0.30	12	25	64	0.8
0.200	-11.6	1.34	48.3	-9.65	0.78	-0.22	14	25	78	1.0
0.100	-19.2	1.42	54.2	-5.46	0.88	-0.12	17	25	93	1.3
0.000	-27.2	1.53	61.8	0.00	1.00	0.00	13	25	72	2.3
-0.100	-35.2	1.67	71.9	7.21	1.16	0.16	25	25	147	1.7
-0.200	-42.8	1.87	85.7	17.1	1.39	0.39	22	25	121	1.6
-0.300	-50.0	2.21	106.0	31.9	1.72	0.72	6	25	32	7.5

Table 6.3: LDA experimental conditions. Each case of a is examined at fixed $\mathrm{Re}_i - \mathrm{Re}_o = 10^6$. $a, \psi, \mathrm{Ta}, \omega_{i,o}, \mathrm{Re}_{i,o}$ as defined before, see also Table 6.1. The minimum and maximum number of detected LDA bursts along the radial scan is given by $\mathrm{N}_{\min}$ and $\mathrm{N}_{\max}$, respectively. Idem for the minimum and maximum average burst rate $F_{s,\min}$ and $F_{s,\max}$.

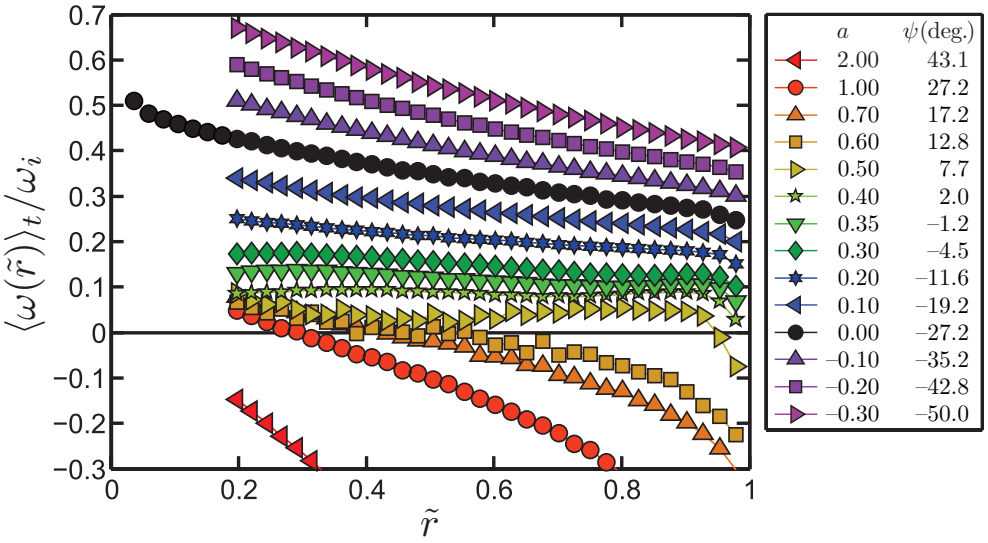

Figure 6.12: Radial profiles of the time-averaged angular velocity $\langle\omega(\tilde{r})\rangle_t$ at fixed height $z/L = 0.44$, normalized by the inner cylinder angular velocity ω_i, for various cases of fixed a, as indicated by the blue filled circles in Fig. 6.5. All profiles are acquired at fixed angular rotation rates of the cylinders in such a way that $\mathrm{Re}_i - \mathrm{Re}_o = 10^6$ is maintained. Instead of measuring at mid-height $z/L = 0.50$ we measure at $z/L = 0.44$, because this axial position encounters less visual obstructions located on the clear acrylic outer cylinder. To improve visual appearance the plotted range does not fully cover the profile corresponding to $a = 2$. The profiles of $a = 0.5$, 0.6, and 0.7 appear less smooth due to a fluctuating neutral line combined with slightly insufficient measuring time, *i.e.* convergence problems.

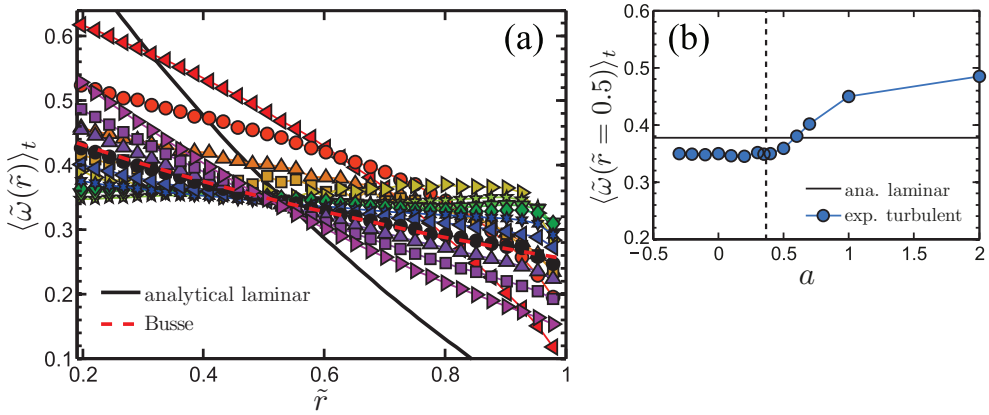

Figure 6.13: (a) Rescaled angular velocity profiles $\langle\tilde{\omega}(\tilde{r})\rangle_t = (\langle\omega(\tilde{r})\rangle_t - \omega_o)/(\omega_i - \omega_o)$ for various a. For $a \lesssim a_{\rm bis} = 0.368$ all of these curves cross the point $(\tilde{r} = 1/2, \langle\tilde{\omega}\rangle_t = 0.35)$. For $a > a_{\rm bis} = 0.368$ this is no longer the case. The transition of the quantity $\langle\tilde{\omega}(\tilde{r} = 1/2)\rangle_t$ when a increases from $a < a_{\rm bis}$ to $a_{\rm bis} < a$ is shown in (b). The dashed vertical line indicates $a_{\rm bis} = 0.368 \approx a_{\rm opt}$. The solid black lines in (a) and (b) show the $\tilde{\omega}(\tilde{r})$ values for the laminar solution (6.7). The dashed red line in (a) shows the Busse upper bound profile (6.19), which is independent of the ratio a and is nearly indistinguishable from the measurement for $a = 0$.

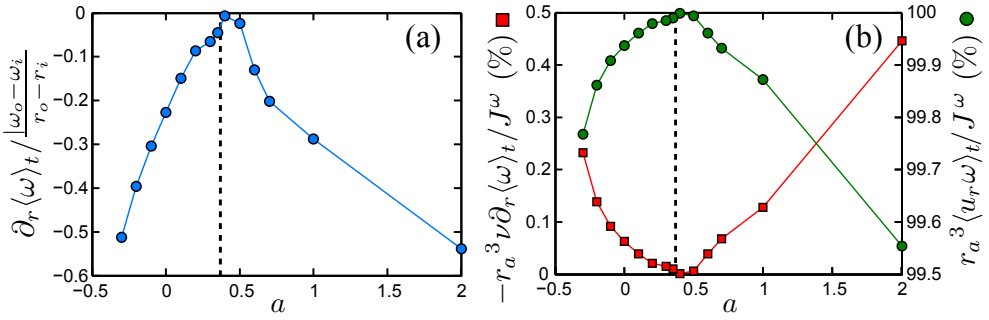

Figure 6.14: (a) Radial gradient $\partial_r\langle\omega\rangle_t$ of the angular velocity profile in the bulk of the flow, non-dimensionalized with the mean ω-slope $|\omega_o - \omega_i|/(r_o - r_i)$. The values are obtained from Fig. 6.12 by fitting a cubic smoothing spline to the profiles in order to increase the accuracy of the gradient amplitude estimate. Note that the radial gradients are *negative* throughout, and approach zero when close to $a = a_{\rm bis} \approx a_{\rm opt}$. (The connecting lines are guides for the eyes.) (b) Resulting ratio of the viscous angular velocity transport term $-r_a^3 \nu \partial_r \langle\omega\rangle_{A,t}$ to the total transport J^ω (red squares and left axis) and ratio of the advective angular velocity transport term $r_a^3 \langle u_r \omega\rangle_{A,t}$ to the total transport J^ω (green circles and right axis) for the various a. These ratios correspond to the second and first term of equation (6.6), respectively.

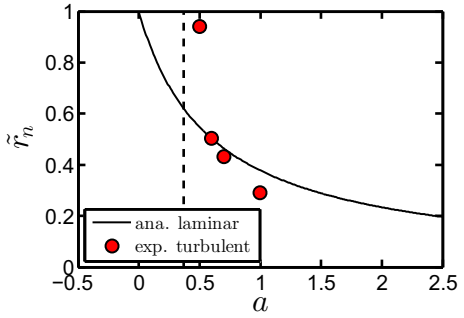

Figure 6.15: The measured radial position $\tilde{r}_n = (r_n - r_i)/(r_o - r_i)$ of the neutral line defined by $\langle\omega(\tilde{r}_n)\rangle_t = 0$ at fixed height $z/L = 0.44$ as function of a, indicated by the circles. The values are obtained from Fig. 6.12 by fitting a cubic smoothing spline to the profiles in order to increase the accuracy of locating $\tilde{r}_n$, resulting in an accuracy equal to the symbol size. The straight vertical line corresponds to $a_{\rm bis} = 0.368$, below which the neutral line is within the outer BL and cannot be resolved by our LDA technique. The solid line corresponds to the neutral line in the laminar case calculated analytically with Eq. (6.7). Note that for significant counter-rotation $a = 1$ and for this particular height, the neutral line in the turbulent case lies farther inside, nearer to the inner cylinder, than in the laminar flow case.

the neutral line inwards, but due to the now *free boundary* between the stable outer r-range and the unstable range between the neutral line and the inner cylinder, the flow structures extend beyond $\tilde{r}_n$. Thus also in the turbulent flow case the unstable range flow extends to the close vicinity of the outer cylinder. The increased shear and the strong turbulence activity originating from the inner cylinder rotation are too strong and prevent that the neutral line is shifted off the outer kinematic BL. As described in Ref. [17], this is the very mechanism which shifts the minimum of the viscous instability curve to the left of the $\mathrm{Re}_i = 0$ axis. Therefore, the observed behavior of the neutral line position as a function of a is another confirmation of above idea that a_{opt} coincides with the angle bisector a_{bis} of the instability range in parameter space. The small Re_o and the large Re_o behaviors perfectly merge. Only for $a > a_{\mathrm{opt}}$ the stabilizing effect from the outer cylinder rotation is strong enough, the width of the stabilized range is broad enough, so that a neutral line $\tilde{r}_n$ can be detected in the bulk of the TC flow. This behavior is similar to what is reported [54], see their Fig. 6.

One would expect that for much weaker turbulence $\mathrm{Ta} \ll 10^{11}$ the capacity of the turbulence around the inner cylinder to push the neutral line outwards would decrease, leading to a smaller a_{opt} for these smaller Taylor numbers. Numerical simulations by H. Brauckmann and B. Eckhardt of the University of Marburg (Ta up to 10^9) and independently ongoing DNS by Ref. [55] of the University of Twente (presently Ta up to 10^8) seem to confirm this view.

For much weaker turbulence one would also expect a more pronounced height-dependence of the neutral line, which will be pushed outwards where the Taylor-rolls are going outwards and inwards where they are going inwards. Based on our height-dependence studies of section 6.2, we expect that this height dependence will be much weaker or even fully washed out in the strongly turbulent regime $\mathrm{Ta} > 10^{11}$ in which we operate the TC apparatus. However, in Fig. 6.15 we observe that the neutral line in the turbulent case lies more inside than in the laminar case, and this result is difficult to rationalize apart from assuming some axial-dependence of the neutral line location, *i.e.* more outwards locations of the neutral line at larger and smaller height. In future work we will study the axial dependence of the neutral line in the turbulent and counter-rotating case in more detail.

For completeness, we also compare our experimental angular velocity profiles with those employed in the upper bound theory [114]. Ref. [114] derived an expression for the angular velocity profiles in the limit of infinite Reynolds number. Translating that expression to the notation used in the present work,

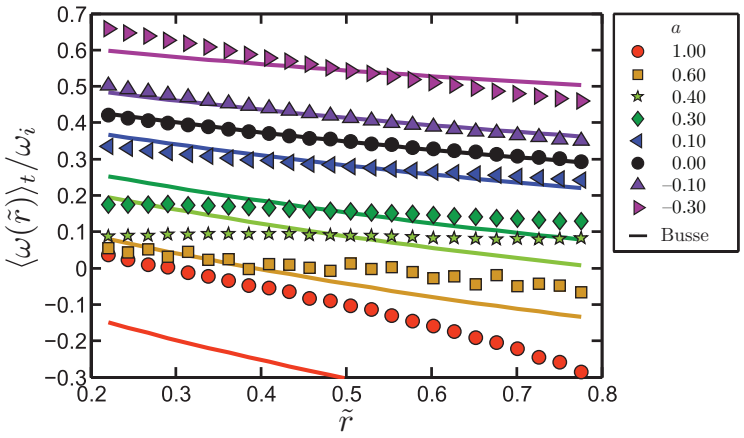

Figure 6.16: Normalized angular velocity $\langle\omega(\tilde{r})\rangle_t/\omega_i$ versus normalized gap distance $\tilde{r}$ for various a. The symbols indicate the experimental data as already presented in Fig. 6.12 and Fig. 6.13a. To improve visual appearance only a selection on the a-cases is shown. The thick solid lines are given by Eq. (6.18) for $\eta = 0.716$.

gives

$$\omega_{\text{Busse}} = \frac{\omega_i - \omega_o}{r^2}\left[\frac{{r_i}^2}{4(1-\eta^2)}\right] + \omega_i\left[\frac{\eta^2 - 2\eta^4}{2-2\eta^4}\right] + \omega_o\left[\frac{2-\eta^2}{2-2\eta^4}\right]. \qquad (6.18)$$

As already shown by Ref. [10], for the case $a = 0$ excellent agreement between the Busse profile and the experimental one is found. However, for a farther away from zero there is more discrepancy between the experimental data and the profiles suggested by the upper-bound theory, as shown in Fig. 6.16a. When we rescale the angular velocity profiles to $\tilde{\omega}$, according to Eq. (6.17), the profiles as given by the upper-bound theory [114] fall on top of each other for all a,

$$\tilde{\omega}_{\text{Busse}} = \frac{\omega_{\text{Busse}} - \omega_o}{\omega_i - \omega_o} = \frac{{r_i}^2}{4\left({r_o}^4 - {r_i}^4\right)}\left[\frac{{r_o}^2\left({r_i}^2 + {r_o}^2\right)}{r^2} + 2{r_o}^2 - 4{r_i}^2\right] \qquad (6.19)$$

In contrast to the collapsing upper-bound profiles, the experimental data in Fig. 6.16b show a different trend. Clearly, the profiles suggested by the upper bound theory are in general not a good description of the physically realized profiles, apart from the $a = 0$ case. Given the complexity of the flow this may not be surprising.

While in this section we have only focused on the time-mean values of the angular velocity, in the following section we will give more details on the probability density functions (PDF) in the two different regimes below and above a_{bis} and thus on the different dynamics of the flow in these two different regimes.

6.5 Turbulent flow organization in the gap between the cylinders

Time series of the angular velocity at $\tilde{r} = 0.60$ below the optimum amplitude at $a = 0.35 < a_{\mathrm{bis}} = 0.368$ (co-rotation dominates) and above the optimum at $a = 0.60 > a_{\mathrm{bis}} = 0.368$ (counter-rotation dominates) are shown in Fig. 6.17a and 6.17b, respectively. While in the former case we always have $\omega(t) > 0$ and a Gaussian distribution (see Fig. 6.18a) in the latter case we find a bimodal distribution with one mode fluctuating around a positive angular velocity and one mode fluctuating around a negative angular velocity. This bimodal distribution of $\omega(t)$ is confirmed in various PDFs shown in Fig. 6.18. We interpret this intermittent behavior of the time series as an indication of turbulent bursts originating from the turbulent region in the vicinity of the inner cylinder and penetrating into the stabilized region near the outer cylinder. We find such bimodal behavior for all $a > a_{\mathrm{bis}}$, see Figs. 6.18d–i, whereas for $a < a_{\mathrm{bis}}$ we find a unimodal behavior, see Figs. 6.18a–c. Apart from one case ($a = 0.50$) we do not find any long-time periodicity of the bursts in $\omega(t)$. In future work we will perform a full spectral analysis of long time series of $\omega(t)$ for various a and $\tilde{r}$.

Three-dimensional visualizations of the $\omega(t)$ PDF for all $0 < \tilde{r} < 1$ are provided in Fig. 6.19 for unimodal cases $a < a_{\mathrm{bis}}$ and in Fig. 6.20 for bimodal cases $a > a_{\mathrm{bis}}$. In the latter figure the switching of the system between positive and negative angular velocity becomes visible.

Further details on the two observed individual modes such as their mean and their mixing coefficient are given in Figs. 6.21 for $a = 0.60$ and $a = 0.70$, both well beyond a_{bis}. In both cases one observes that the contribution from the large-ω-mode (red curve, $\omega > 0$, apart from positions close to the outer cylinder) is as expected highest at the inner cylinder and fades away when going outwards, whereas the small-ω-mode has the reverse trend. Note however that even at $\tilde{r} = 0.20$, *e.g.* relatively close to the inner cylinder, there are moments for which ω is negative, *i.e.* patches of stabilized liquids are advected inwards, just as patches of turbulent flow are advected outwards.

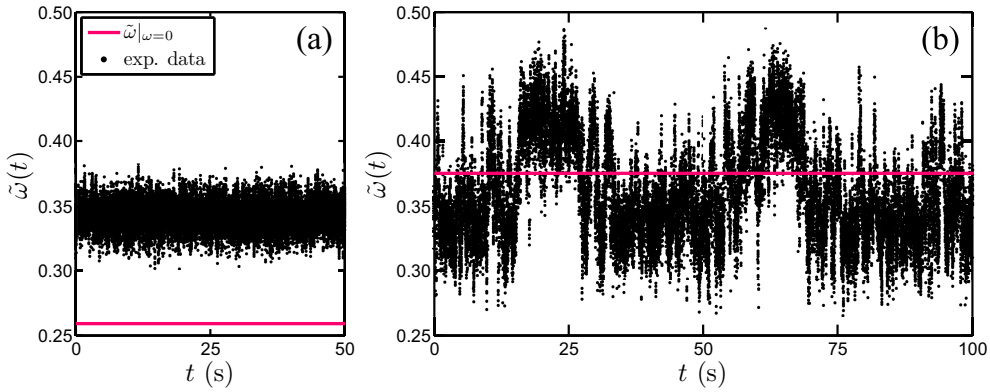

Figure 6.17: Time series of the dimensionless angular velocity $\tilde{\omega}(t)$ as defined in Eq. (6.17) but without t-averaging, acquired with LDA. (a) $a = 0.35$, co-rotation dominates, at $\tilde{r} = 0.60$ with an average data acquisition rate of 456 Hz. (b) $a = 0.60$, counter-rotation dominates, same $\tilde{r} = 0.60$ with an average data acquisition rate of 312 Hz. Figure (a) shows a unimodal velocity distribution whereas Figure (b) reveals a bimodal distribution interpreted as caused by intermittent bursts out of the unstable inner regime with angular velocity between ω_i and $\omega = 0$, *i.e.* $(\omega_o - 0)/(\omega_o - \omega_i) < \tilde{\omega} < 1$ into the stable outer regime with angular velocity between $\omega = 0$ and ω_0, *i.e.* $0 < \tilde{\omega} < (\omega_o - 0)/(\omega_o - \omega_i)$. The solid pink line indicates the neutral line $\omega = 0$, corresponding to $\tilde{\omega} = \omega_o/(\omega_o - \omega_i) = a/(1 + a)$, for the specific a.

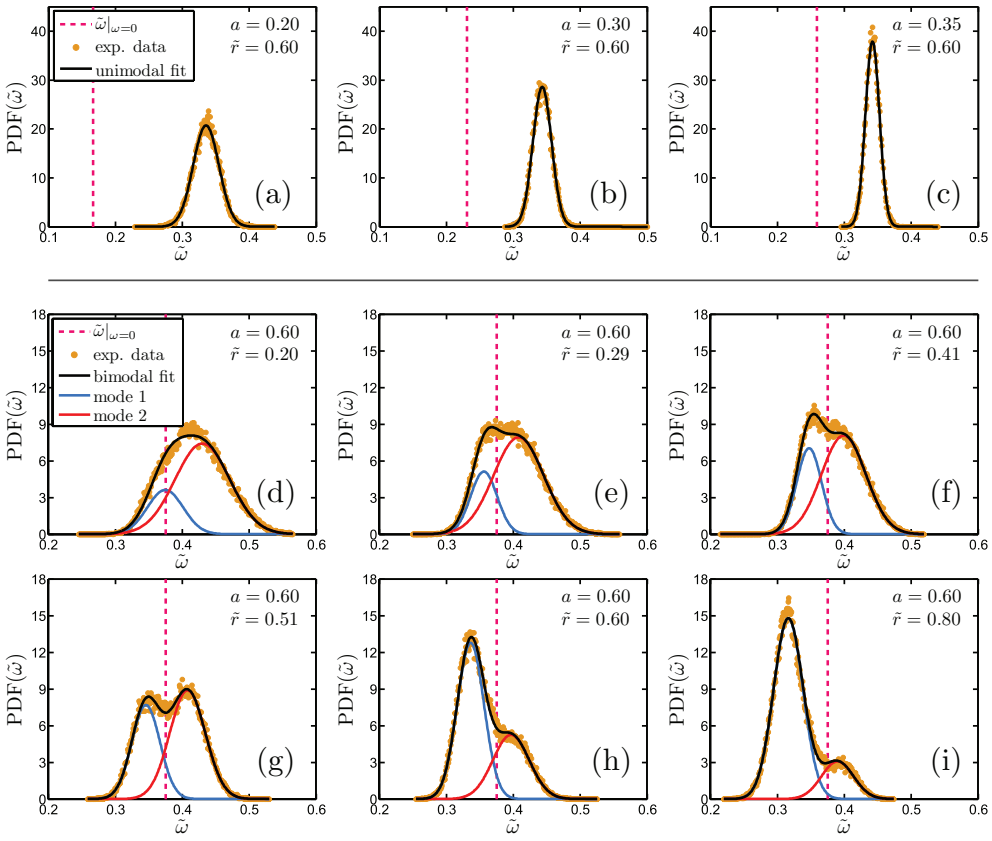

Figure 6.18: Probability density functions of the angular velocity $\tilde{\omega}(t)$ distributions for various cases of a and position $\tilde{r} = (r - r_i)/(r_o - r_i)$. (a) $a = 0.20$, $\tilde{r} = 0.60$, (b) $a = 0.30$, $\tilde{r} = 0.60$, and (c) $a = 0.35$, $\tilde{r} = 0.60$. The other panels all show $a = 0.60$ but at different non-dimensional gap distances $\tilde{r}$. (d) 0.20, (e) 0.29, (f) 0.41, (g) 0.51, (h) 0.60, and (i) 0.80. The gold circles indicate the measured distribution obtained by LDA. While for (a), (b), and (c) one Gaussian distribution (black solid curve) describes the data well, for (e) to (i) a superposition of two Gaussians is needed for a good fit (blue and red curves). We call the two Gaussians the two 'modes' of the flow. The fitting algorithm gives the mean, the standard deviation, and the mixture coefficient of modes 1 and 2, which recombine to the black solid line, describing the measured distribution well. The dashed pink vertical line shows the neutral line $\omega = 0$, implying $\tilde{\omega} = \omega_o/(\omega_o - \omega_i) = a/(1 + a)$.

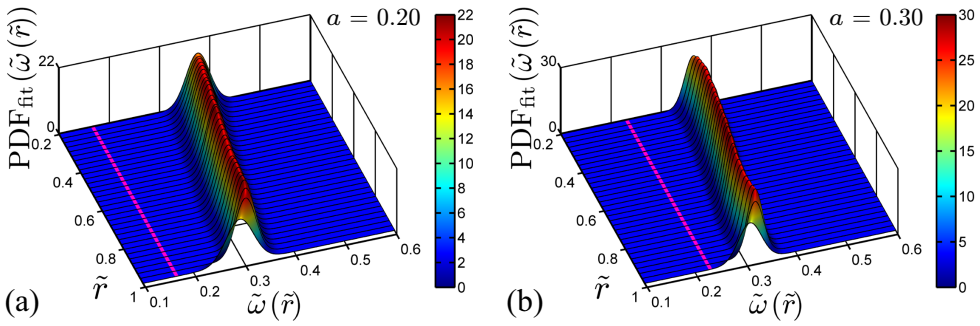

Figure 6.19: Three-dimensional visualization of the (normalized) angular velocity PDF with a contiuous scan of $\tilde{r}$ for two unimodal cases (a) $a = 0.20$ and (b) $a = 0.30$, both being smaller than $a_{\mathrm{bis}} = 0.368$. The pink line corresponds to the neutral line $\omega = 0$, *i.e.* $\tilde{\omega} = \omega_o/(\omega_o - \omega_i) = a/(1 + a)$.

This mechanism resembles the angular velocity exchange mechanism suggested by Ref. [136] just beyond onset of turbulence. These authors suggest that for the counter-rotating case there is an outer region which is centrifugally stable, but subcritically unstable, thus vulnerable to distortions coming from the centrifugally unstable inner region. Inner and outer region are separated by the neutral line. For the low Re of Ref. [136] the inner region is not yet turbulent, but displays interpenetrating spirals, *i.e.* a chaotic flow with various spiral Taylor vortices. For our much larger Reynolds numbers the inner flow will be turbulent and the distortions propagating into the subcritically unstable outer regime will be turbulent bursts. These then will lead to intermittent instabilities in the outer regime. In future work these speculations must further be quantified.

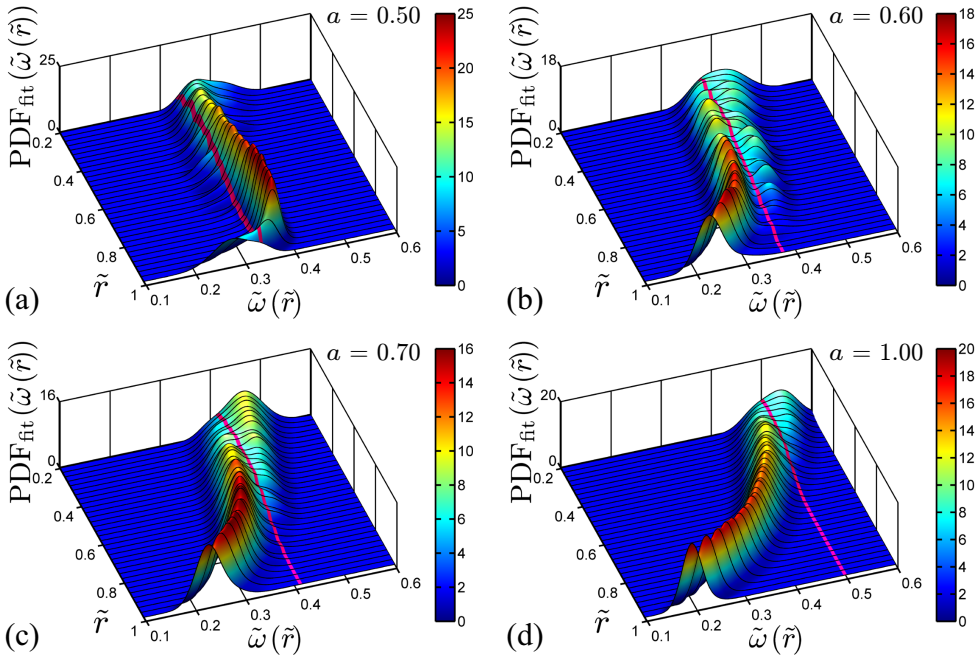

Figure 6.20: Same as in Fig. 6.19, but now for the bimodal cases $a > a_{\mathrm{bis}} = 0.368$. (a) $a = 0.50$, (b) $a = 0.60$, (c) $a = 0.70$, and (d) $a = 1.00$. The bimodal character with one mode being left of the neutral line $\omega = 0$ and the other mode being right of the neutral line becomes particularly clear for (b) and (c).

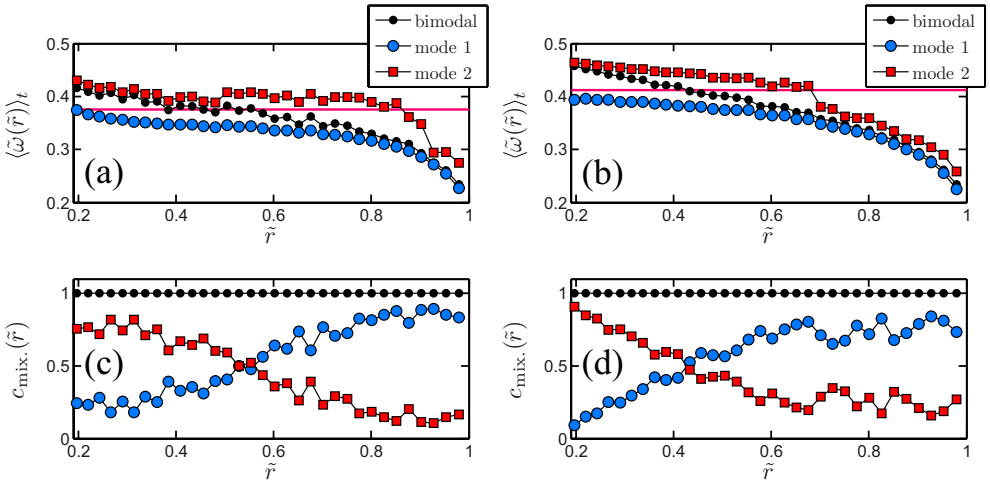

Figure 6.21: (a) The time-averaged, normalized angular velocity $\langle\tilde{\omega}(\tilde{r},t)\rangle_t$ (black symbols) and of the two individual modes (blue and red) for $a = 0.60$. (b) Same as fig. a but for $a = 0.70$. (c) The mixing coefficient $c_{\mathrm{mix.}}(\tilde{r})$ defined as the relative contribution of the area underneath the PDF of the respective individual mode with respect to the total PDF area. (d) Same as fig. c but for $a = 0.70$.

6.6 Summary and discussion

In conclusion, we have experimentally explored strongly turbulent TC flow with $\mathrm{Ta} > 10^{11}$ in the co- and counter-rotating regimes. We find that in this large Taylor number Ta regime and well off the instability lines the dimensionless angular velocity transport flux within experimental precision can be written as $\mathrm{Nu}_\omega(\mathrm{Ta}, a) = f(a) \cdot \mathrm{Ta}^\gamma$ with, within our accuracy, an universal $\gamma = 0.39 \pm 0.03$ for all a. This is the effective scaling exponent of the ultimate regime of TC turbulence predicted by [2] for RB flow and transferred to TC by the close correspondence between RB and TC elaborated in the EGL theory. When starting off counter-rotation, *i.e.* when increasing a beyond zero, the angular velocity flux does not reduce but instead is first further enhanced, due to the enhanced shear, before finally, beyond $a = a_{\mathrm{opt}} \approx 0.33$, the stabilizing effect of the counter-rotation leads to a reduction of the angular velocity transport flux Nu_ω. Around the a_{opt} the mean angular velocity profile was shown to have zero gradient in the bulk for the present large Ta. Despite already significant counter-rotation for $0 < a < a_{\mathrm{opt}}$ there is no neutral line outside the outer BL; furthermore the probability distribution function of the angular velocity has only one mode. For larger a, beyond $a > a_{\mathrm{opt}}$, a neutral line can be detected in the bulk and the PDF here becomes bimodal, reflecting intermittent burst of turbulent patches from the turbulent inner r regime towards the stabilized outer r regime. We offered a hypothesis which gives a unifying view and consistent understanding of all these various findings.

7

Radius ratio dependence°

Taylor-Couette flow with independently rotating inner (i) and outer (o) cylinders is explored numerically and experimentally to determine the effects of the radius ratio η on the system response. Numerical simulations reach Reynolds numbers of up to $\mathrm{Re}_i = 9.5 \cdot 10^3$ and $\mathrm{Re}_o = 5 \cdot 10^3$, corresponding to Ta up to $\mathrm{Ta} = 10^8$ for four different radius ratios $\eta = r_i/r_o$ between 0.5 and 0.909. The experiments, performed in the Twente Turbulent Taylor-Couette ($\mathrm{T}^3\mathrm{C}$) setup, reach Reynolds numbers of up to $\mathrm{Re}_i = 2 \cdot 10^6$ and $\mathrm{Re}_o = 1.5 \cdot 10^6$, corresponding to $\mathrm{Ta} = 5 \cdot 10^{12}$ for $\eta = 0.714 - 0.909$. Effective scaling laws for the torque $J^\omega(\mathrm{Ta})$ are found, which for sufficiently large driving Ta are independent of η. As previously reported for $\eta = 0.714$, optimum transport at a non-zero Rossby number $\mathrm{Ro} = r_i|\omega_i - \omega_o|/[2(r_o - r_i)\omega_o]$ is found in both experiments and numerics. Here $\mathrm{Ro}_{\mathrm{opt}}$ is found to depend on η and Ta. At a driving in the range between $\mathrm{Ta} \approx 3 \cdot 10^8$ and $\mathrm{Ta} \approx 10^{10}$, $\mathrm{Ro}_{\mathrm{opt}}$ saturates to an asymptotic η-dependent value. Theoretical predictions for the asymptotic value of $\mathrm{Ro}_{\mathrm{opt}}$ are compared to the experimental results, and found to differ notably. Furthermore, the local angular velocity profiles from experiments and numerics are compared, and a link between a flat bulk profile and optimum transport for all η is reported.

°Published as: R. Ostilla Mónico **Sander G. Huisman**, Tim. J. G. Jannink, Dennis P.M. van Gils, Roberto Verzicco, Siegfried Grossman, Chao Sun, and Detlef Lohse, *Optimal Taylor-Couette Flow: radius ratio dependence*, J. Fluid. Mech. **747**, 1–29 (2014). Numerical simulations are done by Ostilla Mónico under supervision of Verzicco. Writing of the manuscript about the numerics is done by Ostilla Mónico, experimental part is written by Huisman and Sun. Most of the experiments are performed by Jannink under supervision of Huisman and van Gils. Discussion of the results and proofreading of the manuscript was done by everyone.

7.1 Introduction

Taylor-Couette (TC) flow consists of the flow between two coaxial cylinders that are independently rotating. A schematic drawing of the system can be seen in Fig. 7.1. The rotation difference between the cylinder shears the flow, thus driving the system. This rotation difference has been traditionally expressed by two Reynolds numbers, the inner cylinder $\mathrm{Re}_i = r_i\omega_i d/\nu$ and the outer cylinder $\mathrm{Re}_o = r_o\omega_o d/\nu$ Reynolds numbers, where r_i and r_o are the radii of the inner and outer cylinder, respectively, ω_i and ω_o the inner and outer cylinder angular velocity, $d = r_o - r_i$ the gap width, and ν the kinematic viscosity. The geometry of TC is characterized by two nondimensional parameters, namely the radius ratio $\eta = r_i/r_o$ and the aspect ratio $\Gamma = L/d$. Instead of taking Re_i and Re_o, the driving in TC can alternatively be characterized by the Taylor Ta and a rotation ratio, here chosen to be the Rossby Ro number. The Taylor number can be seen as the non-dimensional forcing (the differential rotation) of the system defined as $\mathrm{Ta} = \sigma(r_o - r_i)^2(r_o + r_i)^2(\omega_o - \omega_i)^2/(4\nu^2)$, or

$$\mathrm{Ta} = \frac{r_a^6 d^2}{r_o^2 r_i^2 \nu^2}(\omega_o - \omega_i)^2. \tag{7.1}$$

Here $\sigma = r_a^4/r_g^4$ with $r_a = (r_o + r_i)/2$ the arithmetic and $r_g = \sqrt{r_o r_i}$ the geometric mean radii. The Rossby number is defined as:

$$\mathrm{Ro} = \frac{|\omega_i - \omega_o| r_i}{2\omega_o d}, \tag{7.2}$$

and can be seen as a measure of the rotation of the system as a whole. Here $\mathrm{Ro} < 0$ corresponds to counter-rotating cylinders, and $\mathrm{Ro} > 0$ to corotating cylinders.

TC is among the most investigated systems in fluid mechanics, mainly owing to its simplicity as an experimental model for shear flows. TC is in addition a closed system, so global balances that relate the angular velocity transport to the energy dissipation can be obtained. Specifically, in Eckhardt, Grossmann & Lohse (2007) [1] (from now on referred to as EGL 2007), an exact relationship between the global parameters and the volume-averaged energy dissipation rate was derived. This relationship has an analogous form to the one that can be obtained for Rayleigh-Bénard (RB) flow, i.e. a flow in which heat is transported from a hot bottom plate to a cold top plate.

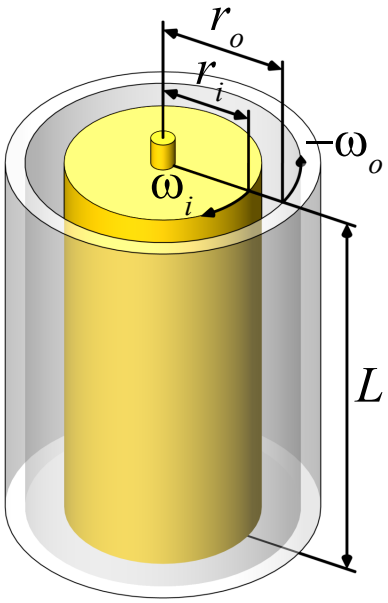

Figure 7.1: Schematic of the Taylor-Couette system. The system consists of two coaxial cylinders, which have an inner cylinder radius of r_i and an outer cylinder radius of r_o. Both cylinders are of length L. The inner cylinder rotates with an angular velocity ω_i and the outer cylinder rotates with an angular velocity of ω_o.

TC and RB flow have been extensively used to explore new concepts in fluid mechanics. Instabilities [137, 19, 109, 138, 139, 140], nonlinear dynamics and chaos [141, 142, 143, 121, 144], pattern formation [18, 20, 145], and turbulence [146, 45, 147, 9, 6, 7] have been studied in both TC and RB, and both numerically and experimentally. The main reasons behind the popularity of these systems are, in addition to the fact that they are closed systems, as mentioned previously, their simplicity due to the high amount of symmetries present. It is also worth noting that plane Couette flow is the limiting case of TC when the radius ratio $\eta = 1$.

Experimental investigations of TC have a long history, dating back to the initial work in the end of the 1800s by [148] in France, who concentrated on outer cylinder rotation and developed the viscometer, and [149] in the United Kingdom, who also rotated the inner cylinder and found indications of turbulence. Later work by [14] and [150], greatly expanded on the system, the former measuring torques and velocities for several radius and rotation ratios in the turbulent case, and the latter being the first to mathematically describe the cells which form if the flow is linearly unstable. The subject can be traced back further to Stokes, and even further to Newton. For a broader historical context, we refer the reader to [151].

Experimental work continued during the years [31, 18, 152, 9, 8, 10, 21, 26, 27, 64] at low and high Ta numbers and for different ratios of the rotation frequencies $a = -\omega_o/\omega_i$; thus a is positive for counter-rotation and negative for co-rotation. Here $-a \equiv \mu$, another measure used for the ratio of rotation frequencies. This work has been complemented by numerical simulations, not only in the regime of pure inner cylinder rotation [153, 136, 53, 154, 155], but also for eigenvalue study [156], and counter-rotation at fixed a [154]. Recently [56, 55], simulations have also explored the effect of the outer cylinder rotation on the system at large Reynolds numbers.

The recent experiments [21, 26, 27, 69] and simulations [56, 55] have shown that at fixed Ta an optimal angular momentum transport is obtained at *non-zero* a_{opt}, and that the location of this maximum a_{opt} varies with Ta. However, both experiments and simulations have been restricted to two radius ratios, namely $\eta = 0.5$ and $\eta = 0.714$. The same radius ratios were also used for studies carried out on scaling laws of the torque and the 'wind' of turbulence at highly turbulent Taylor numbers [10, 27, 26, 64, 69]. Up to now, it is not clear how the radius ratio affects the scaling laws of the system response or the recently found phenomena of optimal transport as a function of Ta.

Two suggestions were made to account for the radius ratio dependence of

optimal transport. Van Gils et. al (2011b) [26] wondered whether the optimal transport in general lies in or at least close to the Voronoi boundary (meaning a line of equal distance) of the Esser-Grossmann stability lines [17] in the $(\mathrm{Re}_o, \mathrm{Re}_i)$ phase space as it does for $\eta = 0.714$. However, this bisector value does not give the correct optimal transport for $\eta = 0.5$ [69, 157]. Therefore [56] proposed a dynamic extension of the Esser-Grossmann instability theory. This model correctly gives the observed optimal transport (within experimental error bars) between $\eta = 0.5$ and $\eta = 0.714$ for three experimental datasets [14, 27, 26] and one numerical data set [157], but it is not clear how it performs outside the η-range $[0.5, 0.714]$.

In this chapter, we study the following questions. How does the radius ratio η affect the flow? How are the scaling laws of the angular momentum transport affected? What is the role of the geometric parameter called pseudo-Prandtl number σ introduced in EGL07? Can the effect of the radius ratio be interpreted as a kind of non-Oberbeck-Boussinesq effect, analogous to this effect in Rayleigh-Bénard flow? Finally, are the predictions and insights of [26], [55] and [157] on the optimal transport also valid for other values of η?

In order to answer these questions, both direct numerical simulations (DNS) and experiments have been undertaken. Numerical simulations, with periodic axial boundary conditions, have been performed using the finite-difference code previously used in [55]. In these simulations, three more values of η have been investigated: one in which the gap is larger ($\eta = 0.5$), and two in which the gap is smaller ($\eta = 0.833$ and 0.909). With the previous simulations from [55] at $\eta = 0.714$, a total of four radius ratios has been analyzed.

In both experiments and numerics, only one aspect ratio Γ has been studied for every radius ratio. Since the work of [158] it is known that multiple flow states with a different amount of vortex pairs can coexist in TC for the same non-dimensional flow parameters. However, with increased driving, the bifurcations become less important and many branches do not survive. Indeed, [10] found that for pure inner cylinder rotation only one branch with 8 vortices (for $\Gamma = 11.4$ and $\eta = 0.714$) remains when Re_i is increased above $2 \cdot 10^4$. As the Reynolds numbers reached in the experiments greatly exceed this value we do not expect to see the effect of multiple states in the current experimental results.

For the numerical simulations, axially periodic boundary conditions have been taken. [56] already studied the effect of the axial periodicity length on the system, and found that for a fixed vortical wavelength, the number of vortices does not affect the overall flow behaviour. It was also found that, in analogy

to experiments, the effect of vortical wavelength, and hence of multiple states, becomes smaller with increased driving. However, changes between states can still be seen for small drivings.
Figure 7.2 shows the (Ta,1/Ro) parameter space explored in the simulations for the four selected values of the radius ratio η. A higher density of points has been used in places where the global response (Nu_ω, Re_w) of the flow shows more variation with the control parameters Ta and 1/Ro. A fixed aspect ratio of $\Gamma = 2\pi$ has been taken for all simulations, and axially periodic boundary conditions have been used. These simulations have the same upper bounds of Ta (or Re_i) as the ones of [55].
In addition to these simulations, experiments have been performed with the Twente Turbulent Taylor-Couette (T^3C) facility, with which we achieve larger Ta numbers. Details of the setup are given in [21]. Once again, four values of η have been investigated, but, due to experimental constraints, we have been limited to investigate only smaller gap widths, *i.e.* values $\eta \geq 0.716$, namely $\eta = 0.716$, 0.769, 0.833, and 0.909. The experimentally explored parameter spaces are shown in Fig. 7.3.

7.2 Numerical method

In this section, the numerical method used is explained in some detail. The rotating frame in which the Navier-Stokes equations are solved and the employed non-dimensionalizations are introduced in the first subsection. This is followed by detailing the spatial resolution checks that have been performed.

7.2.1 Code description

The employed code is a finite difference code, which solves the Navier-Stokes equations in cylindrical coordinates. A second-order spatial discretization is used, and the equations are advanced in time by a fractional time integration method. This code is based on the so-called Verzicco code, whose numerical algorithms are detailed in [159]. A combination of MPI and OpenMP directives are used to achieve large-scale parallelization. This code has been extensively used for Rayleigh-Bénard flow; for recent simulations see [160, 161]. In the context of TC flow, [55] have already validated the code for $\eta = 0.714$.

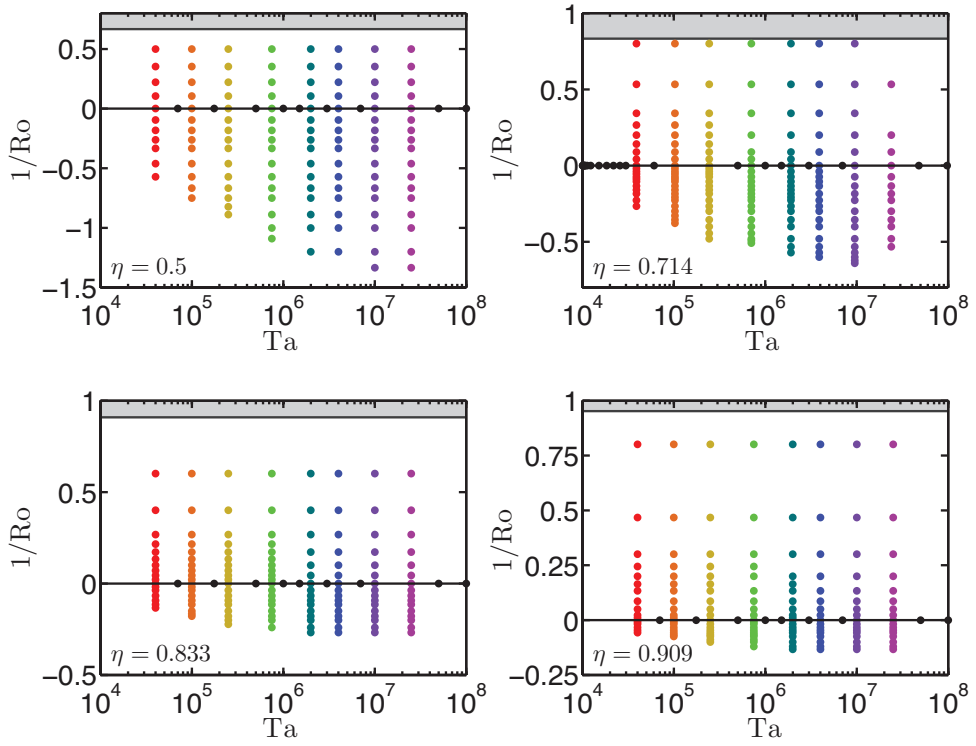

Figure 7.2: The control parameter phase space that was numerically explored in this chapter in the (Ta, 1/Ro) representation. From top-left to bottom-right: $\eta = 0.5$, 0.714, 0.833 and 0.909. Here $\Gamma = 2\pi$ was fixed, and axial periodicity was employed. The grey shaded area signals boundary conditions for which the angular momentum $L = r^2\omega$ of the outer cylinder (L_o) is larger than the angular momentum of the inner cylinder (L_i). This causes the flow to have an overall transport of angular momentum towards the inner cylinder. In this region, the Rayleigh stability criterium applies, which states that if $dL^2/dr > 0$ the flow is linearly stable to axisymmetric perturbations.

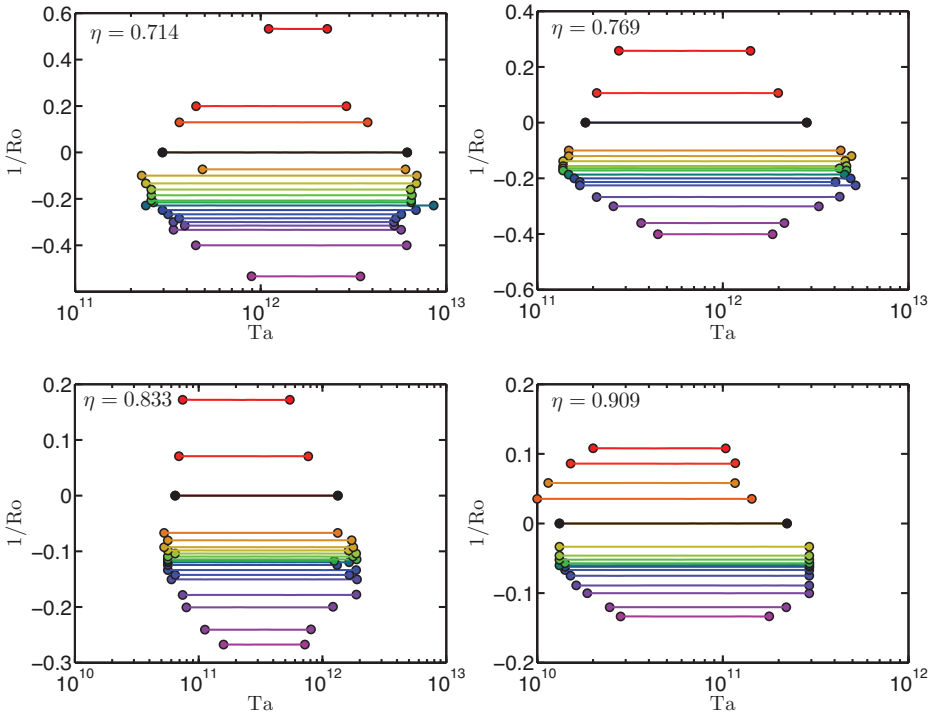

Figure 7.3: Control parameter phase space which was explored in experiments in the (Ta, Ro^{-1}) representation for $\eta = 0.716$ (top-left), $\eta = 0.769$ (top-right), $\eta = 0.833$ (bottom-left) and $\eta = 0.909$ (bottom-right).

The flow was simulated in a rotating frame, which was chosen to rotate with $\Omega = \omega_o \boldsymbol{e}_z$. This was done in order to simplify the boundary conditions. In that frame the outer cylinder is stationary for any value of a, while the inner cylinder has an azimuthal velocity of $u_\theta(r = r_i) = r_i(\omega_i^\ell - \omega_o^\ell)$, where the superscripts ℓ denote variables in the lab frame, while no superscript denotes variables in the rotating frame. We then choose the inner cylinder rotation rate in the rotating frame as the characteristic velocity of the system $U \equiv |u_\theta(r_i)| = r_i|\omega_i - \omega_o|$ and the characteristic length scale d to non-dimensionalize the equations and boundary conditions.
Using this non-dimensionalization, the inner cylinder velocity boundary condition simplifies to: $\hat{u}_\theta(r = r_i) = \mathrm{sgn}(\omega_i - \omega_o)$. In this chapter, $\omega_i - \omega_o$ is always positive. Thus, in this rotating frame the flow geometry is simplified to a pure inner cylinder rotation with the boundary condition $\hat{u}_\theta(r_i) = 1$. The outer cylinder's effect on the flow is felt as a Coriolis force in this rotating frame of reference. The Navier-Stokes equations then read:

$$\frac{\partial \hat{\boldsymbol{u}}}{\partial \hat{t}} + \hat{\boldsymbol{u}} \cdot \hat{\nabla}\hat{\boldsymbol{u}} = -\hat{\nabla}\hat{p} + \left(\frac{f(\eta)}{\mathrm{Ta}}\right)^{1/2} \hat{\nabla}^2 \hat{\boldsymbol{u}} + \mathrm{Ro}^{-1} \boldsymbol{e}_z \times \hat{\boldsymbol{u}}, \tag{7.3}$$

where Ro was defined previously in Eq. 7.2, and $f(\eta)$ is

$$f(\eta) = \frac{(1+\eta)^3}{8\eta^2}. \tag{7.4}$$

It is useful to continue the non-dimensionalization by defining the normalized radius $\tilde{r} = (r - r_i)/d$ and the normalized height $\tilde{z} = z/d$. We define the time- and azimuthally averaged velocity field as:

$$\hat{\bar{\boldsymbol{u}}}(r, z) = \langle \hat{\boldsymbol{u}}(\theta, r, z, t) \rangle_{\theta,t}, \tag{7.5}$$

where $\langle \phi(x_1, x_2, ..., x_n) \rangle_{x_i}$ indicates averaging of the field ϕ with respect to x_i. To quantify the torque in the system, we first note that the angular velocity current

$$J^\omega = r^3(\langle u_r^\ell \omega^\ell \rangle_{\theta,z,t} - \nu \partial_r \langle \omega^\ell \rangle_{\theta,z,t}) \tag{7.6}$$

is conserved, *i.e.* independent on the radius r (EGL 2007). Here J^ω represents the current of angular velocity from the inner cylinder to the outer cylinder (or vice versa). The first term is the convective contribution to the transport, while the second term is the diffusive contribution.
In the state with the lowest driving, and ignoring end plate effects, a laminar, time independent velocity field which is purely azimuthal, $u_\theta^\ell(r) = Ar + B/r$,

with $u_r = u_z = 0$, is induced by the rotating cylinders. This laminar flow produces an angular velocity current J_0^ω, which can be used to nondimensionalize the angular velocity current,

$$\mathrm{Nu}_\omega = \frac{J^\omega}{J_0^\omega}. \tag{7.7}$$

Nu_ω can be seen as an angular velocity 'Nusselt' number.
When J^ω, and therefore Nu_ω are calculated numerically, the values will depend on the radial position, owing to finite time averaging. We can define Δ_J to quantify this radial dependence as:

$$\Delta_J = \frac{\max(J^\omega(r)) - \min(J^\omega(r))}{\langle J^\omega(r)\rangle_r} = \frac{\max(\mathrm{Nu}_\omega(r)) - \min(\mathrm{Nu}_\omega(r))}{\langle \mathrm{Nu}_\omega(r)\rangle_r} \tag{7.8}$$

which analytically equals zero for infinite time but will deviate when calculated numerically for finite time.
The convective dissipation per unit mass can be calculated from its definition as a volume average of the local dissipation rate for an incompressible fluid,

$$\varepsilon_u = \epsilon_u^\ell = \frac{\nu}{2}\left\langle (\partial_i^\ell u_j + \partial_j^\ell u_i)^2 \right\rangle_{V,t}, \tag{7.9}$$

or a global balance can be used. The exact relationship (EGL 2007)

$$\epsilon_u^\ell - \epsilon_{u,0}^\ell = \frac{\nu^3}{d^4}\sigma^{-2}\mathrm{Ta}(\mathrm{Nu}_\omega - 1), \tag{7.10}$$

where $\epsilon_{u,0}$ is the volume averaged dissipation rate in the purely azimuthal laminar flow, links the volume-averaged dissipation to the global driving Ta and response Nu_ω.
This link can be and has been used for code validation and for checking spatial resolution adequateness. The volume-averaged dissipation can be calculated from both (7.9) and (7.10) and later checked for sufficient agreement. We define the quantity Δ_ϵ as the relative difference between the two ways of numerically calculating the dissipation, namely either via Nu_ω with eq. 7.10 or directly from the velocity gradients, eq. 7.9:

$$\Delta_\epsilon = \frac{\nu^3 d^{-4}\sigma^{-2}\mathrm{Ta}(\mathrm{Nu}_\omega - 1) + \epsilon_{u,0} - \frac{\nu}{2}\left\langle (\partial_i u_j^\ell + \partial_j^\ell u_i)^2 \right\rangle_{V,t}}{\frac{\nu}{2}\left\langle (\partial_i^\ell u_j + \partial_j^\ell u_i)^2 \right\rangle_{V,t}}. \tag{7.11}$$

Δ_ϵ is equal to 0 analytically, but will deviate when calculated numerically. The deviation of Δ_J and Δ_ϵ from zero is an indication of the adequateness of the resolution.

We would like to emphasize that the requirement for $\Delta_J < 0.01$ is much stricter than torque balance, which can simply be expressed as $\mathrm{Nu}_\omega(r_i) = \mathrm{Nu}_\omega(r_o)$. As analyzed in [55], a value of less than 1% for Δ_J and about 1% for Δ_ϵ is linked to grid adequateness at the Taylor number simulated. To ensure convergence in time, the time averages of the Nusselt number and the energy dissipation calculated locally (equation 7.9) were also checked to converge in time within 1%.

7.2.2 Resolution checks

Spatial resolution checks were performed in two ways. First, as mentioned previously, the values of Δ_J and Δ_ϵ were checked. As an additional check, simulations at selected values of Ta were performed at a higher resolution. As the explored parameter space is large, these checks were performed only for the highest value of Ta simulated for the grid size. A lower driving of the flow for the same grid size is expected to have a smaller error due to spatial discretization, as spatial discretization errors increase with increased Re, and thus increased Ta.

Concerning the temporal resolution there are numerical and physical constraints; the former requires a time step small enough to keep the integration scheme stable and this is achieved by using an adaptive time step based on a Courant-Frederich-Lewy (CFL) criterium. The third-order Runge-Kutta time-marching algorithm allows for a CFL of up to $\sqrt{3}$, but this can be reduced due to the implicit factorization of the viscous terms. For safety, the maximum CFL has been taken as 1.4. From the physical point of view, the time step size must also be small enough to properly describe the fast dynamics of the smallest flow scale which is the Kolmogorov scale. Although the time step size should be determined by the most restrictive among the two criteria above, our experience suggests that as long as the CFL number criterion is satisfied, which guarantees numerical stability, the results become insensitive to the time step size and all the flow scales are adequately described temporally. Direct confirmation of this statement can be found in [55].

The results for $\eta = 0.5$, 0.833, and 0.909 are presented in Table 7.1. Uniform discretization was used in azimuthal and axial directions. In the radial direc-

tion, points were clustered near the walls by using hyperbolic tangent-type clustering, or a clipped Chebychev type clustering for higher values of Ta. A table including the results for the spatial resolution tests at $\eta = 0.714$ can be found in [55].

7.3 Experimental setup

The T^3C apparatus has been built to obtain high Ta numbers. It has been described in detail in [21] and [41]. The inner cylinder with outside radius $r_i = 0.200$ m consists of three sections. The total height of those axially stacked sections is $L = 0.927$ m. We measure the torque only on the middle section of the inner cylinder, which has a height of $L_{\mathrm{mid}} = 0.536$ m, to reduce the effect of the torque losses at the end-plates in our measurements. This approach has already been validated in [41]. The transparent outer cylinder is made of acrylic and has an inside radius of $r_o = 0.2794$ m. We vary the radius ratio by reducing the diameter of the outer cylinder by adding a 'filler' that is fixed to the outer cylinder and sits between the inner and the outer cylinder, effectively reducing r_o while keeping r_i fixed. We have 3 fillers giving us 4 possible outer radii: $r_o = 0.279$ m (without any filler), 0.26 m, 0.24 m, and 0.22 m, giving experimental access to $\eta = 0.716$, 0.769, 0.833, and 0.909, respectively. Note that by reducing the outer radius, we not only change η, but also change $\Gamma = L/(r_o - r_i)$ from $\Gamma(\eta = 0.716) = 11.68$ to $\Gamma(\eta = 0.909) = 46.35$.
For high Ta the heating up of the system becomes apparent and it has to be actively cooled in order to keep the temperature constant. We cool the working fluid (water) from the top and bottom end plates and maintain a constant temperature within ± 0.5 K throught both the spatial extent and the time run of the experiment. The setup has been constructed in such a way that we can rotate both cylinders independently while keeping the setup cooled.
As said before, we measure the torque on the middle inner cylinder. We do this by measuring the torque that is transferred from the axis to the cylinder by using a load-cell that is inside the aforementioned cylinder. Torque measurements are performed using a fixed procedure. The inner cylinder is spun up to its maximum rotational frequency of 20 Hz and kept there for several minutes. Then the system is brought to rest. The cylinders are then brought to their initial rotational velocities (with the chosen 1/Ro), corresponding to a velocity for which the torque is accurate enough; generally of order 2–3 Hz. We then

η	Ta	$N_\theta \times N_r \times N_z$	Nu_ω	$100\Delta_J$	$100\Delta_\epsilon$	Case
0.5	$2.5 \cdot 10^5$	$100 \times 100 \times 100$	2.03372	0.30	1.11	R
0.5	$2.5 \cdot 10^5$	$150 \times 150 \times 150$	2.03648	0.76	0.89	E
0.5	$7.5 \cdot 10^5$	$150 \times 150 \times 150$	2.56183	0.47	0.92	R
0.5	$7.5 \cdot 10^5$	$256 \times 256 \times 256$	2.55673	0.74	0.31	E
0.5	$1 \cdot 10^7$	$300 \times 300 \times 300$	4.23128	0.33	1.07	R
0.5	$1 \cdot 10^7$	$400 \times 400 \times 400$	4.22574	0.97	1.06	E
0.5	$2.5 \cdot 10^7$	$350 \times 350 \times 350$	5.07899	0.85	1.12	R
0.5	$2.5 \cdot 10^7$	$512 \times 512 \times 512$	5.08193	0.87	1.98	E
0.5	$5 \cdot 10^7$	$768 \times 512 \times 1536$	6.08284	0.45	1.56	R
0.5	$1 \cdot 10^8$	$768 \times 512 \times 1536$	7.48561	1.46	0.88	R
0.833	$2.5 \cdot 10^5$	$180 \times 120 \times 120$	2.72293	0.21	0.76	R
0.833	$2.5 \cdot 10^5$	$300 \times 180 \times 180$	2.72452	0.29	0.29	E
0.833	$1 \cdot 10^7$	$384 \times 264 \times 264$	7.07487	0.29	0.61	R
0.833	$1 \cdot 10^7$	$512 \times 384 \times 384$	7.17245	0.13	1.16	E
0.833	$2.5 \cdot 10^7$	$512 \times 384 \times 384$	8.62497	0.71	1.05	R
0.833	$2.5 \cdot 10^7$	$768 \times 576 \times 576$	8.51678	0.90	1.26	E
0.833	$5 \cdot 10^7$	$512 \times 384 \times 384$	9.68437	0.26	2.92	R
0.833	$1 \cdot 10^8$	$768 \times 576 \times 576$	11.4536	0.89	2.29	R
0.909	$2.5 \cdot 10^5$	$180 \times 120 \times 120$	2.31902	0.16	0.91	R
0.909	$2.5 \cdot 10^5$	$300 \times 200 \times 200$	2.30810	0.07	0.17	E
0.909	$2 \cdot 10^6$	$256 \times 180 \times 180$	3.76826	0.55	0.49	R
0.909	$2 \cdot 10^6$	$384 \times 256 \times 256$	3.77532	0.39	0.21	E
0.909	$2.5 \cdot 10^7$	$384 \times 256 \times 256$	7.83190	0.43	3.15	R
0.909	$2.5 \cdot 10^7$	$450 \times 320 \times 320$	7.86819	0.81	2.07	E
0.909	$5 \cdot 10^7$	$2305 \times 400 \times 1536$	9.74268	0.46	1.02	R
0.909	$1 \cdot 10^8$	$2305 \times 400 \times 1536$	11.3373	0.57	1.06	R

Table 7.1: Resolution tests for $\Gamma = 2\pi$ and $\eta = 0.5$, 0.833, and 0.909. The columns display the radius ratio, the Taylor number, the resolution employed, the calculated Nu_ω, the relative discrepancies Δ_J and Δ_ϵ, and finally the 'case': resolved (R) and error (E) reference. Here Δ_ϵ is positive, and exceeds the 1% threshold reported in [55] for some cases at the largest η, but even so resolution appears to be sufficient as variations of Nu_ω are small.

slowly increase both velocities over 3 to 6 hours to their final velocities while maintaining 1/Ro fixed during the entire experiment. During this velocity ramp we continuously acquire the torque of this quasi-stationary state. The calibration of the system is done in a similar way; first we apply the maximum load on the system, going back to zero load, and then gradually adding weight while recording the torque. These procedures ensure that hysteresis effects are kept to a minimum, and that the system is always brought to the same state before measuring. More details about the setup can be found in [21].
Local velocity measurements are done by laser Doppler anemometry (LDA). We measure the azimuthal velocity component by focusing two beams in the radial-azimuthal plane. We correct for curvature effects of the outer cylinder by using a ray tracer, see [91]. The velocities are measured at midheight ($z = L/2$) unless specified otherwise. For every measurement position we measured long enough such as to have a statistically stationary result, for which about 10^5 samples were required for every data point. This ensured a statistical convergence of $< 1\%$.

7.4 Global response: Torque

In this section, the global response of the TC system for the four simulated radius ratios is presented. This is done by measuring the scaling law(s) of the non-dimensional torque Nu_ω as functions of Ta. The transition between different types of local scaling laws in different Ta-ranges is investigated, and related to previous simulations [55] and experiments [41].

7.4.1 Pure inner cylinder rotation

The global response of the system is quantified by Nu_ω. By definition, for purely azimuthal laminar flow, $\mathrm{Nu}_\omega = 1$. Once the flow is driven stronger than a certain critical Ta, large roll structures appear, which enhance angular transport through a large scale wind.
Figure 7.4 shows the response of the system for increasing Ta in the case of pure inner cylinder rotation for four values of η. Experimental and numerical results are shown in the same panels, covering different ranges, and thus complementary, but consistent with, each other. Numerical results for $\eta = 0.714$ from [162] have been added to both panels.

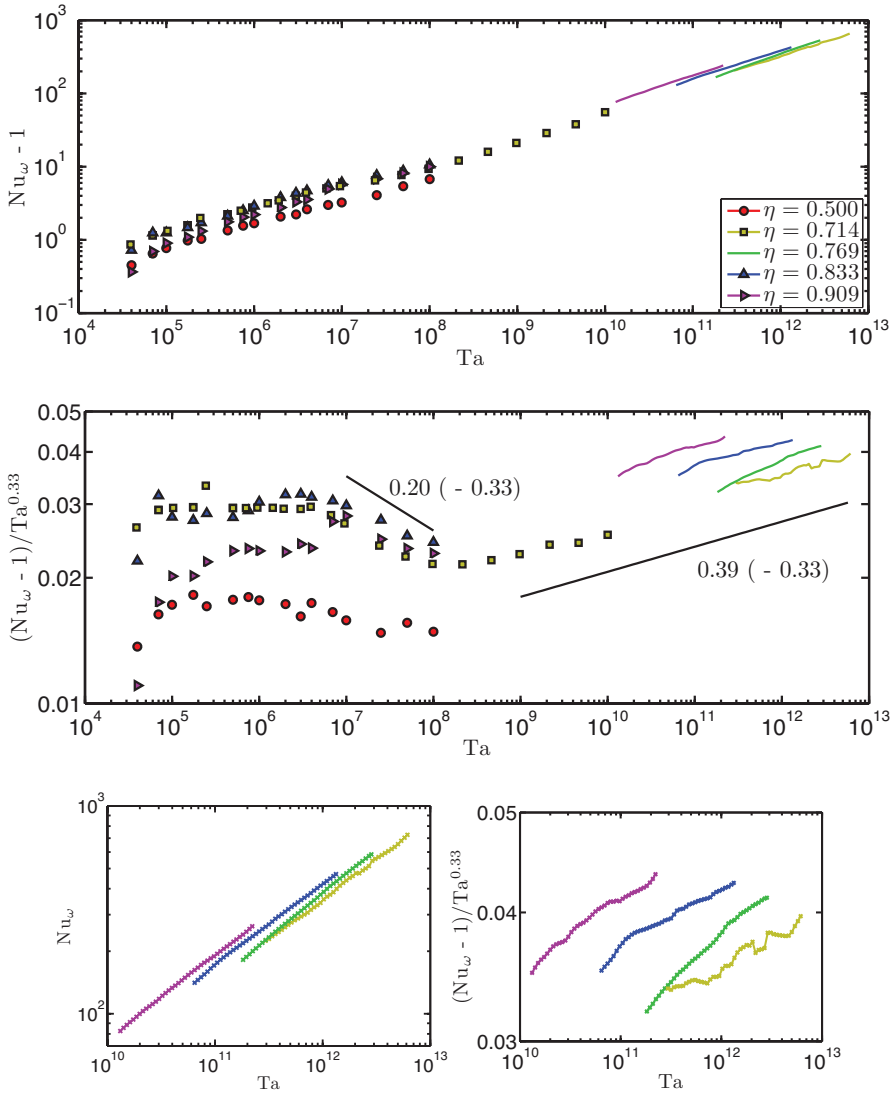

Figure 7.4: The global system response for pure inner cylinder rotation as function of the driving Ta: The top panel shows $\mathrm{Nu}_\omega - 1$ vs Ta for both simulations (points) and experiments (lines). Numerical data from [162] for $\eta = 0.714$ have been added to these figures. The second panel shows the compensated Nusselt versus Ta, with added lines with scaling laws $\mathrm{Ta}^{0.20}$ and $\mathrm{Ta}^{0.39}$ to guide the eye. The bottom two panels show a zoom-in of the experimental data.

As has already been noticed in [55] for $\eta = 0.714$, a change in the local scaling law relating Ta to Nu_ω occurs at around $\mathrm{Ta} \approx 3 \cdot 10^6$. We can interpret these changes in the same way as [55] and relate the transition in the Ta-Nu_ω local scaling law to the break up of coherent structures. A large jump in Nu_ω can be seen around $\mathrm{Ta} \approx 5 \cdot 10^6$ for $\eta = 0.909$, which corresponds to a change in the number of rolls. The system goes from two pairs of rolls to three pairs of rolls.

It is also worth mentioning that the exponent in the local scaling laws in the regime before the transition depends on the radius ratio. This can be seen in the compensated plot, and explains the curve crossings that we see in the graphs.

For experiments (solid lines of figure 7.4), a different local scaling law can be seen. In this case the experiments are performed at much higher Ta than the simulations. The scaling $\mathrm{Nu}_\omega \sim \mathrm{Ta}^{0.38}$ can be related to the so called 'ultimate' regime, a regime where the boundary layers have become completely turbulent [2, 46, 89]. As indicated for the case at $\eta = 0.714$ we expect that for increasing Ta also the simulations become turbulent enough to reach this scaling law (cf. [162]). In this regime, the local scaling law relating Ta and Nu_ω has no dependence on η and thus is universal (apart from a different prefactor).

In the experiments with large Ta, the value of η corresponding to the smallest gap, *i.e.* $\eta = 0.909$, has the highest angular velocity transport (Nu_ω) at a given Ta. This can be phrased in terms of the pseudo-Prandtl-number σ, introduced in EGL2007. As a smaller gap means a smaller σ, we thus find a decrease of Nu_ω with increasing σ, for the drivings explored in experiments, similarly as predicted [127] and found [163] for Nu(Pr) in RB convection for $\mathrm{Pr} > 1$.

7.4.2 Rossby-number dependence

In this subsection, the effect of outer cylinder rotation on angular velocity transport will be studied. Previous experimental and numerical work at $\eta = 0.714$ [27, 26, 55, 164] revealed the existence of an optimum transport where, for a given Ta, the transport of momentum is highest at a Rossby number $\mathrm{Ro}_{\mathrm{opt}}^{-1}$, which depends on Ta and saturates around $\mathrm{Ta} \approx 10^{10}$. In this subsection, this work will be extended to the other values of η.

Figures 7.5 and 7.6 show the results of the numerical exploration of the Ro^{-1} parameter space between $\mathrm{Ta} = 4 \cdot 10^4$ and $\mathrm{Ta} = 2.5 \cdot 10^7$. The shape of

$\mathrm{Nu}_\omega = \mathrm{Nu}_\omega(\mathrm{Ro}^{-1})$ curves and the position of $\mathrm{Ro}_{\mathrm{opt}}^{-1}$ depends very strongly on η in the Ta range studied in numerics. For the largest gap (*i.e.*, $\eta = 0.5$), the optimum can be seen to be in the counter-rotating range (*i.e.*, $\mathrm{Ro}^{-1} < 0$) as long as Ta is high enough. On the other hand, for the smallest gap (*i.e.*, $\eta = 0.909$), the optimum is at co-rotation (i.e., $\mathrm{Ro}^{-1} > 0$) in the whole region studied. The other values of studied η reveal an intermediate behavior. Optimum transport is located for co-rotation at lower values of Ta and slowly moves towards counter-rotation. For all values of η, when the driving is increased, $\mathrm{Ro}_{\mathrm{opt}}^{-1}$ tends to shift to more negative values.
For two values of Ta ($\mathrm{Ta} = 4 \cdot 10^6$ and $\mathrm{Ta} = 10^7$) for a radius ratio $\eta = 0.5$, two distinct peaks can be seen in the $\mathrm{Nu}_\omega(\mathrm{Ro}^{-1})$ curve. This can be understood by looking at the flow topology. For $\mathrm{Ro}^{-1} = 0$, three distinct rolls can be seen. However, when decreasing Ro^{-1}, the rolls begin to break up. Someremnants of large-scale structures can be seen, but these are weaker than in the $\mathrm{Ro}^{-1} = 0$ case. Having a large-scale roll helps the transport of angular momentum, leading to the peak in Nu_ω at $\mathrm{Ro}^{-1} = 0$. Further increasing the driving causes the rolls to also break up for $\mathrm{Ro}^{-1} = 0$, and eliminates the anomalous peak.
The shift seen in the numerics may or may not continue with increasing Ta. The experiments conducted explore a parameter space of $10^{10} < \mathrm{Ta} < 10^{13}$ and thus serve to explore the shift at higher driving. Figure 7.7 presents the obtained results. The left panel shows Nu_ω versus Ta for all measurements. The right panel shows the exponent γ, obtained by fitting a least-square linear fit in the log-log plots. Across the η and Ro^{-1} range studied, the average exponent is $\gamma \approx 0.39$. This value is used in figure 7.8 to compensate Nu_ω. The flat appearance of all data points reflects the good scaling and the universality of this ultimate scaling behaviour $\mathrm{Nu}_\omega \propto \mathrm{Ta}^{0.39}$.
To determine the optimal rotation ratio for the experimental data, a Ta-averaged compensated Nusselt $\langle \mathrm{Nu}_\omega/\mathrm{Ta}^{0.39} \rangle_{\mathrm{Ta}}$ was used. This is defined as:

$$\langle \mathrm{Nu}_\omega/\mathrm{Ta}^{0.39} \rangle_{\mathrm{Ta}} = \frac{1}{\mathrm{Ta}_{\mathrm{max}} - \mathrm{Ta}_{\mathrm{co}}} \int_{\mathrm{Ta}_{\mathrm{co}}}^{\mathrm{Ta}_{\mathrm{max}}} \mathrm{Nu}_\omega/\mathrm{Ta}^{0.39} d\mathrm{Ta}, \tag{7.12}$$

where $\mathrm{Ta}_{\mathrm{max}}$ is the maximum value of Ta for every (η, Ro^{-1}) dataset, and $\mathrm{Ta}_{\mathrm{co}}$ is a cut-off Ta number used for the larger η ($\mathrm{Ta}_{\mathrm{co}} = 2 \cdot 10^{11}$ for $\eta = 0.833$ and $\mathrm{Ta}_{\mathrm{co}} = 3 \cdot 10^{10}$ for $\eta = 0.909$) to exclude the initial part of the $\mathrm{Nu}_\omega/\mathrm{Ta}^{0.39}$ data points which seem to have a different scaling for some of the values of Ro^{-1} explored. For the smaller values of η, $\mathrm{Ta}_{\mathrm{co}} = \mathrm{Ta}_{\mathrm{min}}$, the minimum value of Ta for every (η, Ro^{-1}) dataset. An error bar on this average is estimated as one standard deviation of the data from the computed average.

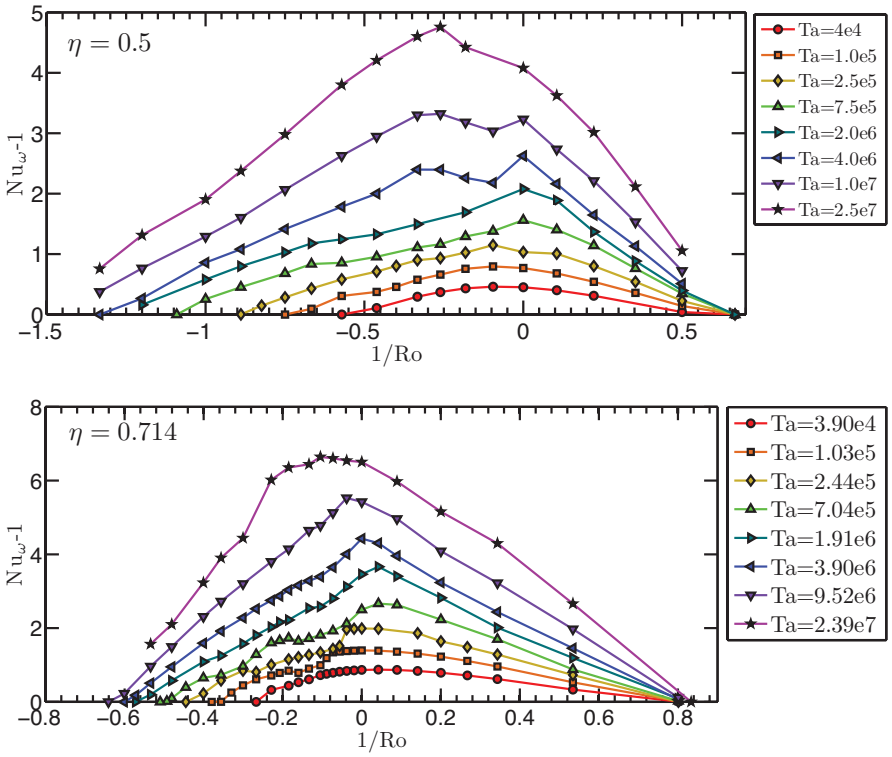

Figure 7.5: $\mathrm{Nu}_\omega - 1$ versus Ro^{-1} for $\eta = 0.5$ and $\eta = 0.714$ studied numerically. The shape of the curve and the position of the maximum depend very strongly on both Ta and η.

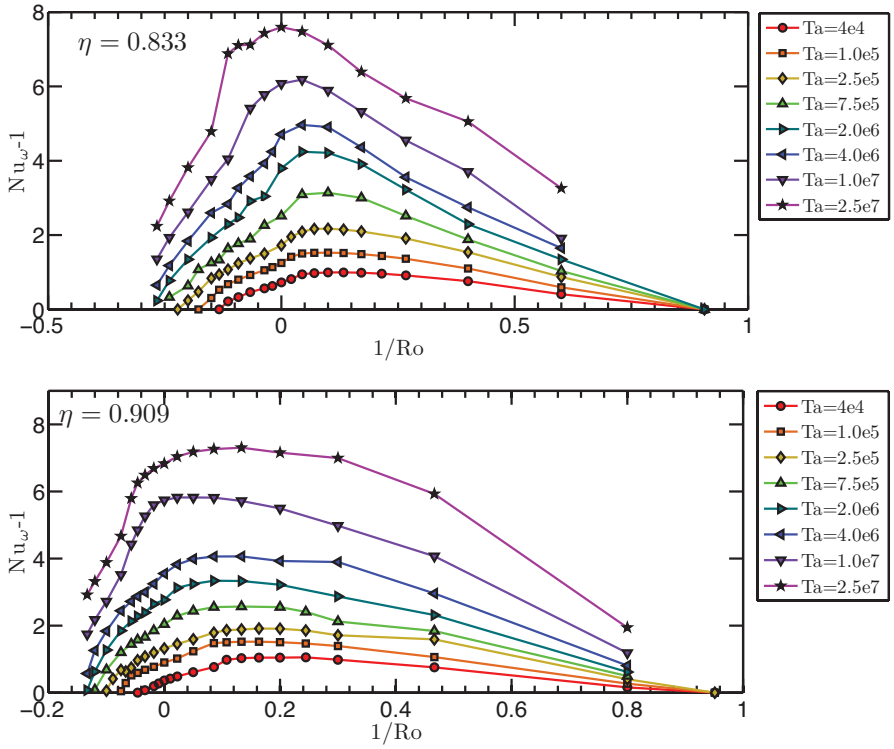

Figure 7.6: $\mathrm{Nu}_\omega - 1$ versus Ro^{-1} for $\eta = 0.833$ and $\eta = 0.909$ studied numerically. The shape of the curve and the position of the maximum depend very strongly on both Ta and η.

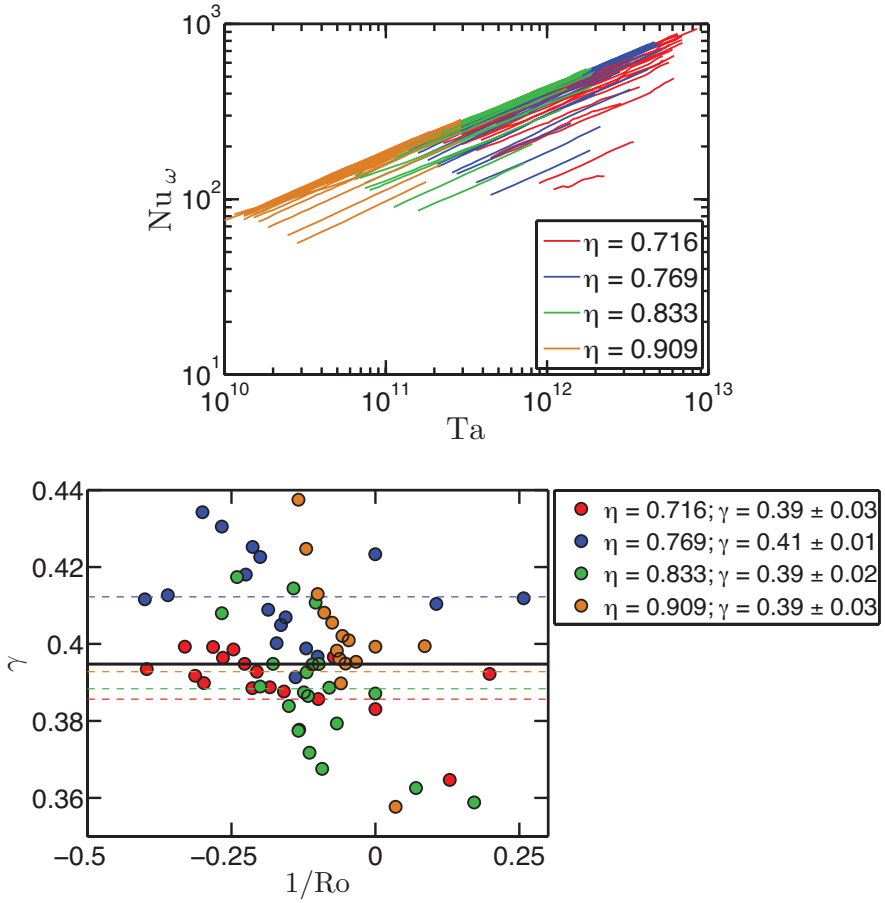

Figure 7.7: The top panel shows Nu_ω versus Ta for all values of η and Ro^{-1} studied in experiments. The bottom panel shows the exponent γ of the scaling law $\mathrm{Nu}_\omega \propto \mathrm{Ta}^\gamma$ for various Ro^{-1}, obtained by a least-squares linear fit in log-log space. The average value of γ for each η is represented by the dashed lines, while the solid line represents the average value of $\gamma = 0.39$ for all η, which will be used for compensating Nu_ω.

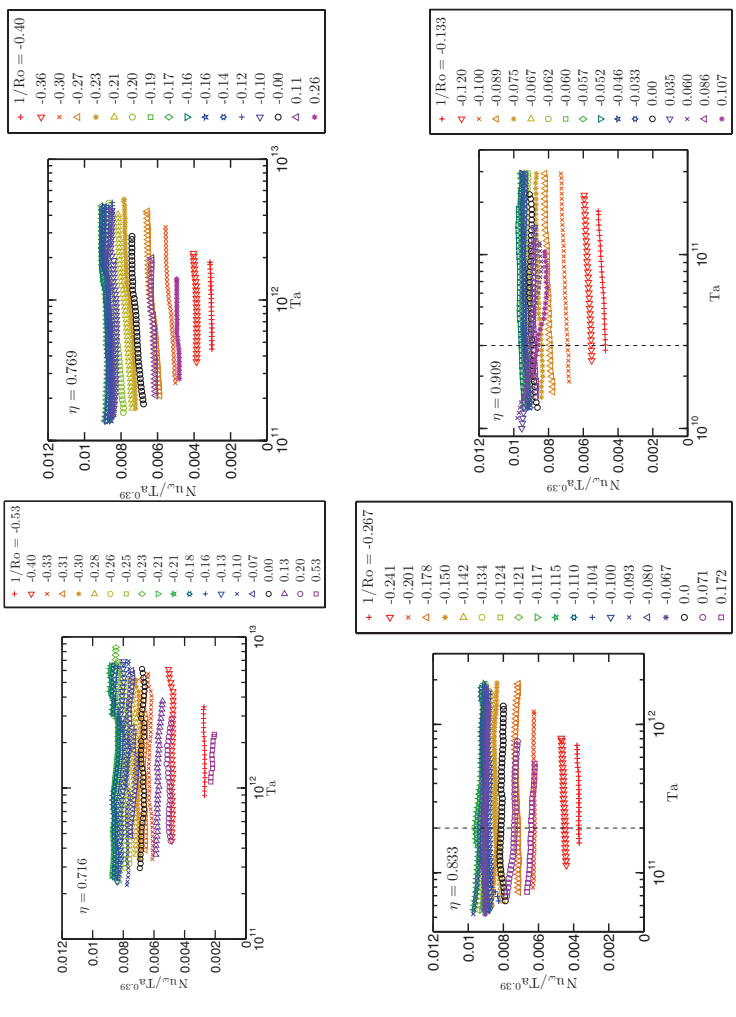

Figure 7.8: $\mathrm{Nu}_\omega/\mathrm{Ta}^{0.39}$ vs. Ta for all explored values of Ro^{-1} for the studied values of η. The scaling law $\mathrm{Nu}_\omega \sim \mathrm{Ta}^{0.39}$ is seen to approximately hold throughout the whole parameter space explored. No trends can be appreciated which would lead us to expect further shift of the optimum with increased driving. Dashed lines, indicating the cut-off regions used for determining $\langle \mathrm{Nu}_\omega/\mathrm{Ta}^{0.39} \rangle_{\mathrm{Ta}}$ have been plotted for $\eta = 0.833$ and $\eta = 0.909$.

Figure 7.9 shows $\langle \mathrm{Nu}_\omega / \mathrm{Ta}^{0.39} \rangle_{\mathrm{Ta}}$ as a function of Ro^{-1} or alternatively of a for the four values of η considered in experiments. The increased driving changes the characteristics of the flow. This is reflected in the very different shapes of the Ro^{-1}-dependence of Nu_ω when comparing figures 7.5 and 7.6 and 7.9, and in the shift of $\mathrm{Ro}_{\mathrm{opt}}^{-1}$.

To summarize these effects, figure 7.10 presents both the 95% peak width $\Delta \mathrm{Ro}_{\mathrm{max}}^{-1}$ and the position of optimal transport $\mathrm{Ro}_{\mathrm{opt}}^{-1}$ determined as the realization with the maximum torque as a function of Ta and η obtained from numerics as well as the asymptotic value from experiments. The peak width $\Delta \mathrm{Ro}_{\mathrm{max}}^{-1}$ is defined as:

$$\Delta \mathrm{Ro}_{\mathrm{max}}^{-1} = \frac{\int_{\mathrm{Ro}_{-0.95}^{-1}}^{\mathrm{Ro}_{0.95}^{-1}} \mathrm{Nu}_\omega(\mathrm{Ro}^{-1}) d\mathrm{Ro}^{-1}}{\max(\mathrm{Nu}_\omega - 1)} \tag{7.13}$$

where $\mathrm{Ro}_{-0.95}^{-1}$ and $\mathrm{Ro}_{0.95}^{-1}$ are the values of Ro^{-1} for which Nu_ω is 95% of the peak value.

The 95% peak width can be seen to vary with driving, reflecting what is seen in figures 7.5 and 7.6. The shape of the Ro^{-1}-Nu_ω curve is highly dependent of both η and Ta. $\mathrm{Ro}_{\mathrm{opt}}^{-1}$ shows a very large variation across the Ta range studied in numerics. The shift of the $\mathrm{Ro}_{\mathrm{opt}}^{-1}$ with Ta is expected to continue until it reaches the values found in the experiments. This can be seen in figures 7.5 and 7.6 for $\eta = 0.5$ to $\eta = 0.833$. For $\eta = 0.909$, the trend seems to change for the last point. However, this is due to the very large and flat peak of the $\mathrm{Nu}_\omega(\mathrm{Ro}^{-1})$ curve—this can also be seen in the left panel and in figure 7.6b.

One may also ask the question: has the value of $\mathrm{Ro}_{\mathrm{opt}}^{-1}$ already saturated in our experiments? Figure 7.8 shows the trend for Nu_ω for increasing Ta. This trend does not seem to vary much for different values of Ro^{-1}. Therefore, we expect the value of Ro_{opt}^{-1} to have already reached saturation in our experiments.

We can compare these new experimental results to the available results from the literature, the speculation made in [41] and the prediction made in [164] for the dependence of the saturated a_{opt} on η. This is shown in figure 7.11. Error bars are either taken from the literature, or computed by fitting a quadratic polynomial to $\mathrm{Nu}_\omega(a)$ for three values of a below the maximum, *i.e.* $a < a_{\mathrm{opt}}$, three values of a after the maximum, *i.e.* $a > a_{\mathrm{opt}}$ and the six values of a, and comparing the different results obtained. Both dependencies are shown to deviate substantially from the experimental results obtained in the present work. Even if the speculation from [41] appears to be better for this η-range,

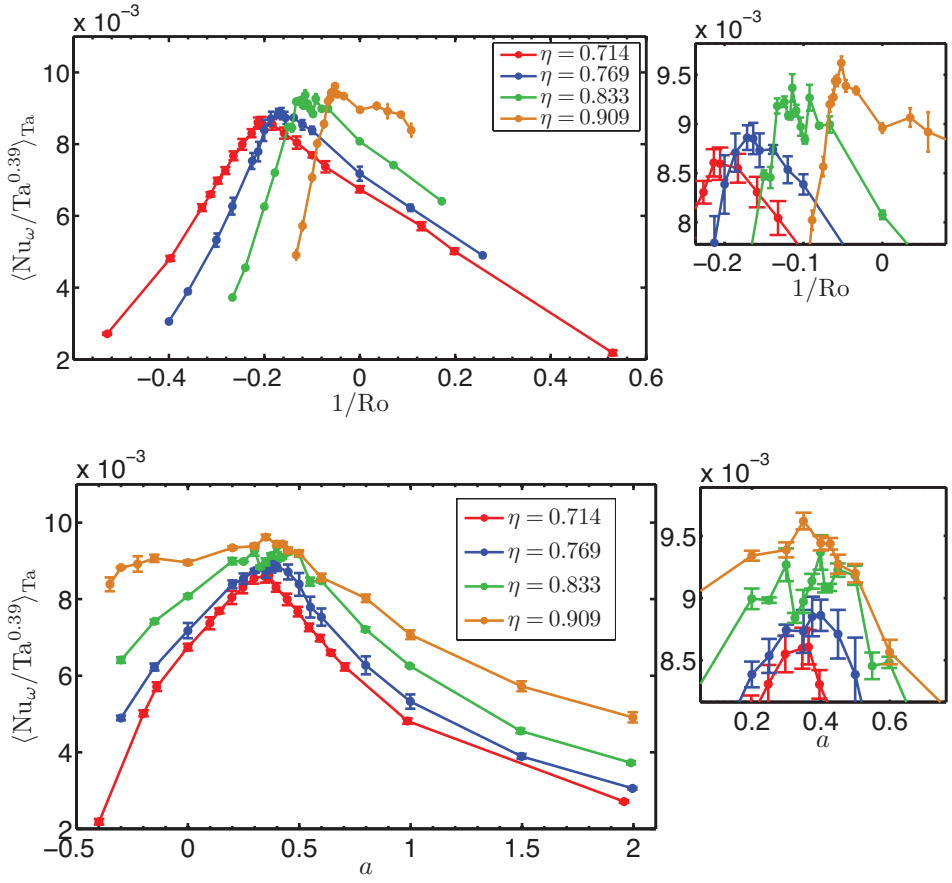

Figure 7.9: The panels show $\langle \mathrm{Nu}_\omega/\mathrm{Ta}^{0.39}\rangle_{\mathrm{Ta}}$ versus either Ro^{-1} (top) or a (bottom) at the cut-off region highlighted in figure 7.8 for the values of η studied experimentally. Zoom-in around the optimum have been added for clarity. Error bars indicate one standard deviation from the mean value, and are too small to be seen for most data points. There is a strong η-dependence of the curve $\mathrm{Nu}_\omega/\mathrm{Ta}^{0.39}$ versus Ro^{-1}, even at the largest drivings studied in experiments. Optimal transport is located at $\mathrm{Ro}_{\mathrm{opt}}^{-1} = -0.20$ for $\eta = 0.714$, $\mathrm{Ro}_{\mathrm{opt}}^{-1} = -0.15$ for $\eta = 0.769$, $\mathrm{Ro}_{\mathrm{opt}}^{-1} = -0.10$ for $\eta = 0.833$ and $\mathrm{Ro}_{\mathrm{opt}}^{-1} = -0.05$ for $\eta = 0.909$, corresponding to $a \approx 0.33 - 0.35$ for all values of η. In the bottom panel, the maximum of the graph is less pronounced, *i.e.* it becomes more flat with increasing η.

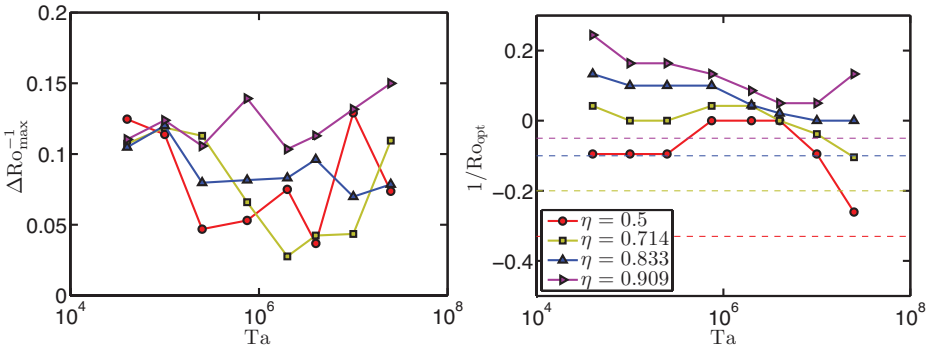

Figure 7.10: Left: The 95% peak width $\Delta \mathrm{Ro}_{\mathrm{max}}^{-1}$ vs Ta for the four values of η analyzed in numerics. The peak width can be seen to vary with driving, and for smaller gaps is larger for larger values of Ta. Right: $\mathrm{Ro}_{\mathrm{opt}}^{-1}$ vs Ta for the same four values of η. The location of the optimal transport has a very strong dependence on the driving, especially for the largest values of η. As driving increases beyond the numerically studied range and overlaps with experiments, $\mathrm{Ro}_{\mathrm{opt}}^{-1}$ should tend to the experimentally found values, represented as dashed lines in the figure. The asymptote for $\eta = 0.5$ is obtained from [165]. The trend appears to be less clear for $\eta = 0.909$, but this might be understandable from the peak width at the highest driving Ta.

for previous experimental data at $\eta = 0.5$, it is clearly different from the experimentally measured value for optimal transport by [165].

This section has shown that the radius ratio has a very strong effect on the global response and especially on optimal transport. Significantly increased transport for co-rotation has been found at the lowest drivings based on the DNS results. This finding was already reported in [55] for $\eta = 0.714$, but the transport increase was marginal. For $\eta = 0.833$ and especially for $\eta = 0.909$ the transport can be increased up to three times. The shift of $\mathrm{Ro}_{\mathrm{opt}}^{-1}$ has also been seen to be much bigger and to happen in a much slower way for smaller gaps. The reason for this will be studied in Section 7.5, using the local data obtained from experiments and numerics.

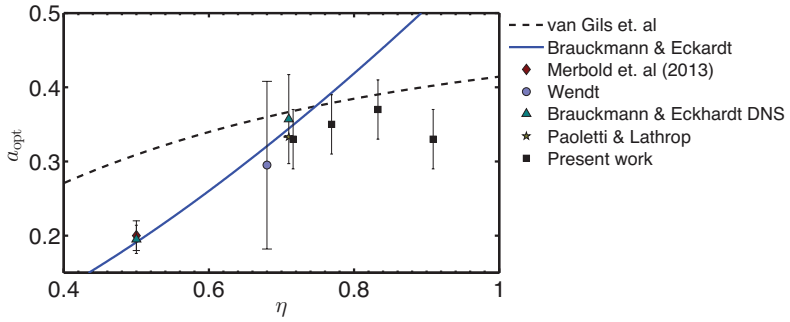

Figure 7.11: Data for $a_{\mathrm{opt}}(\eta)$, from both experiments [14, 27, 165] and numerics [164]. The speculation of [41] and the prediction of [164] are plotted as lines on the graph. The new experimental results deviate substantially from both predictions, even when taking into account error bars.

7.5 Local results

In this section, the local angular velocity profiles will be analyzed. Angular velocity is the transported quantity in TC flow and shows the interplay between the bulk, where the transport is convection-dominated, and the boundary layers, where the transport is diffusion-dominated. Numerical velocity profiles and experimental profiles obtained from LDA will be shown. The angular velocity gradient in the bulk will be analyzed and connected to the optimal transport. In addition, the boundary layers will be analyzed and compared to the results from the analytical formula from EGL 2007 for the BL thickness ratio in the non-ultimate regime.

7.5.1 Angular velocity profiles

Angular velocity ω profiles obtained from numerics are shown in figure 7.12. Results are presented for four values of η and selected values of Ro^{-1} at $\mathrm{Ta} = 2.5 \cdot 10^7$ (and $\mathrm{Ta} = 2.39 \cdot 10^7$ for $\eta = 0.714$). Experimental data obtained by using LDA are shown in figure 7.13 for three values of η: from top-left to bottom, $\eta = 0.714$ for $\mathrm{Re}_i - \mathrm{Re}_o = 10^6$, $\eta = 0.833$ for $\mathrm{Ta} = 5 \cdot 10^{11}$, and $\eta = 0.909$ for $\mathrm{Ta} = 1.1 \cdot 10^{11}$.

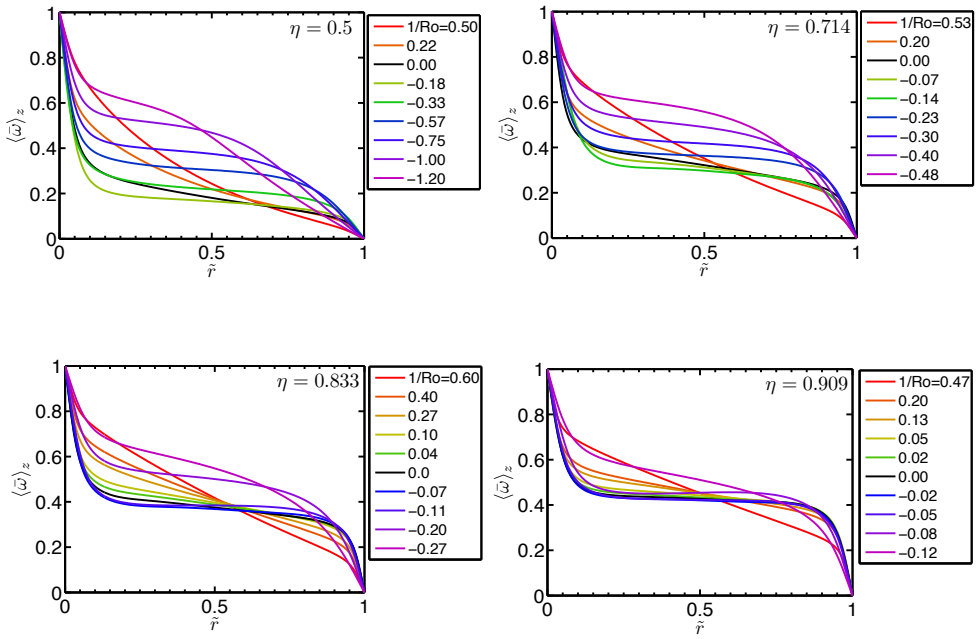

Figure 7.12: Azimuthally, axially and temporally averaged angular velocity $\langle\bar{\omega}\rangle_z$ versus radius $\tilde{r}$ for: $\eta = 0.5$, $\eta = 0.714$, $\eta = 0.833$, and $\eta = 0.909$. Data is for $\mathrm{Ta} = 2.5 \cdot 10^7$ ($\mathrm{Ta} = 2.39 \cdot 10^7$ for $\eta = 0.714$) and selected values of Ro^{-1}. For smaller η, the ω-bulk profiles differ more from a straight line, and have, on average, a smaller value.

The different radius ratios affect the angular velocity profiles on both boundary layers, as the two boundary layers are more asymmetric for the wide gaps; and they affect the bulk, as the bulk angular velocity is smaller for wide gaps. These effects will be analyzed in the next sections.

7.5.2 Angular velocity profiles in the bulk

We now analyze the properties of the angular velocity profiles in the bulk. We find that the slope of the profiles in the bulk is controlled mainly by Ro^{-1} and less so by Ta. This can be understood as follows: The Taylor number Ta acts

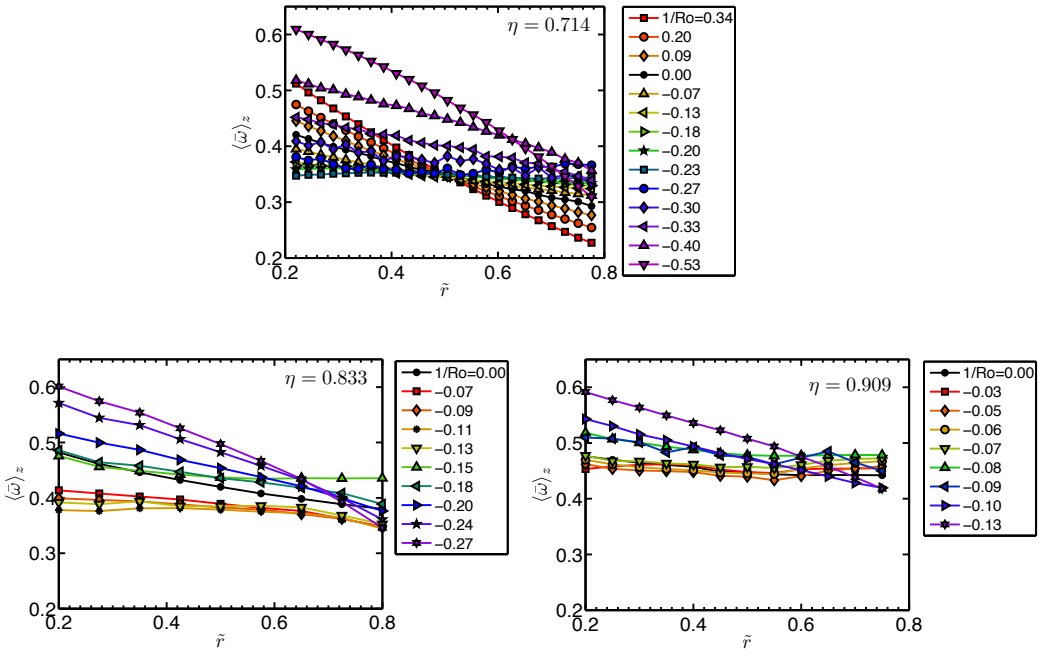

Figure 7.13: Angular velocity profiles obtained by LDA for $\eta = 0.714$ at either $\mathrm{Re}_i - \mathrm{Re}_o = 10^6$ (top), $\eta = 0.833$ or at $\mathrm{Ta} = 5 \cdot 10^{11}$ (bottom-left) and $\eta = 0.909$ at $\mathrm{Ta} = 1.1 \cdot 10^{11}$ (bottom-right), to explore different dependencies in parameter space. Data is taken at a fixed axial height (*i.e.* the cylinder mid-height, $z = L/2$), but as the Taylor number Ta is much larger than in the numerics, the axial dependence is weaker.

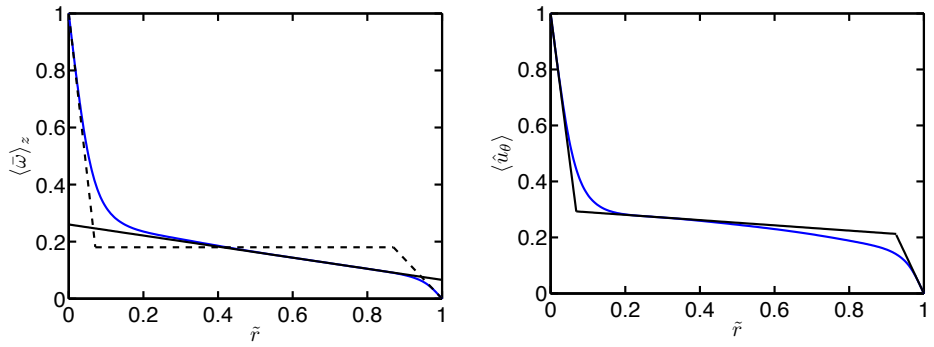

Figure 7.14: An example of the two fitting procedures for the bulk angular velocity gradient and for boundary layer thicknesses done on the DNS data. Both panels show the θ,z, and t averaged azimuthal velocity and angular velocity for $\eta = 0.5$, Ta $= 10^7$, and pure inner cylinder rotation. In the left panel a line is fitted to the bulk of the angular velocity to obtain the bulk gradient. The dashed lines indicate the EGL approximation. The right panel shows the three-lines-fit to the whole profile to obtain the width of its boundary layers, used in Section 7.5.3. Both bulk fits are done at the inflection point, but for different variables ($\bar{\omega}$ or $\bar{u}_\theta$), which gives slightly different slopes (and intersection points).

through the viscous term, dominant in the boundary layers, while Ro^{-1} acts through the Coriolis force, present in the whole domain. These results extend the finding from [55] to other values of η.

To further quantify the effect of Ro^{-1} on the bulk profiles, we calculate the gradient of $\langle\bar{\omega}\rangle_z$. For the DNS data, this is done by numerically fitting a tangent line to the profile at the inflection point using the two neighboring points on both sides (at a distance of $0.01 - 0.02$ r-units); such fit is shown in figure 7.14.

As the spatial resolution of the LDA data is more limited, the fit is done differently. A linear regression to the ω-profile between $0.2 < \tilde{r} < 0.8$ is carried out. The larger range of $\tilde{r}$ is chosen in experiments because: (i) the boundary layers are small enough due to the high Ta that they are outside of the fitting range, and (ii) the fluctuations of the data are much higher in experiments, especially for the LDA of the narrow gaps ($\eta = 0.833$ and $\eta = 0.909$). From this regression, we calculate $\langle\bar{\omega}\rangle_z$, and an error taken from

the covariance matrix of the fit.

Figure 7.15 shows four panels, each containing the angular velocity gradient in the bulk from the numerical simulations and experiments for a given value of η. We first notice that the angular velocity gradients from experiment and numerics are in excellent agreement. Next the connection between a flat angular velocity profile and optimal transport for the highest drivings explored in the experiments can now be seen for other values of η and not just for $\eta = 0.714$ as reported previously [26]. Once $\mathrm{Ro}^{-1} < \mathrm{Ro}_{\mathrm{opt}}^{-1}$, the large scale balance analyzed in [55] breaks down, and a 'neutral' surface that reduces the transport appears in the flow.

In simulations, because of resolution requirements, we are unable of driving the flow strongly enough to see a totally flat bulk profile. Also, the influence of the large scale structures causes a small discrepancy between the flattest profile and the value of $\mathrm{Ro}_{\mathrm{opt}}^{-1}$ measured from Nu_ω. This is expected to slowly dissapear with increasing Ta.

In [55], a linear extrapolation of the bulk angular velocity gradient was done to give an estimate for the case when this profile would become horizontal, *i.e.*, $d\langle\bar{\omega}\rangle_z/d\tilde{r} = 0$, and thus give an estimate of $\mathrm{Ro}_{\mathrm{opt}}^{-1}$. For $\eta = 0.714$ this estimate agreed with the numerical result within error bars. Here, we extend this analysis for the other values of η and, as we shall see, successfully.

As in [55], an almost linear relationship between Ro^{-1} and $d\langle\bar{\omega}\rangle_z/d\tilde{r}$ can be seen. This linear relationship is extrapolated and plotted in each panel. This extrapolation gives an estimate for $\mathrm{Ro}_{\mathrm{opt}}^{-1}(\mathrm{Ta} \to \infty)$, which we can compare to the experimentally determined $\mathrm{Ro}_{\mathrm{opt}}^{-1}(\mathrm{Ta} \to \infty)$. For $\eta = 0.833$, $\mathrm{Ro}^{-1}(\mathrm{Ta} \to \infty) \approx -0.12$ corresponding to $a \approx 0.38$ is obtained, and for $\eta = 0.909$, $\mathrm{Ro}^{-1}(\mathrm{Ta} \to \infty) \approx -0.05$, corresponding to $a \approx 0.31$ is obtained. These values are (within error bars) also obtained for $\mathrm{Ro}_{\mathrm{opt}}^{-1}$ at the large Ta investigated in experiments, namely $\mathrm{Ro}_{\mathrm{opt}}^{-1} = -0.10$ and -0.05, respectively.

For $\eta = 0.5$, $\mathrm{Ro}_{\mathrm{opt}}^{-1}(\mathrm{Ta} \to \infty) \approx -0.33$ is obtained, corresponding to $a \approx 0.2$. This value is consistent with the numerical results in [164], which report $a_{\mathrm{opt}} \approx 0.2$. However, care must be taken, as fitting straight lines to the ω-profiles gives higher residuals for $\eta = 0.5$ as the profiles deviate from straight lines (cf. top-left panel of figure 7.12). A fit to the 'quarter-Couette' profile derived from upper bound theory [140] is much more appropriate for $\eta = 0.5$ at the strongest drivings achieved in experiments [165]. This is because the flow feels much more the effect of the curvature at the small η. At the other end of the scale, the linear relationship works best for smallest gaps, *i.e.* $\eta = 0.909$ (conform figure 7.12) where curvature plays a small effect. To further elaborate the link

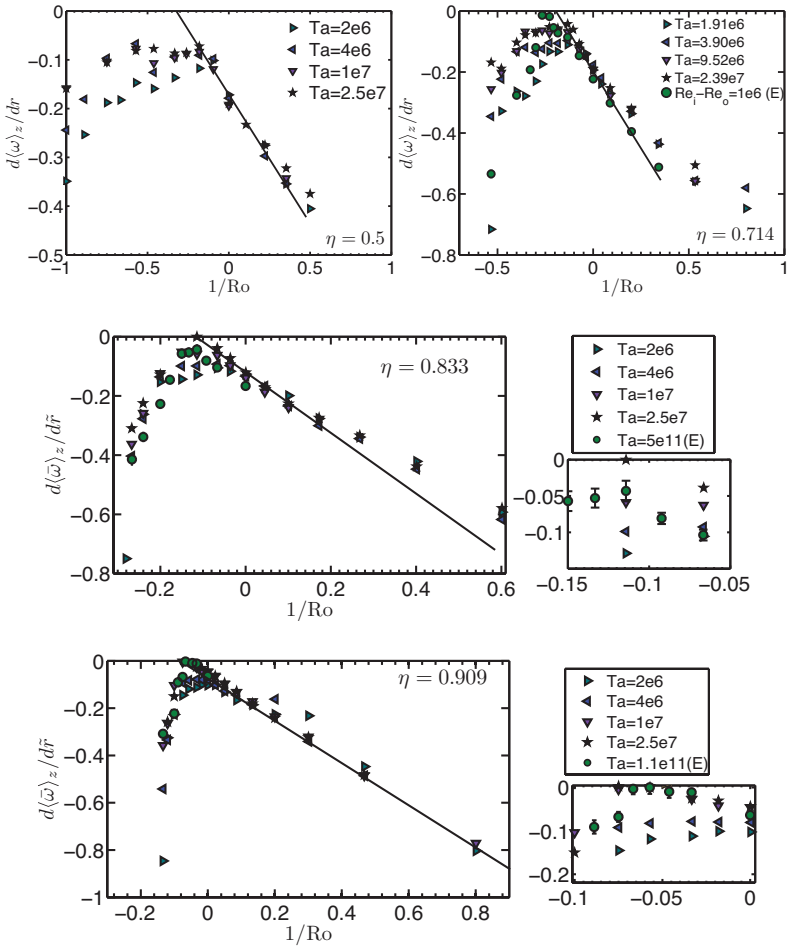

Figure 7.15: Bulk angular velocity gradient $d\langle\bar{\omega}\rangle_z/d\tilde{r}$ against Ro^{-1} for the four values of η explored in simulations, $\eta = 0.5$ (top left), $\eta = 0.714$ (top right), $\eta = 0.833$ (middle), and $\eta = 0.909$ (bottom). Data from experiments obtained by LDA is also plotted for the three values of η for which it was experimentally measured (green circles). For all values of η except $\eta = 0.5$, for co-rotation and slight counter-rotation there is once again an almost linear relationship between Ro^{-1} and $d\langle\bar{\omega}\rangle_z/d\tilde{r}$. A black straight line is added to extrapolate this relationship in order to estimate $\mathrm{Ro}_{\mathrm{opt}}^{-1}$. A plateau, in which the radial gradient of $\langle\bar{\omega}\rangle_z$ is small can be seen around optimal transport, indicating a large convective transport of angular velocity.

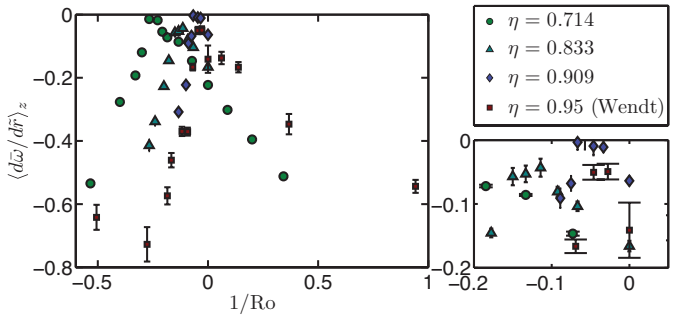

Figure 7.16: Bulk angular velocity gradient $d\langle\bar{\omega}\rangle_z/d\tilde{r}$ against Ro^{-1} for the three values of η explored in experiments, and for $\eta = 0.95$ (digitized from [14]). The error bars of Wendt's data are larger due to the quality of the digitization. As seen previously, the flattest profile occurs around weak counter-rotation, for all values of η including $\eta = 0.95$.

between η, flat ω-profiles and Ro^{-1}, data for the smallest gap $\eta = 0.95$ from [14] has been digitized, and $d\langle\bar{\omega}\rangle_z/d\tilde{r}$ was been determined for it. This data corresponds to a driving of $\mathrm{Ta} \approx 10^8$–10^9. Figure 7.16 shows $d\langle\bar{\omega}\rangle_z/d\tilde{r}$ against Ro^{-1} for Wendt's data and also for the current experimental data. The flattest profile can be seen to occur for increasing (in absolute value) Ro^{-1} for larger gaps, simular to the shift of Ro^{-1}. For $\eta = 0.95$, almost no curvature is felt by the flow and a flat profiles can be seen for $-0.05 < \mathrm{Ro}^{-1} < 0$. However, adding a Coriolis force (in the form of Ro^{-1}) a large ω-gradient is sustained in the bulk. This corroborates the balance between Ro^{-1} and the bulk ω-gradients proposed in [55].

7.5.3 Angular velocity profiles in the boundary layers in the classical turbulent regime

As the driving is increased, the transport is enhanced. To accommodate this, the boundary layers (BLs) become thinner and therefore the ω slopes ($\partial_r\omega$) become steeper. Owing to the geometry of the TC system an intrinsic asymmetry in the BL layer widths is present. More precisely, the exact relationship $\partial_r\langle\omega\rangle|_o = \eta^3\partial_r\langle\omega\rangle|_i$ holds for the slopes of the boundary layers, due to the r independence of J^ω, conform EGL 2007 and eq.(7.6).

An analysis of the boundary layers was not possible in the present experiments because the present LDA measurements have insufficient spatial resolution to resolve the flow in the near-wall region. Therefore, only DNS results will be analyzed here. In simulations the driving is not as large as in experiments, and as a consequence the shear in the BLs is expected to not be large enough to cause a shear instability. This means that the BLs are expected to be of Prandtl-Blasius (*i.e.* laminar) type, even if the bulk is turbulent. On the other hand, in the experiments both boundary layers and bulk are turbulent, *i.e.* the system is in the 'ultimate regime'.
Using the DNS data, we can compare the ratio of the numerically obtained boundary layer widths with the analytical formula for this ratio obtained by EGL 2007 for laminar boundary layers, namely:

$$\frac{\lambda_\omega^o}{\lambda_\omega^i} = \eta^{-3}\frac{|\omega_o - \omega_{\text{bulk}}|}{|\omega_i - \omega_{\text{bulk}}|}, \tag{7.14}$$

where the value of ω_{bulk} is some appropriate value in between for which the angular velocity at the inflection point of the profile might be chosen, *i.e.* the point at which the linear bulk profile fit was done to obtain λ_ω^o and λ_ω^i. The value ω_{bulk} is taken from the numerics, and may bias the estimate.
To calculate the boundary layer thicknesses, the profile of the mean azimuthal velocity $\langle \bar{u}_\theta \rangle_z$ is approximated by three straight lines, one for each boundary layer and one for the bulk. For the boundary layers the slope of the fit is calculated by fitting (by least-mean-squares) a line through the first two computational grid points. For the bulk, first the line is forced to pass through the grid point which is numerically closest to the inflection point of the profile. Then its slope is taken from a least mean square fit using two grid points on both sides of this inflection point. The respective boundary layer line will cross with this bulk line at a point that then defines the thickness of that boundary layer.
The results obtained for $\lambda_\omega^o/\lambda_\omega^i$ both from equation 7.14 and directly from the simulations is shown in figure 7.15. Results are presented for the four values of η and only for the highest value of Ta achieved in the simulations. The boundary layer asymmetry for counter-rotating cylinders (*i.e.*, $\text{Ro}^{-1} < 0$) grows with larger gaps. This is to be expected, as the η^{-3} term is much larger (8) for the largest gap as compared to the smallest gap (≈ 1.3). This is consistent with the η and thus σ restriction in EGL 2007 to a range of smaller gap widths.
As noted already in [55] we find that the fit is not satisfactory for co-rotation (*i.e.* $\text{Ro}^{-1} > 0$) at the lowest values of η, but is satisfactory for counter-

rotation (*i.e.* $\mathrm{Ro}^{-1} < 0$). In EGL 2007, equation (7.14) is obtained by approximating the profile by three straight lines, two for the BLs and a constant ω line for the bulk. Therefore, we expect the approximation to hold best when the bulk has a flat gradient. For co-rotating cylinders and strongly counter-rotating cylinders, the bulk has a steep gradient (see figure 7.15), but characteristically different shapes. The only free parameter in equation (7.14) is ω_{bulk}, which is chosen to be ω at the point of inflection. Owing to the different shapes of the ω-profiles, this choice seems more correct for counter-rotating cylinders, as there is a clear inflection point in the profile. On the other hand, for co-rotating cylinders, the profile appears to be more convex-like, and there, the choice of ω_{bulk} as the inflection point induces errors in the approximation (conform 7.14a). For $\eta = 0.5$, the error from the constant ω approximation is even more pronounced, and the formula fails.

For co-rotation the boundary layers are approximately of the same size, and the ratio $\lambda_\omega^o/\lambda_\omega^i$ is very close to 1. If one inverts equation (7.14) by approximating this ratio by 1, an estimate of what the angular velocity will be in the bulk due to the boundary layer slope asymmetry is obtained:

$$\omega_{\mathrm{bulk}} = \frac{\eta^3}{1+\eta^3}, \tag{7.15}$$

corresponding to:

$$\omega_{\mathrm{bulk}}^\ell = \frac{-\omega_o^\ell + \eta^3\omega_i^\ell}{1+\eta^3}, \tag{7.16}$$

in the lab frame. This expression gives an estimate for ω_{bulk} when the profile is flattest, and has been represented graphically in figure 7.12. Indeed, one can take this estimate (*e.g.* 0.27 for $\eta = 0.714$) and compare it with figures 7.12 and 7.13. We note that the value of ω in the bulk for the flattest profile in the numerics (at $\mathrm{Ro}^{-1} \approx \mathrm{Ro}_{\mathrm{opt}}^{-1}(\mathrm{Ta})$) lies around ω_{bulk}. We can also note that the profiles for $\mathrm{Ro}^{-1} > \mathrm{Ro}_{\mathrm{opt}}^{-1}$ approximately cross each other at the same point, and this point has a value of $\omega \approx \omega_{\mathrm{bulk}}$. This effect can only be seen in the numerics, as these approximations break down once the boundary layers become turbulent. The cross points of the curves are taken as an estimate for ω_{bulk}, and this is represented against eq. 7.15 in figure 7.18.

To understand why the boundary layers are of approximately the same thickness despite the different initial slopes at the cylinders one has to go back to equation (7.6). The angular velocity current has a diffusive part and a convective part. Per definition in the boundary layer the diffusion dominates and in the bulk the convection does. Thus the boundary layer ceases when convection becomes significant. But convection is controlled by the wind. Thus in

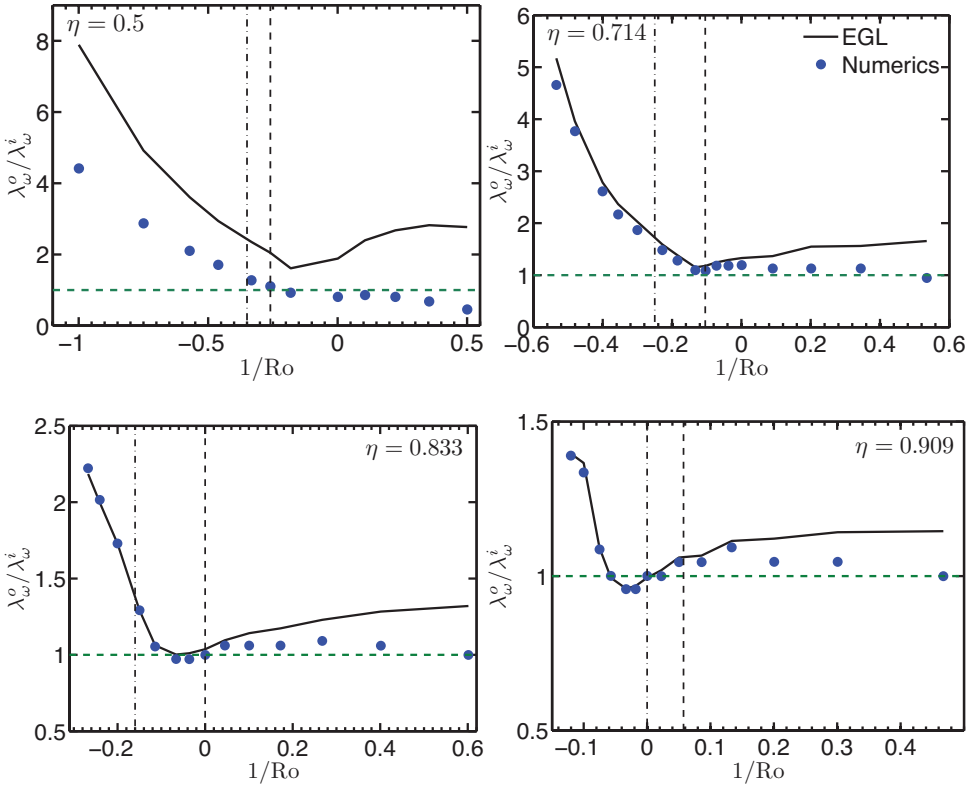

Figure 7.17: $\lambda^o_\omega/\lambda^i_\omega$ from simulations (dots) and from equation (7.14) (solid lines) versus Ro^{-1} for the four values of η studied numerically, $\eta = 0.5$ (top-left), 0.714 (top-right), 0.833 (bottom-left) and 0.909 (bottom-right) at $\mathrm{Ta} = 2.5 \cdot 10^7$. The numerical results and the estimate from equation (7.14) match very well for larger values of η and especially for counter-rotating cylinders ($1/Ro < 0$). The vertical black dashed line indicates $\mathrm{Ro}^{-1}_{\mathrm{opt}}$, while the vertical dash-dot line indicates the 90% peak width on the counter-rotation side. $\lambda^o_\omega/\lambda^i_\omega$ begins to deviate from 1 between the two lines. The asymmetry between the boundary layers can be seen to be larger for smaller values of η, which is expected as equation (7.14) contains the explicit factor η^{-3}.

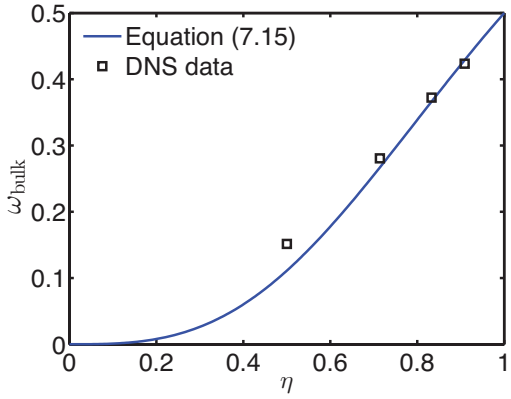

Figure 7.18: Plot of ω_{bulk} as a function of η, taken from both eq. 7.15 and from the crossing points of the ω-profiles in figure 7.12. The trend is the same in both data sets. A smaller value of η decreases the value of the bulk angular velocity.

essence the boundary layer size is controlled by the wind and not immediately by the initial slope at the wall. Owing to continuity, if the rolls penetrate the whole domain the wind may be expected to be the same close to the inner and close to the outer cylinder. This suggests that the flow organizes itself in a way that the boundary layer extensions (or widths) might be similar, even if the initial slopes at the walls are different.

What happens for counter-rotation, or more precisely when $\text{Ro}^{-1} < \text{Ro}_{\text{opt}}^{-1}$? For Ro^{-1} below the optimum $\text{Ro}_{\text{opt}}^{-1}$ a so-called neutral surface will be present in the flow, which separates the Rayleigh-stable and -unstable areas. The wind drastically changes in the Rayleigh-stable areas [55], leading to very different wind velocities close to the outer and inner cylinder, respectively. The wind at the outer cylinder will be weaker, as the rolls cannot fully penetrate the Rayleigh-stable domain. This means that the outer cylinder boundary layer will extend deeper into the flow, in accordance to what is seen in figure 7.17.

7.6 Summary and conclusions

Experiments and direct numerical simulations (DNS) were analysed to explore the effects of the radius ratio η on turbulent Taylor-Couette flow. Numerical results corresponding to Taylor numbers in the range of $10^4 < \mathrm{Ta} < 10^8$ alongside with experiments in a Taylor number range of $10^{10} < \mathrm{Ta} < 10^{12}$ were presented for four values of the radius ratio η.

First the influence of the radius ratio on the global scaling laws $\mathrm{Nu}_\omega \propto \mathrm{Ta}^\gamma$ was studied. The local scaling exponent γ describing the response of the torque caused by a Taylor number increase, is barely modified by varying the radius ratio η. Indeed, in experiments a universal exponent of $\gamma \approx 0.39$ is obtained, independent of radius ratio and outer cylinder rotation. For the numerical simulations at lower Ta similar universal behavior can be observed. The transition associated to the vanishing of coherent structures can also be appreciated at $\mathrm{Ta} \sim 10^6$ for all values of η. Before this transition local exponents of $\gamma \approx 0.33$ are seen and after the transition these decrease to $\gamma \approx 0.2$.

The radius ratio does play a very important role in optimal transport. At smaller gaps, *i.e.*, for larger η, at the lower end of the Ta range a very large increase in transport for corotating cylinders can be seen. The shift towards the asymptotic optimal transport happens in a much slower way for small gaps, but this shift is seen for all studied radius ratios. For the largest gap ($\eta = 0.5$), optimal transport for pure inner cylinder rotation at the lowest drivings is obtained. The shift towards the asymptotic value happens suddenly, as two peaks can be seen in the Nu_ω versus Ro^{-1} curve, and one of the peaks becomes larger than the other one as driving increases. This might point in the direction of different phenomena and transitions in the flow topology happening at larger gaps. Finally, the asymptotic values of $\mathrm{Ro}_{\mathrm{opt}}^{-1}$ obtained in experiments were compared to the speculation of [41] and the prediction of [164]. Both of the models were found to deviate from experimental and numerical results.

When looking at the local results, as in [55] we can link the optimal transport in the smallest gaps to a balance between Coriolis forces and the inertia terms in the equations of motion. The flattest profiles in the bulk are linked to optimal transport in experiments. With the numerics the extrapolation presented in [55] for predicting optimal transport was extended to other radius ratios. It is found to work well for all selected η except for $\eta = 0.5$. At this η, *i.e.*, for the largest gap considered here, the most obvious problem is that

Radius ratio (η)	Extrapolated $\mathrm{Ro}_{\mathrm{opt}}^{-1}/a_{\mathrm{opt}}$	Measured $\mathrm{Ro}_{\mathrm{opt}}^{-1}/a_{\mathrm{opt}}$
0.5	-0.33/0.20	—
0.714	-0.20/0.33	-0.20/0.33
0.769	—	-0.20/0.36
0.833	-0.12/0.41	-0.10/0.37
0.909	-0.05/0.34	-0.05/0.34

Table 7.2: Summary of values obtained for $\mathrm{Ro}_{\mathrm{opt}}^{-1}$ and a_{opt} through both the extrapolation of $d\langle\bar{\omega}\rangle_z/d\tilde{r}$ (Section 7.5.2) and direct measurement of the torque (Section 7.4.2) for the various values of η studied in this chapter.

the ω profiles strongly feel the effect of curvature difference at the inner and outer cylinders and a straight line fit (*i.e.* ω = constant) to the bulk is not appropriate. There may be additional reasons for this discrepancy and optimal transport in large gap TC flow requires more investigation. A summary of the results for determining $\mathrm{Ro}_{\mathrm{opt}}^{-1}$ using both the experimentally measured torque maxima from section 7.4.2 and the numerical extrapolation from section 7.5.2 are presented in table 7.2.

Finally, the boundary layers have been analyzed. The outer boundary layer is found to be much thicker than the inner boundary layer when $\mathrm{Ro}^{-1} < \mathrm{Ro}_{\mathrm{opt}}^{-1}$. We attribute this to the appearance of Rayleigh-stable zones in the flow. This prevents the turbulent Taylor vortices from covering the full domain between the cylinders. As the boundary layer size is essentially determined by the wind, if the rolls penetrate the whole domain (which is the case for $\mathrm{Ro}^{-1} > \mathrm{Ro}_{\mathrm{opt}}^{-1}$), both boundary layers are approximately of the same size. If the rolls do not penetrate the full domain, the outer boundary layer will be much larger than the inner boundary layer, in accordance with the smaller initial slope of $\omega(r)$ at the cylinder walls.

In this work, simulations and experiments have been performed on a range of radius ratios between $0.5 \leq \eta \leq 0.909$. Insights for the small gaps seem to be consistent with what was discussed in [55]. However, for $\eta = 0.5$ the phenomena of optimal transport appears to be quite different. Therefore, our ambition is to extend the DNS towards values of η smaller than 0.5 to improve the understanding of that regime.

8

Laser Doppler anemometry inside Taylor-Couette°

In this chapter it will be shown how the curvature of the outer cylinder affects laser Doppler anemometry measurements inside a Taylor-Couette apparatus. The measurement position and the measured velocity are altered by curved surfaces. Conventional methods for curvature correction are not applicable to our setup, and it will be shown how a ray-tracer can be used to solve this complication. By using a ray-tracer the focal position can be calculated, and the velocity can be corrected. The results of the ray-tracer are verified by measuring an a priori known velocity field, and after applying refractive corrections good agreement with theoretical predictions are found. The methods described in this chapter are applied to measure the azimuthal velocity profiles in high Reynolds number Taylor-Couette flow for the case of outer cylinder rotation.

°Published as: **Sander G. Huisman**, Dennis P.M. van Gils, and Chao Sun, *Applying laser Doppler anemometry inside a Taylor-Couette geometry: using a ray-tracer to correct for curvature effects*, Eur. J. Mech. - B/Fluids **36**, 47 (2012). Theory, experiments, analysis, and writing done by Huisman under supervision of Sun. Discussion of the results and proofreading are done by everyone.

8.1 Introduction

A Taylor-Couette (TC) apparatus consists of two coaxial, differentially rotating, cylinders, see figure 8.1. The annulus between the cylinders is filled with a working fluid; most commonly, as in our case, water is chosen. The apparatus has been used to study hydrodynamic instabilities, pattern formation, turbulence, and was found to have a rich phase diagram with different types of flow structures [166, 94, 19, 107, 18, 121, 108, 109, 8, 110, 17]. To get a deep understanding of these phenomena it is crucial to measure the local flow velocity.

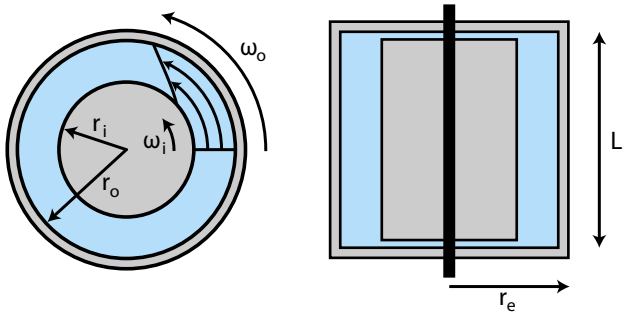

Figure 8.1: *Left:* Top view of TC apparatus, two concentric cylinders are rotating. Control parameters are the rotation rates ω_i and ω_o, where the subscripts denote inner cylinder and outer cylinder, respectively. The inner cylinder has a radius of $r_i = 20$ cm, and the outer cylinder has an inner-radius of $r_o = 28$ cm. *Right:* Vertical cross section of a TC apparatus. The outer cylinder has an outer-radius of $r_e = 30.5$ cm and a height $L = 92.7$ cm. The outer cylinder is made from optically transparent PMMA (*Poly-(methyl methacrylate)*), and is attached to the top and bottom end plates.

Measuring the velocity field inside a TC apparatus was done for a long time using intrusive measurements techniques, *e.g.* constant temperature anemometry [30, 31, 167, 10] and Pitot tubes [14]. Though these techniques are robust and proven to work, they are not ideal for measuring the velocity in TC flow. The aforementioned methods measure the magnitude of the velocity, not the individual components, and are directionally ambiguous using a single probe. Of course, one could use multiple probes [168] to obtain the flow direction.

Another problem is that they alter the flow under consideration. Though this is not an issue for non-recirculating setups, like an open-ended wind tunnel, it can be a severe issue in recirculating (closed) setups, *e.g.* a TC apparatus, a rotating drum, or a Rayleigh-Bénard cell [6]. For a large range of Reynolds numbers it is known that vortices will be shed [169] from these probes, either in the form of a Kármán vortex street or as a turbulent wake, depending on the geometry and Reynolds number. These vortices can survive a full revolution, which has been observed in rotating drum experiments [170].
The TC setup used in this chapter, the Twente Turbulent Taylor-Couette (T^3C) [21], distincts itself from other setups by many features: variable gap and radius ratio, precise temperature control, independently rotatable cylinders, and a fully optically accessible gap. The outer cylinder is constructed from 2.5 cm thick PMMA (*Poly-(methyl methacrylate)*), which enables optical measurement techniques, *e.g.* Particle Tracking Velocimetry (PTV) [171, 172], Particle Imaging Velocimetry (PIV) [173, 15], and Laser Doppler Anemometry (LDA) [174, 175]. These methods, by their very nature, will not disturb the flow under consideration. In addition these techniques are able to measure the velocity components and are directionally sensitive, such that they are capable of detecting flow reversals. The addition of seed particles is imperative for these techniques, and one should check if these particles accurately reflect the velocity of the flow, as discussed below. Additionally, particles should not change the dynamics of the flow, in particular, some particles act as a surfactant in two-phase flows [176, 177, 178].

8.2 Laser Doppler anemometry

LDA is based on the Doppler effect. The most common version of LDA, is a so-called dual beam heterodyne configuration [175], see figures 8.2 and 8.3. In this configuration two beams are crossed and focused in the flow, creating an interference pattern. Seed particles, added to the flow, passing through the interference pattern will scatter light with a specific frequency. This light is then captured by a photo detector and converted to a current from which the Doppler shift can be calculated. Knowing the optical geometry of the setup one can directly calculate the velocity from the Doppler shift [175]:

$$f_d = \frac{2\sin(\theta/2)}{\lambda}|v_k| \tag{8.1}$$

where f_d is the Doppler shift, λ the wavelength of the laser, θ the angle between the beams, and v_k the component of the velocity along $\mathbf{k}_1 - \mathbf{k}_2$, where $\mathbf{k}_i$ are the propagation vectors of the laser beams. To add directional sensitivity one has to frequency shift one of the beams, accomplished by a Bragg cell. More details about the Bragg cell, the fringe-model, and LDA in general, can be found in *e.g.* refs. [175, 179].

Laser Doppler anemometry is a so-called absolute measurement method and therefore does not require calibration against a known flow. This, however, does not mean that a measurement of velocity is error free. Any misalignment in the optical arrangement, and any imperfection in the lenses (*e.g.* astigmatism [180]) will cause errors. In addition, any particle traveling through the beams prior to focussing can have adverse effects on the formation of a well-defined measurement volume. Similarly, any spatial inhomogeneity of the refractive index causes the focal point to shift, and the waists to mismatch in the measurement volume [181]. Furthermore, the number of particles in the interference zone fluctuates; particles move in and out the measurement volume and induce noise in the collected signal.

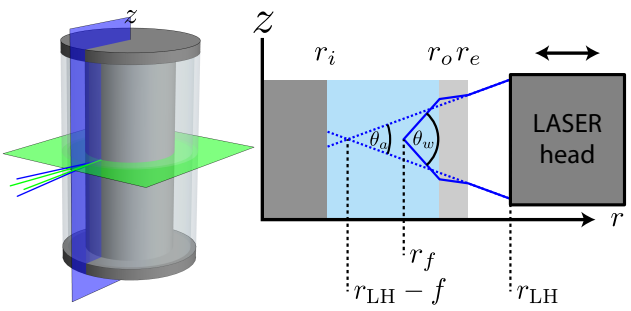

Figure 8.2: *Left:* The azimuthal and axial components of the velocity are measured, laser beams are in the green and blue planes respectively. *Right:* Vertical cross section showing two laser beams. The dashed lines are beams *without* refraction, the angle between the beams is denoted θ_a, where a stands for air. The solid lines are beams *with* refraction, θ_w is the angle between the beams in water. r_{LH} is the position of the laser head and $r_{\mathrm{LH}} - f$ is position of the focus without refraction, while r_f is the real position of the focus.

8.2.1 Curvature effects

In most LDA applications the laser beams travel through flat surfaces, see figure 8.3. In this case, Eq. 8.1 can be simplified by invoking Snell's law:

$$\frac{f_d}{2|v_k|} = \frac{\sin(\theta_\mathrm{w}/2)}{\lambda_\mathrm{w}} = \frac{\sin(\theta_\mathrm{a}/2)}{\lambda_\mathrm{a}} \tag{8.2}$$

where quantities with a subscripts denote quantities in air, and w in water. Equation 8.2 is only applicable if the interfaces are flat and the optical axis is perpendicular to those interfaces; it is only then that $\theta_\mathrm{a}/2$ is the angle of incidence and $\theta_\mathrm{w}/2$ the angle of refraction. The difference in refractive index is absorbed by the changing wavelength. So for the case of flat interfaces, θ_a can be obtained from the focal length and the beam separation, and together with λ_a, given by the laser, the velocity can be calculated from the Doppler shift (Eq. 8.2). Note that the refractive indices of the container and water are irrelevant; they are not used in the calculation of the velocity.

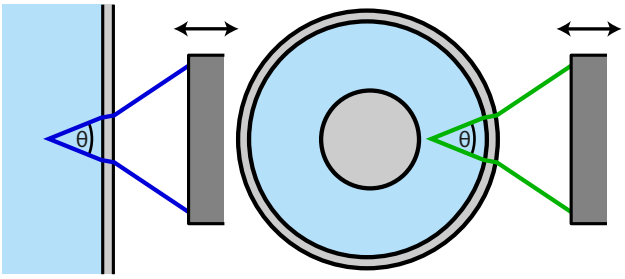

Figure 8.3: *Left:* Typical geometry of LDA, equivalent to the vertical plane in the current application. The beams are passing through flat interfaces, and θ does not vary with laser-head position. *Right:* Horizontal plane: laser beams are affected by the curved interfaces, and therefore θ is a function of radial position.

For the case of a curved surface, see Fig. 8.3, Eq. 8.2 does not hold. For this case Snell's law can not (easily) be applied in order to transform θ_w to θ_a. A prerequisite of calculating the correct velocity is therefore the knowledge of θ_w as a function of gap-position.
Most commonly the calculation of the velocity is implemented in the supplied software and implicitly assumes Eq. 8.2 to hold. For the case of curved

interfaces this equation does not hold, and therefore the measured velocity has to be corrected by multiplying it with a correction factor C_θ:

$$C_\theta = \frac{u_{\phi,\text{real}}}{u_{\phi,\text{measured}}} = \frac{n_a \sin(\theta_a/2)}{n_w \sin(\theta_w/2)}, \tag{8.3}$$

where a subscripts denote quantities in air, and w in water; see also Fig. 8.2.

8.3 Solutions

The problem at hand is predominantly solved by mounting prisms (see *e.g.* [182]) to the outer cylinder of the TC apparatus, or by putting the entire apparatus inside a liquid bath (see *e.g.* [183]) with flat windows. The latter has two purposes: the liquid bath can act as a coolant and match the refractive index of the working fluid. In this way the beams travel through the outer cylinder with less deflection; this solution is, however, not perfect because of the finite thickness of the outer cylinder. Matching the refractive indices of the working fluid, the liquid bath, and the outer cylinder does solve the issue, but becomes cumbersome for large scale devices, or impossible if the studied fluid is a gas. The use of prisms is tantamount to the use of a liquid bath, and is also unable to fully correct for the problem. Furthermore, applying prisms is technically demanding once the outside is in motion. Theoretically one can derive the trajectories of the laser light. Ref. [184] derives these trajectories and even finds simplifications for the solutions found. This analysis is, however, not complete, as it only considers 1 plane of refraction; the inside of the outer cylinder. In our application our cylinder is very thick compared to our measurement range; the gap of our apparatus is 8 cm versus a cylinder of thickness 2.5 cm. Here we will consider both interfaces, and calculate the trajectories by using a ray-tracer, and we will show that taking into account both interfaces is *crucial* for our experiments. Utilizing a ray-tracer has several advantages compared to a theoretical derivation for the present experimental setup (*e.g.* Ref. [184]): a theoretical derivation becomes cumbersome if one tries to find a formula after more than one refraction. The T^3C system will be equipped with multiple outer cylinders to alter the gap-width, a ray-tracer is then more generalized and is able to handle multiple interfaces. The next section describes the use of a ray-tracer in order to account for the effects of the curved interfaces.

8.4 Ray-tracer

A 3D ray-tracer is built in order to calculate two parameters: the angle θ_w for the green beam pair in the horizontal plane, and the position of the crossings of the blue and green beam pairs in the vertical and horizontal plane, respectively. For the blue beam pair (in the axial-radial plane), the curvature effects does not affect the flow velocity measurements, and therefore Eq. 8.2 is applicable; the axial velocity does not require correction. The azimuthal velocity, however, does need correction.
The ray-tracer is based on simple principles: starting at point $\mathbf{p}_i$ with direction $\mathbf{k}_i$, it checks which interfaces are hit for some $t > 0$ at position $\mathbf{p}_i + t\mathbf{k}_i$. The next point in the ray-trace can be defined from the interface that is hit first: $\mathbf{p}_{i+1} = \mathbf{p}_i + t_{\min}\mathbf{k}_i$. The normal of this interface is calculated at position $\mathbf{p}_{i+1}$, and is denoted $\widehat{\mathbf{s}}$, where the hat means the vector has unit length. For the case of reflection the new direction is given by

$$\widehat{\mathbf{k}}_{\mathbf{i+1}} = \widehat{\mathbf{k}}_{\mathbf{i}} - 2(\widehat{\mathbf{k}}_{\mathbf{i}} \cdot \widehat{\mathbf{s}})\widehat{\mathbf{s}}. \tag{8.4}$$

For the case of refraction, Snell's law:

$$n_i(\widehat{\mathbf{k}}_{\mathbf{i}} \times \widehat{\mathbf{s}}) = n_{i+1}(\widehat{\mathbf{k}}_{\mathbf{i+1}} \times \widehat{\mathbf{s}}), \tag{8.5}$$

is solved for $\mathbf{k_{i+1}}$ under the constraint that it has unit length and in the plane spanned by $\widehat{\mathbf{s}}$ and $\widehat{\mathbf{k}}_{\mathbf{i}}$. This can be implemented without the use of trigonometric functions, which can be troublesome in certain fringe cases; see the appendix for more details.
Once the new position and new direction are found, the algorithm can be repeated until it exits the apparatus, or until it is absorbed by a surface.
This algorithm has been applied to the geometry of our LDA and TC setup. Our focal length $f = 0.5$ m, our beam separation is 76 mm for the green beams, and 73 mm for the blue beams. The optical geometry of the TC apparatus [21] used in this chapter can be characterized by 3 radii and 3 refractive indices; see Fig. 8.1 and 8.2 and Table 8.1.

8.4.1 Shift of focal position

In this section the location of the foci (*i.e.* the measurement position) for both pairs of beams are calculated. The position of the laser-head r_{LH} is varied,

Parameter	Symbol	Value	
Radius inner cylinder	r_i	0.20	m
Inner-radius outer cylinder	r_o	0.28	m
Outer-radius outer cylinder	r_e	0.305	m
Refractive index PMMA	n_{PMMA}	1.49	m
Refractive index water	n_{water}	1.333	m

Table 8.1: Parameters describing the optical geometry of the presently used Taylor-Couette apparatus: the T^{3}C [21].

see Fig. 8.2. The focal position of the undisturbed beams is given by $r_{\mathrm{LH}} - f$. For each beam-pair the focal position r_f is calculated as a function of r_{LH}, see Figs. 8.2 and 8.4.

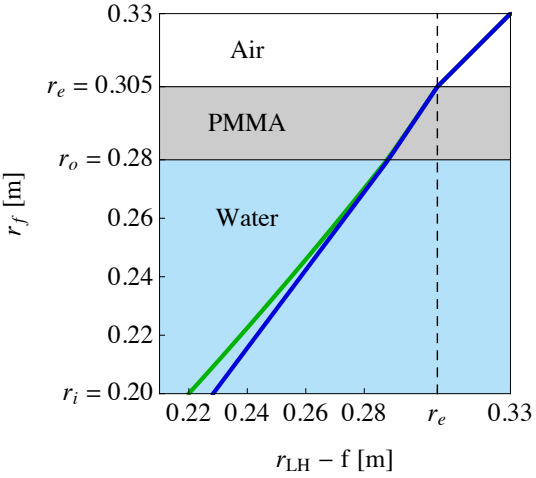

Figure 8.4: The position of the two foci as a function of the position of the laser-head. Colors are in accordance with Fig. 8.2. The trajectory of the blue focus can be described by a piece-wise linear function, while for the green focus it deviates from a linear function due to the curvature of the interfaces. The foci diverge once $r_{\mathrm{LH}} - f < r_e$.

If the focus is outside the apparatus, *i.e.* $r_{\mathrm{LH}} - f > r_e$, the focal position is given by $r_f = r_{\mathrm{LH}} - f$. If the laser head is moved inward (decreasing $r_{\mathrm{LH}} - f$) the beams will first hit the outer cylinder at $r_f = r_e = r_{\mathrm{LH}} - f$.

Moving the laser head further inward will cause the foci to lie inside the PMMA, and moving even further, inside the water. The blue beams are in the azimuthal-radial plane and refract differently from beams traveling in the axial-radial plane. The focus of the blue beams hits the inner cylinder ($r_f = r_i$) at $r_{\mathrm{LH}} - f \approx 0.228$ m, while the focus of the green beams hits the inner cylinder at $r_{\mathrm{LH}} - f \approx 0.22$ m. The distance between the two foci as a function of the radial position is depicted in Fig. 8.5.

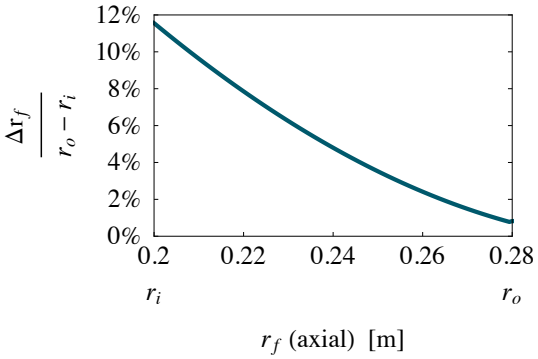

Figure 8.5: The separation between the measurement positions is normalized with the gap width and plotted versus the focal position of the 'axial' beams. Near the inner cylinder the distance between the two foci is the highest and constitutes more than 11% of the gap. Due to the thickness of the outer cylinder there is non-zero distance between the two foci when focused at $r = r_o$.

A pronounced shift of the focal positions is observed, see Fig. 8.5; the foci never coincide, and the maximum separation is 11.5% of the gap. The effects due to curved interfaces can therefore not be neglected. Furthermore, note that the foci do not even coincide at $r = r_o$; this is due to the finite thickness of the outer cylinder, it is therefore necessary to consider both interfaces in the analysis.

8.4.2 Beam angle correction

For the case of flat surfaces (the axial-radial plane) the velocity calculated by the supplier's software does not have to be corrected. Equation 8.2, however, does not hold in the azimuthal-radial plane due to the curved surfaces, and

the velocity has to be corrected by multiplication with C_θ, see Eq. 8.3. The refractive indices are known, and θ_a can be found from the focal length and the beam separation. θ_w can be found by calculating the angle between the focussing rays, see Figs. 8.2 and 8.3. The correction factor can then be calculated, see Fig. 8.6.

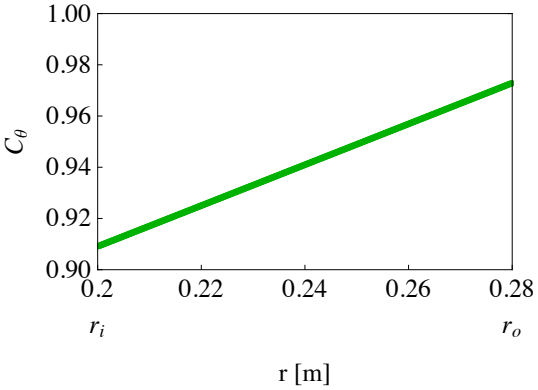

Figure 8.6: Correction factor C_θ (see eq. 8.3) as a function of the radial position r. The azimuthal velocity u_ϕ has to be corrected: $u_{\phi,\text{real}} = C_\theta(r) u_{\phi,\text{measured}}$.

The velocity has to be corrected by 3% to 9%, depending on the radial position. Note that there is a finite correction (about 3% for the optical geometry of the current apparatus) at the water-PMMA interface at $r = r_o$, this is due to the non-zero thickness of the outer cylinder and taking into account both interfaces of the outer cylinder in the analysis.

8.5 Experimental verification

The results obtained from the ray-tracer can be verified by measuring a known flow state. The temperature of the TC system is kept at 20°C with water as the working fluid. Dantec polyamide seed particles ($r_{\text{seed}} = 2.5$ µm) with a density of $1.03 \cdot 10^3$ kg/m^3 are used. One can estimate the minimum velocity difference $\Delta v = |v_{\text{seed}} - v_{\text{fluid}}|$ between a particle v_{seed} and its surrounding fluid v_{fluid} needed for the drag force $F_{\text{drag}} = 6\pi\mu r_{\text{seed}}\Delta v$ to outweigh the centrifugal force $F_{\text{cent}}(r) = \frac{4}{3}\pi {r_{\text{seed}}}^3 (\rho_{\text{seed}} - \rho_{\text{fluid}}) \frac{v^2}{r}$. A typical velocity in the middle of

the gap ($r = 0.24$ m) is $v = 5$ m/s, combining with the density and viscosity of water around 20°C, resulting in $\Delta v \approx 4 \times 10^{-6}$ m/s. This is several orders of magnitude smaller than the typical velocity fluctuation inside the TC-gap of order 10^{-1} m/s and hence centrifugal forces on the seeding particles are negligible.

For TC flow a stable and well-known flow state is solid body rotation; the inner and outer cylinder are both rotated at a fixed speed ω. After sufficient waiting the fluid will have a velocity $u_\phi = \omega r$, and $u_z = u_r = 0$. The experiment has been performed for three rotation rates ω ($\omega/2\pi = 1$ Hz, 2 Hz, and 4 Hz), where the azimuthal velocity has been measured at several radial positions and at mid height. Similar results were found for all three cases, Fig. 8.7 shows the results for the case of $\omega/(2\pi) = 2$ Hz.

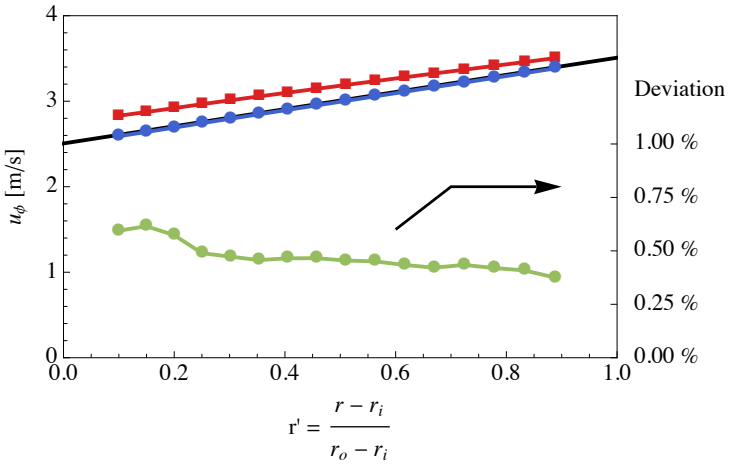

Figure 8.7: In red squares the *uncorrected* azimuthal velocity as a function of radial position is shown, and in blue dots the *corrected* azimuthal velocity. The black solid line is the theoretical flow profile $u_\phi = \omega r$, the deviation from this profile is plotted with green dots, the corresponding scale is on the right. The theoretical and corrected measured profiles are found to be in good accordance.

The measured velocities are shown in red squares, after applying the beam angle correction the data points (blue circles) are found to agree with the theoretical flow profile within 0.75%. Any remaining deviation can be due to *e.g.* optical misalignment or imperfection, spatially inhomogeneous refractive index in the working fluid, or noise created by the amplification and digitalisation

of the optical signal.

8.6 Application

Here the results are shown for the measurement of the azimuthal velocity profile for the case that the inner cylinder is stationary and the outer cylinder is rotating. This case has been studied before [14, 30], and because the flow is laminar, any perturbation due to a measuring probe is likely to survive a full revolution. To accurately obtain the speed of the (undisturbed) flow, it has to be measured non-intrusively. Fig. 8.8 shows the results of three experiments having varying Reynolds number ($Re = \omega_o r_o (r_o - r_i)/\nu$).

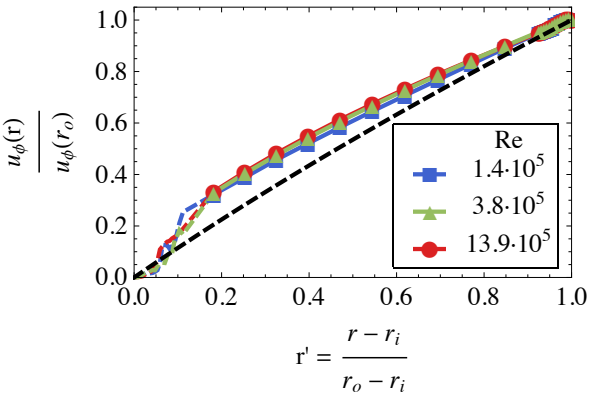

Figure 8.8: For three rotation rates the azimuthal velocity is measured along the gap. This velocity is normalized by the driving velocity in order to collapse the data, and compared to the laminar velocity profile for infinite aspect ratio (dashed line). The profile is found to be nearly independent of the Reynolds number.

For three rotation rates the obtained profiles are found to collapse over a decade of Reynolds number, but deviate from the laminar velocity profile for infinite aspect-ratio. Due to a finite aspect ratio of the setup the presence of the end plates will create a secondary flow, modifying the azimuthal velocity profile. The velocity close to the inner cylinder is currently unattainable by LDA due to reflections coming of the inner cylinder surface. These reflections create spurious, unreliable data and therefore the profiles are shown dashed

in that region. The present system will, in the future, be equipped with a transparent inner cylinder, which will significantly reduce the reflections.

8.7 Conclusion

In order to measure correct velocities inside a TC apparatus using LDA, one has to correct for the effects of the curved interfaces. Not only do the positions of the measurement volumes depend non-trivially on the position of the laser head, but also the measured velocity has to be corrected. A ray tracer has been used in order to calculate the position of the foci, but also to calculate the correction factor C_θ as a function of radial position. We showed that for our application it is crucial to take into account both interfaces of the outer cylinder. The measurement positions do not coincide and the velocity has to be corrected even at $r = r_o$. Our ray-tracer is verified by measuring the velocity for the case of solid body rotation; good agreement with the theoretical prediction has been found. For pure outer cylinder rotation it is found that the velocity deviates from the laminar velocity profile for infinite aspect ratio due to the presence of the end plates.

Appendix

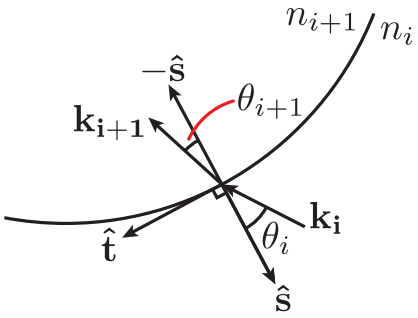

Figure 8.9: Sketch of the rays in the plane of refraction.

For each interface one has to solve Snell's law $n_i(\widehat{\mathbf{k_i}} \times \widehat{\mathbf{s}}) = n_{i+1}(\widehat{\mathbf{k_{i+1}}} \times \widehat{\mathbf{s}})$ for $\mathbf{k_{i+1}}$. From the vector equation one can see that the solution is not unique; but the solution is unique if we require the solution to be in the plane spanned by $\widehat{\mathbf{s}}$ and $\widehat{\mathbf{k_i}}$ (called the plane of refraction). In this plane the solution can be rewritten as follows: $n_i \sin(\theta_i) = n_{i+1} \sin(\theta_{i+1})$. $\mathbf{k_{i+1}}$ can be decomposed in to two parts; one in the direction of $\widehat{\mathbf{s}}$ and one that is tangential to the interface and in the plane of refraction, denoted $\widehat{\mathbf{t}}$, see figure 8.9. By simple geometry one can find that $\mathbf{k_{i+1}} = \sin(\theta_{i+1})\widehat{\mathbf{t}} + \cos(\theta_{i+1})(-\widehat{\mathbf{s}})$. The direction of $\mathbf{t}$ can be found by subtracting the normal component of the incident ray: $\mathbf{t} = \widehat{\mathbf{k_i}} - (\widehat{\mathbf{k_i}} \cdot \widehat{\mathbf{s}})\widehat{\mathbf{s}}$. From the definition of the cross product ($|\mathbf{a} \times \mathbf{b}| = |\mathbf{a}||\mathbf{b}| \sin(\alpha)$, where α is the angle between vectors $\mathbf{a}$ and $\mathbf{b}$) and Snell's law, one can derive that $\sin(\theta_{i+1}) = \frac{n_1}{n_2} \left| \widehat{\mathbf{k_i}} \times \widehat{\mathbf{s}} \right|$, and using the Pythagorean identity one writes $\cos(\theta_{i+1}) = \sqrt{1 - \sin(\theta_{i+1})^2}$. Note that one does not need to calculate the angles θ_i or θ_{i+1}, it is only necessary to know the sine and or cosine of the angles. The direction for the outgoing ray can now be found by substituting all the values: $\mathbf{k_{i+1}} = \sin(\theta_{i+1})\widehat{\mathbf{t}} + \cos(\theta_{i+1})(-\widehat{\mathbf{s}})$.

Conclusions

In this thesis high Reynolds number Taylor-Couette flow has been examined. We set out to explore *'terra incognita'*, and done so by performing local and global measurements in the Twente turbulent Taylor-Couette facility[21]. The predictive power of highly turbulent Taylor-Couette flow has grown significantly due to the results presented in this thesis. The major findings of each chapter are listed below.

In chapter 1 (page 5) the *'terra incognita'* was defined, and we were the first to explore it. During the exploration of the unknown land (figure 1.1, page 8) we found that not only for inner-cylinder rotation but also for counterrotation and in the linearly unstable regime $G \propto \mathrm{Re}^{1.76}$ [9], or a universal scaling exponent $\gamma = 0.38$ for $\mathrm{Nu}_\omega \propto \mathrm{Ta}^\gamma$ (in the present Ta regime) in the terminology borrowed from Rayleigh-Bénard (figure 1.3, page 11); showing and confirming the analogy between the two systems[1]. We defined the new driving ratio $a = -\omega_o/\omega_i$ which focuses on the counterrotation phase space, and found that the torque (transport of angular velocity) scales best if one follows a path in phase space with constant a. Surprisingly, it was found that the transport is enhanced for slight counter-rotation and that the transport maximizes for $a \approx 0.4$, having over 20% more transport as compared to the case of pure inner cylinder rotation $a = 0$, see figure 1.4 (page 12).

In chapter 2 (page 15) we set out to measure the *local* flow properties. We did so using particle imaging velocimetry for the case of fixed outer cylinder ($a = 0$). We found that the wind Reynolds number $\mathrm{Re}_w = 0.0424\mathrm{Ta}^{0.495\pm0.010}$ over more than 3 decades in Taylor number: $3.8 \cdot 10^9 < \mathrm{Ta} < 6.2 \cdot 10^{12}$, see figure 2.1 (page 18). This scaling is consistent with the prediction $\mathrm{Re}_w \propto \mathrm{Ta}^{1/2}$ made by [2], but inconsistent with predictions made for thermal convection [29] which can be translated to the Taylor-Couette language using [1]. From the Navier Stokes we can find that the local transport is given by: $J_\omega = r^3 \left(u_r\omega - \nu\partial_r\omega\right)$ [1]. Where the convective term dominates the diffusive term in the bulk once we average over time (and space). We show that u_r and ω

are indeed positively correlated (which is needed to have a positive convective transport outwards) by simultaneously measuring both u_r and ω, see figure 2.4 (page 24). In addition, we found that the local convective angular velocity flux fluctuates tremendously in time and space; for the case of $\mathrm{Ta} = 1.5 \cdot 10^{12}$ we find that Nu_ω ranges from -10^5 to 10^5 and beyond while the average is $\mathrm{Nu}_\omega = \mathcal{O}(300)$, see figure 2.2 (page 20) for the standardized normalized local convective angular velocity flux probability density function. We found that the transport has a height dependence, but that the global results—obtained by torque measurements—were reproduced copacetically, see figure 2.3 (page 23).

In chapter 3 (page 25) we performed high resolution profile measurements using particle imaging velocimetry. The mean velocity distribution was computed using a single-pixel ensemble correlation method [65, 73], which provided a very high spatial resolution, see figure 3.2 (page 29). Using the global torque values we were able to calculate the wall stress τ_w and plot our profiles in terms of wall units, see figure 3.3 on page 30. We see the emergence of a log-profile for increasing Ta, and fit the law of the wall $u^+ = 1/\kappa \ln y^+ + B$ to these profiles. We find that the inverse prefactor (κ) goes towards its classical value of 0.4 for increasing Ta, see figure 3.4 (page 32). We note that the law of the wall was derived under the assumption of a flat wall, we therefore look at the ratio of the upper edge of our fitting regime to the radius of curvature of the cylinder to quantify the possible influence of the curvature. We find that this ratio goes to $\approx 1\%$ for $\mathrm{Ta} = 10^{12}$, and that a significant influence of the curvature can not be excluded for lower Taylor numbers, see figure 3.4 (page 32). Furthermore, the variance of the local azimuthal velocity was calculated for the boundary layer of the inner cylinder, see figure 3.5 on page 34. We found that the height of the peak of the variance collapses best when the velocity is rescaled with the driving velocity rather than the wall velocity, and that the peak is around $y^+ = 12$; as found in pipe and channel flows (see *e.g.* [59, 60]). Lastly, we also find the log-law for the velocity variance—as found by [62]—for $y^+ > 50$, see figure 3.5 on page 34.

In chapter 4 (page 37) the possibility of multiple states for very high Reynolds number is demonstrated by combined global (torque) and local (laser Doppler anemometry) measurements. The Twente turbulent Taylor-Couette [21] was upgraded and outfitted with a hollow flanged reaction torque transducer, improving the accuracy of the measurements. With this new sensor the transport was found to scale as $\mathrm{Nu}_\omega \propto \mathrm{Ta}^{0.40}$ as opposed to previous measurements indicating an exponent of ≈ 0.38. It was thought that local structures would

vanish for sufficiently high Reynolds numbers, and indeed this was the conclusion of Ref. [63], which showed that for $a = 0$ the structure seems to disappear for $\mathrm{Re} = 1.2 \cdot 10^5$. We did not find any clear roll structure for the case of $a = 0$ for $\mathrm{Re} = 10^6$ ($\mathrm{Ta} = 10^{12}$) in the laser Doppler anemometry data, but *did* find them for $a \neq 0$ for the same Ta, see figures 4.3c and 4.3d on page 44. Furthermore, once a trajectory in phase-space was traversed (see figure 4.2 on page 40), it was found that the system was hysteretic and that it can go in to a 'high' or a 'low' state, see figure 4.3 on page 44. It was found that multiple states can occur for rotation ratios $0.17 < a < 0.51$. For $0 \leq a \leq 0.17$ we only found one state, and for $a > 0.51$ we could not find a clear roll structure in the system. The presence of flow structure for such high Reynolds number questions Kolmogorov's paradigm, though structures might disappear for even much higher Taylor numbers. The value for a_{opt} was improved from $a = 0.4$ (chapter 1, page 5) and $a = 0.33 \pm 0.04$ (chapter 6, page 67) to $a = 0.36 \pm 0.005$. Our results also suggest that the optimal transport is connected to the existence of very stable and strong coherent structures inside the fluid.

In chapter 5 (page 49) the statistical properties of the velocity fluctuations of the local flow were examined. The local velocity was measured using laser Doppler anemometry for varying amounts of counterrotation (*i.e.* changing a), see figures 5.1 (page 51) and 5.2 (page 54). For various a between 0 and 2 we measure $5 \cdot 10^6$ data points and carefully perform statistical analysis on them. We find that for all powers p and for all a the longitudinal structure functions do not show an inertial subrange. Using extended self-similarity [96] we extract the structure functions exponents. We find that they are in good agreement with results found by [10] using hot-film anemometry, which did similar analysis but only for $a = 0$ and for $\mathrm{Re} = 6.9 \cdot 10^4$ and $\mathrm{Re} = 5.4 \cdot 10^5$, while the current findings are for $\mathrm{Re} = 1.38 \cdot 10^6$. It was found that the exponents are almost independent of Re over the range $\mathrm{Re} = 6.9 \cdot 10^4$–$1.38 \cdot 10^6$, or roughly 2.6 decades in Taylor number. Furthermore, it seems that the exponents only weakly depend on the amount of counter-rotation, though for $a \geq 1$ we find that for $p = 6$ the exponents are slightly higher than for $0 \leq a < 1$. We find that for $a \in \{0.6, 0.8, 1.0\}$ the spectra shows a clear power law scaling in the spectra, while for $a \in \{0.2, 0.3, 0.4, 2\}$ the power law is less clear, and for $a = 0$ there is no power law at all. For $a = 0$ we find that the exponent is a constantly changing and does not show any Kolmogorov inertial subrange scaling of $-5/3$. Though we find clear power law scaling in the spectra for $a \in \{0.6, 0.8, 1.0\}$, we do not see clear scaling in

the second-order structure functions.

In chapter 6 (page 67) global measurements were performed in order to enhance the resolution of figure 1.4, and to get new insight by performing global measurement using laser Doppler anemometry as well. In this chapter we find that the optimal is at $a_{\mathrm{opt}} = 0.33 \pm 0.04$, and improvement of the $a_{\mathrm{opt}} = 0.4$ found in chapter 1 (page 5), though we later improved the resolution of a_{opt} to $a = 0.36 \pm 0.005$ in chapter 4 (page 37). We find that (compared to the case of $a = 0$) the transport is enhanced if counter rotation is added by the outer cylinder, despite the stabilizing effect of the outer cylinder. Once one increases the outer cylinder rotation more the stabilizing effect takes over and reduces the transport. We find that the velocity gradient goes to zero in the bulk for a around a_{opt}, and we find that for $0 < a < a_{\mathrm{opt}}$ we do not see the 'neutral line' inside the bulk of the flow; the neutral line is somewhere very close to the outer cylinder. In addition, in this range of a we find that the velocity if monomodal. For $a > a_{\mathrm{opt}}$ we *do* find a neutral line in the bulk of the flow, and the probability density function of the flow becomes bimodal. We provide a hypothesis to understand the bimodality in combination with the neutral line.

In chapter 7 (page 109) we set out to explore the η dependence of Taylor-Couette flow. This was done both numerically (the work of Rodolfo Ostilla Mónico) and experimentally. The radius ratio was changed from 0.5 to 0.909 in the numerics and 0.716 to 0.909 in experiments. We find that the transport has an exponent $\gamma \approx 0.39$ for the high Ta, *i.e.* $\mathrm{Nu}_\omega \propto \mathrm{Ta}^{0.39}$, independent of the rotation ratio a and η, see figures 7.4 (page 123) and 7.7 (page 128). We find that for high Taylor number the optimum a—the a with the heighest transport—depends on the radius ratio η if one expresses it in terms of the Rossby number: $\mathrm{Ro}_{\mathrm{opt}}^{-1} = -0.20$ ($\eta = 0.716$), $\mathrm{Ro}_{\mathrm{opt}}^{-1} = -0.15$ ($\eta = 0.769$), $\mathrm{Ro}_{\mathrm{opt}}^{-1} = -0.10$ ($\eta = 0.833$), $\mathrm{Ro}_{\mathrm{opt}}^{-1} = -0.05$ ($\eta = 0.909$), but roughly collapses in terms of a: $a \approx 0.33$–0.35 for all η examined (see figures 7.9 on page 131 and 7.10 on page 132). Also local velocity profiles were measured using laser Doppler anemometry (and obtained in the DNS simulations). It was found that for $a = a_{\mathrm{opt}}$ ($\mathrm{Ro}^{-1} = \mathrm{Ro}_{\mathrm{opt}}^{-1}$) and for all η that the velocity profiles are remarkably flat in the bulk.

In chapter 8 (page 147) we show how one can perform laser Doppler measurements inside a Taylor-Couette apparatus. The measurement of the velocity using laser Doppler anemometry is complicated by the curved surface of the outer cylinder. We explain how the LDA-rays can be traced using a 3D ray tracer. We show how the measurements position depends non-trivially on the

position of the laser head, and how the velocity of the measured velocity is affected by the curvature of the outer cylinder (figure 8.6 on page 156). In addition we show that it is crucial to take the refraction at both interfaces of the outer cylinder in to account. We test out the ray-tracer by measuring flow of solid body rotation, see figure 8.7 on page 157. The corrected flow profile is benchmarked against high resolution magnetic encoders and we find that the error has been substantially reduced and is within 0.75% of the expected profile. In the appendix of that chapter (page 160) the algorithm is detailed and it is shown how the algorithm can be implemented without the use of trigonometric functions.

References

[1] B. Eckhardt, S. Grossmann, and D. Lohse, "Torque scaling in turbulent Taylor-Couette flow between independently rotating cylinders", J. Fluid Mech. **581**, 221–250 (2007).

[2] S. Grossmann and D. Lohse, "Multiple scaling in the ultimate regime of thermal convection", Phys. Fluids **23**, 045108 (2011).

[3] A. G. Smart, "Exploring the extremes of turbulence", Physics Today **64**, 18 (2011).

[4] P. Bradshaw, "The analogy between streamline curvature and buoyancy in turbulent shear flow", J. Fluid Mech. **36**, 177–191 (1969).

[5] B. Dubrulle and F. Hersant, "Momentum transport and torque scaling in Taylor-Couette flow from an analogy with turbulent convection", Eur. Phys. J. B **26**, 379–386 (2002).

[6] G. Ahlers, S. Grossmann, and D. Lohse, "Heat transfer and large scale dynamics in turbulent Rayleigh-Bénard convection", Rev. Mod. Phys. **81**, 503 (2009).

[7] D. Lohse and K.-Q. Xia, "Small-scale properties of turbulent Rayleigh-Bénard convection", Ann. Rev. Fluid Mech. **42**, 335–364 (2010).

[8] D. P. Lathrop, J. Fineberg, and H. L. Swinney, "Transition to shear-driven turbulence in Couette-Taylor flow", Phys. Rev. A **46**, 6390–6405 (1992).

[9] D. P. Lathrop, J. Fineberg, and H. L. Swinney, "Turbulent flow between concentric rotating cylinders at large Reynolds numbers", Phys. Rev. Lett. **68**, 1515–1518 (1992).

[10] G. S. Lewis and H. L. Swinney, "Velocity structure functions, scaling, and transitions in high-Reynolds-number Couette-Taylor flow", Phys. Rev. E **59**, 5457–5467 (1999).

[11] T. H. van den Berg, C. Doering, D. Lohse, and D. Lathrop, "Smooth and rough boundaries in turbulent Taylor-Couette flow", Phys. Rev. E **68**, 036307 (2003).

[12] B. Eckhardt, S. Grossmann, and D. Lohse, "Scaling of global momentum transport in Taylor-Couette and pipe flow", Eur. Phys. J. B **18**, 541–544 (2000).

[13] B. Eckhardt, S. Grossmann, and D. Lohse, "Fluxes and energy dissipation in thermal convection and shear flows", Europhys. Lett. **24001**, 78 (2007).

[14] F. Wendt, "Turbulente Strömungen zwischen zwei rotierenden konaxialen Zylindern", Arch. Applied Mech. **4**, 577–595 (1933).

[15] F. Ravelet, R. Delfos, and J. Westerweel, "Influence of global rotation and reynolds number on the large-scale features of a turbulent Taylor-Couette flow", Phys. Fluids **22**, 055103 (2010).

[16] B. Dubrulle, O. Dauchot, F. Daviaud, P.-Y. Longaretti, D. Richard, , and J.-P. Zahn, "Stability and turbulent transport in taylor–couette flow from analysis of experimental data", Phys. Fluids (2005).

[17] A. Esser and S. Grossmann, "Analytic expression for Taylor-Couette stability boundary", Phys. Fluids **8**, 1814–1819 (1996).

[18] C. D. Andereck, S. S. Liu, and H. L. Swinney, "Flow regimes in a circular Couette system with independently rotating cylinders", J. Fluid Mech. **164**, 155 (1986).

[19] G. Pfister and I. Rehberg, "Space dependent order parameter in circular couette flow transitions", Phys. Lett. **83**, 19–22 (1981).

[20] M. C. Cross and P. C. Hohenberg, "Pattern formation outside of equilibrium", Rev. Mod. Phys. **65**, 851 (1993).

[21] D. P. M. van Gils, G.-W. Bruggert, D. P. Lathrop, C. Sun, and D. Lohse, "The Twente turbulent Taylor–Couette (T3C) facility: Strongly turbulent (multiphase) flow between two independently rotating cylinders", Review of Scientific Instruments **82**, – (2011).

[22] J. Niemela, L. Skrbek, K. R. Sreenivasan, and R. Donnelly, "Turbulent convection at very high Rayleigh numbers", Nature **404**, 837–840 (2000).

[23] X. Chavanne, F. Chilla, B. Castaing, B. Hebral, B. Chabaud, and J. Chaussy, "Observation of the ultimate regime in Rayleigh-Bénard convection", Phys. Rev. Lett. **79**, 3648–3651 (1997).

[24] X. Chavanne, F. Chilla, B. Chabaud, B. Castaing, and B. Hebral, "Turbulent Rayleigh-Bénard convection in gaseous and liquid He", Phys. Fluids **13**, 1300–1320 (2001).

[25] F. H. Busse, "The twins of turbulence research", Physics **5**, 4 (2012).

[26] D. P. M. van Gils, S. G. Huisman, G. Bruggert, C. Sun, and D. Lohse, "Torque scaling in turbulent Taylor-Couette flow with co- and counter-rotating cylinders", Phys. Rev. Lett. **106** (2011).

[27] M. S. Paoletti and D. P. Lathrop, "Angular momentum transport in turbulent flow between independently rotating cylinders", Phys. Rev. Lett. **106**, 024501 (2011).

[28] G. Ahlers, D. Funfschilling, and E. Bodenschatz, "Addendum to transitions in heat transport by turbulent convection at Rayleigh numbers up to 10^{15}", New J. Phys. **13**, 049401 (2011).

[29] R. H. Kraichnan, "Turbulent thermal convection at arbritrary Prandtl number", Phys. Fluids **5**, 1374–1389 (1962).

[30] D. Coles and C. Van Atta, "Measured distortion of a laminar circular Couette flow by end effects", J. Fluid Mech. **25**, 513 (1966).

[31] G. P. Smith and A. A. Townsend, "Turbulent Couette flow between concentric cylinders at large Taylor numbers", J. Fluid Mech. **123**, 187–217 (1982).

[32] T. Mullin, G. Pfister, and A. Lorenzen, "New observations on hysteresis effects in Taylor-Couette flow", Phys. Fluids (1982).

[33] A. Lorenzen, G. Pfister, and T. Mullin, "End effects on the transition to time-dependent motion in the Taylor experiment", Phys. Fluids (1983).

[34] Z.-S. She, K. Ren, G. S. Lewis, and H. L. Swinney, "Scalings and structures in turbulent Couette-Taylor flow", Phys. Rev. E **64**, 016308 (2001).

[35] J. Langenberg, M. Heise, G. Pfister, and J. Abshagen, "Convective and absolute instabilities in counter-rotating spiral Poiseuille flow", Theor Comp Fluid Dyn **18**, 97–103 (2004).

[36] J. Abshagen, M. Heise, C. Hoffmann, and G. Pfister, "Direction reversal of a rotating wave in Taylor–Couette flow", J. Fluid Mech. (2008).

[37] Litron, LDY 300 Series, dual-cavity pulsed Nd:YLF PIV Laser System .

[38] Photron, FastCam 1024 PCI, operating at 1024 px $\times$ 1024 px resolution, and, at most $f = 1$ kHz .

[39] X.-L. Qiu and P. Tong, "Large-scale velocity structures in turbulent thermal convection", Phys. Rev. E **64**, 036304 (2001).

[40] X. He, D. Funfschilling, H. Nobach, E. Bodenschatz, and G. Ahlers, Submitted to Phys. Rev. Lett. (2011).

[41] D.P.M. van Gils, S. G. Huisman, S. Grossmann, C. Sun, and D. Lohse, "Optimal taylor-couette turbulence", J. Fluid Mech. **708**, 118 (2012).

[42] X. D. Shang, X. L. Qiu, P. Tong, and K.-Q. Xia, "Measured local heat transport in turbulent Rayleigh-Bénard convection", Phys. Rev. Lett. **90**, 074501 (2003).

[43] X. D. Shang, P. Tong, and K.-Q. Xia, "Scaling of the local convective heat flux in turbulent Rayleigh-Bénard convection", Phys. Rev. Lett. **100**, 244503 (2008).

[44] W. Shew, Y. Gasteuil, M. Gibert, P. Metz, and J. Pinton, "Instrumented tracer for Lagrangian measurements in Rayleigh-Bénard convection", Rev. Sci. Instr. **78**, 065105 (2007).

[45] S. Grossmann and D. Lohse, "Scaling in thermal convection: A unifying view", J. Fluid Mech. **407**, 27–56 (2000).

[46] S. Grossmann and D. Lohse, "Logarithmic temperature profiles in the ultimate regime of thermal convection", Phys. Fluids **24**, 125103 (2012).

[47] X. He, D. Funfschilling, H. Nobach, E. Bodenschatz, and G. Ahlers, "Transition to the ultimate state of turbulent rayleigh-bénard convection", Phys. Rev. Lett. **108**, 024502 (2012).

[48] G. I. Taylor, "Stability of a viscous liquid contained between two rotating cylinders", Philos. Trans. R. Soc. London Ser. A **223**, 289–343 (1923).

[49] S. Huisman, C. Sun, and D. Lohse, unpublished .

[50] C. Sun, Y. H. Cheung, and K. Q. Xia, "Experimental studies of the viscous boundary layer properties in turbulent Rayleigh-Bénard convection", J. Fluid Mech. **605**, 79 – 113 (2008).

[51] Q. Zhou and K. Q. Xia, "Measured instantaneous viscous boundary layer in turbulent rayleigh-bénard convection", Phys. Rev. Lett. **104**, 104301 (2010).

[52] S. T. Wereley and R. M. Lueptow, "Spatio-temporal character of non-wavy and wavy taylor couette flow", J. Fluid Mech. **364**, 59–80 (1998).

[53] S. Dong, "Direct numerical simulation of turbulent Taylor-Couette flow", J. Fluid Mech. **587**, 373–393 (2007).

[54] R. van Hout and J. Katz, "Measurements of mean flow and turbulence characteristics in high-reynolds number counter-rotating taylor-couette flow", Phys. Fluids **23**, 105102 (2011).

[55] R. Ostilla, R. J. A. M. Stevens, S. Grossmann, R. Verzicco, and D. Lohse, "Optimal taylor–couette flow: direct numerical simulations", J. Fluid Mech. **719**, 14–46 (2013).

[56] H. J. Brauckmann and B. Eckhardt, "Direct numerical simulations of local and global torque in taylor–couette flow up to re = 30 000", J. Fluid Mech. **718**, 398–427 (2013).

[57] G. Ahlers, E. Bodenschatz, D. Funfschilling, S. Grossmann, X. He, D. Lohse, R. J. A. M. Stevens, and R. Verzicco, "Logarithmic temperature profiles in turbulent rayleigh-bénard convection", Phys. Rev. Lett. **109**, 114501 (2012).

[58] T. Wei and W. W. Willmarth, "Reynolds-number effects on the structure of a turbulent channel flow", J. Fluid Mech. **204**, 57–95 (1989).

[59] I. Marusic, B. J. McKeon, P. A. Monkewitz, H. M. Nagib, A. J. Smits, and K. R. Sreenivasan, "Wall-bounded turbulent flows at high reynolds numbers: Recent advances and key issues", Phys. Fluids **22**, 065103 (2010).

[60] M. Hultmark, M. Vallikivi, S. C. C. Bailey, and A. J. Smits, "Turbulent pipe flow at extreme reynolds numbers", Phys. Rev. Lett. **108**, 094501 (2012).

[61] I. Marusic, J. P. Monty, M. Hultmark, and A. J. Smits, "On the logarithmic region in wall turbulence", J. Fluid Mech. **716**, R3 (2013).

[62] C. Meneveau and I. Marusic, "Generalized logarithmic law for high-order moments in turbulent boundary layers", J. Fluid Mech. **719**, R1 (2013).

[63] D. P. Lathrop, J. Fineberg, and H. L. Swinney, "Transition to shear-driven turbulence in couette-taylor flow", Phys. Rev. A **46**, 6390–6405 (1992).

[64] S. G. Huisman, D. P. M. van Gils, S. Grossmann, C. Sun, and D. Lohse, "Ultimate turbulent Taylor-Couette flow", Phys. Rev. Lett. **108**, 024501 (2012).

[65] C. J. Kähler, S. Scharnowski, and C. Cierpka, "On the resolution limit of digital particle image velocimetry", Exp. Fluids **52**, 1629–1639 (2012).

[66] C. J. Kähler, S. Scharnowski, and C. Cierpka, "On the uncertainty of digital piv and ptv near walls", Exp. Fluids **52**, 1641–1656 (2012).

[67] S. Scharnowski, R. Hain, and C. J. Kähler, "Reynolds stress estimation up to single-pixel resolution using piv-measurements", Exp. Fluids **52**, 985–1002 (2012).

[68] H. Ji, M. Burin, E. Schartman, and J. Goodman, "Hydrodynamic turbulence cannot transport angular momentum effectively in astrophysical disks", Nature (2006).

[69] S. Merbold, H. J. Brauckmann, and C. Egbers, "Torque measurements and numerical determination in differentially rotating wide gap taylor-couette flow", Phys. Rev. E **87**, 023014 (2013).

[70] Dantec, `FPP-RhB-10`, fluorescent polymer tracer particles 1–20 µm water suspension .

[71] Innolas, Flash lamp-pumped Nd:YAG laser Spitlight 400 .

[72] pco, pco.edge camera, 2560px × 2160px resolution with 6.5 µm pixel size in front a 50 mm objective lens is mounted with a working distance of approximately 600 mm giving a scaling factor of ≈ 54 µm/px .

[73] C. J. Kähler, U. Scholz, and J. Ortmanns, "Wall-shear-stress and near-wall turbulence measurements up to single pixel resolution by means of long-distance micro-piv", Experiments in Fluids **41**, 327–341 (2006).

[74] Infinity, K2 long-distance microscope focal length of 300 mm .

[75] S. B. Pope, *Turbulent Flows* (Cambridge University Press, , Cambridge) (2000).

[76] S. A. Balbus, "Enhanced angular momentum transport in accretion disks", Annu. Rev. Astronomy and Astrophysics **41**, 555–597 (2003).

[77] H. Ji and S. Balbus, "Angular momentum transport in astrophysics and in the lab", Phys. Today **66**, 27–33 (2013).

[78] A. N. Kolmogorov, "The local structure of turbulence in imcompressible viscous fluid for very large Reynolds numbers", Dokl. Akad. Nauk. SSSR. **30**, 299–303 (1941).

[79] A. N. Kolmogorov, "On degeneration of isotropic turbulence in an incompressible viscous liquid", Dokl. Akad. Nauk. SSSR. **31** (1941).

[80] H.-D. Xi and K.-Q. Xia, "Flow mode transitions in turbulent thermal convection", Physics of Fluids (1994-present) **20**, – (2008).

[81] E. P. van der Poel, R. J. A. M. Stevens, and D. Lohse, "Connecting flow structures and heat flux in turbulent Rayleigh-Bénard convection", Phys. Rev. E **84**, 045303 (2011).

[82] S. Weiss and G. Ahlers, "Effect of tilting on turbulent convection: cylindrical samples with aspect ratio Γ=0.50", J. Fluid. Mech. **715**, 314–334 (2013).

[83] G. Ahlers, D. Funfschilling, and E. Bodenschatz, "Heat transport in turbulent Rayleigh-Bénard convection for Pr $\simeq$ 0.8 and Ra $\lesssim 10^{15}$", J. Phys.: Conf. Series **318**, 082001 (2011).

[84] F. Ravelet, L. Marié, A. Chiffaudel, and F. Daviaud, "Multistability and memory effect in a highly turbulent flow: Experimental evidence for a global bifurcation", Phys. Rev. Lett. **93**, 164501 (2004).

[85] F. Ravelet, A. Chiffaudel, and F. Daviaud, "Supercritical transition to turbulence in an inertially driven von Kámán closed flow", J. Fluid Mech. **601**, 339–364 (2008).

[86] P.-P. Cortet, A. Chiffaudel, F. Daviaud, and B. Dubrulle, "Experimental evidence of a phase transition in a closed turbulent flow", Phys. Rev. Lett. **105**, 214501 (2010).

[87] D. S. Zimmerman, S. A. Triana, and D. P. Lathrop, "Bi-stability in turbulent, rotating spherical Couette flow", Physics of Fluids (1994-present) **23**, – (2011).

[88] R. Ostilla-Mónico, E. P. van der Poel, R. Verzicco, S. Grossmann, and D. Lohse, "Boundary layer dynamics at the transition between the classical and the ultimate regime of Taylor-Couette flow", Physics of Fluids (1994-present) **26**, – (2014).

[89] S. G. Huisman, S. Scharnowski, C. Cierpka, C. Kähler, D. Lohse, and C. Sun, "Logarithmic boundary layers in strong Taylor-Couette turbulence", Phys. Rev. Lett. **110**, 264501 (2013).

[90] P. R. Fenstermacher, H. L. Swinney, and J. P. Gollub, "Dynamical instabilities and the transition to chaotic Taylor vortex flow", J. Fluid Mech. **94**, 103–128 (1979).

[91] S. G. Huisman, D. P. van Gils, and C. Sun, "Applying laser doppler anemometry inside a taylor–couette geometry using a ray-tracer to correct for curvature effects", European Journal of Mechanics - B/Fluids **36**, 115 – 119 (2012).

[92] A. Chouippe, "Etude numérique de la réduction de traînée par injection de bulles en écoulement de Taylor-Couette", PhD thesis, l'Institute National Polytechnique de Toulouse (INPT) (2012).

[93] M. López-Caballero and J. Burguete, "Inverse cascades sustained by the transfer rate of angular momentum in a 3d turbulent flow", Phys. Rev. Lett. **110**, 124501 (2013).

[94] G. I. Taylor, "Stability of a viscous liquid contained between two rotating cylinders", Phil. Trans. R. Soc. Lond. A **223**, 289 (1923).

[95] H. Ji, M. Burin, E. Schartman, and J. Goodman, "Hydrodynamic turbulence cannot transport angular momentum effectively in astrophysical disks", Nature **444**, 343–346 (2006).

[96] R. Benzi, S. Ciliberto, R. Tripiccione, C. Baudet, F. Massaioli, and S. Succi, "Extended self-similarity in turbulent flows", Phys. Rev. E **48**, R29–R32 (1993).

[97] U. Frisch, *Turbulence* (Cambridge University Press, Cambridge) (1995).

[98] S. Grossmann, D. Lohse, and A. Reeh, "Different intermittency for longitudinal and transversal turbulent fluctuations", Physics of Fluids **9**, 3817–3825 (1997).

[99] S. Grossmann, D. Lohse, and A. Reeh, "Application of extended self-similarity in turbulence", Phys. Rev. E **56**, 5473–5478 (1997).

[100] G. Stolovitzky and K. R. Sreenivasan, "Scaling of structure functions", Phys. Rev. E **48**, R33–R36 (1993).

[101] J. Herweijer and W. van de Water, "Universal shape of scaling functions in turbulence", Phys. Rev. Lett. **74**, 4651–4654 (1995).

[102] R. Ostilla, R. J. A. M. Stevens, S. Grossmann, R. Verzicco, and D. Lohse, "Optimal taylor–couette flow: direct numerical simulations", J. Fluid Mech. **719**, 14–46 (2013).

[103] Z.-S. She and E. Leveque, "Universal scaling laws in fully developed turbulence", Phys. Rev. Lett. **72**, 336–339 (1994).

[104] S. Grossmann, D. Lohse, and A. Reeh, "Scaling of the irreducible so(3)-invariants of velocity correlations in turbulence", Journal of Statistical Physics **93**, 715–724 (1998).

[105] L. Biferale and I. Procaccia, "Anisotropy in turbulent flows and in turbulent transport", Physics Reports **414**, 43 – 164 (2005).

[106] D. Coles, "Transition in circular Couette flow", J. Fluid Mech. **21**, 385–425 (1965).

[107] R. C. DiPrima and H. L. Swinney, "Instabilities and transition in flow between concentric rotating cylinders", Hydrodynamic Instabilities and the Transition to Turbulence (ed. H. L. Swinney & J. P. Gollub), Springer. (1981).

[108] T. Mullin, K. A. Cliffe, and G. Pfister, "Unusal time-dependent phenomena in Taylor-Couette flow at moderately low Reynolds-numbers", Phys. Rev. Lett. **58**, 2212–2215 (1987).

[109] G. Pfister, H. Schmidt, K. A. Cliffe, and T. Mullin, "Bifurcation phenomena in Taylor-Couette flow in a very short annulus", J. Fluid Mech. **191**, 1–18 (1988).

[110] P. Buchel, M. Lucke, D. Roth, and R. Schmitz, "Pattern selection in the absolutely unstable regime as a nonlinear eigenvalue problem: Taylor vortices in axial flow", Phys. Rev. E **53**, 4764–4777 (1996).

[111] D. Richard, "Instabilités Hydrodynamiques dans les Ecoulements en Rotation Différentielle", Ph.D. thesis, Université Paris VII (2001).

[112] D. Borrero-Echeverry, M. F. Schatz, and R. Tagg, "Transient turbulence in Taylor-Couette flow", Phys. Rev. E **81** (2010).

[113] M. J. Bruin, E. Schartman, and H. Ji, "Local measurements of turbulent angular momentum transport in circular couette flow", Exp. Fluids **48**, 763–769 (2010).

[114] F. H. Busse, "The bounding theory of turbulence and its physical significance in the case of turbulent Couette flow", Statistical models and turbulence, the Springer Lecture Notes in Physics **12**, 103 (1972).

[115] D. Coles and C. van Atta, "Measured distortion of a laminar circular Couette flow by end effects", J. Fluid Mech. **25**, 513 (1966).

[116] R. Hollerbach and A. Fournier, "End-effects in rapidly rotating cylindrical Taylor-Couette flow", in *MHD Couette flows: experiments and models*, edited by R. Rosner, G. Rudiger, and A. Bonanno, volume 733 of *AIP conference proceedings*, 114–121, INAF; Catania Univ; Banca Roma (American Institute of Physics) (2004).

[117] R. Tagg, "The Couette-Taylor problem", Nonlinear Science Today **4**, 1 (1994).

[118] L. D. Landau and E. M. Lifshitz, *Fluid Mechanics* (Pergamon Press, Oxford) (1987).

[119] H. P. Greenspan, *The theory of rotating fluids* (Breukelen Press, USA) (1990).

[120] M. A. Dominguez-Lerma, G. Ahlers, and D. S. Cannell, "Marginal stability curve and linear growth rate for rotating Couette-Taylor flow and Rayleigh-Bénard convection", Phys. Fluids **27**, 856 (1984).

[121] M. A. Dominguez-Lerma, D. S. Cannell, and G. Ahlers, "Eckhaus boundary and wave-number selection in rotating Couette-Taylor flow", Phys. Rev. A **34**, 4956–4970 (1986).

[122] P. E. Roche, B. Castaing, B. Chabaud, and B. Hebral, "Observation of the 1/2 power law in Rayleigh-Bénard convection", Phys. Rev. E **63**, 045303 (2001).

[123] D. Lohse and F. Toschi, "The ultimate state of thermal convection", Phys. Rev. Lett. **90**, 034502 (2003).

[124] E. Calzavarini, D. Lohse, F. Toschi, and R. Tripiccione, "Rayleigh and Prandtl number scaling in the bulk of Rayleigh-Bénard turbulence", Phys. Fluids **17**, 055107 (2005).

[125] C. Doering and P. Constantin, "Variational bounds on energy-dissipation in incompressible flow: shear flow", Phys. Rev. E **49**, 4087–4099 (1994).

[126] K. Sugiyama, E. Calzavarini, S. Grossmann, and D. Lohse, "Non-Oberbeck-Boussinesq effects in Rayleigh-Bénard convection:beyond boundary-layer theory", Europhys. Lett. **80**, 34002 (2007).

[127] S. Grossmann and D. Lohse, "Thermal convection for large Prandtl number", Phys. Rev. Lett. **86**, 3316–3319 (2001).

[128] S. Grossmann and D. Lohse, "Prandtl and Rayleigh number dependence of the Reynolds number in turbulent thermal convection", Phys. Rev. E **66**, 016305 (2002).

[129] S. Grossmann and D. Lohse, "Fluctuations in turbulent Rayleigh-Bénard convection: The role of plumes", Phys. Fluids **16**, 4462–4472 (2004).

[130] H. Effinger and S. Grossmann, "Static structure function of turbulent flow from the Navier-Stokes equation", Z. Phys. B **66**, 289 (1987).

[131] Q. Zhou, R. J. A. M. Stevens, K. Sugiyama, S. Grossmann, D. Lohse, and K.-Q. Xia, "Prandtl-Blasius temperature and velocity boundary layer profiles in turbulent Rayleigh-Bénard convection", J. Fluid Mech. **664**, 297 (2010).

[132] S. Grossmann, "The onset of shear flow turbulence", Rev. Mod. Phys. **72**, 603–618 (2000).

[133] C. Dutcher and S. Muller, "Explicit analytic formulas for Newtonian Taylor-Couette primary instabilities", Phys. Rev. E **75**, 047301 (2007).

[134] P. S. Marcus, "Simulation of Taylor-Couette flow. Part 1. Numerical methods and comparison with experiment", J. Fluid Mech. **146**, 45–64 (1984).

[135] S. T. Wereley and R. M. Lueptow, "Azimuthal velocity in supercritical circular Couette flow", Exp. Fluids **18**, 1–9 (1994).

[136] K. Coughlin and P. S. Marcus, "Turbulent Bursts in Couette-Taylor Flow", Phys. Rev. Lett. **77**, 2214–2217 (1996).

[137] H. L. Swinney and J. P. Gollub, *Hydrodynamic instabilities and the transition to turbulence*, volume 45 (Topics in Applied Physics) (Springer-Verlag, Berlin) (1981).

[138] S. Chandrasekhar, *Hydrodynamic and Hydromagnetic Stability* (Dover, New York) (1981).

[139] P. Drazin and W. H. Reid, *Hydrodynamic stability* (Cambridge University Press, Cambridge) (1981).

[140] F. H. Busse, "The stability of finite amplitude cellular convection and its relation to an extremum principle", J. Fluid Mech. **30**, 625–649 (1967).

[141] E. N. Lorenz, "Deterministic nonperiodic flow", J. Atmos. Sci **20**, 130–141 (1963).

[142] G. Ahlers, "Low temperature studies of the Rayleigh-Bénard instability and turbulence", Phys. Rev. Lett. **33**, 1185–1188 (1974).

[143] R. P. Behringer, "Rayleigh-Bénard convection and turbulence in liquid-helium", Rev. Mod. Phys. **57**, 657 – 687 (1985).

[144] S. H. Strogatz, *Nonlinear dynamics and chaos* (Perseus Press, Reading) (1994).

[145] E. Bodenschatz, W. Pesch, and G. Ahlers, "Recent developments in Rayleigh-Bénard convection", Ann. Rev. Fluid Mech. **32**, 709–778 (2000).

[146] E. D. Siggia, "High Rayleigh number convection", Annu. Rev. Fluid Mech. **26**, 137–168 (1994).

[147] L. P. Kadanoff, "Turbulent heat flow: Structures and scaling", Phys. Today **54**, 34–39 (2001).

[148] M. Couette, *Études sur le frottement des liquides* (Gauthier-Villars et fils) (1890).

[149] A. Mallock, "Experiments on fluid viscosity", Phil. Trans. R. Soc. Lond. A **187**, 41–56 (1896).

[150] G. I. Taylor, "Fluid friction between rotating cylinders", Proc. R. Soc. London A **157**, 546–564 (1936).

[151] R. Donnelly, "Taylor-Couette flow: the early days", Physics Today 32–39 (1991).

[152] P. Tong, W. I. Goldburg, J. S. Huang, and T. A. Witten, "Anisotropy in turbulent drag reduction", Phys. Rev. Lett. **65**, 2780–2783 (1990).

[153] H. Fasel and O. Booz, "Numerical investigation of supercritical taylor-vortex flow for a wide gap", J. Fluid Mech. **138**, 21–52 (1984).

[154] S. Dong, "Turbulent flow between counter-rotating concentric cylinders: a direct numerical simulation study", J. Fluid Mech. **615**, 371–399 (2008).

[155] D. Pirrò and M. Quadrio, "Direct numerical simulation of turbulent Taylor–Couette flow", European Journal of Mechanics - B/Fluids **27**, 552 – 566 (2008).

[156] T. Gebhardt and S. Grossmann, "The taylor-couette eigenvalue problem with independently rotating cylinders", Zeitschrift für Physik B Condensed Matter **90**, 475–490 (1993), URL `http://dx.doi.org/10.1007/BF01308827`.

[157] H. J. Brauckmann and B. Eckhardt, "Intermittent boundary layers and torque maxima in Taylor-Couette flow", Phys. Rev. E **87**, 033004 (2013).

[158] T. B. Benjamin, "Bifurcation phenomena in steady flows of a viscous liquid", Proc. R. Soc. London A **359**, 1–43 (1978).

[159] R. Verzicco and P. Orlandi, "A finite-difference scheme for three-dimensional incompressible flow in cylindrical coordinates", J. Comput. Phys. **123**, 402–413 (1996).

[160] R. J. A. M. Stevens, R. Verzicco, and D. Lohse, "Radial boundary layer structure and Nusselt number in Rayleigh-Benard convection", J. Fluid Mech. **643**, 495–507 (2010).

[161] R. J. A. M. Stevens, D. Lohse, and R. Verzicco, "Prandtl and Rayleigh number dependence of heat transport in high Rayleigh number thermal convection", J. Fluid Mech. **688**, 31–43 (2011).

[162] R. Ostilla, R. J. A. M. Stevens, S. Grossmann, R. Verzicco, and D. Lohse, "Optimal Taylor-Couette flow: direct numerical simulations", J. Fluid Mech. **719**, 14–46 (2013).

[163] K.-Q. Xia, S. Lam, and S. Q. Zhou, "Heat-flux measurement in high-Prandtl-number turbulent Rayleigh-Bénard convection", Phys. Rev. Lett. **88**, 064501 (2002).

[164] H. Brauckmann and B. Eckhardt, "Direct Numerical Simulations of Local and Global Torque in Taylor-Couette Flow up to Re=30.000", J. Fluid Mech. **718**, 398–427 (2013).

[165] S. Merbold, H. Brauckmann, and C. Egbers, "Torque measurements and numerical determination in differentially rotating wide gap Taylor-Couette flow", Phys. Rev. E. **87.2** (2013).

[166] L. Rayleigh, "On the dynamics of revolving fluids", Proc. R. Soc. Lond. A **93**, 148–154 (1917).

[167] G. S. Lewis, "Velocity fluctuations, wall shear stress and the transition in torque scaling at Re = 13000 in turbulent Couette-Taylor flow", Ph.D. thesis, University of Texas at Austin (1996).

[168] J. M. Wallace and P. V. Vukoslavčević, "Measurement of the velocity gradient tensor in turbulent flows", Annual Review of Fluid Mechanics **42**, 157–181 (2010).

[169] R. King, "A review of vortex shedding research and its application", Ocean Engineering **4**, 141 – 171 (1977).

[170] C. Sun, T. Mullin, L. van Wijngaarden, and D. Lohse, "Drag and lift forces on a counter-rotating cylinder in rotating shear flow", J. Fluid Mech. **664**, 150–173 (2010).

[171] H. G. Maas, A. Gruen, and D. Papantoniou, "Particle tracking velocimetry in three-dimensional flows", Exp. Fluids **15**, 133–146 (1993).

[172] N. Ouellette, H. Xu, and E. Bodenschatz, "A quantitative study of three-dimensional Lagrangian particle tracking algorithms", Exp. Fluids **40**, 301–313 (2006).

[173] M. Raffel, C. Willert, S. Wereley, and J. Kompenhans, *Partical Image Velocimetry: A practical guide* (Springer) (2007).

[174] Y. Yeh and H. Z. Cummins, "Localized fluid flow measurements with an He-Ne laser spectrometer", Applied Physics Letters **4**, 176–178 (1964).

[175] H.-E. Albrecht, M. Borys, N. Damaschke, and C. Tropea, *Laser Doppler and phase Doppler measurements techniques* (Springer) (2003).

[176] R. E. Davis and A. Acrivos, "The influence of surfactants on the creeping motion of bubbles", Chem. Eng. Sci. **21**, 681 – 685 (1966).

[177] R. M. Griffith, "The effect of surfactants on the terminal velocity of drops and bubbles", Chem. Eng. Sci. **17**, 1057 – 1070 (1962).

[178] R. B. Fdhila and P. C. Duineveld, "The effect of surfactant on the rise of a spherical bubble at high Reynolds and Peclet numbers", Phys. Fluids **8**, 310–321 (1996).

[179] L. Drain, *The laser doppler technique* (J. Wiley) (1980).

[180] Z. Zhang and K. Eisele, "The effect of astigmatism due to beam refractions on the formation of the measurement volume in LDA measurements", Exp. Fluids **20**, 466–471 (1996).

[181] C. Resagk, R. Puits, and A. Thess, "Error estimation of laser-Doppler anemometry measurements in fluids with spatial inhomogeneities of the refractive index", Exp. Fluids **35**, 357–363 (2003).

[182] L. D. Castello, "Table-top rotating turbulence: an experimental insight through particle tracking", PhD thesis, Eindhoven University of Technology, the Netherlands (2010).

[183] C. Sun, K.-Q. Xia, and P. Tong, "Three-dimensional flow structures and dynamics of turbulent thermal convection in a cylindrical cell", Phys. Rev. E **72**, 026302 (2005).

[184] Z. Zhang, "Optical guidelines and signal quality for LDA applications in circular pipes", Experiments in Fluids **37**, 29–39 (2004).

Summary

The ubiquity of turbulent flows in nature and technology makes it of utmost importance to fundamentally understand turbulence. In this thesis the realm of highly turbulent Taylor-Couette flow is explored in order to improve said understanding. Local and global measurements are performed in order to strengthen the knowledge of the Taylor-Couette flow geometry. First, the dependence of the driving strength on the angular velocity transport is examined and was found to universally scale as $G \propto \mathrm{Re}_i^{1.76}$ (or, by using the analogy between Taylor-Couette and Rayleigh-Bénard, $\mathrm{Nu}_\omega \propto \mathrm{Ta}^{0.38}$) in the present parameter regime in the ultimate Taylor-Couette regime. The system was found to have maximum transport for the case where the cylinders are in a counter rotation at $a = -\omega_o/\omega_i \approx 0.4$, see chapter 1. In chapter 2 local measurements using particle imaging velocimetry reveal that the 'wind' Reynolds number scales as $\mathrm{Re}_w \propto \mathrm{Ta}^{0.495\pm0.010}$, very close to predictions made for the ultimate turbulence regime. In addition local measurements of the angular velocity flux are provided, and they exhibit very large fluctuations (more than $300\times$ their mean). Despite these large fluctuation it was found that the local transport measurements agree with the global torque measurements. Chapter 3 explores the boundary layer properties of turbulent Taylor-Couette flow using high resolution, single-pixel, particle image velocimetry measurements. The profile is fitted with the law of the wall by von Kármán ($u^+ = \frac{1}{\kappa} \ln y^+ + B$) and the von Kármán constant κ is found to approach 0.4 with increasing Ta. The variance profiles of the local azimuthal velocity are found to display a peak around $y^+ = 12$ and collapse when rescaled with the driving velocity, rather than with the friction velocity found in other flows. In the outer layer ($y^+ > 50$) the variance profile show logarithmic dependence as found in channel and pipe flows. In chapter 4 Kolmogorov's 1941 paradigm is questioned. Conclusive evidence of multiple turbulent states for very large Reynolds number ($\mathrm{Re} = 10^6$) Taylor-Couette flow is presented. Combined global torque- and local-velocity measurements exemplify the existence of multiple states. In chapter 5 the

statistics of turbulent fluctuations are presented. Laser Doppler anemometry measurements are performed in the center of the gap of the Taylor-Couette apparatus. The structure function exponents are extracted from the longitudinal structure functions using extended self-similarity introduced by Benzi *et al.* in 1993. The exponents are found to weakly depend on a in the range 0–2. The measurements for $a = 0$ are in good agreement with the measurements of Lewis and Swinney in 1999 and the power spectra show $-5/3$ scaling for $a \in \{0.6, 0.8, 1.0\}$, rough $-5/3$ scaling for $a \in \{0.2, 0.3, 0.4, 2.0\}$, and no clear scaling for $a = 0$. In chapter 6 the value of a_{opt} is updated to $a_{\text{opt}} = 0.33 \pm 0.04$ (from $a = 0.4$ in chapter 1). Local velocity profiles are presented over a wide range of a. For certain values of a and for certain radial positions the probability density function of the local velocity are shown to be bimodal. The results are interpreted as a competition between destabilizing inner cylinder rotation and stabilizing, but shear enhancing, outer cylinder rotation. In chapter 7 the dependence of the radius ratio $\eta = r_i/r_o$ (the third control parameter next to Ta and a) is explored. Numerical simulations (contributed by Rodolfo Ostilla Mónico) and experimental measurements are combined and show the effects of η over the range 0.5–0.909. The transport Nu_ω is found to scale as $\text{Nu}_\omega \propto \text{Ta}^{0.39}$ for high Ta, and the exponent is nearly independent of η and a. In terms of the Rossby number the rotation rates for which the transport is maximum (Ro_{opt}) is found to depend on η, but in terms of a they are very close and nearly independent of η—at least in the range of η explored. In chapter 8 it is shown how the curvature of the curved outer cylinder affects the focal position and a velocity measurement using laser Doppler measurement. It is shown how the correction factors can be calculated using a ray tracer in order to correct for the curved surface. Using these correction factors it is shown that the velocity profile is significantly improved.

Summary (Frisian)

Turbulinte streamings binne oeral fertsjintwurdige yn 'e natoer en technyk, en it is dêrom wichtich om se fûneminteel te begripen. Yn dit proefskrift wurdt it domein fan heechturbulinte Taylor-Couette-streamings ûndersocht om dat fûnemintele begripen te ferbetterjen. Lokale en globale mjittings binne útfierd om de kennis fan streamings yn 'e Taylor-Couette-geometry te ferbetterjen. Op 't foarste plak is de ôfhinklikens fan de draaifaasje op it hoekfaasjetransport ûndersocht. It die bliken dat dy universeel te skalen wie as $G \propto \mathrm{Re}^{1.76}$ (of as $\mathrm{Nu}_\omega \propto \mathrm{Ta}^{0.38}$, útdrukt yn 'e terminology dy't liend is fan Rayleigh-Bénard-konveksje) yn it hjoeddeiske parameterrezjym yn it ultime Taylor-Couette-rezjym. It systeem hat in maksimaal transport yn it gefal dat de silinders tsjin inoar yn draaie mei $a = -\omega_o/\omega_i \approx 0.4$, sjoch haadstik 1. Gebrûk meitsjend fan PIV (streamingsmjitting mei help fan dieltsjes) wurdt yn haadstik 2 oan it ljocht brocht dat it 'wyn'-Reynoldsgetal skaalt as $\mathrm{Re}_w \propto \mathrm{Ta}^{0.495\pm0.010}$; tige ticht by de foarsizzings makke foar it ultime turbulinte rezjym. Der binne ek mjittings oan de lokale hoekfaasjestream útfierd, en dy fertoane tige grutte fluktuaasjes (mear as 300× harren trochsnee). Nettsjinsteande dy grutte fluktuaasjes komme de trochsneewearden oerien mei de globale keppelmjittings. De grinslaacheigenskippen fan turbulinte Taylor-Couette-streamings binne ûndersocht mei hege resolúsje, inkelde-piksel, PIV-mjittings, sjoch haadstik 3. It profyl wurdt ferlike mei de muorrewet fan von Kármán ($u^+ = \frac{1}{\kappa}\ln y^+ + B$), dêr't út bliken docht dat de von Kármán konstante κ 0.4 benei komt foar tanimmende Ta. De fariânsjeprofilen fan de lokale azimutale faasje litte in pyk sjen om $y^+ = 12$ hinne en de gegevens falle oer inoar hinne as dy skaald wurde mei de oandriuwfaasje mar net, lykas by oare floeistofstreamings, as dy skaald wurde mei de wriuwingsfaasje. De fariânsjeprofilen fertoane in logaritmyske ôfhinklikens yn 'e bûtenlaach ($y^+ > 50$), krekt lykas yn kanaal- en piipstreamings. Yn haadstik 4 wurdt it paradigma út 1941 fan Kolmogorov yn twivel lutsen. Der wurdt in slutend bewiis foar meardere turbulinte tastannen yn Taylor-Couette-streamings foar tige hege Reynolds-getallen ($\mathrm{Re} = 10^6$) jûn.

Kombinearre globale keppel- en lokalefaasjemjittings yllustrearje it bestean fan meardere tastannen. Yn haadstik 5 wurde de statistyske eigenskippen fan turbulinte fluktuaasjes toand. Laser-Doppler-anemometrymjittings wurde útfierd yn it midden fan de Taylor-Couette-silinders. Troch gebrûk te meitsjen fan útwreide selsgelikenis, yntrodusearre troch Benzi et al. yn 1993, binne de struktuerfunksje-eksponinten út de longitudinale struktuerfunksjes helle. De eksponinten hingje swak ôf fan a yn it berik 0–2. De $a = 0$ mjittings komme goed oerien mei de resultaten fan Lewis en Swinney yn 1999. De fermogensspektrums litte in $-5/3$-skaling sjen foar $a \in \{0.6, 0.8, 1.0\}$, likernôch $-5/3$-skaling foar $a \in \{0.2, 0.3, 0.4, 2.0\}$, en gjin dúdlike skaling foar $a = 0$. Yn haadstik 6 is de wearde fan a_{opt} oanpast fan $a = 0.4$ yn haadstik 1 nei $a_{\mathrm{opt}} = 0.33 \pm 0.04$. Lokalefaasjeprofilen wurde toand foar in breed skala oan a's. Foar guon wearden fan a en foar guon radiële posysjes binne de wierskynlikheidstichtensfunksjes fan de lokale faasje bimodaal. De resultaten wurde ynterpretearre as in kompetysje tusken destabilisearjende binnensilinderrotaasje en in stabilisearjende, mar ôfskospanningfergrutsjende, bûtensilinderrotaasje. Yn haadstik 7 wurdt de ôfhinklikens fan de strielferhâlding $\eta = r_i/r_o$ (de tredde stjoerparameter njonken Ta en a) ûndersocht. Resultaten fan numerike simulaasjes (bydroegen troch Rodolfo Ostilla Mónico) en eksperimintele mjittings wurde gearfoege en litte it effekt fan η sjen oer it berik 0.5–0.909. It transport Nu_ω skaalt as $\mathrm{Nu}_\omega \propto \mathrm{Ta}^{0.39}$ foar grutte Ta, en de eksponinten binne suver ûnôfhinklik fan η en a. Yn termen fan it Rossbygetal is it maksimale transport ($\mathrm{Ro}_{\mathrm{opt}}$) ôfhinklik fan η, lykwols yn termen fan a is it maksimale transport suver ûnôfhinklik fan η—alteast yn it ferkende berik. Yn haadstik 8 wurdt toand hoe't de kromming fan de bûtensilinder ynfloed hat op de fokusposysje en faasjemjittings fan de laser-Doppler-anemometry. Der wurdt toand hoe't de korreksjefaktoaren berekkene wurde kinne mei help fan in raytracer om de gefolgen fan it kromde oervlak te kompensearjen. De faasjeprofilen wurde sinjifikant ferbettere troch gebrûk te meitsjen fan de korreksjefaktoaren.

Summary (Dutch)

Turbulente stromingen zijn alomvertegenwoordigd in de natuur en techniek, en het is daarom belangrijk om ze fundamenteel te begrijpen. In dit proefschrift wordt het domein van hoogturbulente Taylor-Couette-stromingen onderzocht om dit fundamentele begrip te verbeteren. Lokale en globale metingen zijn uitgevoerd om de kennis van stromingen in de Taylor-Couette-geometrie te verbeteren. Allereerst is de afhankelijkheid van de draaisnelheid op het hoeksnelheidstransport onderzocht. Deze bleek universeel te schalen als $G \propto \mathrm{Re}^{1.76}$ (of als $\mathrm{Nu}_\omega \propto \mathrm{Ta}^{0.38}$ als deze wordt uitgedrukt in de terminologie geleend van Rayleigh-Bénard-convectie) in het huidige parameterregime in het ultieme Taylor-Couette-regime. Het systeem heeft een maximaal transport in het geval dat de cilinders tegen elkaar in draaien met $a = -\omega_o/\omega_i \approx 0.4$, zie hoofdstuk 1. Gebruikmakend van PIV (stromingsmeting m.b.v. deeltjes) wordt aan het licht gebracht in hoofdstuk 2 dat het 'wind'-Reynoldsgetal schaalt als $\mathrm{Re}_w \propto \mathrm{Ta}^{0.495\pm0.010}$; zeer dicht bij de voorspellingen gemaakt voor het ultieme turbulente regime. Ook zijn metingen aan de lokale hoeksnelheidsstroom uitgevoerd, en deze vertonen zeer grote fluctuaties (meer dan 300× hun gemiddelde). Ondanks deze grote fluctuaties komen de gemiddelde waarden overeen met de globale koppelmetingen. De grenslaageigenschappen van turbulente Taylor-Couette-stroming zijn onderzocht met hoge resolutie, enkele-pixel, PIV metingen, zie hoofdstuk 3. Het profiel wordt vergeleken met de muurwet van von Kármán ($u^+ = \frac{1}{\kappa} \ln y^+ + B$) waaruit blijkt dat de von Kármán constante κ 0.4 nadert voor toenemende Ta. De variantieprofielen van de lokale azimuthale snelheid tonen een piek rond $y^+ = 12$ en de data vallen over elkaar heen als deze worden geschaald met de aandrijfsnelheid maar niet, zoals bij andere vloeistofstromingen, als deze worden geschaald met de wrijvingssnelheid. De variantieprofielen vertonen een logaritmische afhankelijkheid in de buitenlaag ($y^+ > 50$), net zoals in kanaal- en pijpstromingen. In hoofdstuk 4 wordt het paradigma uit 1941 van Kolmogorov in twijfel getrokken. Sluitend bewijs voor meerdere turbulente toestanden in Taylor-Couette-stromingen voor zeer

hoge Reynolds-getallen (Re = 10^6) wordt getoond. Gecombineerde globale koppel- en lokalesnelheidsmetingen illustreren het bestaan van meerdere toestanden. In hoofdstuk 5 worden de statistische eigenschappen van turbulente fluctuaties getoond. Laser-Doppler-anemometriemetingen worden uitgevoerd in het midden van de Taylor-Couette-cilinders. Door gebruik te maken van uitgebreide zelf-gelijkenis, geïntroduceerd door Benzi *et al.* in 1993, zijn de structuurfunctie-exponenten uit de longitudinale structuurfuncties gehaald. De exponenten hangen zwak af van a in het bereik 0–2. De $a = 0$ metingen komen goed overeen met de resultaten van Lewis en Swinney in 1999. De vermogensspectra laten een $-5/3$-schaling zien voor $a \in \{0.6, 0.8, 1.0\}$, ongeveer $-5/3$-schaling voor $a \in \{0.2, 0.3, 0.4, 2.0\}$, en geen duidelijke schaling voor $a = 0$. In hoofdstuk 6 is de waarde van a_{opt} geüpdatet van $a = 0.4$ in hoofdstuk 1 naar $a_{\mathrm{opt}} = 0.33 \pm 0.04$. Lokalesnelheidsprofielen worden getoond voor een breed scala aan a's. Voor bepaalde waarden van a en voor bepaalde radiële posities zijn de waarschijnlijkheidsdichtheidfuncties van de lokale snelheid bimodaal. De resultaten worden geïnterpreteerd als een competitie tussen destabiliserende binnencilinderrotatie en een stabiliserende, maar afschuifspanningvergrotende, buitencilinderrotatie. In hoofdstuk 7 wordt de afhankelijkheid van de straalverhouding $\eta = r_i/r_o$ (de derde stuurparameter naast Ta en a) onderzocht. Resultaten van numerieke simulaties (bijgedragen door Rodolfo Ostilla Mónico) en experimentele metingen worden samengevoegd en laten het effect van η zien over het bereik 0.5–0.909. Het transport Nu_ω schaalt als $\mathrm{Nu}_\omega \propto \mathrm{Ta}^{0.39}$ voor grote Ta, en de exponenten zijn bijna onafhankelijk van η en a. In termen van het Rossbygetal is het maximale transport ($\mathrm{Ro}_{\mathrm{opt}}$) afhankelijk van η, echter in termen van a is het maximale transport bijna onafhankelijk van η—tenminste in het verkende bereik. In hoofdstuk 8 wordt getoond hoe de kromming van de buitencilinder invloed heeft op de focuspositie en snelheids metingen van de laser-Doppler-anemometrie. Er wordt getoond hoe de correctiefactoren kunnen worden berekend met behulp van een raytracer om de gevolgen van het gekromde oppervlak te compenseren. De snelheidsprofielen worden significant verbeterd door gebruik te maken van de correctiefactoren.

Acknowledgements

Let me start the acknowledgements with a small story:
It was the end of 2008 or perhaps the beginning of 2009 that I had a meeting with Detlef. I'm not really sure what the original intention was of the meeting, I think it was mainly about doing a capita selecta in his group. The subject changed to my internship plans, which I, at the time, didn't have. Detlef proposed that I should go to Toulouse for my internship, as he already proposed before in a typical Detlef-style e-mail:

> Have you thought of Toulouse imft for your internship? Great place. De
>
> Sent from my iPhone

I agreed that we should contact Véronique Roig and Dominique Legendre, and so we did. And, indeed, the place turned out to be great. Now back to the story. You would think that that would have been an efficient meeting; discussing a capita selecta and an internship. And I would agree with you, but the story is a little bit more involved; let me explain. After deciding on my internship, he asked me if I had any idea for my master thesis. I told him that I hadn't given it much thought yet; I knew about the cool setups in the various labs, and the stuff the group had; I played with them several years before, opening Grolsch beer bottles for science while recording video and audio of them using high speed cameras and microphones (yeah, I know!). Detlef showed me some (yellow-on-blue) slides of projects and told me about this new setup that was under construction. It was rotating, about turbulence, and Detlef thought I would be the perfect guy to do this project. To this day I'm still not sure how Detlef decided that I was a good candidate for the project; we basically only met during the Physics of Fluids course a couple years before, but he was spot-on. I was intrigued; turbulence, a big experimental setup, something new, something that wasn't done before on

such a scale: count me in! And there we were, we discussed the capita selecta, my internship, and my master thesis project. Now you would agree that that was an efficient (less than an hour) meeting. But the story is a even more involved, because in that very meeting he also brought up the possibility of doing the PhD in his group, on the same subject; the rotating turbulence device thingy. He told me I would have a head start if I combine the master and PhD on the same subject. After an hour or so I walked out of ME261, having just discussed my capita selecta, decided my internship, my master project, and the topic of my PhD thesis. It was the most efficient meeting ever, my future 5 years were straightened out. I soon embarked on an epic scientific journey.

This PhD thesis is the culmination of nearly four years of work in the Physics of Fluids group. It was a blast! I've been very fortunate to be around very talented and knowledgeable people. The great atmosphere in the Physics of Fluids group certainly helped in making this thesis. I'd particulary like to thank some of the many people who made this thesis possible:

Gert-Wim, for being the best technician one could wish for. I was very fortunate that you created many parts for me: removable top-windows, laser-extension-tubes, a traversing system, a laser-car, a calibration frame, calibration rings, flow-reversal-valves, a new locking-pin, a magnetic trigger, a new torque sensor, a frame for the LDA, new belt-tensioners, and many many more parts to refine and enhance the Taylor-Couette apparatus, and on top of that a totally new boiling Taylor-Couette setup! You always aim for perfection when you sculpt your art in SolidWorks. I learned a tremendous amount from you about mechanical design and even some skills to draw things myself. During the design of the boiling Twente Taylor Couette I spent many hours in your office, we bounced ideas back and forth and the collaboration was very pleasant. The end result for all this design-work paid off; the group has a beautiful new toy in ME101. I realize I was probably one of the most demanding students of the group (keeping a very complicated system running, and designing a new system as well!), but despite that, you were always there to answer my questions. Thanks for helping me out during my master and PhD, it was a true pleasure.

Martin, also for you holds: you're one of the best technician one could wish for. Countless of times I asked you for cutting, drilling, lathing, milling, and tapping parts. We had many great conversations in the office and in the workshop. Your knowledge about machining and technical *stuff* (for lack of a better term) is very broad, and you taught me many things. Also I'd like to

thank you for helping in the design of many parts, you and Gert-Wim both worked together to make some of the best components. Furthermore, I'd like to thank you for helping out in the lab, you helped me countless times to assemble and disassemble the Taylor-Couette. Without you and Gert-Wim the group wouldn't be where it is now.

Detlef, for always having faith in me, for being an excellent mentor, and providing me with the PhD opportunity. Though the number of meetings we had was quite limited, they were always very fruitful. And it was very satisfying to see that your left whiteboard—containing a list of unsolved problems in Taylor-Couette flow—slowly emptied. Also it was great to confirm the presence of multiple states after your *physicalezing* that posed this very question. Thank you for showing me the good practices for writing papers and presentations; your comments on how to improve our publications were invaluable. But also for giving me the opportunity to help with teaching; the turbulence course thrice and heat and mass transfer twice. I admire your leadership and scientific abilities, I hope I grasped some of those assets. I hope we stay in touch and that we continue to collaborate. It was an honor to be part of your group.

Chao, for being the best supervisor ever (really!). We had many great conversations about work, Apple *stuff* and other things during many lunches and dinners, and many laughs during and after work. You explained to me many concepts in turbulence and I was very fortunate to have the very expert on experimental techniques on my side. I master now most experimental techniques in fluid dynamics due to your excellent didactic skills. I remember that we measured together the data for the torque scaling paper during the summer, every day we would measure 2, perhaps 3, data points and we would get more and more excited after every day; it was a true pleasure. The same holds for the ultimate paper; when we found out that the wind Reynolds number had a scaling exponent of 0.495; very close to the predicted 1/2. I also like that you joined us countless times in the lab to look at 'fresh' data and you would become really excited, which made us even more excited; your enthusiasm is very contagious. Also thank you for the invaluable help to shape our papers, and for helping me with my upcoming post-doctoral endeavour. In addition, I'd like to thank you and your wife for the hospitality and for the nice dinners in Mooienhof and Kompasstraat. I'm sure we'll stay in contact, and let's hope that we can collaborate in the future.

Enrique, for being a very good friend and colleague. Thank you for enhancing my (Mexican) Spanish vocabulary, and for sharing your cooking and party

skills. I enjoyed our trips to the Frisian islands Terschelling and Texel, the Twickel castle, and our train trip to Cologne very much. We always have a good laugh; at work, outside work, and through the internet. I'm very happy you'll be next to me on the big day.

Roeland, I've spend most of the time in the lab with you; first introducing you to our current Taylor-Couette setup, and later getting the new Taylor-Couette up and running. In addition we also measured data together for some papers, the collaboration was always very pleasant. We also shared the office and I enjoyed the many laughs we had. It was very nice to have someone who shares the passion for photography, and one that always aims for perfection. Furthermore, I enjoyed the USA road trip, our exploration of Hong Kong, Thailand, and Cambodia, and the times we went mountain biking. I'm very happy that you'll be next to me on the big day.

Roeland van der Veen, Dennis van Gils, Tim Jannink, Ruben Verschoof, Daniela Narezo Guzmán and others who spent time in ME101, the Taylor-Couette lab. Thank you all helping me out in the lab, for collaborating, and for contributing to my thesis.

I also like to thank all the people in ME102—the water tunnel lab—for all the help, discussions, and pleasant conversations: Daniel Chehata Gómez, Julián Martínez Mercado, Vivek Prakash, and Varghese Mathai.

Devaraj van der Meer: I enjoyed working together on the heat and mass transfer course for two years, I admire your teaching skills very much; you always seem to be able to explain complicated things in a very simple way.

Bas Benschop: Thank you for taking care of many new computers, arranging the essentials for the new website, various electronics for the Taylor-Couette, and many other things.

Joanita Leferink: Thanks for taking care of many of the forms, tickets, e-mails, and all the other administrative tasks. I enjoyed it very much to organize the International Couette-Taylor Workshop together with you. Together with Martin, Bas, and Gert-Wim, you are part of the ancillary quadrumvirate that keeps the group going.

To all my fellow ME249'ers over the years: Richard Stevens, Dennis van Gils, Marine Guémas, Erwin van der Poel, Roeland van der Veen, Rodolfo Ostilla Mónico, Xiaojue Zhu, Xiumei Liu. Thank you for all the good laughs we had, for the scientific discussions we had, and about all the other topics covered. Thanks for being such a good company.

To all the people with whom I had discussions over the years: B. Eckhardt, D. P. Lathrop, S. Grossmann, G. Pfister, E. van Rietbergen, M. Hultmark, I.

Marusic, P. Monkewitz, A.J. Smits, R. Verzicco, G.J. van Heijst, G. Ahlers, H. Ji, J. Abshagen, R. Delfos, F. Ravelet, J. Westerweel, H. Brauckmann, F.H. Busse, F. Nordsiek, M.S. Paoletti, S. Merbold, M. Salewski, and countless others during the ICTW conferences in Princeton, Leeds, and Enschede and many other conferences all around the world.

Furthermore, I'd like to thank everybody from TCO that helped me directly or indirectly. You realized many of the designs of Gert-Wim. A special thanks to: Rindert Nauta, Sip Jan Boorsma, Gerard Oude Meijers, Henk Waayer, Dominic Post, and Geert Mentink: Thank you all for all your efforts.

In addition, I'd like to thank all the members of the group very much. The group is now so big that there is always an 'expert' on something; be it electronics, volleyball, Spanish, cars, metalworking, cameras, juggling, or anything in between, it's a pleasure to discuss such a broad range of topics with very smart people. I'd like to thank everyone, you made me feel at home.

Outside work I also made a lot of new friends and had many great experiences.

First of all I would like to thank the entire Latin community. The dozens of people I met through LA voz, Rico Latino and at the performances of the Chilangos Habaneros; thank you Oscar Enríquez for introducing me to this world. I will try to compile a list of all the Latin people that I'd like to thank for such a wonderful experience; I'm sure I will forget someone, I apologize in advance. Thank you Enrique, Oscar, Federico, Rodrigo, Julián, Andrea EV, Andrea S, Arturo B, Arturo SA, Lila, Daniela FMB, Daniela GN, Daniela NG, David, Diruji, Loreto, Leo, Lissy, Diego, Nicolás, Gustavo, César, Mafer, Alejandro, Manuel, Marina, Michael, Daniel, Norma, Elia, Olga, Esli, Adriana, Patti, Vicky, Vania, Valentina, Andrés, Jorge, Maite, Lidia, Nayeli, Juan Carlos, and Paola for showing me the Latin side of the world. I had a lot of fun, and learned about your culture, food, music *et cetera* and I learned quite some Spanish words in the process. *Muchas gracias a todos!*

Apart from the Physics world, and the Latin world, I also—quite literally—dived into another world; the underwater world. I'd like to thank all the diving people of ZPV Piranha for the hospitality and the skills you taught me! I had a lot of fun!

Also, I'd like to thank my roommates: Federico Hernández Sánchez, Adriana Rodríquez, and Manuel Garcia: thanks for all the conversations we had about varying topics. It was great to live with you all.

Most of you know that I love to travel, and during the last years I had a lot of opportunities to travel. I dived in Cenotes, walked the Chinese great wall, swam the dead sea, snow-mobiled across white fields of snow and ice, hiked up

to Machu Picchu, snorkelled around Thai islands, climbed Mexican pyramids, seen the Big Ben, enjoyed the view from the Burj Khalifa, visited Angkor Wat, experienced Hong Kong and Bangkok, explored Washington D.C., picnicked at castle Twickel, bargained بطيخ in Lebanon, travelled the Italian peninsula, flew a plane, road-tripped the west of the USA, walked through Central Park, trekked in the Pyrenees, slept in the Wadi Rum desert, ran the Rocky steps in Philadelphia, photographed dolphins and the stunning green shades of the dancing aurora borealis, swam with Galapagos' sharks, visited the Escher museum, cycled around Toulouse, paraglided in Ecuador, and many more... I was very fortunate to be able to share these wonderful trips with friends and colleagues. I'd like to thank all of my travel-companions on my trips: Aditya Konduri, Álvaro Gómez Marín, Andreea Niculescu, Bartjan de Vries, Carla Bahri, Chao Sun, Christophe Loquineau, Daniela Flores Magon Bustamante, Dennis van Gils, Enrique Sandoval, Erwin van der Poel, Esli Trejo, Federico Hernandez Sanchez, Femke Brouwer, Francisco Gómez, François-Henry Rouet, Gerben Morsink, Guillaume Lajoinie, Hikmat Achkar, Jair Santanna, John Durso, Julian Martinez Mercado, Lissy La Paix Puello, Luis Romero Cortés, María Balaguer Ramírez, Micheline Abbas, Mohamad Nasr-Azadani, Nikolai Oudalov, Parvez Sukheswalla, Peter Dung, Oscar Enriquez, Richard Stevens, Rodolfo Ostilla Monico, Roeland van der Veen, Rodrigo Pereira, Rudolf Huisman, Rutger Huisman, Sander Wildeman, Sergio Alonso Castaño, Tetje van de Sluis, Tineke Huisman, Vamsi Spandan, Varun Hiremath, Vivek Prakash, Vivian Madesclair, Vivian Sun and those I unfortunately forgot. Thank you all for exploring the world with me. By themselves these experiences were amazing, but by sharing them with others they were truly epic. These holidays were an excellent way to focus on photography and to 'refresh'. I captured tens of thousands of photos during these trips, some of which I've shared on my website. Thank you all for the very fond memories of all the places we've visited, these experiences will stay with me forever. Thank you all!

In addition, I'd like to thank all my other friends, old schoolmates, online friends, friends that I met during traveling and friends that I met during workshop and conferences. Thank you all!

Lastly, I'd like to thank my parents, Rudolf and Tineke, my brother, Rutger, sister-in-law, Femke, and other relatives for always being there. Bedankt!

Bio

Sander Gerard Huisman was born in Sneek, The Netherlands on July 2nd, 1987. He grew up in Bolsward and attended the elementary school 'De Hoeksteen' and 'De Bron'. After that he attended 'Het Marne college' where he got his high school diploma in 2005. In the summer of 2005 he moved to Enschede to pursue his interest in Physics. He received his bachelor's degree in applied physics with honors from the University of Twente. He did his internship at the Institut de Méchanique des Fluides de Toulouse (IMFT) in France, studying the coalescence of bubbles in a thin cell, which led to a joint publication. On November 8th, 2010 he received his master's degree in Applied Phyics with honors for his work on the Twente Turbulent Taylor-Couette facility in the Physics of Fluids group at the University of Twente under the supervision of Detlef Lohse and Chao Sun. He continued his PhD in the same research group on the same topic. Apart from physics he takes an interest in traveling, photography, diving, and many other things.

Scientific output

Publications

- **2014:** *Multiple states in highly turbulent Taylor-Couette flow*
  Sander G. Huisman, Roeland C.A. van der Veen, Chao Sun, Detlef Lohse
  Nat. Commun. 5, 3820
- **2012:** *Ultimate turbulent Taylor-Couette Flow*
  Sander G. Huisman, Dennis P.M. van Gils, Siegfried Grossmann, Chao Sun, Detlef Lohse
  Phys. Rev. Lett., **108**, 024501
- **2011:** *Torque scaling in turbulent Taylor-Couette flow with co- and counter-rotating cylinders*
  Dennis P.M. van Gils, **Sander G. Huisman**, Gert-Wim H. Bruggert, Chao Sun, Detlef Lohse
  Phys. Rev. Lett., **106**, 024502
- **2013:** *Logarithmic Boundary Layers in Strong Taylor-Couette Turbulence*
  Sander G. Huisman, Sven Scharnowski, Christian Cierpka, Christian J. Kähler, Detlef Lohse, Chao Sun
  Phys. Rev. Lett., **110**, 264501
- **2013:** *Statistics of turbulent fluctuations in counter-rotating Taylor-Couette flows*
  Sander G. Huisman, Detlef Lohse, Chao Sun
  Phys. Rev. E, **88**, 063001
- **2012:** *Interaction and coalescence of large bubbles rising in a thin gap*
  Sander G. Huisman, Patricia Ern, Véronique Roig
  Phys. Rev. E, **85**, 027302
- **2012:** *Optimal Taylor-Couette turbulence*
  Dennis P.M. van Gils, **Sander G. Huisman**, Siegfried Grossmann,

Chao Sun, Detlef Lohse
J. Fluid Mech., **706**, 118

- **2014:** *Optimal Taylor-Couette flow: Radius ratio dependence*
  Rodolfo Ostilla Monico, **Sander G. Huisman**, Tim J.G. Jannink, Dennis P.M. van Gils, Roberto Verzicco, Siegfried Grossmann, Chao Sun, Detlef Lohse
  J. Fluid Mech., **747**, 1–29
- **2012:** *Applying laser Doppler anemometry inside a Taylor-Couette geometry using a ray-tracer to correct for curvature effects*
  Sander G. Huisman, Dennis P.M. van Gils, Chao Sun
  European Journal of Mechanics - B/Fluids, **36**, 115

Organizing activities

- **2013:** Organized the 18$^{\text{th}}$ International Couette-Taylor Workshop (ICTW), *University of Twente* (100+ attendees)

Design activities

- **2013/2014:** Designing a new boiling Taylor-Couette device.

Outreach

- Peer-review: Refereeing forthe Journal of Fluid Mechanics and for the Journal of Mechanical Engineering Science.
- Outreach: Numerous lab demonstrations for a wide variety of audiences.

Teaching activities

- **2009/2010:** Teaching assistant in a graduate course on Turbulence, *University of Twente*
- **2010/2011:** Teaching assistant in a graduate course on Turbulence, *University of Twente*
- **2011/2012:** Teaching assistant in a graduate course on Turbulence, *University of Twente*
- **2013:** Teaching assistant in a undergraduate course on Heat and Mass Transfer, *University of Twente*

- **2014:** Teaching assistant in a undergraduate course on Heat and Mass Transfer, *University of Twente*
- **2014:** Teaching assistant in a graduate course on Experimental Techniques in Physics of Fluids, *University of Twente*

Student supervision

- Bachelor project: Sam Sloetjes and Marise Gielen
- Intern: On Yu (*Peter*) Dung
- Master thesis project: Tim Jannink
- Capita selecta: Marise Gielen and Maarten Kok
- Experimental techniques in physics of fluids: Berkan Basel and Hans Ligtenberg

Poster sessions

- **2014:** *"Boiling Twente Taylor Couette"*
  Physics@FOM, Veldhoven, The Netherlands
- **2012:** *"Ultimate Turbulent Taylor-Couette Flow"*
  Mesa+ meeting, Enschede, The Netherlands
- **2012:** *"Ultimate Turbulent Taylor-Couette Flow"*
  Hands-On Research School in Complex Systems, Shanghai, China
- **2012:** *"Ultimate Turbulent Taylor-Couette Flow"*
  Physics@FOM, Veldhoven, The Netherlands
- **2012:** *"Ultimate Turbulent Taylor-Couette Flow"*
  JMBC Burgersdag, University of Eindhoven, Eindhoven, The Netherlands
- **2011:** *"Turbulent statistics in Taylor-Couette flow"*
  Physics@FOM, Veldhoven, The Netherlands
- **2010:** *"Twente Turbulent Taylor-Couette T^3C"*
  Physics@FOM, Veldhoven, The Netherlands
- **2010:** *"Twente Turbulent Taylor-Couette T^3C"*
  JMBC Burgersdag, University of Twente, Enschede, The Netherlands

Attended conferences/workshops

- **2012:** *62^{nd} Lindau Nobel Laureate Meeting*, Lindau, Germany

- **2012:** *Hands-On Research School in Complex Systems*, Shanghai Jiao Tong University, Shanghai, China
- **2010:** *3rd FERMaT-IMPACT-GIMFus meeting*, Engineering school of Seville, Sevilla, Spain
- **2010:** *2010 Tutorial School on Fluid Dynamics: Topics in Turbulence*, University of Maryland, Maryland, United States of America
- **2009:** *COST (European Cooperation in Science and Technology) action program MP0806: 'Particles in Turbulence'*, ETH Hönggerberg, Zürich, Switzerland

Peer Reviewed Conference Talks

- **2011:** *"Ultimate turbulent Taylor-Couette flow"*
  European Turbulence Conference 13 (ETC13)
  Warsaw, Poland
- **2011:** *"Torque scaling in turbulent Taylor-Couette flow with co- and counter-rotating cylinders"*
  5th European Postgraduate Fluid Dynamics Conference (EPFDC)
  Göttingen, Germany
- **2011:** *"Ultimate turbulent Taylor-Couette flow"*
  17th International Couette-Taylor Workshop (ICTW)
  Leeds, England, United Kingdom
- **2010:** *"Twente Turbulent Taylor-Couette Laser Doppler Anemometry"*
  Taylor-Couette Workshop in Twente
  University of Twente, Enschede, The Netherlands
- **2009:** *"Relative motion of coalescence of a pair of two-dimensional bubbles rising in tandem"*
  2nd FERMaT-IMPACT meeting
  University of Twente, Enschede, The Netherlands
- **2009:** *"Twente Turbulent Taylor-Couette (T^3C)"*
  16th International Couette-Taylor Workshop (ICTW)
  Princeton University, New Jersey, United States of America

Contributed conference talks

- **2013:** *"Experimental study of the boundary layer properties in ultimate Taylor-Couette flow"*
  Physics@FOM
  Veldhoven, The Netherlands
- **2012:** *"Statistics in turbulent Taylor-Couette flow with independently rotating cylinders"*
  International Conference on Rayleigh-Bénard Turbulence
  Hong Kong
- **2012:** *"Experimental study of the boundary layer properties in ultimate Taylor-Couette flow"*
  65th Annual Meeting of the APS Division of Fluid Dynamics
  San Diego, California, United States of America
- **2011:** *"Optimal Taylor-Couette turbulence"*
  64th Annual Meeting of the APS Division of Fluid Dynamics
  Baltimore, Maryland, United States of America
- **2010:** *"Velocity profile measurements in high Reynolds number Taylor-Couette flow for pure outer-cylinder rotation"*
  63rd Annual Meeting of the APS Division of Fluid Dynamics
  Long Beach, California, United States of America

Seminars

- **2011:** *"Taylor-Couette flows"*
  Synopsis: A talk about a variety of topics: velocity profiles, Eckman pumping and Taylor columns, application of laser Doppler anemometry and the use of a ray-tracer, turbulent flow statistics, and torque scaling with co- and counter-rotating cylinders.
  Institut de Méchanique des Fluides de Toulouse (IMFT), Toulouse, France
- **2014:** *"Turbulent Taylor-Couette flows"*
  Synopsis: A talk about torque scaling, 'wind'-velocity measurement, boundary layer measurements, and multiple states.
  École Normale Supérieure de Lyon (ENS), Lyon, France

Awards

- **2012:** *Jury poster award*, Hands-On Research School in Complex Systems, Shanghai, China

Media coverage

Huisman has been featured by The New York Times, Discovery Channel's 'Daily Planet', Scientific American (30 under 30), NRC (Dutch newspaper), RNW (Radio Netherlands Worldwide), Deutschlandfunk (German radio station), Stichting voor de Technische Wetenschappen (STW), and the University Twente news featured him thrice (Once about going to the Lindau Nobel laureate meeting, once about his Nature Communications article, and lastly by his exposure in the New York Times). His articles also got attention by others:

- **2012:** Physics **5**, 4 (2012): *"Viewpoint: The Twins of Turbulence Research"* by Friedrich H. Busse.
  Based on the publication: *"Ultimate turbulent Taylor-Couette Flow"*, Phys. Rev. Lett., **108**, 024501
  Synopsis: Two new experiments on fluid turbulence have attained conditions needed to establish asymptotic scalings for turbulent transports of heat and angular momentum.
- **2011:** Physics Today **64**, 18 (2011): *"Exploring the extremes of turbulence"* by Ashley G. Smart.
  Based on the publication: *"Torque scaling in turbulent Taylor-Couette flow with co- and counter-rotating cylinders"*, Phys. Rev. Lett., **106**, 024502
  Synopsis: Two experiments yield similar data but tell different stories about momentum transport at high Reynolds numbers.
- **2011:** Nature **470**, 475–476 (2011): *"Fluid Dynamics: A turbulent Matter"* by Steven A. Balbus.
  Based on the publication: *"Torque scaling in turbulent Taylor-Couette flow with co- and counter-rotating cylinders"*, Phys. Rev. Lett., **106**, 024502
  Synopsis: A long-standing controversy about whether the motions within a typical astrophysical disk of gas are stable or unstable has resurfaced. The answer has profound significance for our understanding of how stars and planets form.